Development and Photophysical Properties of Mixed-Anion and Mixed-Cation Dinitridocarbonates

Dissertation

der Mathematisch-Naturwissenschaftlichen-Fakultät

der Eberhard Karls Universität Tübingen

zur Erlangung des Grades eines

Doktors der Naturwissenschaften

(Dr. rer. nat.)

vorgelegt von

M. Sc. Albert T. Schwarz

aus Barcelona (Spanien)

Tübingen

2026

Gedruckt mit Genehmigung der Mathematisch-Naturwissenschaftlichen-Fakultät der Eberhard Karls Universität Tübingen.

Tag der mündlichen Qualifikation:	10.07.2026
Dekan:	Prof. Dr. Thilo Stehle
1. Berichterstatter:	Prof. Dr. Hans-Jürgen Meyer
2. Berichterstatter:	Prof. Dr. Eberhard Schweda

Acknowledgements

First of all, I would like to thank my supervisor, Prof. Dr. Hans-Jürgen Meyer, for the opportunity to work in his group on this particularly interesting topic. The possibility to work independently, the support whenever needed, and the many insightful pieces of advice are greatly appreciated.

Moreover, I owe special thanks to Dr. Markus Ströbele for performing and refining the single-crystal X-ray diffraction measurements and for his support in solid-state chemistry in general.

I would like to express my gratitude to Prof. Dr. Thomas Jüstel and Dr. David Enseling for performing many photoluminescence measurements, for their help and advice on all questions regarding photoluminescence, and for the overall productive cooperation.

Furthermore, I thank Dr. Carl Romao for the theoretical calculations. I am also grateful to Dr. Jochen Glaser for his valuable advice on dinitridocarbonates and for many insightful discussions.

I would also like to thank Prof. Dr. Adam Slabon and Nele Petersen for the photocatalytic measurements and their support on photocatalysis-related topics. I am grateful to Dr. Klaus Eichele for their help and advice in the field of solid-state NMR.

I thank Peter Janoschek for recording the reflection spectra.

Further, profuse thanks go to Dr. Fabian Grahlow, Jan Beitlberger, Patrick Schmidt, Dr. Elaheh Bayat, Dr. Florian Pachel, Catharina Brand, and Melena Groß. It was a pleasure to work with you and to spend time with you. I could not have asked for better colleagues.

I would also like to thank all students I had the pleasure to supervise for their dedication and for the pleasant atmosphere during the lab courses and theses.

I am also very thankful to the teams of ward 46 and ward 50 at the University Hospital Tübingen for their emotional support, the friendly atmosphere, and the welcome distraction in difficult situations. Within this team, I would especially like to thank Marc Doberenz.

I would also like to express my gratitude to my parents for their continuous emotional support throughout my research.

Finally, I would like to thank my brothers, Frederic and Stefan, as well as Alesia and Maik, for their constant encouragement and support throughout all these years.

Table of Contents

List of Abbreviations

AM 1.5G	Standard solar spectrum at air mass 1.5 (global)
CBM	Conduction band minimum
CCDC	Cambridge Crystallographic Data Centre
DFT	Density functional theory
DRIFT	Diffuse reflectance infrared Fourier-transform spectroscopy
DSC	Differential scanning calorimetry
DTA	Differential thermal analysis
EDX	Energy-dispersive X-ray spectroscopy
EPD	Electrophoretic deposition
FT-IR	Fourier-transform infrared spectroscopy
FTO	Fluorine-doped tin oxide (transparent conducting oxide)
GGA	Generalized gradient approximation (in DFT)
IR	Infrared spectroscopy
KPi	Potassium phosphate buffer electrolyte
MAS	Magic-angle spinning (solid-state NMR)
MEC	Mode effective charge (from vibrational/DFT analysis)
NMR	Nuclear magnetic resonance
PAW	Projector-augmented-wave method (DFT)
PBE	Perdew–Burke–Ernzerhof exchange–correlation functional (GGA)
PMT	Photomultiplier tube
PXRD	Powder X-ray diffraction
RHE	Reversible hydrogen electrode
SCXRD	Single-crystal X-ray diffraction
TG	Thermogravimetry / thermogravimetric analysis
UV-Vis	Ultraviolet–visible spectroscopy
XRD	X-ray diffraction (general)
XAS	X-ray absorption spectroscopy

Summary

This work explores mixed-anion and mixed-cation metal dinitridocarbonates based on the $[NCN]^{2-}$ building unit and relates their structural motifs to optical and (photo)electronic properties, using solid-state synthesis (solid-state metathesis, ceramic routes, and related high-temperature reactions) to obtain crystalline, largely phase-pure materials for characterization.

Within this scope, the lead carbodiimides $Pb_7I_6(CN_2)_4$, $Pb_8O_4I_6(CN_2)$, $Pb_9O_2I_8(CN_2)_3$, and $Pb_{16}O_5I_{14}(CN_2)_4$ form a coherent series in which iodide/oxide and $[NCN]^{2-}$ combine into extended lattices while the carbodiimide units remain largely linear. All four phases were obtained by ceramic routes starting from PbI_2 and $Pb(CN_2)$; for the oxide-containing members, PbO was added to the precursor mixture. Across the series, IR spectroscopy consistently shows the asymmetric N=C=N stretch and characteristic deformation modes, supporting predominantly carbodiimide-type $[NCN]^{2-}$ groups, and all four compounds are semiconductors with band gaps around 2.4–2.6 eV that exhibit broad green Pb^{2+}-based photoluminescence near 520–525 nm at low temperatures. Notably, oxide incorporation introduces heterocubane-related motifs and for $Pb_8O_4I_6(CN_2)$, photoelectrical measurements indicate n-type conduction with band-edge positions compatible with oxygen reduction, suggesting potential relevance for photocatalytic concepts. The compositions of all four compounds were corroborated by EDX analyses.

To place these Pb-based materials in a broader chemical context, the gallium dinitridocarbonates $LiGa(CN_2)_2$, $Li_{13.6}Ga_{2.8}(CN_2)_{10}I_2$, and $SrGa_2(CN_2)_4$ provide a complementary main-group perspective. These compounds were accessed via optimized solid-state metathesis conditions and feature $[NCN]^{2-}$-linked Ga-centered tetrahedral frameworks, $SrGa_2(CN_2)_4$ is air-stable and classifies as a wide-band-gap semiconductor (about 3.04 eV indirect and 3.30 eV direct). In addition to Infrared (IR) measurements evidence for carbodiimide- and cyanamide-type environments, ^{7}Li-MAS NMR was used to support the lithium incorporation in $LiGa(CN_2)_2$ and $Li_{13.6}Ga_{2.8}(CN_2)_{10}I_2$.

Moving from main-group frameworks to rare-earth hosts, $NaLa_2F_3(CN_2)_2$ extends the mixed-anion concept by combining $[NCN]^{2-}$ units with fluoride in a robust La-based network synthesized by solid-state metathesis (from LaF_3 and $Na_2(CN_2)$). Its IR spectrum shows the expected N=C=N stretch near 2000 cm^{-1} together with characteristic bending modes, and Eu^{3+} doping yields the expected $^5D_0 \rightarrow 7F_J$ emission pattern (J = 1–4) with a pronounced $^5D_0$->$^7F_4$ transition, reflecting a low-symmetry activator environment and the high polarizability of the carbodiimide unit. Finally, $La_2S_2(CN_2)$ demonstrates that these concepts can be transferred to

sulfide-containing systems; it was synthesized via a straightforward solid-state metathesis reaction ($LaCl_3/La_2S_3$ with $Li_2(CN_2)$) and retains the essential spectroscopic signatures of carbodiimide unit.

Overall, the study provides a coherent comparison across Pb-, Ga-, and La-based dinitridocarbonates, showing how mixed-anion and mixed-cation chemistry preserve the robust $[NCN]^{2-}$ motif while enabling diverse framework architectures and, in turn, tunable band gaps and characteristic photoluminescence relevant to modern functional materials.

Zusammenfassung

Diese Arbeit untersucht gemischt-anionische und gemischt-kationische-Metall-Dinitridocarbonate auf Basis der Baueinheit $[NCN]^{2-}$ und verknüpft deren Strukturmotive mit optischen und (photo)elektronischen Eigenschaften. Hierzu werden Festkörpersynthesen (Festkörpermetathese, keramische Routen und verwandte Hochtemperaturreaktionen) eingesetzt, um kristalline, weitgehend phasenreine Materialien für die Charakterisierung zu erhalten.

Innerhalb dieses Rahmens bilden die Bleicarbodiimide $Pb_7I_6(CN_2)_4$, $Pb_8O_4I_6(CN_2)$, $Pb_9O_2I_8(CN_2)_3$ und $Pb_{16}O_5I_{14}(CN_2)_4$ eine zusammenhängende Serie, in der Iodid/Oxid und $[NCN]^{2-}$ zu ausgedehnten Gerüsten verknüpft sind, während die Carbodiimid-Einheiten weitgehend linear bleiben. Alle vier Phasen wurden über keramische Routen ausgehend von PbI_2 und $Pb(CN_2)$ erhalten; für die oxidhaltigen Vertreter wurde PbO der Ausgangsmischung zugesetzt. In der gesamten Serie zeigen IR-Spektren konsistent die asymmetrische N=C=N-Valenzschwingung sowie charakteristische Deformationsmoden, was überwiegend carbodiimidartige $[NCN]^{2-}$-Gruppen belegt, und alle vier Verbindungen sind Halbleiter mit Bandlücken von etwa 2,4–2,6 eV, die bei tiefen Temperaturen eine breite grüne, Pb^{2+}-basierte Photolumineszenz bei circa 520–525 nm aufweisen. Bemerkenswerterweise führt die Einbringung von Oxid zu heterokubanverwandten Motiven, und für $Pb_8O_4I_6(CN_2)$ zeigen photoelektrische Messungen n-leitendes Verhalten mit Bandkantenlagen, die mit der Reduktion von Sauerstoff kompatibel sind, was auf eine potenzielle Relevanz für photokatalytische Konzepte hinweist. Die Zusammensetzungen aller vier Verbindungen wurden durch EDX-Analysen untermauert.

Um diese Pb-basierten Materialien in einen breiteren chemischen Kontext zu stellen, liefern die Gallium-Dinitridocarbonate $LiGa(CN_2)_2$, $Li_{13.6}Ga_{2.8}(CN_2)_{10}I_2$ und $SrGa_2(CN_2)_4$ eine komplementäre Hauptgruppenperspektive. Diese Verbindungen wurden unter optimierten Festkörper-Metathesebedingungen dargestellt und besitzen über $[NCN]^{2-}$-Einheiten verknüpfte, Ga-zentrierte tetraedrische Gerüste; $SrGa_2(CN_2)_4$ ist luftstabil und lässt sich als Breitbandlücken-Halbleiter (etwa 3,04 eV indirekt und 3,30 eV direkt) einordnen. Neben Infrarot (IR)-Messungen, die auf Carbodiimid- und Cyanamid-Umgebungen hinweisen, wurde ^{7}Li-MAS-NMR eingesetzt, um die Lithiumintegration in $LiGa(CN_2)_2$ und $Li_{13.6}Ga_{2.8}(CN_2)_{10}I_2$ zu belegen.

Beim Übergang von Hauptgruppen-Gerüsten zu Seltenerd-Wirtsgittern erweitert $NaLa_2F_3(CN_2)_2$ das Mischanionenkonzept, indem $[NCN]^{2-}$-Einheiten mit Fluorid in einem robusten, La-basierten Netzwerk kombiniert werden, das durch Festkörpermetathese (ausgehend von LaF_3 und $Na_2(CN_2)$) synthetisiert wurde. Das IR-Spektrum zeigt die erwartete N=C=N-

Valenzschwingung bei etwa 2000 cm^{-1} zusammen mit charakteristischen Deformationsmoden, und Eu^{3+}-Dotierung führt zum typischen $^5D_0 \rightarrow {}^7F_J$-Emissionsmuster ($J$ = 1–4) mit einer ausgeprägten $^5D_0 \rightarrow {}^7F_4$-Transition, was auf eine niedrigsymmetrische Aktivatorumgebung und die hohe Polarisierbarkeit der Carbodiimid-Einheit hinweist. Schließlich zeigt $La_2S_2(CN_2)$, dass sich diese Konzepte auch auf sulfidhaltige Systeme übertragen lassen; es wurde über eine einfache Festkörper-Metathesereaktion ($LaCl_3/La_2S_3$ mit $Li_2(CN_2)$) erhalten und behält die wesentlichen spektroskopischen Merkmale der Carbodiimid-Einheit bei.

Insgesamt bietet die Arbeit einen kohärenten Vergleich zwischen Pb-, Ga- und La-basierten Dinitridocarbonaten und zeigt, wie Mischanionen- und Mischkationenchemie das robuste $[NCN]^{2-}$-Motiv erhält und zugleich vielfältige Gerüstarchitekturen ermöglicht, die wiederum zu einstellbaren Bandlücken und charakteristischer Photolumineszenz führen, wie sie für moderne funktionelle Materialien von Interesse ist.

List of Publications

Publication 1:

The luminescent semiconductor $Pb_7I_6(CN_2)_4$

Albert T. Schwarz, Markus Ströbele, Carl P. Romao, David Enseling, Thomas Jüstel, Hans-Jürgen Meyer

Dalton Trans., **2024**, *53*, 6416-6422.

Publication 2:

The Mixed-Anion Compound $La_2S_2(CN_2)$

Albert T. Schwarz, Markus Ströbele, Hans-Jürgen Meyer

Z. Anorg. Allg. Chem. **2024**, 650, e202400038.

Publication 3:

Characterizing Gallium Dinitridocarbonates: A Focus on $LiGa(CN_2)_2$, $Li_{13.6}Ga_{2.8}(CN_2)_{10}I_2$, and $SrGa_2(CN_2)_4$

Albert T. Schwarz, Oleksander Kysliak, Klaus Eichele, Markus Ströbele, Hans-Jürgen Meyer

Z. Anorg. Allg. Chem. **2025**, 0, e202500085.

Publication 4:

A mixed-anion compound based upon a $[Pb_4O_4]$ heterocubane unit: synthesis, structure and electronic properties of $Pb_8O_4I_6(CN_2)$

Albert T. Schwarz, Nele Petersen, Markus Ströbele, David Enseling, Thomas Jüstel, Adam Slabon, Hans-Jürgen Meyer

Dalton Trans., **2025**, Advance Article

Publication 5:

From Heterocubane Units to Extended Networks: Synthesis, Structure, and Optical Properties of $Pb_9O_2I_8(CN_2)_3$ and $Pb_{16}O_5I_{14}(CN_2)_4$

Albert T. Schwarz, Markus Ströbele, David Enseling, Thomas Jüstel, Hans-Jürgen Meyer,

Z. Anorg. Allg. Chem. **2025**, 0, e202500205.

Publication 6:

Synthesis, Structure, and Eu^{3+}-Activated Photoluminescence of the Mixed-Anion Carbodiimide $NaLa_2F_3(CN_2)_2$

Albert T. Schwarz, Markus Ströbele, David Enseling, Thomas Jüstel, H.-Jürgen Meyer,

Z. Anorg. Allg. Chem. **2025**, 0, e202500221.

Scientific Contribution

Publication 1:

The luminescent semiconductor $Pb_7I_6(CN_2)_4$

The manuscript was prepared in collaboration with Prof. Dr. H.-J. Meyer and edited by Dr. Carl P. Romao. I conceived the synthetic strategy, planned the syntheses, and conducted all synthetic experiments on $Pb_7I_6(CN_2)_4$. I collected single-crystal and powder X-ray diffraction (PXRD) data; structure solution and refinement were performed by Dr. M. Ströbele. ELF calculations were carried out by Dr. Carl P. Romao. Reflection measurements were recorded by P. Janoschek and evaluated by me. I measured and interpreted the infrared (IR) spectra. Photoluminescence and the luminescence lifetime were measured by Dr. D. Enseling; these data were analyzed and interpreted by me in collaboration with Prof. T. Jüstel. Energy-dispersive X-ray spectroscopy (EDX) was measured by E. Nadler and evaluated by me.

Publication 2:

The Mixed-Anion Compound $La_2S_2(CN_2)$

The manuscript was written by me under the supervision of Prof. Dr. H.-J. Meyer. I conceived the synthetic strategy, planned the syntheses, and carried out all synthetic experiments on $La_2S_2(CN_2)$. I collected single-crystal and powder X-ray diffraction (PXRD) data; structure solution and refinement were performed by Dr. M. Ströbele. I performed and interpreted the diffuse reflectance infrared Fourier transform (DRIFT) measurement.

Publication 3:

Characterizing Gallium Dinitridocarbonates: A Focus on $LiGa(CN_2)_2$, $Li_{13.6}Ga_{2.8}(CN_2)_{10}I_2$, and $SrGa_2(CN_2)_4$

The manuscript was prepared in collaboration with Prof. Dr. H.-J. Meyer and Dr. K. Eichele. For $LiGa(CN_2)_2$, I conceived the synthetic strategy, executed all syntheses, and collected the single-crystal X-ray diffraction (SCXRD) data. For $Li_{13.6}Ga_{2.8}(CN_2)_{10}I_2$, I likewise planned and performed all syntheses and collected the SCXRD data. For $SrGa_2(CN_2)_4$, the synthesis was performed in collaboration with Dr. O. Kysliak, who also collected the SCXRD data. Structure solution and refinement of all single-crystal datasets were carried out by Dr. M. Ströbele. All powder X-ray diffraction (PXRD) measurements were recorded by me. Infrared spectra were measured and interpreted by me. Diffuse-reflectance measurements were performed by P. Janoschek and interpreted by me. Solid-state ^{7}Li-NMR was performed and interpreted by Dr. K. Eichele, with sample preparation undertaken by me.

Publication 4:

A mixed-anion compound based upon a [Pb_4O_4] heterocubane unit: synthesis, structure and electronic properties of $Pb_8O_4I_6(CN_2)$

The manuscript was prepared and written by me under the supervision of Prof. Dr. H.-J. Meyer, Prof. Dr. T. Jüstel, and Prof. Dr. A. Slabon. I conceived the synthetic strategy, planned the syntheses, and performed all synthetic experiments. The powder X-ray diffraction (PXRD) measurements and single-crystal X-ray diffraction (SCXRD) data were collected by me; structure solution and refinement were undertaken by Dr. M. Ströbele. For the electronic-structure and photoelectrochemical investigations, N. Petersen prepared the electrodes and performed the Mott–Schottky and cyclic voltammetry measurements; the resulting data were evaluated by her in collaboration with me. Reflectance measurements were conducted by P. Janoschek and evaluated by me. Photoluminescence and the luminescence lifetime were measured by Dr. D. Enseling and evaluated by me. Infrared (IR) spectra were recorded and analyzed by me. Energy-dispersive X-ray spectroscopy (EDX) was measured by E. Nadler and evaluated by me.

Publication 5:

From Heterocubane Units to Extended Networks: Synthesis, Structure, and Optical Properties of $Pb_9O_2I_8(CN_2)_3$ and $Pb_{16}O_5I_{14}(CN_2)_4$

The manuscript was prepared and written by me under the supervision of Prof. Dr. H.-J. Meyer and Prof. Dr. T. Jüstel. I conceived the synthetic strategy, planned the syntheses, and performed all synthetic experiments for both compounds. Single-crystal and powder X-ray diffraction (SCXRD, PXRD) data were collected by me; structure solution and refinement were undertaken by Dr. M. Ströbele. Reflectance measurements were conducted by P. Janoschek and interpreted by me. Photoluminescence and the luminescence lifetime were measured by Dr. D. Enseling and evaluated by me. Infrared (IR) spectra were recorded and analyzed by me. Energy-dispersive X-ray spectroscopy (EDX) was measured by E. Nadler and evaluated by me.

Publication 6:

Synthesis, Structure, and Photoluminescence of the Mixed-Anion Carbodiimide $NaLa_2F_3(CN_2)_2$

The manuscript was prepared and written by me under the supervision of Prof. Dr. H.-J. Meyer and Prof. Dr. T. Jüstel. I conceived the synthetic strategy and collected the single-crystal and powder X-ray diffraction (SCXRD, PXRD) data; structure solution, refinement, and the Rietveld refinements were performed by Dr. M. Ströbele. I recorded and interpreted the infrared (IR) spectra. I prepared all samples for the luminescence experiments; the measurements were carried out by Dr. D. Enseling and the resulting data were interpreted by me.

1. Introduction

1.1 Dinitridocarbonate

Dinitridocarbonates play an important role in inorganic and solid-state chemistry, where they serve as versatile building blocks for functional anions in extended structures. Closely related to these are the [N–C–N]-based species derived from cyanamide, which exists in a tautomeric equilibrium with its carbodiimide form HN=C=NH on the molecular level. The carbodiimide tautomer has been detected spectroscopically in an argon matrix already in 1971. [1] The key structural difference between the two tautomer (Figure 1) lies in the bonding situation and geometry of the [N–C–N] unit. In the cyanamide form, the nitrogen atom N^1 is bound to carbon via a C≡N triple bond (≈ 1.15 Å), while the nitrogen atom N^2 is connected through a C–N single bond (≈ 1.32 Å).[2] In contrast, in the carbodiimide tautomer, both nitrogen atoms are coordinated to the carbon atom through nearly equal C=N double bonds (≈ 1.22–1.23 Å).[3] This results in sp^2 hybridization at the nitrogen centers and an approximately linear, CO_2-analogous $[NCN]^{2-}$ unit in carbodiimides, whereas in the cyanamide form one terminal nitrogen (N^2) more closely exhibits sp^3 hybridization with a tetrahedral environment.[2-5]

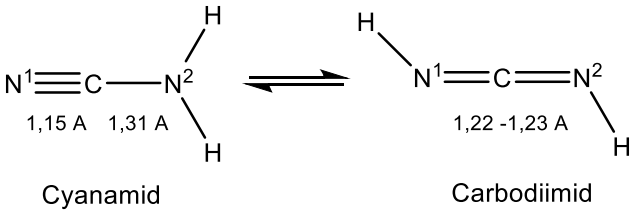

Figure 1: Tautomerism of cyanamide: molecular structures of the cyanamide and carbodiimide forms, highlighting key N−C bond lengths (in Å).

Building on this tautomerism concept, inorganic metal dintridocarboates can be classified into two structural types. Compounds containing bent $[NCN]^{2-}$ anions (cyanamide type) and those comprising linear, CO_2-isosteric $[NCN]^{2-}$ anions (carbodiimide type).[6] The type of structure in a given compound depends largely on the nature of the metal cation and can be rationalized qualitatively using Pearson's HSAB (Hard and Soft Acids and Bases) concept.[7] Hard cations such as Li^+, Ca^{2+} or Mn^{2+} preferentially stabilize the linear, $D_{\infty h}$-symmetric $[NCN]^{2-}$ unit in carbodiimides, leading to predominantly ionic M−N interactions.[5, 8-12] Softer, more polarizable cations such as Pb^{2+}, Hg^+ or Ag^+, on the other hand, favor the bent, C_{2v}-symmetric cyanamide form, in which more pronounced covalent bonding contributions are observed.[4, 13-16] Due to the differing symmetry and connectivity of the $[NCN]^{2-}$ units, cyanamides and carbodiimides

can be distinguished by IR spectroscopy, as the characteristic stretching vibrations of the $[NCN]^{2-}$ fragment differ in each case.[17] The first metal dinitridocarbonate compound to be prepared was calcium cyanamide, $Ca(CN_2)$ and was first synthesized in 1895 by A. Frank and N. Caro, obtained by reacting calcium carbide with elemental nitrogen at about 1000 °C.[9, 18-20] Industrial production of cyanamide still largely follows the Frank−Caro process. The trigonal crystal structure of $Ca(CN_2)$ was first determined in 1927 by Dehlinger[21] and revised later by improved measurements.[8, 10, 11, 22] Technical-grade calcium cyanamide is known as "nitrolime" and is widely used as a fertilizer.[23] Upon application to soil, it decomposes to urea and $Ca(OH)_2$; the urea is then further converted into ammonia and CO_2.[24] Owing to this conversion chemistry, calcium cyanamide was an important industrial precursor for ammonia before the Haber-Bosch process was established.[25] Following the discovery of calcium cyanamide, many more compounds containing the $[NCN]^{2-}$ unit have been reported over time. Among these are pseudo-binary dinitridocarbonates with alkali metals such as Li, Na, and K.[12, 26, 27] In addition, binary dinitridocarbonates of alkaline earth metals (Mg, Ca, Sr, Ba)[9, 10, 17], main-group metals (Sn, Pb, In, Tl)[14, 28-30], transition metals,[5, 31-35] and rare-earth (*RE*)[3, 36-38] elements are known. In this context, the realization of the previously unknown $La_2(CN_2)_3$ completes the pseudo-binary rare-earth dinitridocarbonate series.[37]

Over the past decades, various synthetic approaches for dinitridocarbonates have been established. One of the earliest $[NCN]^{2-}$ based compounds was $Li_2(CN_2)$, which was first obtained in the 1970s by reacting Li_3N with Li_2C_2 at 600 °C.[12] Later, alternative routes to $Li_2(CN_2)$ were developed to improve the efficiency of the process, in particular the so-called melamine route (Figure 2, No. 1), which employs metal nitrides or hydrides together with melamine.[39] Using metal hydrides as precursors also enabled an efficient synthesis of $K_2(CN_2)$ and $Na_2(CN_2)$,[27] which had previously been prepared from the corresponding metal amides and the hydrogen-containing intermediates $Na(HCN_2)$ and $K(HCN_2)$.[26, 40] By applying the melamine route to suitable metal nitrides, the chemistry of alkali metal dinitridocarbonates could be extended to the alkaline earth metal dinitridocarbonates, including $Mg(CN_2)$, $Sr(CN_2)$ and $Ba(CN_2)$.[17] In the context of $Li_2(CN_2)$, $Na_2(CN_2)$ and $K_2(CN_2)$, a broad range of $[NCN]^{2-}$ based compounds has furthermore been accessed by solid-state metathesis (SSM) reactions (Figure 2, No. 2).[41] In this approach, metal halides are reacted with alkali metal dinitridocarbonates to yield the corresponding metal dinitridocarbonates. Beyond SSM, the targeted thermal decomposition of metal cyanurates to the corresponding dinitridocarbonates has been reported[42, 43] as an efficient and straightforward route (Figure 2, No. 3). Also the so−called cermaic methode[44], which

includes the homogenization and grinding of the starting material, has been reported to synthesis dinitidocarbonates (Figure 2, No. 4).[45, 46]

In addition to solid-state methods (Figure 2, orange), a number of dinitridocarbonates have been synthesized from solution (Figure 2, red). For example, $Fe(CN_2)$ was prepared from $(NH_4)_2Fe(SO_4)_2 \cdot 6H_2O$, H_2CN_2 and aqueous ammonia (Figure 2, No. 5).[31] Solutions of metal halides, cyanamide and ammonia led to $Co(CN_2)$, $Ni(CN_2)$,[34] $Cu(CN_2)$[47] and $Cd(CN_2)$[48]. In aqueous solution, $Zn(CN_2)$ was obtained from $ZnSO_4$ and $Na_2(CN_2)$,[35] while $Pb(CN_2)$ was precipitated from cyanamide, lead acetate and a few drops of ammonia (Figure 2, No. 6).[14]

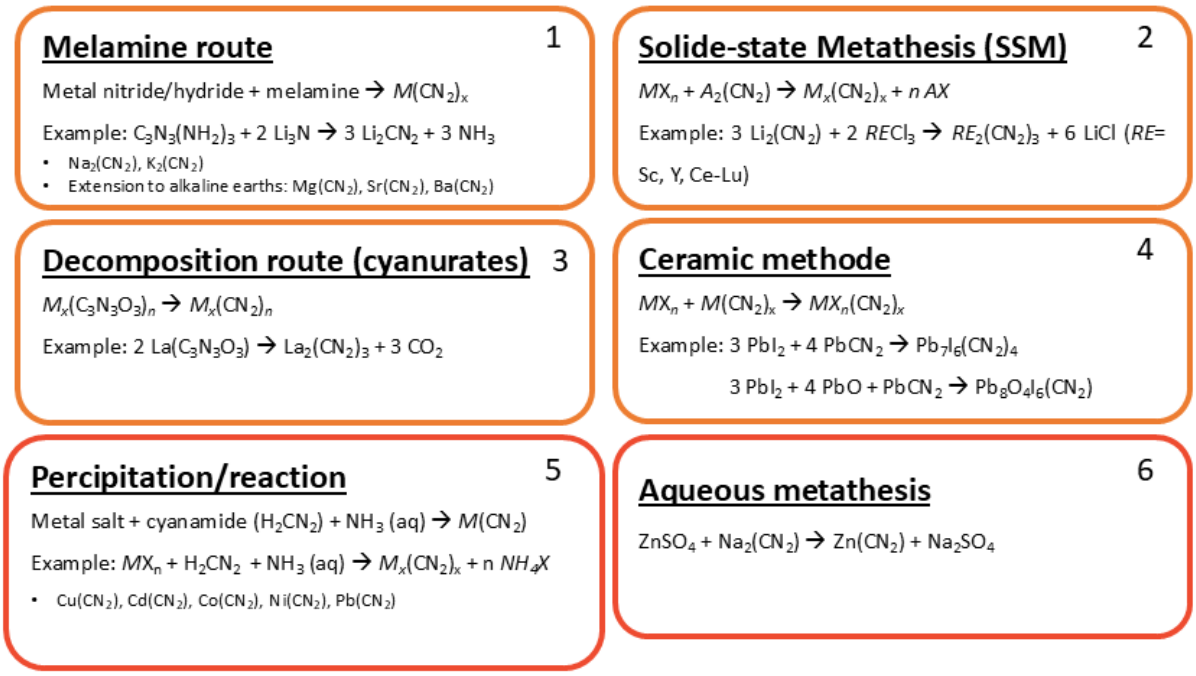

Figure 2: Summary of commonly used synthetic routes to dinitridocarbonates; orange boxes indicate solid-state reactions; red boxes indicate solution-based methods.

As will be discussed in the following section, solid-state routes can also be exploited to access more complex dinitridocarbonates, containing additional anions such as S^{2-}, O^{2-} and halides (X^- = F^-, Cl^-, Br^-, I^-), thus giving rise to the important subgroup of heteroanionic dinitridocarbonates.

1.2 Mixed-Anion and Mixed-Cation Dinitridocarbonates

The chemistry of dinitridocarbonates has evolved from simple binary salts to a wide variety of complex $[NCN]^{2-}$ based solids. A key reason is the structural flexibility of the $[NCN]^{2-}$ unit, which can behave like a pseudo-chalcogenide, replace oxide or sulfide, and act as a linear linker

in extended frameworks. By combining the $[NCN]^{2-}$ unit with different cations and anions, a broad range of architectures and properties has become accessible.

1.2.1 Mixed-Anion Dinitridocarbonates

In mixed-anion dinitridocarbonates, the cation sublattice is usually relatively simple, whereas the anion sublattice, in addition to $[NCN]^{2-}$, contains further anions such as O^{2-}, S^{2-}, F^{-}, Cl^{-}, CN^{-}, H^{-} or more complex nitrogen-based anions. This class of compounds very clearly demonstrates the pseudo-chalcogenide character of $[NCN]^{2-}$ and shows that it can adopt the structural role of O^{2-} or S^{2-} in many classical oxide, nitride and halide structure types.

A central role is played by oxide carbodiimides of rare-earth and early transition metals. The layered phases $RE_2O_2(CN_2)$ (*RE* = Y, La–Gd, Dy–Yb)[49-51] consist of fluorite-like $[RE_2O_2]^{2+}$ double layers separated by nearly linear $[NCN]^{2-}$ anions and are structurally closely related to the well-known oxychalcogenides of the type RE_2O_2Ch.

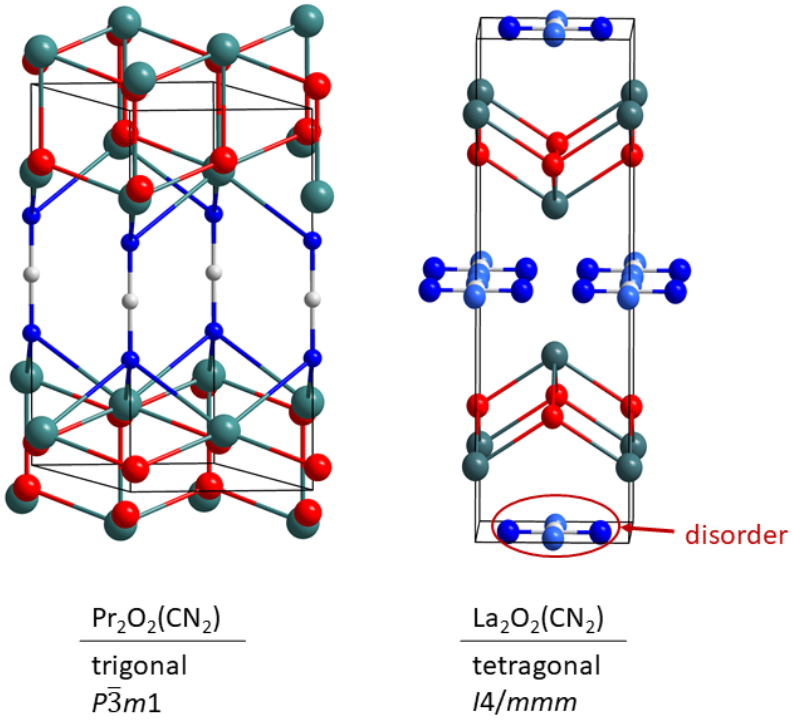

Figure 3: Comparison of the crystal structures of the heavier analogue $Pr_2O_2(CN_2)$[50] with $La_2O_2(CN_2)$[51], highlighting the orientational disorder of the $[NCN]^{2-}$ groups in $La_2O_2(CN_2)$. Lanthanum and Praseaodym atoms are shown in turquoise, oxygen in red, carbon in grey and nitrogen in blue.

$La_2O_2(CN_2)$ is a special case, crystallizing in the tetragonal space group *I*4/*mmm* and showing orientational disorder of the $[NCN]^{2-}$ groups, whereas the heavier analogues adopt trigonal structures with ordered carbodiimide layers (Figure 3). Building on this motif, oxycarbodiimides such as $La_2O(CN_2)_2$[52] have been described, in which La-O polyanions are linked by two crystallographically distinct $[NCN]^{2-}$ units, as well as carbodiimide silicates

RE$_2$(CN$_2$)(SiO$_4$),[53] whose anion substructure consists of a combination of [SiO$_4$]$^{4-}$ tetrahedra and [NCN]$^{2-}$ units. Oxidocarbodiimides of scandium such as Sc$_2$O$_2$(CN$_2$) further demonstrate that the PbO-type motif can be transferred directly into dinitridocarbonate chemistry.[33] With La$_2$S$_2$(CN$_2$), a sulfide-carbodiimide is now also known, in which La^{3+} is coordinated within layers of S^{2-} and [NCN]$^{2-}$, that are structurally closely related to La$_2$O$_2$C$_2$, with the (C$_2$)$^{2-}$ anion formally replaced by [N=C=N]$^{2-}$.[54] Closely related are halidocarbodiimides in which halide ions complement the [NCN]$^{2-}$ frameworks. Early examples are *RE*Cl(CN$_2$) (*RE* = La, Ce, Pr)[55] , *RE*$_2$Cl(CN$_2$)N (*RE* = La, Ce),[39] which consist of layers or chains of *Ln* polyhedra linked by [NCN]$^{2-}$ anions and completed by Cl$^-$ and N^{3-}. Analogous fluoride carbodiimides such as LaF(CN$_2$) and Li*RE*$_2$F$_3$(CN$_2$)$_2$ (*RE* = Ce-Gd) are obtained by metathesis from *RE*F$_3$ and Li$_2$(CN$_2$) and can be interpreted as oxide-like fluoride/NCN layers.[56] Cluster-based oxy- and halidocarbodiimides of the type *RE*$_8$O(CN$_2$)$_{10}$Br$_2$ (*RE* = La-Nd)[57] further demonstrate how mixed-anionic design can be combined with complex cation chemistry. In these compounds, [*RE*$_6$O] cluster cores are connected via Br$^-$ and [NCN]$^{2-}$ into three-dimensional networks. Multiple rare-earth sites, oxide and bromide anions, and carbodiimide ligands all contribute to the overall charge balance and connectivity, providing a striking example of how cluster-based building units can be integrated into [NCN]$^{2-}$ frameworks.

In main-group chemistry, Sn$_2$O(CN$_2$) shows that oxidocarbodiimides are likewise accessible for tin(II). Sn^{2+} centers form a three-dimensional network of Sn−O and Sn−N bonds in which [NCN]$^{2-}$ acts as a linear bridge between SnO-like fragments and significantly modifies the electronic structure compared to SnO.[58] Tin(II) halidocarbodiimides provide further examples of mixed-anionic [NCN]$^{2-}$ frameworks. Sn$_4$Cl$_2$(CN$_2$)$_3$ and its bromide analogue Sn$_4$Br$_2$(CN$_2$)$_3$ are obtained by solid-state metathesis of Li$_2$(CN$_2$) with the corresponding tin halides and adopt layered structures in which Sn^{2+} ions are octahedrally coordinated by three [NCN]$^{2-}$ units and three halide ions.[30, 59] Even more complex is the oxidochloridocarbodiimide Sn$_9$O$_5$Cl$_{14}$(CN$_2$)$_2$, whose structure contains [Sn$_8$O$_3$] cluster-like arranged in hexagonal bipyramids and linked into chains by additional Sn and O atoms; chloride and [NCN]$^{2-}$ anions connect these chains into a

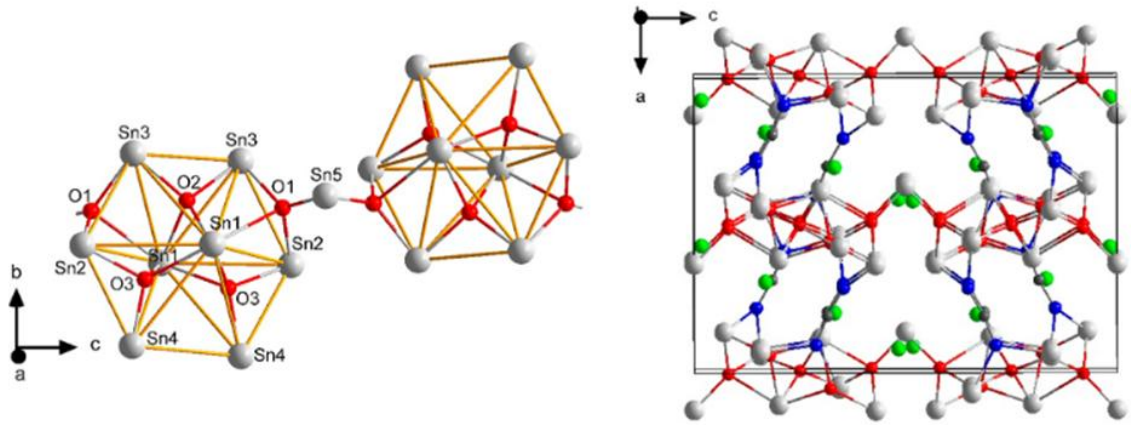

Figure 4: Section and projection of the crystal structure of $Sn_9O_5Cl_4(CN_2)_2$, showing chains of $[Sn_8O_3]$ clusters running along [001]. Two $[Sn_8O_3]$ clusters are highlighted, interconnected by oxygen (O1) and tin (Sn5) into chains; oxide ions (red) occupy approximately tetrahedral sites. Tin is shown in white, oxygen in red, chloride in green, carbon in black and nitrogen in blue. The illustration is reproduced from the published crystal-structure description. [60]

three-dimensional framework (Figure 4).[60] These tin compounds illustrate how oxide and halide anions can be combined with $[NCN]^{2-}$ in one structure while maintaining the carbodiimide character of the $[NCN]^{2-}$ unit.

Nitridometalate-containing carbodiimides push the chemistry further towards nitride-type frameworks. In $[Sr_6N][CoN_2][CN_2]_2$[61], isolated, formally low-valent $[CoN_2]^{5-}$ units coexist with $[NCN]^{2-}$ anions and N^{3-} within a common strontium nitride network; the carbodiimide acetonitriletriide $Sr_4N(CN_2)C_2N$[62] is closely related and stabilizes both $[NCN]^{2-}$ and $[C_2N]^{3-}$ in one phase. Mixed-anion dinitridocarbonate chemistry also includes systems in which $[NCN]^{2-}$ appears together with CN^- or H^-. The early mixed cyanamide/cyanides $Ba_2(CN_2)(CN)_2$ and $Sr_2(CN_2)(CN)_2$[63] contain both $[NCN]^{2-}$ (cyanamide) and CN^- anions in a defective anti-NiAs framework and demonstrate that both species can be structurally accommodated within a common cation lattice. Later, alkali-rich carbodiimide cyanides such as $Na_5(CN_2)_2(CN)$ and $(Li,Na)_5(CN_2)_2(CN)$,[64] as well as hydride phases such as $K_5(CN_2)_2H$,[65] were obtained, in which $[NCN]^{2-}$ is combined with CN^- and H^-. These examples show that the anion sublattice in dinitridocarbate chemistry can be varied far beyond simple "NCN + O" or "NCN + *X*" (*X* = F, Cl, Br, I) combinations without fundamentally compromising the stability of the linear $[NCN]^{2-}$ unit.

1.2.2 Mixed-Cation Dinitridocarbonates

In mixed-cation dinitridocarbonates, $[NCN]^{2-}$ generally remains the only, or at least the dominant, anion type, while the cation sublattice contains two or more distinct metal cations in an ordered fashion. Here the focus is less on expanding the anion chemistry and more on

deliberately choosing and arranging different cations in order to fine-tune coordination environments, symmetry and electronic structure.

An established entry point into this chemistry is the Li*RE*$(CN_2)_2$ family (*RE* = La, Ce, Y, and others),[66-68] which can be prepared by metathesis from *REX*$_3$ (*X*$^-$ = F$^-$, Cl$^-$) and $Li_2(CN_2)$. These compounds are structurally closely related to the NiAs archetype (Figure 5).[69] Formally, the $[NCN]^{2-}$ units occupy the anion positions of the NiAs−type, while the Ni-type cation sites are split into two ordered sublattices that are selectively filled by Li^+ and RE^{3+}. By introducing additional cations, these motifs can be extended, as illustrated by $Li_2Gd_2Sr(CN_2)_5$,[70] in which Li^+, Gd^{3+} and Sr^{2+} are arranged within a common $[NCN]^{2-}$ framework and the cations occupy different coordination polyhedra without disrupting the underlying carbodiimide network.

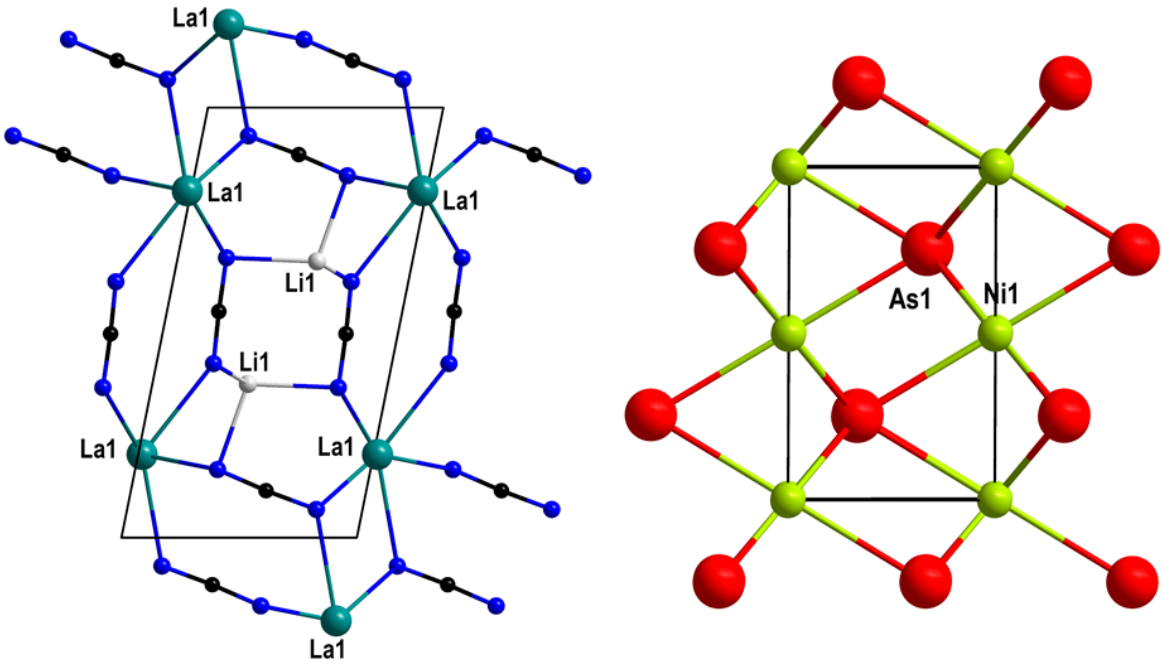

Figure 5: Comparison of the crystal structures of LiLa$(CN_2)_2$[66] (left) and NiAs [69] (right), illustrating the relationship of LiLa$(CN_2)_2$ to the NiAs archetype. In LiLa$(CN_2)_2$, the nearly linear $[NCN]^{2-}$ units occupy the anion positions corresponding to As in NiAs, while the single Ni cation site is split into two distinct cation sites that are selectively occupied by Li and La. In the representation used here, Li atoms are shown in grey, La in turquoise, carbon in black and nitrogen in blue; in the NiAs structure, Ni atoms are shown in green and arsenic in red.

In the field of post-transition-metal carbodiimides, $SrZn(CN_2)_2$[71] and $BaZn(CN_2)_2$[72]exemplify the transferability of classical oxide and oxysulfide structure types into dinitridocarbnate chemistry. $SrZn(CN_2)_2$ crystallizes in the BaZnSO structure type.[73] $[ZnN_4]$ tetrahedra and $[SrN_6]$ prisms are connected exclusively via $[NCN]^{2-}$ and form a layered framework with a significantly reduced band gap compared to $SrZnO_2$.[74] $BaZn(CN_2)_2$ represents the highly symmetric istotype of this family and serves as a reference for cation exchange and further substitution.

An even higher level of complexity is found in quaternary cyanamides such as $Li_2MgSn_2(CN_2)_6$.[75] This compound has a layered structure with distinct Li^+/Mg^{2+} and Sn^{4+} sublayers, each linked by formally cyanamide-like $[NCN]^{2-}$ units. It can be regarded as a cation-ordered variant of a NiAs-like *M*−NCN framework and stands in close relation to known structures such as $Li_2Zr(CN_2)_3$[76] or $Cr_2(CN_2)_3$[32]. Related series such as $A_2MSn_2(CN_2)_6$ (*M* = Mn, Fe, Co, and Ni, *A* = Li, Na) or $A_2Sn(CN_2)_3$ (*A* = Li, Na) show that tin(IV) carbodiimides can be stably anchored in such framework structures.[76-78]

A particularly versatile subgroup is formed by homoleptic tetracyanamidometallates with isolated $[M(CN_2)_4]^{n-}$ tetrahedra (*M* = Si, Ge, Al, Ga). More recently, the quasi-binary lithium tetracyanamidometallates $Li_4[Si(CN_2)_4]$ and $Li_4[Ge(CN_2)_4]$ have been crystallized as fundamental members of this family, further underscoring the close analogy to orthosilicates and orthogermanates.[79]

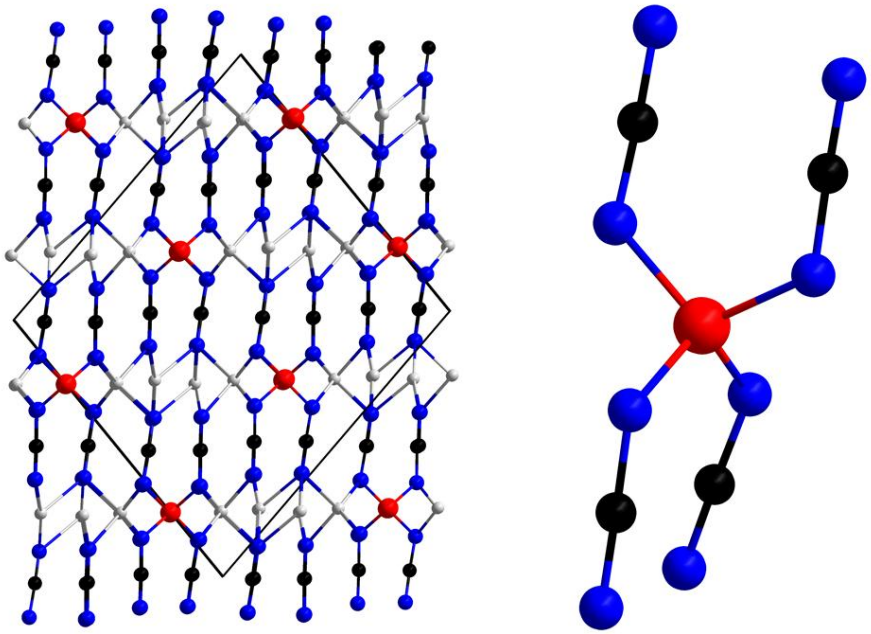

Figure 6: Crystal structure of $Li_4[Si(CN_2)_4]$[79] viewed along [010], together with an isolated $[Si(CN_2)_4]^{4-}$ tetrahedron (right).[76] *Silicon is shown in red, carbon in black, nitrogen in blue and lithium in white.*

The silicates *ARE*$[Si(CN_2)_4]$ (*A* = K, Rb, Cs; *RE* = Y, La–Lu),[36, 80, 81] the aluminates $LiBa_2[Al(CN_2)_4]$[82] and $LiM_2[Al(CN_2)_4]$ (*M* = Sr, Eu),[83] as well as the germanates *ARE*$[Ge(CN_2)_4]$ (*A* = Rb, *RE* = Y, La - Lu)[84-86] demonstrate that four nearly linear $[NCN]^{2-}$ groups can coordinate to a central tetrel or p-block cation to form orthosilicate- or orthogermanate-like anions. These tetrahedra are surrounded by alkali and rare-earth cations in densely packed three-dimensional frameworks and form robust host lattices with wide band gaps and pronounced Ce^{3+}, Eu^{3+} and Tb^{3+} emission. Although formally only $[NCN]^{2-}$-based anions are

present, these materials are clearly mixed-cationic and show how classical silicate and germanate chemistry can be translated into the dinitridocarbonate domain.

1.2.3 Mixed-Anion and -Cation Dinitiridocarbonate Frameworks

The structurally most complex dinitridocarbonates and carbodiimides are those in which both the anion and cation sublattices are mixed. In such compounds, several types of metal cations – for example alkali, alkaline-earth, rare-earth and post-transition-metal ions – interact with an anion mixture composed of $[NCN]^{2-}$ and O^{2-}, S^{2-}, F^-, Cl^-, Br^-, N^{3-}, CN^- or other polyatomic anions.

A prototypical example is the fluoridocarbodiimide family $LaSr_3F_5(CN_2)_2$ / $Eu_4F_5(CN_2)_2$.[87, 88] In $LaSr_3F_5(CN_2)_2$, La^{3+} and Sr^{2+} share a cation site, while the anion substructure consists of F^- and $[NCN]^{2-}$ anions, yielding a highly symmetric framework that serves as a structural prototype for the mixed-valent $Eu_4F_5(CN_2)_2$. In the europium system, Eu^{2+} and Eu^{3+} coexist within a common fluoride/NCN framework; differences in Eu–N and Eu–F distances and in the orientation of the $[NCN]^{2-}$ units make the charge distribution structurally visible. Similarly, complex situations arise in Eu carbodiimide halides such as $Eu_4(CN_2)_3Cl_3$, $LiEu_2(CN_2)Cl_3$ and $Na_2Eu_{14}(CN_2)_3Cl_{24}$,[89] as well as in $LiEu_2(CN_2)I_3$ and $LiEu_4(CN_2)_3I_3$,[90] where $[Eu_4]$ tetrahedra are surrounded by $[NCN]^{2-}$ units, while alkali and halide ions occupy channels and interstitial sites and thus strongly influence the dimensionality of the framework, the Eu^{2+}/Eu^{3+} ratio and the luminescence properties. There are also many main-group examples in which both degrees of freedom are combined. The bideauxite-related lead carbodiimides $APb_2Cl_3(CN_2)$ with A =

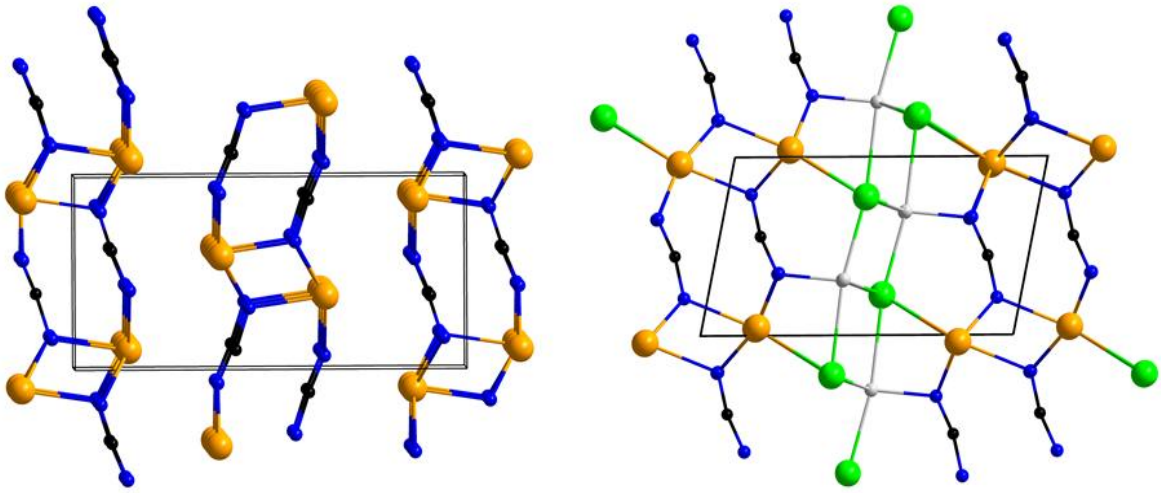

Figure 7: Comparison of the unit cell of $PbCN_2$ (left)[14] and $LiPbCl(CN_2)$ (right).[91] In both images, lead atoms are shown in ochre, chloride in green, carbon in black, nitrogen in blue, and lithium in white.

Li, Na, Ag[91] consist of two interpenetrating networks: one built from [ACl$_6$] octahedra, and the other from [Pb$_4$] tetrahedra linked by [NCN]$^{2-}$ anions into a three-dimensional cluster-like framework. LiPbCl(CN$_2$)[91] can be understood as a LiCl-intercalated modification of Pb(CN$_2$),[14] in which Pb and Li layers alternate and [NCN]$^{2-}$ is coordinated between both cation surfaces (Figure 7).

In Pb$_{14.66}$Sn$_{7.34}$Br$_{26}$(CN$_2$)$_7$O$_2$,[92] a highly complex situation arises in which Pb^{2+}, Sn^{2+} and Sn^{4+} share a common polyhedral network together with Br$^-$, O^{2-} and multiply coordinated [NCN]$^{2-}$; despite the high coordination number, the [NCN]$^{2-}$ units retain predominantly carbodiimide-like character. Mixed-anionic and mixed-cationic behavior is also clearly expressed in fluoride carbodiimides such as Ba$_4$MgF$_2$(CN$_2$)$_4$.[93] In this compound, Ba^{2+} and Mg^{2+} occupy distinct crystallographic sites, while the anion sublattice contains both F$^-$ and [NCN]$^{2-}$. Mg^{2+} is octahedrally coordinated by six nitrogen atoms of carbodiimide ligands, forming extended [MgN$_6$] layers, whereas Ba^{2+} adopts larger, more irregular coordination environments. The combination of two different cation types with two different anion species in a single extended framework makes Ba$_4$MgF$_2$(CN$_2$)$_4$ a characteristic example of a simultaneously mixed-anionic and mixed-cationic [NCN]$^{2-}$ solid. Strontium gallate carbodiimides such as Sr$_4$GaN$_3$(CN$_2$)[94] can likewise be regarded as simultaneously mixed-anionic and mixed-cationic [NCN]$^{2-}$ frameworks. They can be viewed as [NCN]$^{2-}$ analogues of the corresponding oxides Sr$_4$GaN$_3$O, where the role of oxide is taken over by a linear carbodiimide ligand. This relationship can be emphasized in an ionic formulation by writing the compositions as (Sr^{2+})$_4$[GaN$_3$O]$^{8-}$ for Sr$_4$GaN$_3$O and (Sr^{2+})$_4$[GaN$_3$(CN$_2$)]$^{8-}$ for Sr$_4$GaN$_3$(CN$_2$), such that the anionic units [GaN$_3$O]$^{8-}$ and [GaN$_3$(CN$_2$)]$^{8-}$ appear as closely related building blocks. In this way, Sr$_4$GaN$_3$(CN$_2$) naturally fits into the same structural family as the oxide Sr$_4$GaN$_3$O, while simultaneously combining two cation types (Sr^{2+}, Ga^{3+}) with two nitrogen-based anions (N^{3-} and [NCN]$^{2-}$).

.

2. Objective

Modern semiconductor and electronic technologies, such as light-emitting diodes, power electronics, photovoltaic and photoelectrochemical devices, require materials that combine chemical robustness with a tunable electronic structure. Photocatalytic processes likewise depend on semiconductors whose band gaps are matched to visible or near-UV excitation. Mixed-anion and mixed-cation solids meet these demands by enabling systematic property tuning through the careful choice and connectivity of cations and anions.

As metal dinitridocarbonates, most of which are thermodynamically stable and chemically robust, have evolved from simple binary phases into structurally more complex compounds featuring mixed cations and/or mixed anions, they provide a particularly well-suited platform for investigating structure–property relationships. This dissertation therefore focuses on the development and characterization of new dinitridocarbonates of lead, lanthanum and gallium in mixed-anion and mixed-cation frameworks.

Materials containing lead and gallium are relevant in semiconductor and photocatalysis research, while lanthanum compounds also play an important role in optical materials. Robust low-temperature solid-state routes, in particular solid-state metathesis and ceramic methods, provide access under moderate conditions to dinitridocarbonates, which would often decompose under conventional high-temperature conditions, and are used in this work both to extend established $[NCN]^{2-}$-based chemistries.

3. Summary of the main results

Single-crystal X-ray diffraction

The single-crystal X-ray diffraction (XRD) studies on the obtained compounds $Pb_7I_6(CN_2)_4$ (CCDC: 2211751), $La_2S_2(CN_2)$ (CCDC: 2284703), $LiGa(CN_2)_2$ (CCDC: 2245222), $Li_{13.6}Ga_{2.8}(CN_2)_{10}I_2$ (CCDC: 2250452), $SrGa_2(CN_2)_4$ (CCDC: 2321110), $Pb_8O_4I_6(CN_2)$ (CCDC: 2389167), $Pb_9O_2I_8(CN_2)_3$ (CCDC: 2385668) $Pb_{16}O_5I_{14}(CN_2)_4$ (CCDC: 2415837) and $NaLa_2F_3(CN_2)_2$ (CCDC: 2326720) were performed on a Rigaku XtaLAB Synergy (Dualflex, HyPix) diffractometer. Data were collected under a nitrogen cryostream at 100–200 K (typically 150 K), with Mo–K_α radiation (λ = 0.71073 Å) for all datasets except $Li_{13.6}Ga_{2.8}(CN_2)_{10}I_2$, which was measured with Cu–K_α radiation (λ = 1.54184 Å). Absorption corrections, data reduction, and scaling were carried out with CrysAlisPro (Rigaku Oxford Diffraction; versions 1.171.42–1.171.43 as appropriate), employing numerical/empirical procedures based on spherical harmonics (SCALE3 ABSPACK) or Gaussian integration over a multifaceted crystal model; for $Pb_7I_6(CN_2)_4$ an analytical numeric correction following Clark & Reid was applied. Structures were solved by SHELXT (2018/2) and refined against F^2 by full-matrix least squares with SHELXL (2018/3 or 2019/3) within Olex2 (v1.5); $La_2S_2(CN_2)$ was solved by SHELXS (2008).

Photoluminescence studies

Steady-state excitation and emission spectra for the carbodiimide materials ($Pb_7I_6(CN_2)_4$, $Pb_8O_4I_6(CN_2)$, $Pb_9O_2I_8(CN_2)_3$, $Pb_{16}O_5I_{14}(CN_2)_4$, and Eu-doped $NaLa_2F_3(CN_2)_2$) were recorded on an *Edinburgh Instruments* FLS920 fluorescence spectrometer equipped with a 450 W xenon discharge lamp. Powder samples were measured using the mirror-optic accessory in front-face geometry, with detection by a Hamamatsu R2658P single-photon-counting PMT. Where required, long-pass filters were inserted to suppress higher-order excitation. Temperature-dependent spectra were collected with an Oxford Instruments MicrostatN cryostat using liquid nitrogen; low-temperature data were acquired at 77–80 K. All photoluminescence spectra were recorded with 1 nm spectral resolution, a dwell time of 0.5 s in 1 nm steps, and 2–5 repeats. Photoluminescence decay curves were acquired on the same platform using a 375 nm picosecond laser diode as the excitation source.

UV-Vis in diffuse reflectance

Diffuse-reflectance UV–Vis spectra of $Pb_7I_6(CN_2)_4$, $Pb_8O_4I_6(CN_2)$, $Pb_9O_2I_8(CN_2)_3$, $Pb_{16}O_5I_{14}(CN_2)_4$, $LiGa(CN_2)_2$, $Li_{13.6}Ga_{2.8}(CN_2)_{10}I_2$, and $SrGa_2(CN_2)_4$ were recorded on an

OceanOptics Maya 2000 Pro spectrometer equipped with a Harrick Praying Mantis diffuse-reflectance accessory and a deuterium–tungsten DH-200-BAL light source. Data acquisition used OceanView 1.6.7 (lite) with scans to average = 100, boxcar width = 10, and integration time = 300 ms. Reflectance data were converted to pseudo-absorbance using the Kubelka–Munk function, and optical band gaps were estimated, where applicable, from Tauc plots according to $(\alpha \cdot h\nu)^{(1/r)} = A(h\nu - Eg)$, with r = 1/2 for direct-allowed and r = 2 for indirect-allowed transitions.

Powder X-ray diffraction (PXRD)

Powder patterns of well-ground samples were recorded at room temperature on a STOE STADI-P diffractometer equipped with a Ge-monochromator, Cu-$K_{\alpha 1}$ radiation (λ = 1.540598 Å), and a position-sensitive (Mythen-1) detector. Data were typically collected over $5° \leq 2\theta \leq 120°$; narrower ranges were used for selected phases as appropriate. Phase identity and purity were assessed by comparison with patterns calculated from the corresponding single-crystal models; where applicable, Rietveld refinements were performed using the FullProf/WinPLOTR suite.

Fourier-Transformed-Infrared spectroscopy (FT-IR)

FT-IR spectra of $Pb_7I_6(CN_2)_4$, $LiGa(CN_2)_2$, $Li_{13.6}Ga_{2.8}(CN_2)_{10}I_2$, $SrGa_2(CN_2)_4$ $Pb_8O_4I_6(CN_2)$, $Pb_9O_2I_8(CN_2)_3$, $Pb_{16}O_5I_{14}(CN_2)_4$, and $NaLa_2F_3(CN_2)_2$. were recorded on a Bruker VERTEX 70 FT-IR spectrometer in the range 400–4000 cm^{-1} using KBr pellets. Samples were prepared in a glove box under argon atmosphere.

Diffuse reflectance infrared Fourier transformed (DRIFT) spectroscopy

Diffuse-reflectance FT-IR spectra of $La_2S_2(CN_2)$ were recorded at room temperature on a Bruker VERTEX 70 spectrometer using a Harrick "Praying Mantis" accessory, a DTGS detector, and a KBr beamsplitter over 400–4000 cm^{-1}. Finely ground samples were mixed with dry KBr and measured against dried KBr as background.

Photoelectrochemistry

Thin-film electrodes of $Pb_8O_4I_6(CN_2)$ on FTO were prepared by electrophoretic deposition (EPD) from acetone containing iodine as a charging agent (20 mg I_2 in 20 mL acetone). About 100 mg of powder were dispersed and sonicated for 60 min; deposition was carried out at 45 V using FTO as working electrode and a Pt wire as counter electrode. The films were rinsed with water and acetone and dried overnight. Photoelectrochemical measurements were performed

with a BioLogic SP-300 potentiostat in a three-electrode configuration with floating ground, employing the prepared film as working electrode, a Pt wire as counter electrode, and an Ag/AgCl (sat. KCl) reference electrode. Potentials were recorded versus Ag/AgCl and converted to the reversible hydrogen electrode (RHE) using E_{RHE} (V) = 0.197 + $E_{Ag/AgCl}$ + 0.059·pH at 25 °C. A 0.1 M potassium phosphate buffer (pH 7) served as electrolyte. Mott–Schottky measurements were acquired in the dark with an AC amplitude of 10 mV over 0.7–700 Hz to determine the flat-band potential from $1/C_{sc^2}$ versus E plots. Chronoamperometry was recorded at 0 V vs. RHE under AM 1.5G illumination (100 mW·cm^{-2}) with 30 s light/30 s dark chopping; measurements were initiated in the dark.

Density Functional Theory (DFT) Calculations

Density functional theory (DFT) calculations were carried out using the ABINIT software package. For all calculations, the projector-augmented-wave (PAW) method was employed together with a plane-wave basis set and periodic boundary conditions.

For $Pb_7I_6(CN_2)_4$, DFT calculations were performed with ABINIT (version 9)[95] using the Perdew–Burke–Ernzerhof (PBE) exchange–correlation functional.[96] The PAW method[97] was applied with an energy cutoff of 25 Ha outside the PAW spheres and 125 Ha inside them. A 3 × 3 × 2 Monkhorst–Pack grid of k points was used to sample reciprocal space.[98] Methfessel–Paxton cold smearing was employed for the electronic occupations.[99] To account for the partial occupation of the Pb5 site and to preserve the correct stoichiometry in the model, a Pb5 vacancy was explicitly included in the unit cell. Due to this vacancy and the structural complexity of $Pb_7I_6(CN_2)_4$, a full structural optimization prior to the electronic band-structure calculation was not carried out. Special k points and paths in the Brillouin zone for the band-structure plots were chosen according to the scheme of Hinuma et al.[100]

Energy Dispersive X-ray spectroscopy

The Energy Dispersive X-ray (EDX) spectroscopy was performed with a Hitachi SU8030 scanning electron microscope equipped with a Bruker QUANTAX 6G EDX detector.

3.1 The Luminescent Semiconductor $Pb_7I_6(CN_2)_4$ (Publication 1)[45]

The paper reports the synthesis, crystal structure, and optoelectronic properties of the lead iodide carbodiimide $Pb_7I_6(CN_2)_4$ and links its cluster-based framework to semiconducting and photoluminescent behavior. Reactions of lead carbodiimide with lead iodide yield a phase-pure, dark-yellow product; EDX confirms the composition, and PXRD matches the pattern calculated from the single-crystal X-ray refinement, establishing bulk identity. Single-crystal X-ray diffraction refines the structure in the hexagonal space group $P6_3/mmc$ with Z = 5.

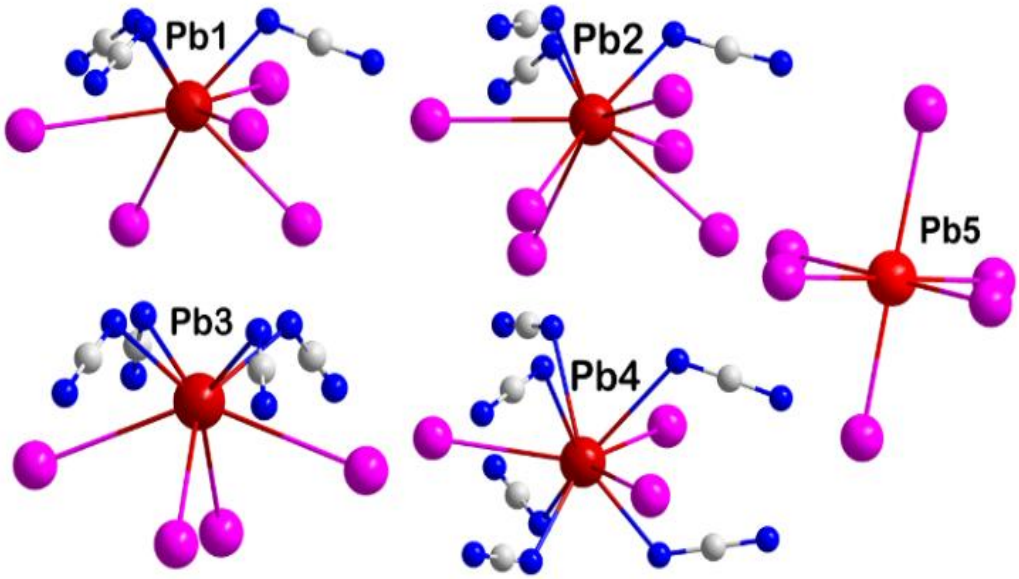

Figure 8: Different coordination environments of lead atoms in $Pb_7I_6(CN_2)_4$. Iodine is shown in purple, carbon in white and nitrogen in blue. Reproduced from Publication 1.

The asymmetric unit contains five distinct Pb sites (Figure 8). Pb1 adopts an eightfold coordination environment built from five iodide and three $[NCN]^{2-}$ units. Pb2 is ninefold coordinated in a distorted tricapped trigonal antiprism with six iodide and three $[NCN]^{2-}$ ligands. Pb3 is eightfold coordinated by four iodide and four $[NCN]^{2-}$ ligands, whereas Pb4 is coordinated by three iodide and six $[NCN]^{2-}$ ligands and Pb5 (site-occupation factor 0.75) forms a distorted PbI_6 octahedron. The three independent carbodiimide anions show nearly uniform C–N metrics; two reside in trigonal-antiprismatic Pb_6 cages and one in a trigonal-prismatic environment. The structure contains a triple-Pb_4 tetrahedral unit in which edge- and face-sharing Pb_4 tetrahedra assemble into a tetrahedron−trigonal-bipyramidal motif; $[NCN]^{2-}$ anions cap the open trigonal faces and partially occupied $[PbI_6]$ octahedra (Pb5) interconnect these clusters into a three-dimensional framework (Figure 9).

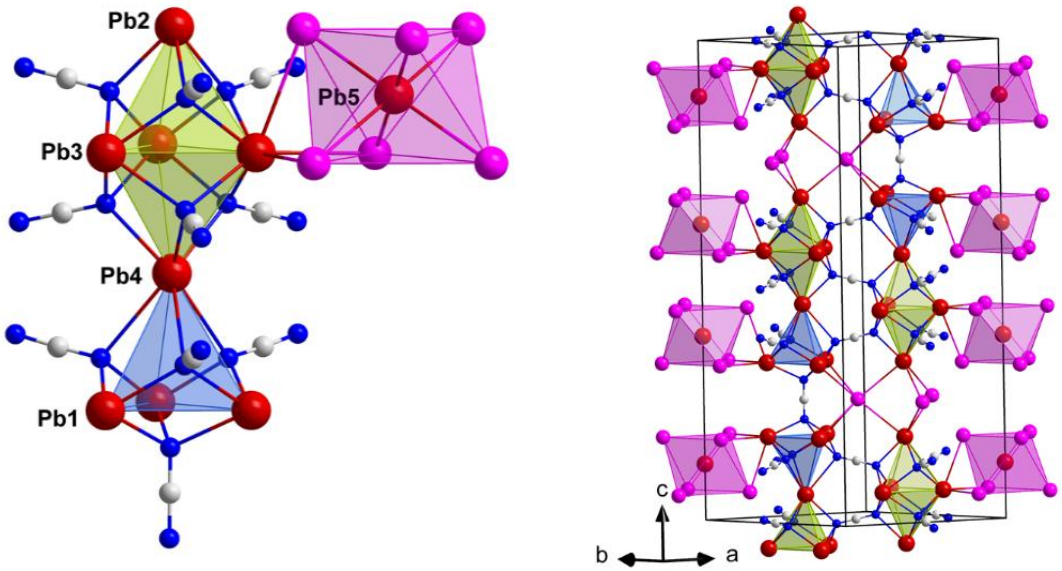

Figure 9: Face-shared and edge-shared triple-Pb_4-tetrahedra fragment with face- capping carbodiimide ions and an associated [PbI_6] octahedron (purple) (left). Section of the crystal structure of $Pb_7I_6(CN_2)_4$ (right). Iodine atoms are shown in purple, lead in red, carbon in white and nitrogen in blue. Modified from Publication 1.

Diffuse-reflectance analysis (Tauc) indicates an indirect allowed optical transition with Eg ≈ 2.38 eV, while DFT yields an indirect band gap of about 1 eV with relatively flat dispersions; the valence-band maximum is largely iodine character with contributions from the carbodiimide nitrogens, and vacancy effects at Pb5 are included. Luminescence behavior is characterized by Pb^{2+}-centered emission (Figure 10, left). The excitation spectrum monitored at 525 nm shows bands at 302, 333, and 378 nm (consistent with $^1S_0 \rightarrow {}^1P_1$ and $^1S_0 \rightarrow {}^3P_2$, $^3P_1$ transitions, Figure 10, right)), and the emission appears as a single broad green band at 525 nm (2.36 eV)

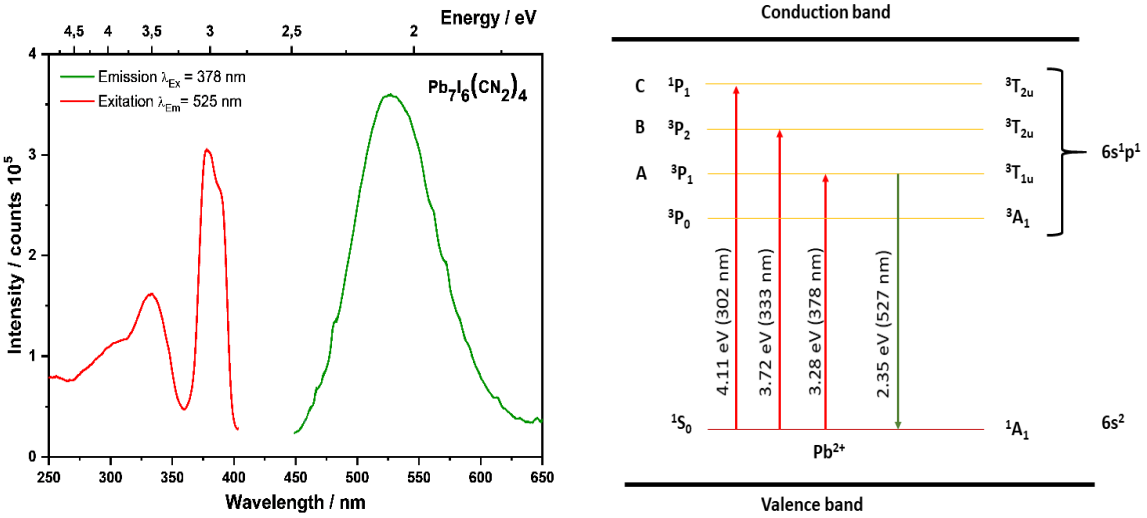

Figure 10: Excitation and emission spectra of $Pb_7I_6(CN_2)_4$ at 77 K (left). Energy level scheme of a free Pb^{2+} ion (right). Modified from Publication 1.

with an essentially mono-exponential lifetime of about 356 ns; the large Stokes shift (~7500 cm^{-1}) correlates with quenching under conditions favoring nonradiative relaxation.

3.2 The Mixed-Anion Compound $La_2S_2(CN_2)$ (Publication 2)[54]

The mixed-anion compound $La_2S_2(CN_2)$ was synthesized by solid-state metathesis, and its crystal structure was determined from single-crystal X-ray diffraction. The product constitutes the first sulfide–carbodiimide and crystallizes in the monoclinic space group *C*2/*m*. The structure adopts a simple layered arrangement composed of alternating lanthanum, sulfide, and carbodiimide sheets; along [001] the stacking can be described by the sequence (NCN)-La-S–S-La. This topology is characteristic of metal carbodiimides and closely related to $La_2O_2C_2$ through substitution of the $(C_2)^{2-}$ unit by the linear $[N{=}C{=}N]^{2-}$ anion (Figure 11) while retaining the same symmetry.

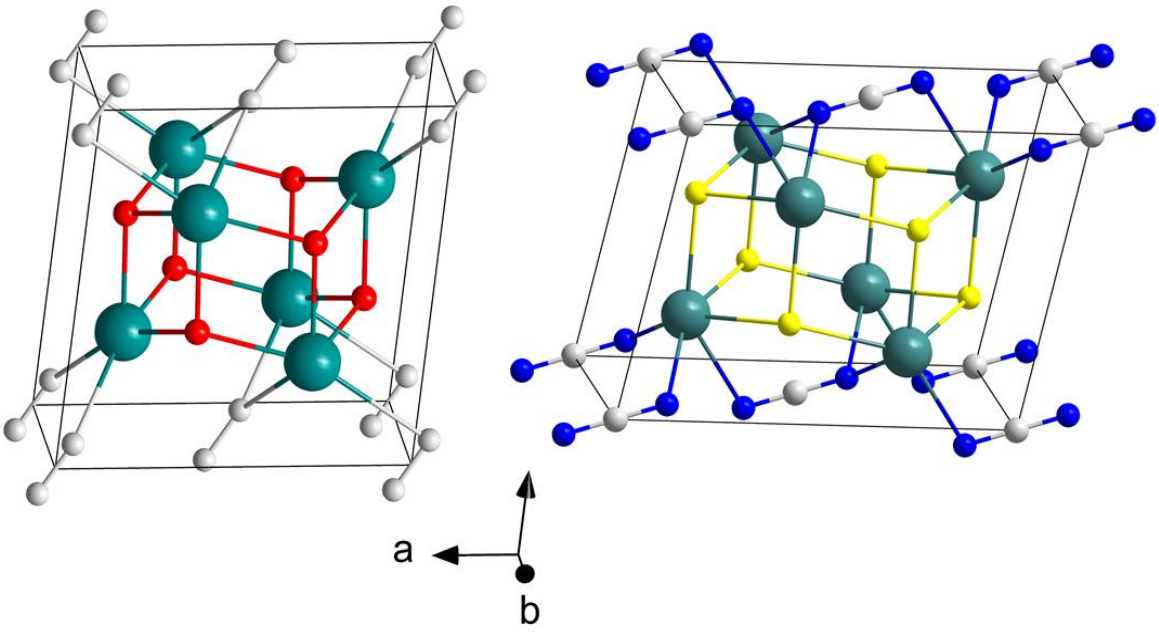

Figure 11: Comparison of unit cells of $La_2O_2C_2$ (left) and $La_2S_2(CN_2)$ (right). Lanthanum atoms are shown in dark turquoise, sulfur in yellow, oxygen in red, nitrogen in blue, and carbon in grey. Reproduced from Publication 2.

From the sulfur perspective, the lanthanum−sulfide layer consists of corner-sharing $[La_4S]$ tetrahedra, and lanthanum exhibits sevenfold coordination by four sulfide and three carbodiimide units (Figure 12). Powder X-ray diffraction reproduces the Bragg positions calculated from the refined single-crystal structure, and diffuse-reflectance infrared spectra display the diagnostic bands of the carbodiimide unit (asymmetric stretch at 1951 cm^{-1} and bending mode at 653 cm^{-1}); minor additional IR features are consistent with a small side phase indicated by the powder pattern.

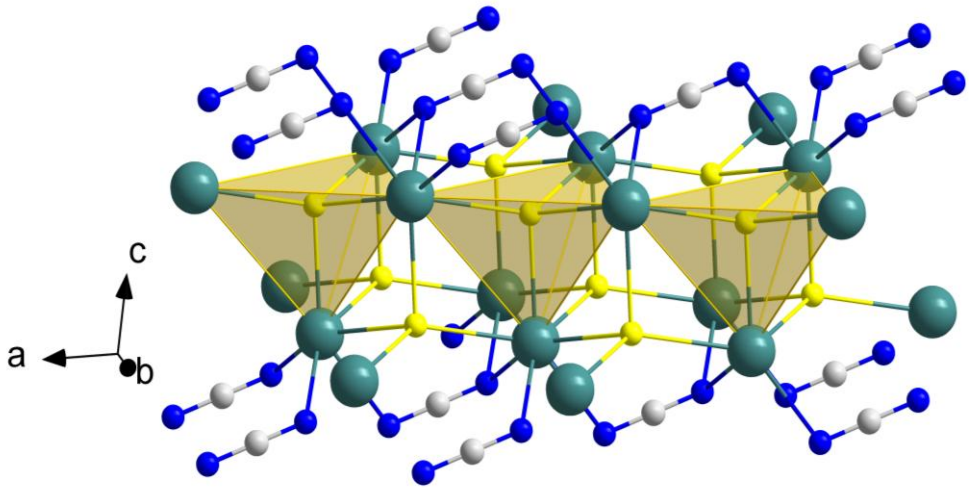

Figure 12: A section of the layered arrangement in the structure of $La_2S_2(CN_2)$. Environments of sulfur atoms are highlighted as yellow tetrahedra. Reproduced from Publication 2.

Crystallographically, the structure is straightforward, with one independent position for each element, and the combination of layered stacking, sevenfold lanthanum coordination, and sulfur-centered [La_4S] connectivity (Figure 13) captures the essential features of $La_2S_2(CN_2)$. The

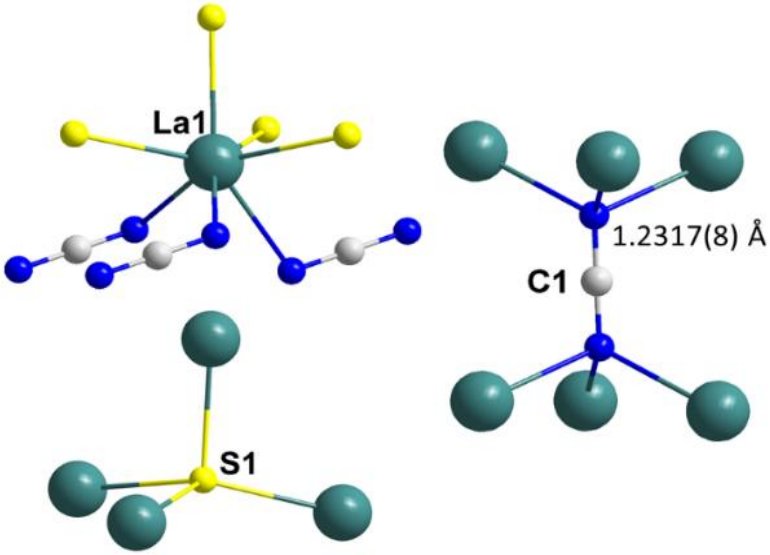

Figure 13: Coordination environments in $La_2S_2(CN_2)$ of La1, S1, and the carbodiimide unit . Reproduced from Publication 2.

same structural motif is also realized in the neodymium and samarium analogues, and $La_2S_2(CN_2)$ is isotypic with the corresponding $Nd_2S_2(CN_2)$ (CCDC: 2338177) and $Sm_2S_2(CN_2)$ (CCDC: 2338101) phases.

3.3 Characterizing Gallium Dinitridocarbonates: A Focus on $LiGa(CN_2)_2$, $Li_{13.6}Ga_{2.8}(CN_2)_{10}I_2$, and $SrGa_2(CN_2)_4$ (Publication 3)[101]

This study reports the synthesis and characterization of three gallium dinitridocarbonates, $LiGa(CN_2)_2$, $Li_{13.6}Ga_{2.8}(CN_2)_{10}I_2$, and $SrGa_2(CN_2)_4$, prepared by solid-state metathesis (SSM) and examined by single-crystal and powder X-ray diffraction, infrared spectroscopy, solid-state NMR, and optical diffuse reflectance. Stoichiometric reactions of $GaCl_3$ or GaI_3 with $Li_2(CN_2)$ yield $LiGa(CN_2)_2$ and $Li_{13.6}Ga_{2.8}(CN_2)_{10}I_2$, respectively; $SrGa_2(CN_2)_4$ forms from $SrCl_2$, $GaCl_3$, and $Na_2(CN_2)$. All products are obtained as crystalline powders in high yields; $LiGa(CN_2)_2$ and $Li_{13.6}Ga_{2.8}(CN_2)_{10}I_2$ are moisture-sensitive, whereas $SrGa_2(CN_2)_4$ remains unchanged over several days in air under ambient conditions. Powder diffraction patterns matches the calculated pattern from the refined single-crystal structures. Single-crystal X-ray diffraction assigns the space group of $LiGa(CN_2)_2$ to $I2_12_12_1$, $Li_{13.6}Ga_{2.8}(CN_2)_{10}I_2$ to *Imma*, and $SrGa_2(CN_2)_4$ to $P2_1/c$. In all three structures, metal-centered tetrahedral units are linked by $[NCN]^{2-}$ groups.

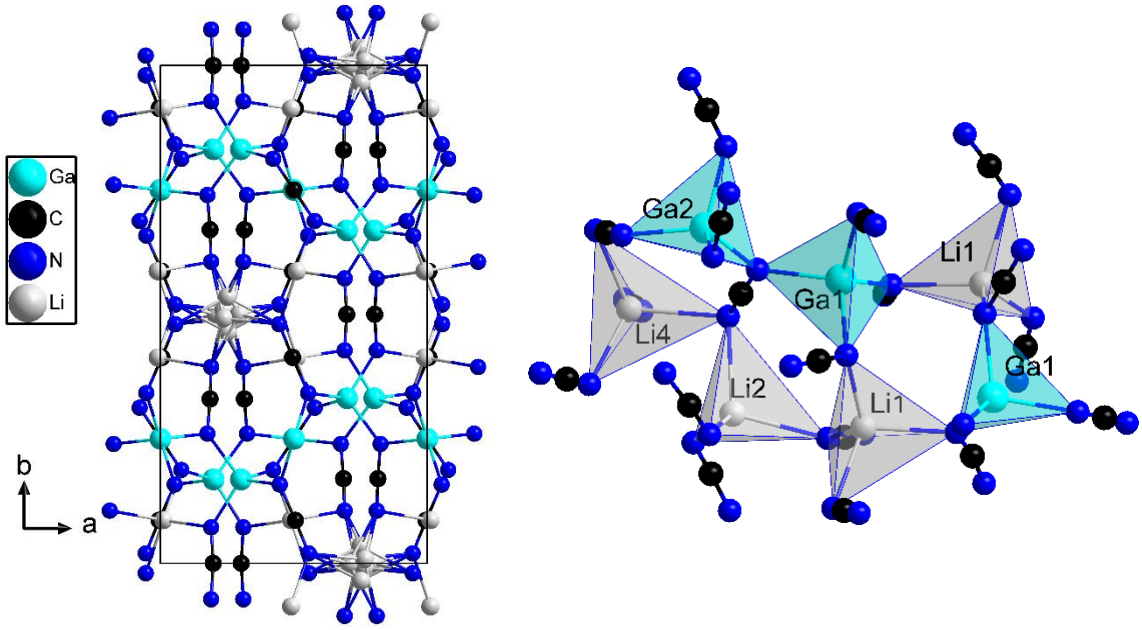

Figure 14: The unit cell of the $LiGa(CN_2)_2$ with the disordered lithium ions in channels along the c-axis (left). Section of the structure of $LiGa(CN_2)_2$, showing the tetrahedral environments of the lithium and gallium atoms. Here Li is grey, Ga turquoise, C black and N blue. Modified from Publication 3.

For $LiGa(CN_2)_2$, the framework comprises Ga- and Li-centered tetrahedra (Figure 14), some corner-connected via nitrogen, with positional disorder of lithium along channels parallel to *c*-axis.

The $[NCN]^{2-}$ anions occur in both carbodiimide-like (near-linear, more symmetric) and cyanamide-like (asymmetric) environments, consistent with dual spectroscopic signatures.

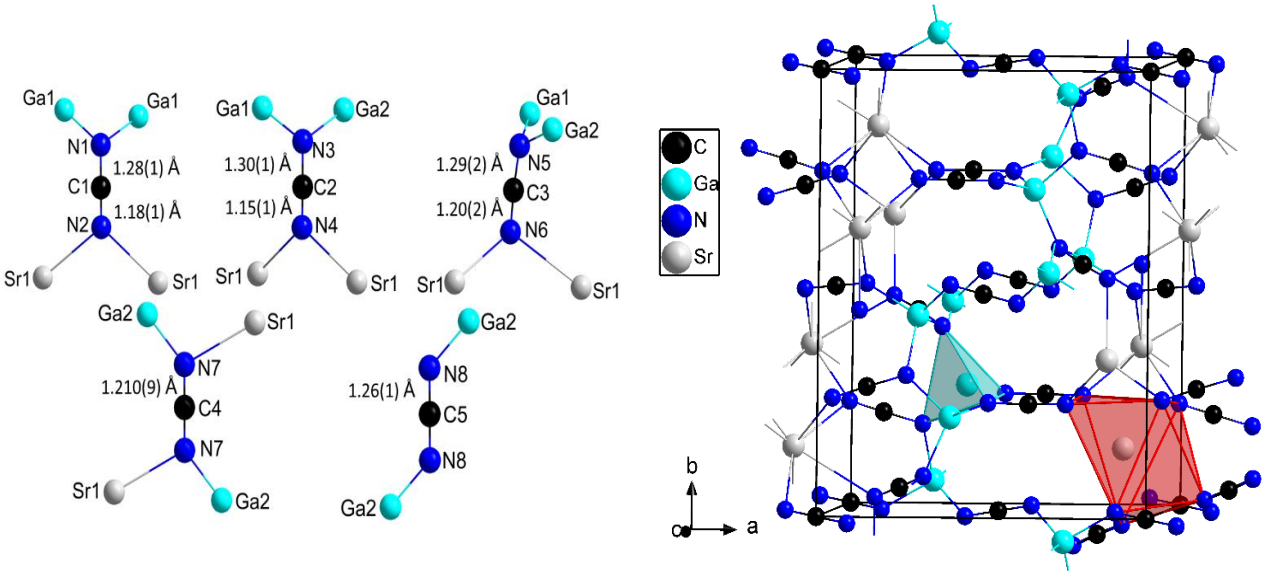

Figure 15: Coordination environments of each crystallographically independent $[NCN]^{2-}$ ion in the structure of $SrGa_2(CN_2)_4$ (left). Unit cell of $SrGa_2(CN_2)_4$ showing network of Ga^{3+} and Sr^{2+} cations interconnected via carbodiimide bridges (right). Modified from Publication 3.

$SrGa_2(CN_2)_4$ contains a mixed-cation network of Ga^{3+} and Sr^{2+} interconnected by five crystallographically distinct $[NCN]^{2-}$ groups (Figure 15, left) and is built from condensed tetracyanamidogallate chains of the –Ga–NCN–Ga–NCN– type; gallium remains tetrahedrally coordinated by nitrogen, while strontium adopts a higher coordination (Figure 15, right).

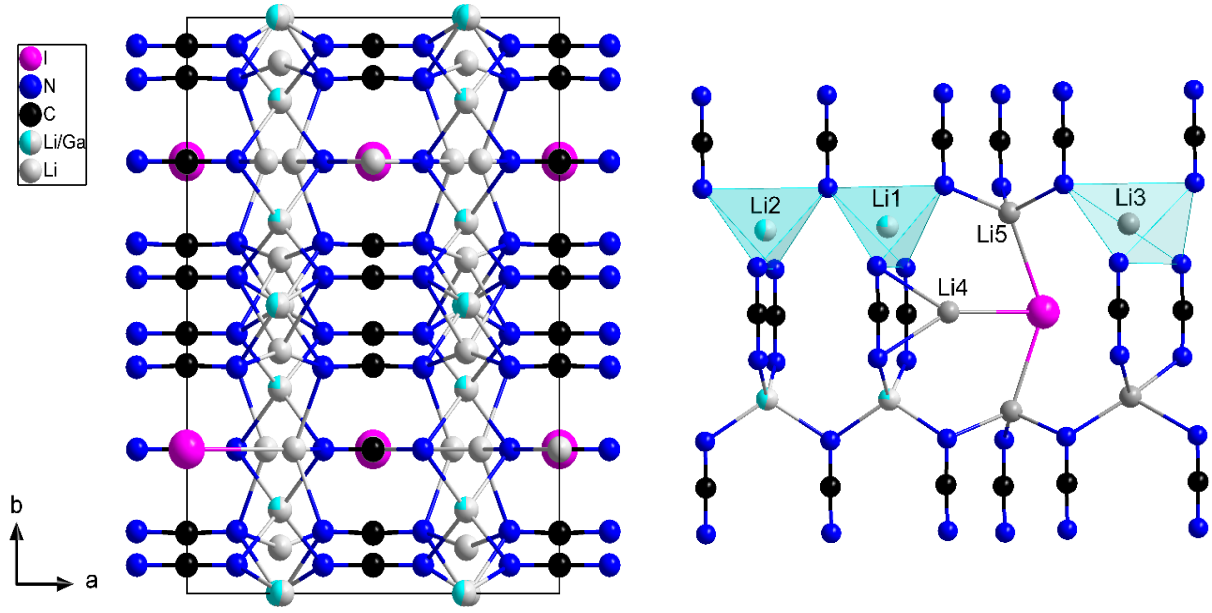

Figure 16: Layered arrangement of the compound $Li_{13.6}Ga_{2.8}(CN_2)_{10}I_2$ (left). A section of the metal carbodiimide layer in the structure of $Li_{13.6}Ga_{2.8}(CN_2)_{10}I_2$, with highlighted Li1/Ga1, Li2/Ga2 and Li3 tetrahedra, with the respective lithium portion shown in grey color (right). Modified from Publication 3.

$Li_{13.6}Ga_{2.8}(CN_2)_{10}I_2$ is described by a layered arrangement (Figure 16) of alternating cation and $[NCN]^{2-}$ layers, with mixed Li/Ga occupancies on two cation sites rationalized by similar radii and common tetrahedral preferences; the remaining lithium positions complete the cation sublattice and may be partially occupied to satisfy charge balance. The $[NCN]^{2-}$ groups adopt nearly trigonal-prismatic coordination by surrounding cations as dictated by symmetry, and iodide resides within the cation layer. Infrared spectra corroborate the anion assignments: $LiGa(CN_2)_2$ shows two prominent asymmetric stretches indicative of coexisting carbodiimide- and cyanamide-type units, with additional features in the symmetric-stretch and bending regions; $Li_{13.6}Ga_{2.8}(CN_2)_{10}I_2$ exhibits asymmetric stretches and deformations consistent with multiple, symmetry-distinct carbodiimide groups; $SrGa_2(CN_2)_4$ displays a dominant band near 2125 cm^{-1} together with bands in the 1275–1194 cm^{-1} and 781–692 cm^{-1} ranges matching the expected ν_{as}, ν_s, and δ modes of $[NCN]^{2-}$, with occasional extra bands attributable to minor side phases or incipient hydrolysis.

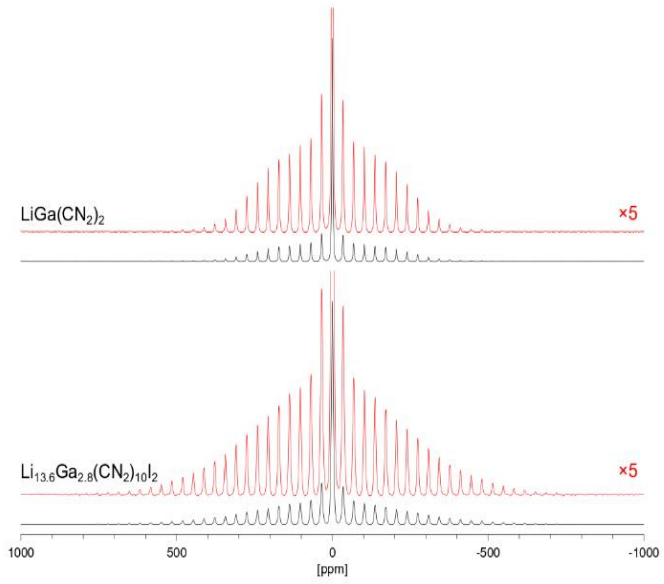

Figure 17: Lithium-7 MAS NMR spectra of $LiGa(CN_2)_2$ and $Li_{13.6}Ga_{2.8}(CN_2)_{10}I_2$ obtained at 7.05 T and a spinning rate of 4 kHz. Modified from Publication 3.

Solid-state ^7Li MAS NMR (Figure 17) confirms the presence and heterogeneity of lithium sites in the Li-containing phases: $LiGa(CN_2)_2$ gives a sharp isotropic resonance near 0.3 ppm with a sideband envelope indicating more than one Li environment and disorder along channels, while $Li_{13.6}Ga_{2.8}(CN_2)_{10}I_2$ shows a similar isotropic shift with a broader sideband manifold consistent with several lithium positions of different occupancy and multiplicity; the absence of a ^{127}I MAS signal characteristic of LiI helps exclude this contaminant. For $SrGa_2(CN_2)_4$, Kubelka–Munk/Tauc analysis of diffuse-reflectance data indicates an indirect band gap of about 3.04 eV and a direct transition near 3.30 eV, placing this compound among wide-gap semiconductors.

3.4 A Mixed-Anion Compound Based Upon a [Pb_4O_4] Heterocubane Unit: Synthesis, Structure and Electronic Properties of $Pb_8O_4I_6(CN_2)$ (Publication 4)[46]

The mixed-anion compound $Pb_8O_4I_6(CN_2)$ is obtained as an air-stable, dark-yellow crystalline material by a ceramic route from PbI_2, PbO, and $Pb(CN_2)$ (3:4:1). Single-crystal X-ray diffraction assigns the monoclinic space group *C*2/*c* and reveals a heterocubane-type [Pb_4O_4] unit that is interconnected by iodide bridges and $[NCN]^{2-}$ ligands; the composition and phase purity are supported by EDX and powder X-ray diffraction. The $[NCN]^{2-}$ anion is essentially linear and displays IR bands characteristic of a symmetric carbodiimide (deformation near 638 cm^{-1} and asymmetric stretch near 1908 cm^{-1}). Within the crystal structure, layers containing chains of alternating [Pb_4O_4] units and $[NCN]^{2-}$ linkers extend in the *bc*-plane and are tied together along *c* by iodide (Figure 18; left), these heterocubane-based layers alternate with iodide-only planes to produce a stacked architecture. The [Pb_4O_4] motif (Figure 18, right), known from oxide-halide chemistry,[102] appears here as the first structurally characterized dinitridocarbonate example in which the stereochemically active $6s^2$ lone pair of Pb^{2+} shapes local coordination.

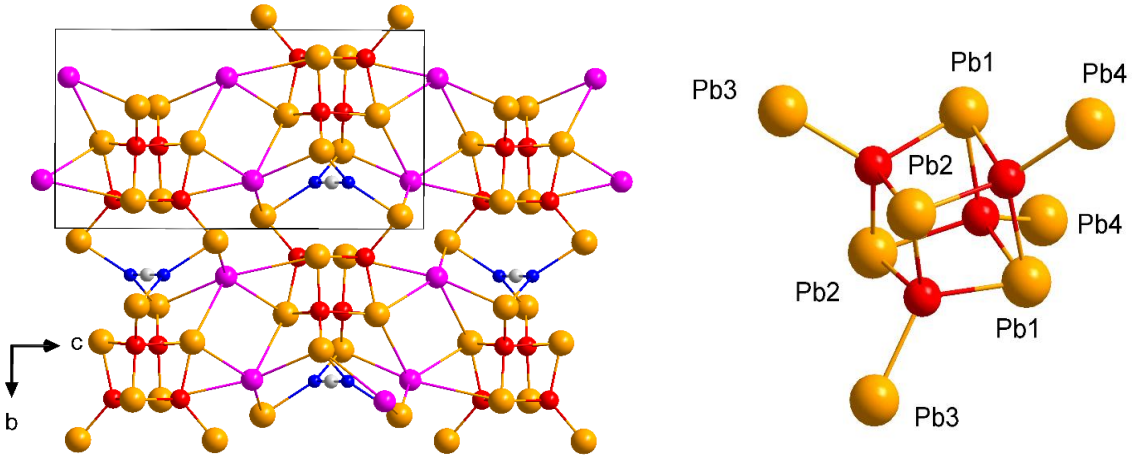

Figure 18: Representation of the atomic arrangement within a single layer of the $Pb_8O_4I_6(CN_2)$ structure (left). The heterocubane motif with surrounding lead atoms (Pb3 and Pb4) in the structure of $Pb_8O_4I_6(CN_2)$ (right). Modified from Publication 4.

Diffuse-reflectance spectroscopy analyzed via the Kubelka–Munk/Tauc formalism indicates indirect and direct optical band gaps of 2.58 eV and 2.63 eV, respectively. Mott–Schottky measurements (0.1 M phosphate buffer, pH 7) show positive slopes consistent with n-type behavior and yield a flat-band potential of about 0.09 V vs. RHE; using the optical gaps, the valence-band edge is positioned near 2.67–2.72 V vs. RHE (Figure 19, left), placing the material in the regime relevant for photoanodic oxygen evolution. Chronoamperometry under chopped AM

1.5G illumination confirms photoresponse (Figure 19, right), and cyclic voltammetry before and after Mott–Schottky analysis indicates electrochemical stability.

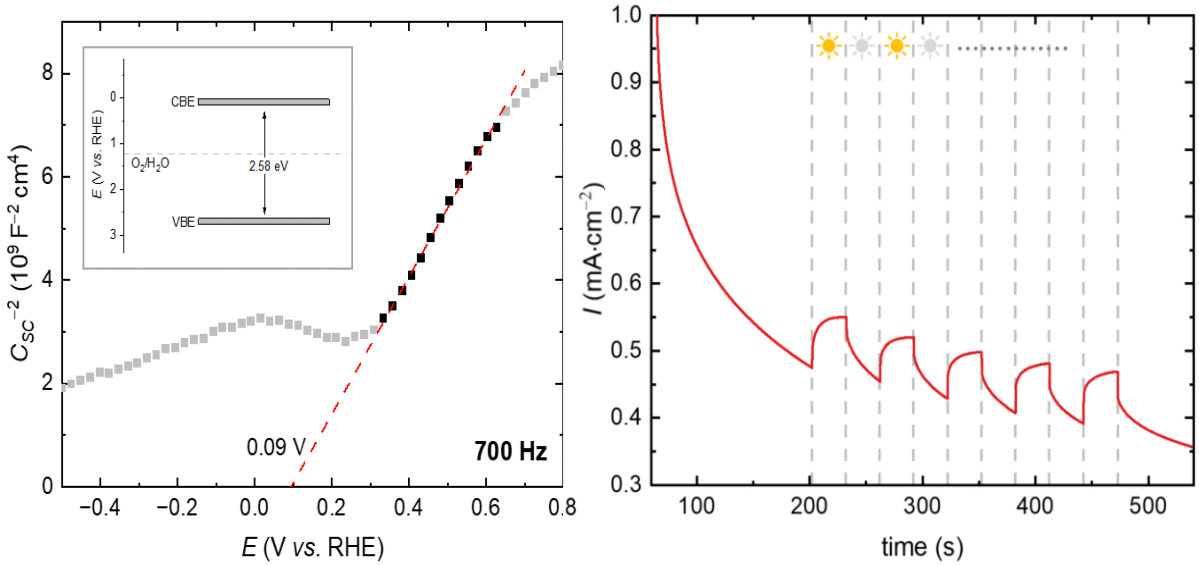

Figure 19: Mott−Schottky plot of $Pb_8O_4I_6(CN_2)$ on FTO substrate in 0.1M KPi−electrolyte (Sørensen) with pH 7.0 at a frequency of 700 Hz. Inserted is a schematic representation of the energy levels for $Pb_8O_4I_6(CN_2)$ (left). CA curves recorded at 0 V vs. RHE of $Pb_8O_4I_6(CN_2)$ in 0.1 M KPi (pH 7.0) under interrupted AM 1.5G illumination (right). The light source is switched on in areas marked with a yellow sun and switched off in time intervals marked with a grey sun. Modified from Publication 4.

Low-temperature photoluminescence complements the electronic picture. At 80 K, excitation monitored at 520 nm resolves sub-bands at 310, 333, and 376 nm attributable to $^1S_0 \rightarrow {}^3P_0$, $^3P_1$, $^3P_2$ transitions of Pb^{2+}; emission (excitation 377 nm) appears as a broad band centered at 520 nm and is nearly quenched by 150 K. Time-resolved data at 80 K show mono-exponential decay with a lifetime of roughly 380 ns. Together with the optical and electrochemical results, these spectra establish $Pb_8O_4I_6(CN_2)$ as an n-type semiconductor featuring a heterocubane-linked framework with carbodiimide and iodide ligation.

3.5 From Heterocubane Units to Extended Networks: Synthesis, Structure, and Optical Properties of $Pb_9O_2I_8(CN_2)_3$ and $Pb_{16}O_5I_{14}(CN_2)_4$ (Publication 5)[103]

$Pb_9O_2I_8(CN_2)_3$ and $Pb_{16}O_5I_{14}(CN_2)_4$ were prepared by ceramic solid-state reactions from PbI_2, PbO and $Pb(CN_2)$ at 420 °C to give air-stable yellow powders. Both phases were verified by single-crystal X-ray diffraction and optical spectroscopy. To confirm composition, EDX spot analyses on crystallites gave Pb:I ratios of 9:7.99(8) for $Pb_9O_2I_8(CN_2)_3$ and 16:14.01(3) for $Pb_{16}O_5I_{14}(CN_2)_4$, in good agreement with the ideal stoichiometry. $Pb_9O_2I_8(CN_2)_3$ crystallizes orthorhombically in *Pbcn*. The structure features five distinct Pb^{2+} sites in hemidirected to holodirected environments that are built from iodide, oxygen and carbodiimide. Two nearly linear $[NCN]^{2-}$ units occupy crystallographically distinct positions and are each coordinated in a trigonal-antiprismatic fashion by Pb, acting as multibridging ligands. The key building block is a heterocubane-type $[Pb_4O(CN_2)_{3/2}]$ unit (Figure 20) with an oxygen atom in μ_3-coordination. These heterocubane units connect via shared $[NCN]^{2-}$ ligands into a tetrahedral arrangement, with an additional linkage provided through a shared oxygen atom.

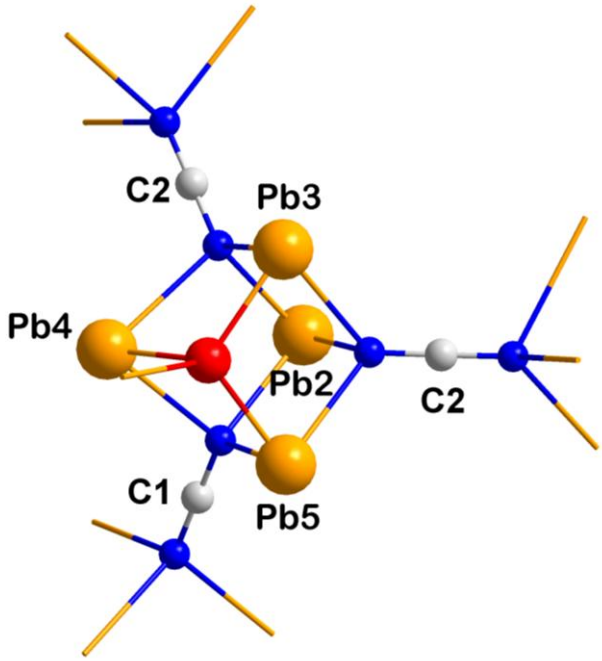

Figure 20: The heterocubane $[Pb_4O(CN_2)_{3/2}]$ unit in a tetrahedral surrounding. Oxygen is shown in red, carbon in white, and nitrogen in blue. Iodide atoms are omitted for clarity to highlight the unit. Reproduced from Publication 5.

Starting from this building block, the framework forms an annular assembly of six heterocubane units arranged into a ring, stabilized by a central octahedral $[PbI_6]^{4-}$ unit (Figure 21, left). Within the unit cell, these heterocubane-based ring systems form structural layers that propagate diagonally relative to the *ac* plane and are interconnected through bridging $[NCN]^{2-}$ units, iodide ions and common oxygen atoms to produce an extended three-dimensional network (Figure 21, right). In analogy to silicates and aluminosilicates, where corner-sharing $[SiO_4]$/$[AlO_4]$ tetrahedra form rings and layers, these heterocubane-based rings act as a cationic counterpart to such tetrahedral building units.

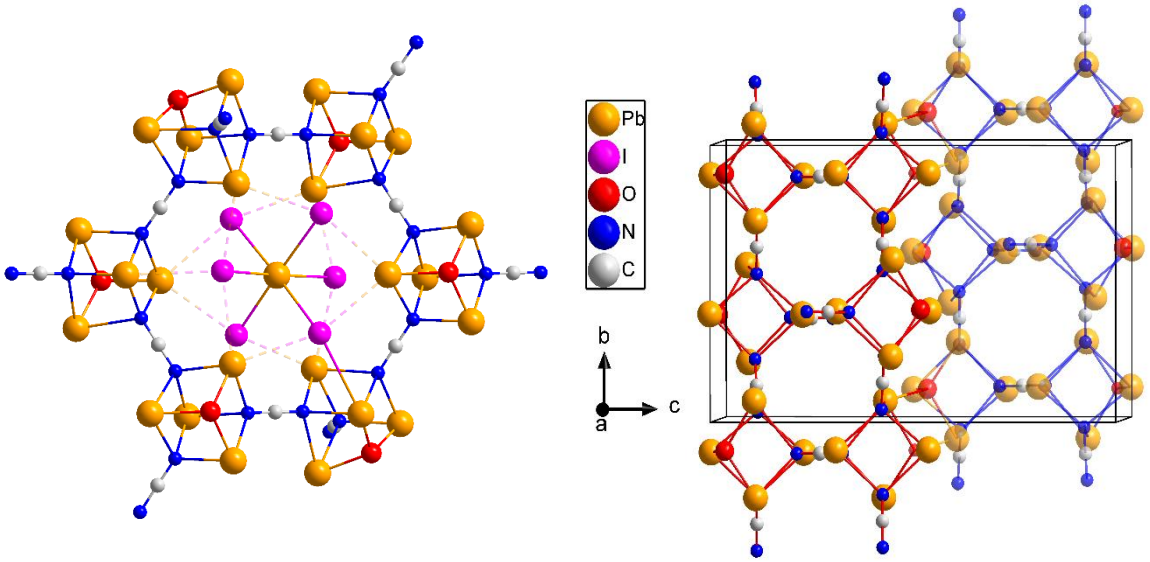

Figure 21: The annular assembly of the heterocubane units (ring system) in $Pb_9O_2I_8(CN_2)_3$. The $[PbI_6]^{4-}$ octahedron serves as the cohesive agent, binding the constituent units together (left). Section of a heterocubane-based ring system in the unit cell of $Pb_9O_2I_8(CN_2)_3$. For clarity, the lead–iodide octahedra ($[PbI_6]^{4-}$) and iodide ions have been removed, and each ring is shown with different transparency levels and colors to enhance visual distinction (right). Modified from Publication 5.

.$Pb_{16}O_5I_{14}(CN_2)_4$ crystallizes monoclinic in $P2_1/n$. Sixteen crystallographically independent Pb^{2+} centers span coordination numbers from five to nine. Four distinct $[NCN]^{2-}$ groups are each embraced in trigonal-antiprismatic Pb environments and connect cluster subunits. Two motifs dominate the framework. The first motif (Figure 22, left) consists of two corner linked heterocubanes that share lead and oxygen to give a $[Pb_7O_3(CN_2)_{4/2}]$ cluster in which each oxygen is tetrahedrally coordinated by four lead atoms. The second motif (Figure 22, right) couples a heterocubane to a face-capped, distorted trigonal-bipyramidal $[Pb_5]$ fragment best viewed as two face sharing $[Pb_4]$ tetrahedra with additional caps by iodide or oxide on one side and by $[NCN]^{2-}$ on the other, written as $[Pb_7I_2(CN_2)_{4/2}O_2]$. These two motifs alternate within layers that are separated and further connected by iodide ions and $[PbI_6]^{4-}$ octahedra, yielding a zigzag-chain like arrangement within each sheet and a lamellar stacking overall. Infrared spectroscopy supports the assignment of carbodiimide ligands. $Pb_9O_2I_8(CN_2)_3$ shows the asymmetric

N=C=N stretch near 1881 cm^{-1}, together with a deformation mode near 625 cm^{-1}, while $Pb_{16}O_5I_{14}(CN_2)_4$ exhibits the asymmetric stretch near 1924 cm^{-1} and a deformation near 656 cm^{-1}. The band positions together with the near linear $[NCN]^{2-}$ geometry is consistent with predominant carbodiimide character under mixed-anion coordination.

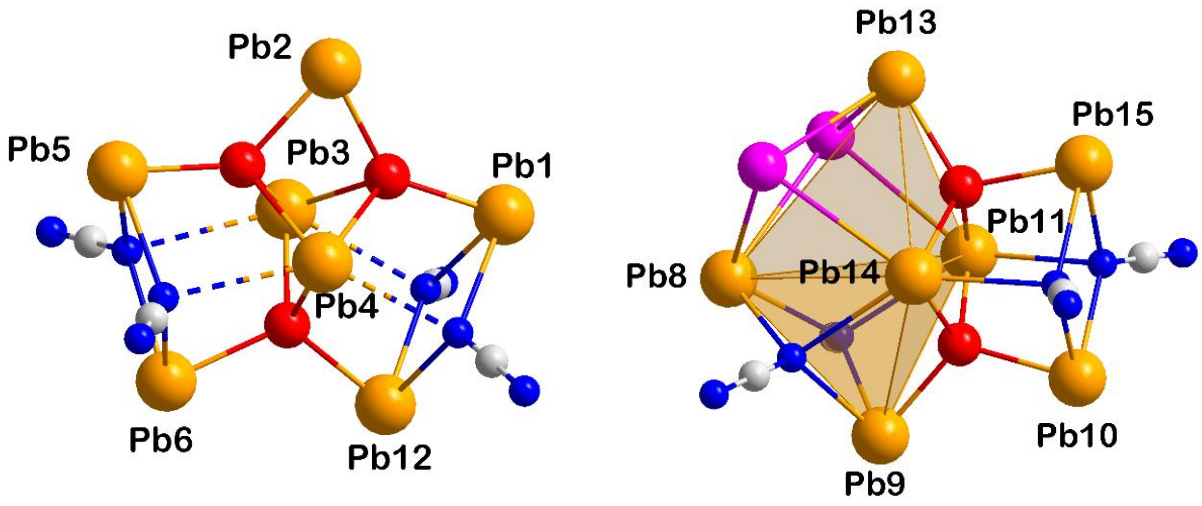

Figure 22: Section of the $[Pb_7O_3(CN_2)_{4/2}]$ cluster-like arrangement in the compound $Pb_{16}O_5I_{14}(CN_2)_4$. (left). Section of the $[Pb_7I_2(CN_2)_{4/2}O_2]$ unit in the compound $Pb_{16}O_5I_{14}(CN_2)_4$ (right). Lead is shown in orange, iodine in purple, oxygen in red, carbon in white and nitrogen in blue. For clarity the trigonal bipyramidal Pb_5-polyhedra in the $[Pb_7I_2(CN_2)_{4/2}O_2]$ unit is highlighted. Modified from Publication 5.

Diffuse-reflectance spectroscopy evaluated with the Kubelka-Munk function and Tauc plots indicates indirect band gaps of about 2.35 eV for $Pb_9O_2I_8(CN_2)_3$ and about 2.36 eV for $Pb_{16}O_5I_{14}(CN_2)_4$ with closely lying direct allowed transitions. The magnitude of these gaps makes both compounds plausible candidates for photocatalysis under visible to near UV excitation, though a robust assessment requires band edge alignment relative to the relevant redox potentials and verification of stability and activity under operating conditions. Photoluminescence at 80 K displays broad green emissions centered near 520 nm for both compounds with excitation bands around 301 to 377 nm (Figure 23). The emission is assigned to the $^3P_1 \rightarrow {}^1S_0$ transition of Pb^{2+} in a $6s^2$ configuration and is consistent with mono-exponential decays of roughly 361 ns for $Pb_9O_2I_8(CN_2)_3$ and 265 ns for $Pb_{16}O_5I_{14}(CN_2)_4$, and both emissions are largely quenched by 150 K. Taken together, the two structures demonstrate how $[NCN]^{2-}$ ligands stabilize heterocubane based Pb-O cores and mediate their fusion into extended networks alongside iodide and $[PbI_6]^{4-}$ units. The combination of lone pair driven coordination variability, cluster to framework assembly and mixed anion bonding yields semiconducting hosts with characteristic low temperature green emission and band gaps that are compatible with

photocatalytic concepts, underscoring the structural and optical versatility of lead oxide iodide carbodiimides.

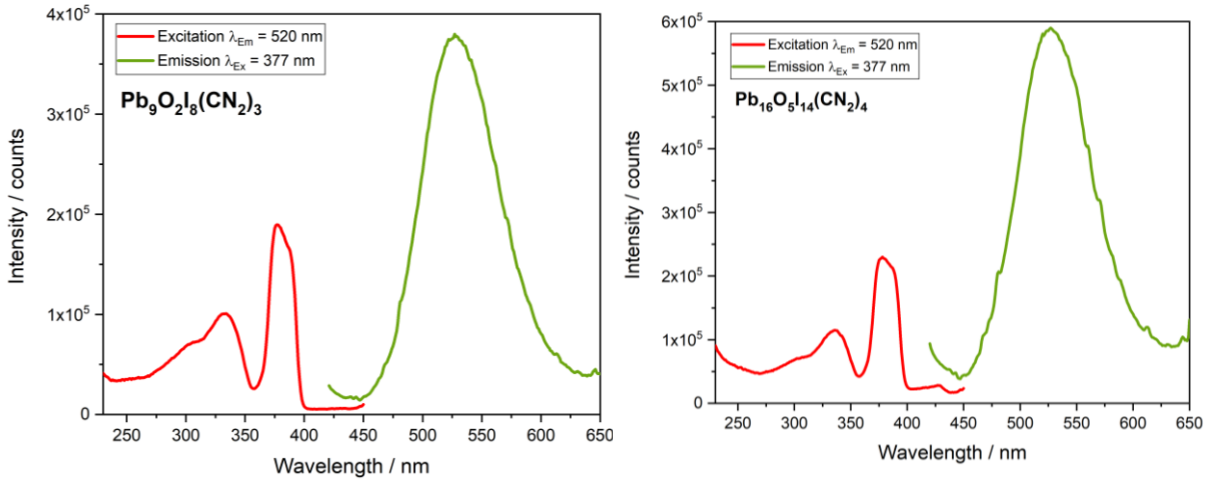

Figure 23: Excitation and emission spectra of $Pb_9O_2I_8(CN_2)_3$ at 80 K (left). Excitation and emission spectra of $Pb_{16}O_5I_{14}(CN_2)_4$ at 80 K (right). Modified from Publication 5.

3.6 Synthesis, Structure, and Eu^{3+}-Activated Photoluminescence of the Mixed-Anion Carbodiimide $NaLa_2F_3(CN_2)_2$ (Publication 6)[104]

$NaLa_2F_3(CN_2)_2$ was obtained in high yield through solid-state metathesis of LaF_3 with $Na_2(CN_2)$, affording an air- and moisture-stable white powder. Single-crystal X-ray diffraction shows a monoclinic structure in space group *I*2/*a* that is isotypic with the Li*RE*$_2$F$_3$(CN$_2$)$_2$ (*RE* = Ce, Pr, Nd, Sm, Eu, Gd)[56] family known in the symmetry-equivalent *C*2/*c* setting.

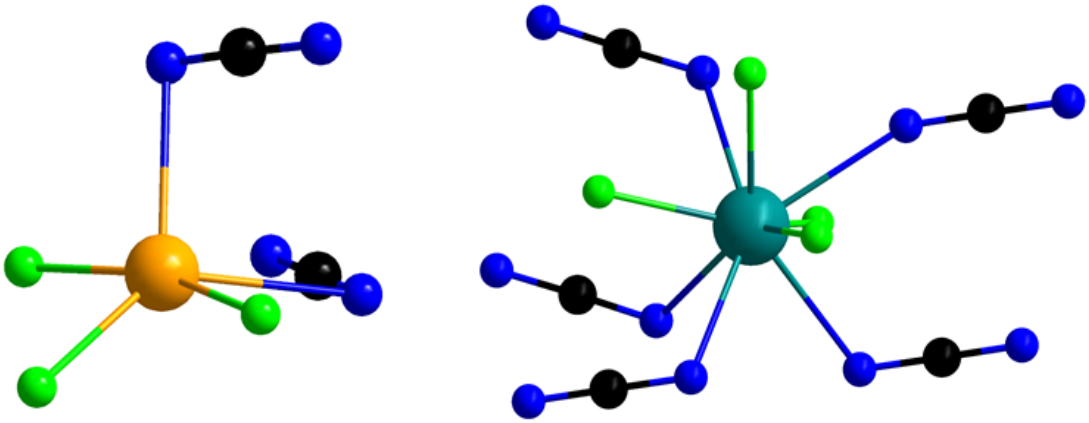

Figure 24: Coordination environment of the sodium atoms (left) and of the lanthanum atoms (right). Fluorine atoms are shown in green, lanthanum in turquoise, sodium in orange, carbon in black and nitrogen in blue. Reproduced from Publication 6.

The framework contains one crystallographic La^{3+} and one Na^+ site. La^{3+} is coordinated by five nitrogen from nearly linear carbodiimide anions together with four fluoride ligands to form a distorted tricapped trigonal-prism described as [La(NCN)$_5$F$_4$]. Na^+ adopts a distorted tetragonal-pyramidal environment (Figure 24). The $[NCN]^{2-}$ group bridges between La-centered polyhedra and at the same time links into the Na sublattice, and infrared spectra recorded between 400 and 4000 cm^{-1} display the asymmetric N=C=N stretch near 2011 cm^{-1} together with a *pseudo*-symmetric stretch near 1255 cm^{-1} and bending modes around 683 to 656 cm^{-1}, in line with a carbodiimide environment in mixed-anion hosts. Comparison with $La_2(CN_2)_3$[37] underscores the impact of mixed-anion chemistry (Figure 25). Both compounds crystallize in *I*2/*a* and show layered arrangements. $La_2(CN_2)_3$ features nearly regular [La(NCN)$_8$] dodecahedra and a more compact stacking motif. In $NaLa_2F_3(CN_2)_2$ the competition between F^- and $[NCN]^{2-}$ at La produces pronounced polyhedral distortions and a more open stacking with Na^+ incorporated into the carbodiimide layers. The composition can be rationalized by replacing one $[NCN]^{2-}$ unit of the binary parent with Na^+ and balancing the charge with three additional

fluoride ions, which corresponds to an $[NaF_3][La_2(CN_2)_2]$ partition or alternatively a NaF adduct to $LaF(CN_2)$.

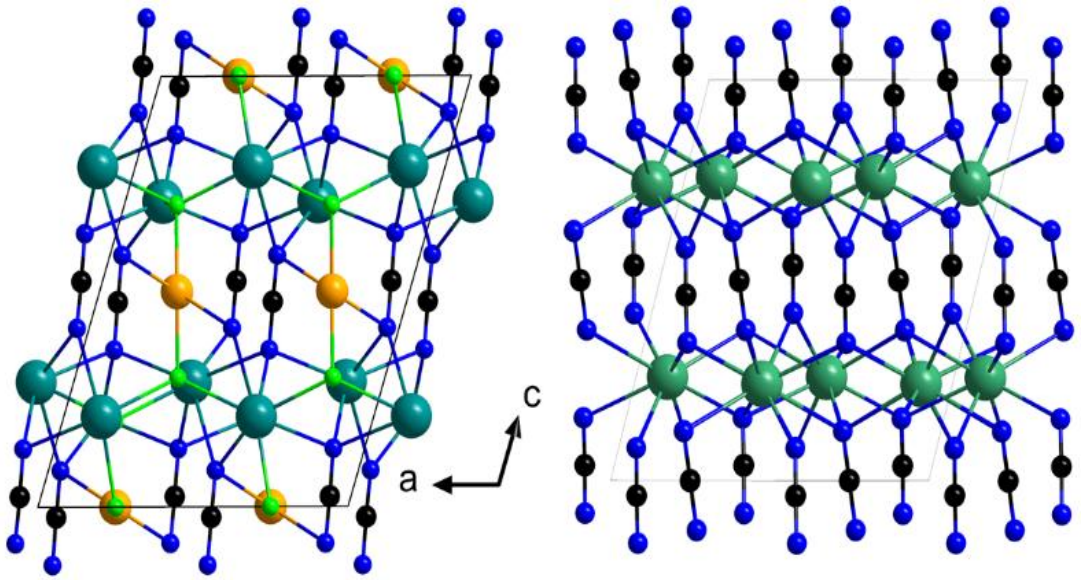

Figure 25: Comparison of the unit cell of $NaLa_2F_3(CN_2)_2$ (left) and $La_2(CN_2)_3$ (right). Fluorine atoms are shown in green, lanthanum in turquoise, sodium in orange, carbon in black, and nitrogen in blue. Reproduced from Publication 6.

Eu^{3+} doping produces a broad ligand-to-metal charge-transfer excitation near 302 nm together with the characteristic $^5D_0 \rightarrow {}^7F_J$ emissions with $J = 0–4$ and an unusually intense $^5D_0 \rightarrow {}^7F_4$ band (Figure 26). The high intensity of this transition is attributed to the low symmetry of the

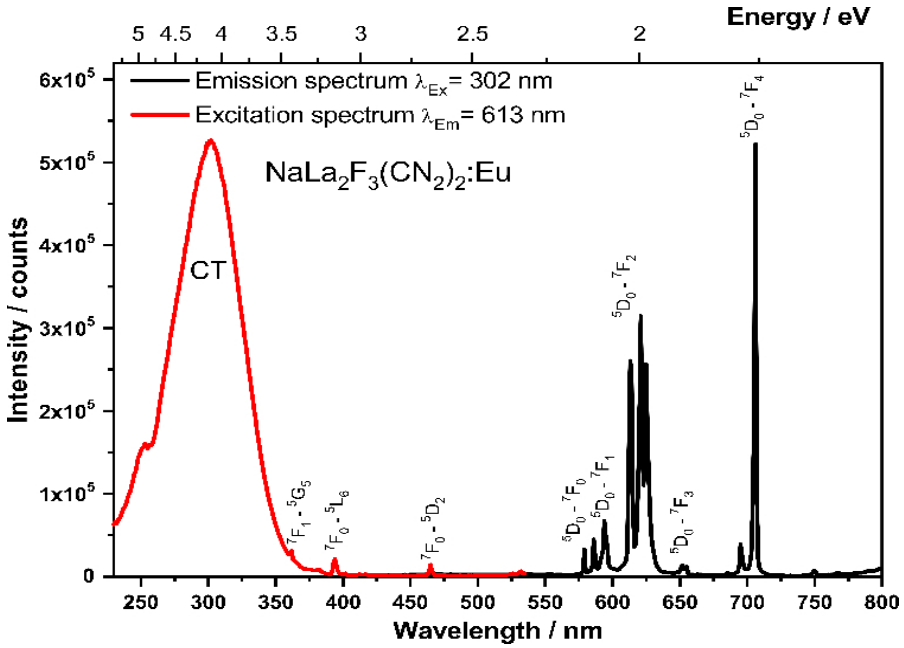

Figure 26: Excitation and emission spectra of $NaLa_2F_3(CN2)2:Eu^{3+}$. Modified from Publication 6.

activator site and the high polarizability of the surrounding carbodiimide environment, which increase the Judd-Ofelt parameter Ω_4 within the framework of Judd-Ofelt analysis.

4. Conclusions

This dissertation demonstrates that $[NCN]^{2-}$ based nitridocarbonates form a versatile mixed-anion and mixed-cation design space in which structure, bonding, and optoelectronic function can be tuned in a controlled way, enabled by robust moderate-temperature solid-state synthesis routes (especially solid-state metathesis and complementary ceramic reactions) that yield single crystals and near phase-pure powders suitable for comprehensive characterization. A central outcome is the systematic development of mixed-anion lead carbodiimides including $Pb_7I_6(CN_2)_4$, $Pb_8O_4I_6(CN_2)$, $Pb_9O_2I_8(CN_2)_3$, and $Pb_{16}O_5I_{14}(CN_2)_4$, which progress from an iodide-carbodiimide framework with Pb cluster-like motifs to oxide, iodide and carbodiimides built around discrete $[Pb_4O_4]$ heterocubanes and further to heterocubane-derived extended networks; across this series, the compounds behave as semiconductors (optical band gaps around 2.4 – 2.6 eV) and show characteristic broad green Pb^{2+} emission near 520 – 525 nm at low temperatures, with mono-exponential lifetimes on the order of a few nanoseconds and pronounced thermal quenching by about 150 K. Beyond establishing structure – property continuity within the Pb systems, $Pb_8O_4I_6(CN_2)$ is identified as an n-type semiconductor by Mott-Schottky analysis and demonstrates photoresponse under AM 1.5G illumination, linking the structural concept of heterocubane-based mixed-anion frameworks directly to photoelectrochemical relevance.

The dissertation also expands the chemistry in complementary directions. $La_2S_2(CN_2)$ constitutes the first sulfide-carbodiimide and transfers a known layered rare-earth motif into dinitridocarbonate chemistry by formally replacing $[C_2]^{2-}$ with linear $[N=C=N]^{2-}$, while retaining clear carbodiimide vibrational signatures. In main-group chemistry, the gallium dinitridocarbonates $LiGa(CN_2)_2$, $Li_{13.6}Ga_{2.8}(CN_2)_{10}I_2$, and $SrGa_2(CN_2)_4$ show how tetrahedrally coordinated Ga units linked by $[NCN]^{2-}$ generate either 3D frameworks or layered arrangements, with $SrGa_2(CN_2)_4$ being air-stable and exhibiting wide-gap semiconducting behavior (indirect/direct gaps 3.04/3.30 eV), and the IR spectra indicating coexisting carbodiimide- and cyanamide-types in selected structures.

Finally, $NaLa_2F_3(CN_2)_2$ establishes a robust carbodiimide–fluoride rare-earth host lattice that is stable in air and moisture and supports Eu^{3+}-activated photoluminescence with the expected $^5D_0 \rightarrow {}^7F_J$ emission pattern and a notably intense $^5D_0 \rightarrow {}^7F_4$ transition attributed to low local symmetry and a highly polarizable carbodiimide environment. Taken together, the work provides a coherent structure – property picture in which the $[NCN]^{2-}$ unit serves as a structurally adaptable linker across halide-, oxide-, sulfide-, and fluoride-containing lattices, while mixed-

anion chemistry and local coordination (including lone-pair effects in Pb^{2+}) control framework connectivity, band gaps, and emission behavior; these insights suggest clear future pathways in targeted anion/cation substitution and defect control to tune band edges and thermal luminescence stability, and in systematic (photo)electrochemical benchmarking of the most promising mixed-anion semiconductors under operating conditions.

5. References

[1] S. King and J. Strope, *Infrared Spectra of the Argon Matrix-Isolated Cyanamide, Cyanamide-d_2, and Carbodiimide.* The Journal of Chemical Physics, 1971. **54**(3): p. 1289-1295.

[2] L. Denner, P. Luger, and J. Buschmann, *X-ray structure of cyanamide at 108 K.* Acta Crystallographica Section C: Crystal Structure Communications, 1988. **44**(11): p. 1979-1981.

[3] O. Reckeweg and F.J. DiSalvo, *$EuCN_2$ — The First, but Not Quite Unexpected Ternary Rare Earth Metal Cyanamide.* Zeitschrift fur Anorganische und Allgemeine Chemie, 2003. **629**(2): p. 177-179.

[4] O. Reckeweg and A. Simon, *Azide und Cyanamide–ähnlich und doch anders.* Zeitschrift für Naturforschung B, 2003. **58**: p. 1097-1104.

[5] X. Liu, M. Krott, P. Müller, C. Hu, H. Lueken, and R. Dronskowski, *Synthesis, Crystal Structure, and Properties of MnNCN, the First Carbodiimide of a Magnetic Transition Metal.* Inorganic Chemistry, 2005. **44**(9): p. 3001-3003.

[6] G. Steinman, R. M. Lemmon, and M. Calvin, *Cyanamide: a possible key compound in chemical evolution.* Proceedings of the National Academy of Sciences, 1964. **52**(1): p. 27-30.

[7] R. G. Pearson, *Hard and Soft Acids and Bases.* Journal of the American Chemical Society, 1963. **85**(22): p. 3533-3539.

[8] O. Reckeweg and F. J. Di Salvo, *Calcium Carbodiimide Compounds Revisited–Syntheses, Single Crystal Structure Determination and Vibrational Spectra of $Ca_{11}N_6[CN_2]_2$, $Ca_4N_2[CN_2]$ and $Ca[CN_2]$.* Zeitschrift für Naturforschung B, 2008. **63**(5): p. 530-536.

[9] M. L. Kastens and W. G. McBurney, *Calcium Cyanamid.* Industrial & Engineering Chemistry, 1951. **43**(5): p. 1020-1033.

[10] M. A. Bredig, *The Crystal Structure of Calcium Cyanamide.* Journal of the American Chemical Society, 1942. **64**(7): p. 1730-1731.

[11] N. -G. Vannerberg, G. Claeson, L. Schotte, A. Block-Bolten, J. Toguri, and H. Flood, *The Crystal Structure of Calcium Cyanamide.* Acta Chemica Scandinavica, 1962. **16**: p. 2263-2266.

[12] M. G. Down, M. J. Haley, P. Hubberstey, R. J. Pulham, and A. E. Thunder, *Solutions of lithium salts in liquid lithium: preparation and X-ray crystal structure of the dilithium salt of carbodi-imide (cyanamide).* Dalton Transactions, 1978(10): p. 1407-1411.

[13] R. G. Pearson, *Absolute electronegativity and hardness: application to inorganic chemistry.* Inorganic Chemistry, 1988. **27**(4): p. 734-740.

[14] X. Liu, A. Decker, D. Schmitz, and R. Dronskowski, *Crystal structure refinement of lead cyanamide and the stiffness of the cyanamide anion.* Zeitschrift für Anorganische und Allgemeine Chemie, 2000. **626**: p. 103.

[15] M. Becker, J. Nuss, and M. Jansen, *Kristallstruktur und schwingungsspektroskopische Daten von Silbercyanamid / Crystal Structure and Spectroscopic Data of Silver Cyanamide.* Zeitschrift für Naturforschung B, 2000. **55**(5): p. 383-385.

[16] X. Liu, P. Müller, P. Kroll, and R. Dronskowski, *Synthesis, structure determination, and quantum-chemical characterization of an alternate HgNCN polymorph.* Inorganic Chemistry, 2002. **41**(16): p. 4259-4265.

[17] U. Berger and W. Schnick, *Syntheses, crystal structures, and vibrational spectroscopic properties of $MgCN_2$, $SrCN_2$, and $BaCN_2$.* Journal of Alloys and Compounds, 1994. **206**(2): p. 179-184.

[18] F. Schnorf, *Über die Herstellung von Calciumcyanamid aus Calciumcarbonat*. 1950, ETH Zurich.

[19] K. -D. Wehrstedt, W. Wildner, T. Güthner, K. Holzrichter, B. Mertschenk, and A. Ulrich, *Safe transport of cyanamide.* Journal of Hazardous materials, 2009. **170**(2): p. 829-835.

[20] N. Caro and A. Frank, *Verfahren zur Darstellung von Cyanverbindungen aus Carbiden*. 1895, Deutsches Reichspatent: Germany.

[21] U. Dehlinger, *Über die Raumgruppe von $(CN_2H_2)_2$ und die Kristallstruktur von $CaCN_2$*. Zeitschrift für Kristallographie - Crystalline Materials, 1927. **65**: p. 286-290.

[22] Y. Yamamoto, K. Kinoshita, K. Tamaru, and T. Yamanaka, *Redetermination of the crystal structure of calcium cyanamide.* Bulletin of the Chemical Society of Japan, 1958. **31**(4): p. 501-502.

[23] K. Suzuki, N. Kashiwa, K. Nomura, R. Asiloglu, and N. Harada, *Impacts of application of calcium cyanamide and the consequent increase in soil pH on*

N_2O emissions and soil bacterial community compositions. Biology and Fertility of Soils, 2021. **57**(2): p. 269-279.

[24] F. Di Gioia, M. Gonnella, V. Buono, O. Ayala, J. Cacchiarelli, and P. Santamaria, *Calcium cyanamide effects on nitrogen use efficiency, yield, nitrates, and dry matter content of lettuce.* Agronomy Journal, 2017. **109**(1): p. 354-362.

[25] B. Johnson, *The State of Ammonia Synthesis at the Turn of the Twentieth Century: The Arena for Discovery*, in *Making Ammonia: Fritz Haber, Walther Nernst, and the Nature of Scientific Discovery*. 2022, Springer International Publishing: Cham. p. 77-89.

[26] M. Becker, J. Nuss, and M. Jansen, *Synthese und Charakterisierung von Natriumcyanamid.* Zeitschrift für Anorganische und Allgemeine Chemie, 2000. **626**(12): p. 2505-2508.

[27] M. Ströbele, E. Bayat, and H.-J. Meyer, *A Systematic Study of the Solid-State Pathway from Melamine via Melaminate to Carbodiimide under Evolution of Hydrogen.* Inorganic Chemistry, 2024. **63**(35): p. 16565-16572.

[28] L. Stork, X. Liu, B.P.T. Fokwa, and R. Dronskowski, *Crystal Structure Determination of Thallium Carbodiimide, Tl_2NCN.* Zeitschrift für Anorganische und Allgemeine Chemie, 2007. **633**(9): p. 1339-1342.

[29] R. Dronskowski, *$In_{2.24}(NCN)_3$ and $NaIn(NCN)_2$: Synthesis and Crystal Structures of New Main Group Metal Cyanamides.* Zeitschrift für Naturforschung B, 1995. **50**(8): p. 1245-1251.

[30] M. Löber, K. Dolabdjian, M. Ströbele, C.P. Romao, and H.-J. Meyer, *Synthesis, Structure, and Electronic Properties of $Sn(CN_2)$ and $Sn_4Cl_2(CN_2)_3$.* Inorganic Chemistry, 2019. **58**(12): p. 7845-7851.

[31] X. Liu, L. Stork, M. Speldrich, H. Lueken, and R. Dronskowski, *FeNCN and $Fe(NCNH)_2$: Synthesis, Structure, and Magnetic Properties of a Nitrogen-Based Pseudo-oxide and -hydroxide of Divalent Iron.* Chemistry – A European Journal, 2009. **15**(7): p. 1558-1561.

[32] X. Tang, H. Xiang, X. Liu, M. Speldrich, and R. Dronskowski, *A Ferromagnetic Carbodiimide: $Cr_2(NCN)_3$.* Angewandte Chemie International Edition, 2010. **49**(28): p. 4738-4742.

[33] P. Kallenbach, M. Ströbele, and H.-J. Meyer, *Missing Carbodiimide and Oxide Carbodiimide of Scandium: $Sc_2(CN_2)_3$ and $Sc_2O_2(CN_2)$.* Zeitschrift für Anorganische und Allgemeine Chemie, 2020. **646**(15): p. 1281-1284.

[34] M. Krott, X. Liu, B.P.T. Fokwa, M. Speldrich, H. Lueken, and R. Dronskowski, *Synthesis, Crystal-Structure Determination and Magnetic Properties of Two New Transition-Metal Carbodiimides: CoNCN and NiNCN.* Inorganic Chemistry, 2007. **46**(6): p. 2204-2207.

[35] M. Becker and M. Jansen, *Zinc cyanamide, $Zn(CN_2)$.* Acta Crystallographica Section C: Crystal Structure Communications, 2001. **57**: p. 347.

[36] D. Dutczak, M. Ströbele, D. Enseling, T. Jüstel, and H.-J. Meyer, *$Eu_2(CN_2)_3$ and $KEu[Si(CN_2)_4]$: Missing Members of the Rare Earth Metal Carbodiimide and Tetracyanamidosilicate Series.* European Journal of Inorganic Chemistry, 2016. **2016**(25): p. 4011-4016.

[37] P. Schneiderhan, E. Bayat, M. Ströbele, D. Enseling, T. Jüstel, and H.-J. Meyer, *$La_2(CN_2)_3$ – the missing link of rare-earth carbodiimides, prepared through an efficient synthetic route and its Ce^{3+} activated photoluminescence.* Dalton Transactions, 2025. **54**(12): p. 4909-4917.

[38] J. Glaser, L. Unverfehrt, H. Bettentrup, G. Heymann, H. Huppertz, T. Jüstel, and H.-J. Meyer, *Crystal Structures, Phase-Transition, and Photoluminescence of Rare Earth Carbodiimides.* Inorganic Chemistry, 2008. **47**(22): p. 10455-10460.

[39] R. Srinivasan, M. Ströbele, and H.-J. Meyer, *Chains of $[RE_6]$ octahedra coupled by (NCN) links in the network structure of $RE_2Cl(CN_2)N$. Synthesis and structure of two novel rare earth chloride carbodiimide nitrides with structures related to the RE_2Cl_3 type.* Inorganic Chemistry, 2003. **42**(11): p. 3406-3411.

[40] M. Becker, M. Jansen, A. Lieb, W. Milius, and W. Schnick, *Synthese, Kristallstruktur und Festkörper-NMR-spektroskopische Untersuchungen von K5H(CN2)3.* Zeitschrift für Anorganische und Allgemeine Chemie, 1998. **624**(1): p. 113-118.

[41] H.-J. Meyer, *Solid state metathesis reactions as a conceptual tool in the synthesis of new materials.* Dalton Transactions, 2010. **39**(26): p. 5973-5982.

[42] P. Schneiderhan, M. Ströbele, and H.-J. Meyer, *Single-Source Cyanurate Precursor for Making Manganese Carbodiimide and the Second Harmonic Generation Effect of the Intermediate Manganese Monohydrocyanurate $Mn(HC_3N_3O_3)$.* European Journal of Inorganic Chemistry 2025, 28, e202500499.

[43] A. Klimek, J. Yount, D. Wozniak, M. Zeller, and D.G. Piercey, *A laboratory preparation of high-purity calcium cyanamide.* Inorganic Chemistry, 2023. **62**(40): p. 16280-16282.

[44] *Ceramic Methods*, in *Essentials of Inorganic Materials Synthesis*. 2015. p. 17-21.

[45] A.T. Schwarz, M. Ströbele, C.P. Romao, D. Enseling, T. Jüstel, and H.-J. Meyer, *The luminescent semiconductor $Pb_7I_6(CN_2)_4$.* Dalton Transactions, 2024. **53**(14): p. 6416-6422.

[46] A.T. Schwarz, N. Petersen, M. Ströbele, D. Enseling, T. Jüstel, A. Slabon, and H.-J. Meyer, *A Mixed-Anion Compound based upon a $[Pb_4O_4]$ Heterocubane Unit: Synthesis, Electronical and Optical Properties of $Pb_8O_4I_6(CN_2)$.* Dalton Trans., 2025.

[47] X. Liu, M.A. Wankeu, H. Lueken, and R. Dronskowski, *A Novel Method for Synthesizing Crystalline Copper Carbodiimide, CuNCN. Structure Determination by X-Ray Rietveld Refinement.* Zeitschrift für Naturforschung B, 2005. **60**(6): p. 593-596.

[48] G. Baldinozzi, B. Malinowska, M. Rakib, and G. Durand, *Crystal structure and characterisation of cadmium cyanamide.* Journal of Materials Chemistry, 2002. **12**(2): p. 268-272.

[49] M. Li, W. Yuan, J. Wang, C. Gu, and H. Zhao, *Syntheses and crystal structures of trigonal rare-earth dioxymonocyanamides, $Ln_2O_2CN_2$ (Ln=Dy, Ho, Er, Tm, Yb).* Powder Diffraction, 2007. **22**(1): p. 59-63.

[50] H. Yasuhiro, T. Masao, K. Shinichi, and K. Fumikazu, *Syntheses of Rare Earth Dioxymonocyanamides ($Ln_2O_2CN_2$, Ln = La, Ce, Pr, Nd, Sm, Eu, Gd).* Chemistry Letters, 1994. **23**(10): p. 1963-1966.

[51] Y. Hashimoto, M. Takahashi, S. Kikkawa, and F. Kanamaru, *Synthesis and Crystal Structure of a New Compound, Lanthanum Dioxymonocyanamide ($La_2O_2CN_2$).* Journal of Solid State Chemistry, 1995. **114**(2): p. 592-594.

[52] R. Srinivasan, S. Tragl, and H.-J. Meyer, *Synthesis and Structure of the New Compound $La_2O(CN_2)_2$ Possessing an Interchanged Anion Proportion Compared to the Parent $La_2O_2(CN_2)$.* Zeitschrift für Anorganische und Allgemeine Chemie, 2005. **631**(4): p. 719-722.

[53] M. Kubus, J. Glaser, A. Kłonkowski, and H.-J. Meyer, *Rare Earth Carbodiimide Silicates: $RE_2(CN_2)(SiO_4)$* Zeitschrift für Anorganische und Allgemeine Chemie, 2010. **636**(6): p. 991-995.

[54] A.T. Schwarz, M. Ströbele, and H.-J. Meyer, *The Mixed-Anion Compound $La_2S_2(CN_2)$.* Zeitschrift für Anorganische und Allgemeine Chemie, 2024. **650**(15), e202400038.

[55] R. Srinivasan, J. Glaser, S. Tragl, and H.-J. Meyer, *$LnCl(CN_2)$ with Ln = La, Ce, and Pr: Synthesis and Structure of a New Lanthanide Chloride Cyanamide Related to the PbFCl-Type Structure.* Zeitschrift für Anorganische und Allgemeine Chemie, 2005. **631**(2-3): p. 479-483.

[56] L. Unverfehrt, J. Glaser, M. Ströbele, S. Tragl, K. Gibson, and H.-J. Meyer, *The Versatility of Solid-State Metathesis Reactions: From Rare Earth Fluorides to Carbodiimides.* Zeitschrift für Anorganische und Allgemeine Chemie, 2009. **635**(3): p. 479-483.

[57] A. Siai, C.-D. Brand, M. Ströbele, D. Enseling, T. Jüstel, and H.-J. Meyer, *Carbodiimide Bridged Network Structure of $[RE_6O(NCN)_6]$ Clusters in the Structure of $RE_8O(CN_2)_{10}Br_2$, RE = La, Ce, Pr, Nd.* Journal of Cluster Science, 2023. **34**(2): p. 1001-1008.

[58] K. Dolabdjian, A.L. Görne, R. Dronskowski, M. Ströbele, and H.-J. Meyer, *Tin(ii) oxide carbodiimide and its relationship to SnO.* Dalton Transactions, 2018. **47**(38): p. 13378-13383.

[59] M. Löber, M. Ströbele, C.P. Romao, and H.-J. Meyer, *Synthesis, Structure, and Thermoelastic Properties of $LiSn_2Br_3(CN_2)$ and $Sn_4Br_2(CN_2)_3$.* European Journal of Inorganic Chemistry, 2021. **2021**(44): p. 4572-4578.

[60] M. Löber, C.S. Geißenhöner, M. Ströbele, S. Indris, C.P. Romao, and H.-J. Meyer, *Synthesis, Structure, and Electronic Properties of $Sn_9O_5Cl_4(CN_2)_2$.* Inorganic Chemistry, 2019. **58**(21): p. 14560-14567.

[61] J.K. Bendyna, P. Höhn, W. Schnelle, and R. Kniep, *$[Sr_6N][CoN_2][CN_2]_2$: The first low-valency nitridometalate carbodiimide.* Science and Technology of Advanced Materials, 2007. **8**(5): p. 393-398.

[62] F. Jach, P. Höhn, Y. Prots, and M. Ruck, *$Sr_4N[CN_2][C_2N]$: The First Carbodiimide Acetonitriletriide.* European Journal of Inorganic Chemistry, 2019. **2019**(9): p. 1207-1211.

[63] U. Berger, W. Milius, and W. Schnick, *$Ba_2(CN_2)(CN)_2$ und $Sr_2(CN_2)(CN)_2$ – die ersten gemischten Cyanamid-cyanide.* Zeitschrift für Anorganische und Allgemeine Chemie, 1995. **621**(12): p. 2075-2082.

[64] S. Zhang, D.A. Zherebtsov, F.J. DiSalvo, and R. Niewa, *$Na_5[CN_2]_2[CN]$, $(Li, Na)_5[CN_2]_2[CN]$, and $K_2[CN_2]$: Carbodiimides from High-Pressure Synthesis.* Zeitschrift für Anorganische und Allgemeine Chemie, 2012. **638**(12-13): p. 2111-2116.

[65] R. Niewa, P. Höhn, R. Kniep, A. Weiske, and H. Jacobs, *Crystal structure of pentapotassium dicarbodiimide monohydride, $K_5[CN_2]_2H$.* Zeitschrift für Kristallographie - New Crystal Structures, 2001. **216**(1-4): p. 357-358.

[66] L. Unverfehrt, M. Ströbele, J. Glaser, and H.-J. Meyer, *The Many Faces of Rare Earth Carbodiimide Compounds.* Zeitschrift für Anorganische und Allgemeine Chemie, 2009. **635**(12): p. 1947-1952.

[67] L. Unverfehrt, M. Ströbele, and H.-J. Meyer, *Synthesis and Crystal Structure of $LiY(CN_2)_2$, Having a Structure Related to That of NiAs.* Zeitschrift für Anorganische und Allgemeine Chemie, 2013. **639**(1): p. 22-24.

[68] M. Kubus, R. Heinicke, M. Ströbele, D. Enseling, T. Jüstel, and H.-J. Meyer, *Synthesis of new structurally related cyanamide compounds $LiM(CN_2)_2$ where M is Al^{3+}, In^{3+} or Yb^{3+}.* Materials Research Bulletin, 2015. **62**: p. 37-41.

[69] J.G. Thompson, A.D. Rae, R.L. Withers, T.R. Welberry, and A.C. Willis, *The crystal structure of nickel arsenide.* Journal of Physics C: Solid State Physics, 1988. **21**(22): p. 4007.

[70] L. Unverfehrt, M. Ströbele, and H.-J. Meyer, *The New Carbodiimide $Li_2Gd_2Sr(CN_2)_5$ Having a Crystal Structure Related to That of $Gd_2(CN_2)_3$.* Zeitschrift für Anorganische und Allgemeine Chemie, 2013. **639**(1): p. 84-88.

[71] A. J. Corkett, P. M. Konze, and R. Dronskowski, *The Ternary Post-transition Metal Carbodiimide $SrZn(NCN)_2$.* Zeitschrift für Anorganische und Allgemeine Chemie, 2017. **643**(21): p. 1456-1461.

[72] A. J. Corkett, P. M. Konze, and R. Dronskowski, *Synthesis, crystal structure, and chemical-bonding analysis of $BaZn(NCN)_2$.* Inorganics, 2017. **6**(1): p. 1.

[73] S. Broadley, Z. A. Gál, F. Corà, C. F. Smura, and S. J. Clarke, *Vertex-linked ZnO_2S_2 tetrahedra in the oxysulfide BaZnOS: a new coordination environment for zinc in a condensed solid.* Inorganic Chemistry, 2005. **44**(24): p. 9092-6.

[74] T. Okamoto, T. Ogita, S. Harako, S. Komuro, and X. Zhao, *Photocatalytic effect of $SrZnO_2$ thin films.* MRS Proceedings, 2013. **1601**: p. jsapmrs-13-1601.

[75] X. Qiao, A.J. Corkett, R.P. Stoffel, and R. Dronskowski, *Synthesis and characterisation of the quaternary cyanamide $Li_2MgSn_2(NCN)_6$.* Zeitschrift für Anorganische und Allgemeine Chemie, 2021. **647**(22): p. 2162-2166.

[76] K. Dolabdjian, C. Castro, and H.-J. Meyer, *Layered Carbodiimides $A_2M(CN_2)_3$ with Tetravalent Cations M = Sn, Zr, and Hf.* European Journal of Inorganic Chemistry, 2018. **2018**(14): p. 1624-1630.

[77] M. Vorholt, A. J. Corkett, A. Drichel, L. M. Lindenbeck, A. Slabon, and R. Dronskowski, *Topotactic Transformation of the Transition-Metal Cyanamide $Li_2MnSn_2(NCN)_6$.* Chemistry of Materials, 2025. **37**(20): p. 8337-8344.

[78] A.J. Corkett, Z. Chen, C. Ertural, A. Slabon, and R. Dronskowski, *Synthetic Engineering in $Na_2MSn_2(NCN)_6$ (M = Mn, Fe, Co, and Ni) Based on Electronic Structure Theory.* Inorganic Chemistry, 2022. **61**(45): p. 18221-18228.

[79] K. D. Röseler, K. Eichele, M. Ströbele, and H.-J. Meyer, *Crystallization of the Fundamental Tetracyanamidometallates $Li_4[Si(CN_2)_4]$ and $Li_4[Ge(CN_2)_4]$ from Polymeric Li-T-(NCN)-I Precursors (T=Si, Ge).* European Journal of Inorganic Chemistry, 2024. **27**(14): p. e202300713.

[80] J. Glaser and H.-J. Meyer, *Multilateral Solid-State Metathesis Reactions for the Preparation of Materials with Heteroanions: The $[Si(CN_2)_4]^{4-}$ Ion.* Angewandte Chemie International Edition, 2008. **47**(39): p. 7547-7550.

[81] J. Glaser, H. Bettentrup, T. Jüstel, and H.-J. Meyer, *Synthesis and properties of tetracyanamidosilicates $ARE[Si(CN_2)_4]$.* Inorganic Chemistry, 2010. **49**(6): p. 2954-2959.

[82] L. Unverfehrt, M. Ströbele, and H.-J. Meyer, *The New Homoleptic Tetracyanamidoaluminate $LiBa_2[Al(CN_2)_4]$.* Zeitschrift für Anorganische und Allgemeine Chemie, 2013. **639**(10): p. 1722-1725.

[83] L. Unverfehrt, M. Kalmutzki, M. Ströbele, and H.-J. Meyer, *Solid state synthesis of homoleptic tetracyanamidoaluminates.* Dalton Transactions, 2011. **40**(38): p. 9921-9924.

[84] M. Kalmutzki, M. Ströbele, S. Kroeker, J. E. C. Wren, and H.-J. Meyer, *Synthesis and Characterization of the First Tetracyanamidogallate.* European Journal of Inorganic Chemistry, 2013. **2013**(36): p. 6091-6096.

[85] K. Dolabdjian, C. Schedel, D. Enseling, T. Jüstel, and H.-J. Meyer, *Synthesis, Luminescence and Nonlinear Optical Properties of Homoleptic Tetracyanamidogermanates ARE[Ge(CN$_2$)$_4$] (A = K, Cs, and RE = La, Ce, Pr, Nd, Sm, Eu, Gd).* Zeitschrift für Anorganische und Allgemeine Chemie, 2017. **643**(7): p. 488-494.

[86] M. Kalmutzki, D. Enseling, J.E. Wren, S. Kroeker, V.V. Terskikh, T. Jüstel, and H.J. Meyer, *Solid State Complex Chemistry: Formation, Structure, and Properties of Homoleptic Tetracyanamidogermanates RbRE[Ge(CN$_2$)$_4$] (RE= La, Pr, Nd, Gd).* Inorganic Chemistry, 2013. **52**: p. 12372.

[87] L. Unverfehrt, M. Ströbele, and H.-J. Meyer, *LaSr$_3$F$_5$(CN$_2$)$_2$: A Prototype Structure for Mixed-Valent Eu$_4$F$_5$(CN$_2$)$_2$.* Inorganic Chemistry, 2012. **51**(23): p. 12925-12928.

[88] L. Unverfehrt, M. Ströbele, J. Glaser, T. Langer, R.-D. Hoffmann, R. Pöttgen, and H.-J. Meyer, *Refined Crystal Structure and Idealized Structure of Mixed-Valent Eu$_4$F$_5$(CN$_2$)$_2$: Transition Possible.* Inorganic Chemistry, 2011. **50**(13): p. 6010-6018.

[89] O. Kysliak, M. Ströbele, D. Enseling, T. Jüstel, and H.-J. Meyer, *Cationic Control of the Formation of Europium Carbodiimide Chlorides.* European Journal of Inorganic Chemistry, 2024. **27**(34): p. e202400437.

[90] W. Liao, C. Hu, R.K. Kremer, and R. Dronskowski, *Formation of Complex Three- and One-Dimensional Interpenetrating Networks within Carbodiimide Chemistry: NCN^{2-}-Coordinated Rare-Earth-Metal Tetrahedra and Condensed Alkali-Metal Iodide Octahedra in Two Novel Lithium Europium Carbodiimide Iodides, LiEu$_2$(NCN)I$_3$ and LiEu$_4$(NCN)$_3$I$_3$.* Inorganic Chemistry, 2004. **43**(19): p. 5884-5890.

[91] K. Dolabdjian and H.-J. Meyer, *Lead Carbodiimides Related to the Mineral Bideauxite.* Zeitschrift für Anorganische und Allgemeine Chemie, 2017. **643**(23): p. 1898-1903.

[92] M. Löber, M. Ströbele, and H.-J. Meyer, *Synthesis and crystal structure of Pb$_{14.66}$Sn$_{7.34}$Br$_{26}$(CN$_2$)$_7$O$_2$, a complex member of group 14 carbodiimides.* Zeitschrift für Anorganische und Allgemeine Chemie, 2021. **647**(20-21): p. 1973-1977.

[93] A. Olivé Corral, M. Kubus, M. Ströbele, and H.-J. Meyer, *Preparation and Crystal Structure of $Ba_4MgF_2(CN_2)_4$.* Zeitschrift für Anorganische und Allgemeine Chemie, 2014. **640**(5): p. 902-904.

[94] P.M. Mallinson, Z.A. Gál, and S.J. Clarke, *Two New Structurally Related Strontium Gallium Nitrides: Sr_4GaN_3O and $Sr_4GaN_3(CN_2)$.* Inorganic Chemistry, 2006. **45**(1): p. 419-423.

[95] X. Gonze, B. Amadon, G. Antonius, F. Arnardi, L. Baguet, J.-M. Beuken, J. Bieder, F. Bottin, J. Bouchet, E. Bousquet, N. Brouwer, F. Bruneval, G. Brunin, T. Cavignac, J.-B. Charraud, W. Chen, M. Côté, S. Cottenier, J. Denier, G. Geneste, P. Ghosez, M. Giantomassi, Y. Gillet, O. Gingras, D. R. Hamann, G. Hautier, X. He, N. Helbig, N. Holzwarth, Y. Jia, F. Jollet, W. Lafargue-Dit-Hauret, K. Lejaeghere, M. A. L. Marques, A. Martin, C. Martins, H. P. C. Miranda, F. Naccarato, K. Persson, G. Petretto, V. Planes, Y. Pouillon, S. Prokhorenko, F. Ricci, G.-M. Rignanese, A. H. Romero, M. M. Schmitt, M. Torrent, M. J. van Setten, B. Van Troeye, M. J. Verstraete, G. Zérah, and J. W. Zwanziger, *The Abinit Project: Impact, environment and recent developments.* Computer Physics Communications, 2020. **248**: p. 107042.

[96] J. P. Perdew, K. Burke, and M. Ernzerhof, *Generalized Gradient Approximation Made Simple.* Physical Review Letters, 1996. **77**(18): p. 3865-3868.

[97] M. Torrent, N. A. W. Holzwarth, F. Jollet, D. Harris, N. Lepley, and X. Xu, *Electronic structure packages: Two implementations of the projector augmented wave (PAW) formalism.* Computer Physics Communications, 2010. **181**(11): p. 1862-1867.

[98] H. J. Monkhorst and J. D. Pack, *Special points for Brillouin-zone integrations.* Physical Review B, 1976. **13**(12): p. 5188-5192.

[99] M. Methfessel and A. T. Paxton, *High-precision sampling for Brillouin-zone integration in metals.* Physical Review B, 1989. **40**(6): p. 3616-3621.

[100] Y. Hinuma, G. Pizzi, Y. Kumagai, F. Oba, and I. Tanaka, *Band structure diagram paths based on crystallography.* Comput. Mater. Sci., 2017. **128**: p. 140.

[101] A. T. Schwarz, O. Kysliak, K. Eichele, M. Ströbele, and H.-J. Meyer, *Characterizing Gallium Dinitridocarbonates: A Focus on $LiGa(CN_2)_2$, $Li_{13.6}Ga_{2.8}(CN_2)_{10}I_2$, and $SrGa_2(CN_2)_4$.* Zeitschrift für Anorganische und Allgemeine Chemie, 2025. **651**(17), e202500085.

[102] T. Oldag and H.-L. Keller, *Synthese und Kristallstruktur von Blei(II)-oxidhalogenid-Alkoholaten mit unterschiedlichen Verknüpfungsvarianten von Pb_4O_4-Heterokubaneinheiten.* Zeitschrift für Anorganische und Allgemeine Chemie, 2006. **632**(7): p. 1267-1272.

[103] A. T. Schwarz, M. Ströbele, D. Enseling, T. Jüstel, and H.-J. Meyer, *From Heterocubane Units to Extended Networks: Synthesis, Structure, and Optical Properties of $Pb_9O_2I_8(CN_2)_3$ and $Pb_{16}O_5I_{14}(CN_2)_4$.* Zeitschrift fur Anorganische und Allgemeine Chemie 2025, 0, e202500205.

[104] A.T. Schwarz, M. Ströbele, D. Enseling, T. Jüstel, and H.-J. Meyer, *Synthesis, Structure, and Eu3+-Activated Photoluminescence of the Mixed-Anion Carbodiimide NaLa2F3(CN2)2.* Zeitschrift fur Anorganische und Allgemeine Chemie 2025, 0, e202500221.

Table 2: Selected crystal and refinement data.

Empirical formula	$LiGa(CN_2)_2$	$Li_{13.6}Ga_{2.8}(CN_2)_{10}I_2$	$SrGa_2(CN_2)_4$	$NaLa_2F_3(CN_2)_2$
CCDC	2245222	2250452	2321110	2326720
Formula Weight ($g \cdot mol^{-1}$)	156.68	942.76	387.18	437.85
Wavelength	0.71073	1.54184	0.71073	0.71073
Crystal System	orthorhombic	orthorhombic	monoclinic	monoclinic
Space Group	$I2_12_12_1$	*Imma*	$P2_1/c$	*I2/a*
Unit cell dimensions	a = 8.7490(3) b = 16.3146(5) c = 8.6435(3)	a = 9.1235(3) b = 12.9465(4) c = 10.8785(3)	a= 10.4444(5) b= 13.1942(5) c= 6.5215(2)	a = 8.5848(7) b = 6.7559(4) c = 11.3786(8) β = 107.621(8)
Volume ($Å^3$)	1233.75(7)	1284.94(7)	872.52(6)	628.97(8)
Z	12	2	4	4
Density (calculated)(g cm-3)	2.531	2.437	2.947	4.624
Absorption coefficient (mm^{-1})	6.520	22.703	12.196	13.464
Final R indices (I>2σ(I)	R_1 = 0.0140, wR_2 = 0.0391	R_1 = 0.0287, wR_2 = 0.0694	R_1= 0.0476, wR_2 = 0.1188	R_1 = 0.0104 wR_2 = 0.0209
R indices (all data)	R_1 = 0.0144, wR_2 = 0.0393	R_1 = 0.0289, wR_2 = 0.0695	R_1 = 0.0490, wR_2 = 0.1192	R_1 = 0.0112 wR_2 = 0.0212
GooF	1.082	1.272	1.409	1.139

7. Publications

Publication 1:

The Luminescent Semiconductor $Pb_7I_6(CN_2)_4$

Publication 2:

The Mixed-Anion Compound $La_2S_2(CN_2)$

Publication 3:

Characterizing Gallium Dinitridocarbonates: A Focus on $LiGa(CN_2)_2$, $Li_{13.6}Ga_{2.8}(CN_2)_{10}I_2$, and $SrGa_2(CN_2)_4$

Publication 4:

A Mixed-Anion Compound based upon a $[Pb_4O_4]$ Heterocubane Unit: Synthesis, Structure and Electronic Properties of $Pb_8O_4I_6(CN_2)$

Publication 5:

From Heterocubane Units to Extended Networks: Synthesis, Structure, and Optical Properties of $Pb_9O_2I_8(CN_2)_3$ and $Pb_{16}O_5I_{14}(CN_2)_4$

Publication 6:

Synthesis, Structure, and Eu^{3+}-Activated Photoluminescence of the Mixed-Anion Carbodiimide $NaLa_2F_3(CN_2)_2$

Publication 1

The Luminescent Semiconductor $Pb_7I_6(CN_2)_4$

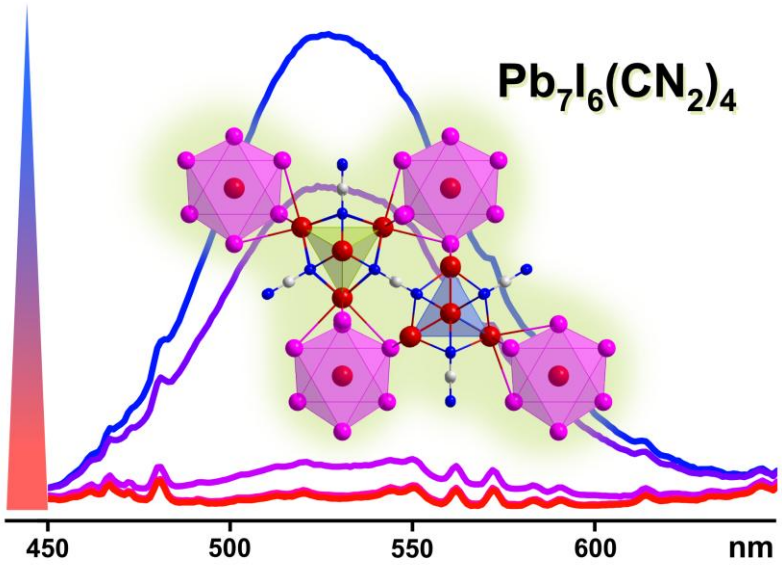

https://doi.org/10.1039/D4DT00369A

Reproduced from

Dalton Trans., **2024**, *53*, 6416-6422

with permission from

Copyright © 2024 The Royal Society of Chemistry

Dalton Transactions

ROYAL SOCIETY OF CHEMISTRY

PAPER

View Article Online
View Journal | View Issue

Check for updates

Cite this: *Dalton Trans.*, 2024, **53**, 6416

The luminescent semiconductor $Pb_7I_6(CN_2)_4$†

Albert T. Schwarz, [a] Markus Ströbele, [a] Carl P. Romao, [b] David Enseling, [c] Thomas Jüstel [c] and H.-Jürgen Meyer *[a]

Received 6th February 2024,
Accepted 12th March 2024

DOI: 10.1039/d4dt00369a

rsc.li/dalton

The development of new compounds in the domain of metal dinitridocarbonates is most efficiently performed *via* solid-state metathesis or simply by addition reactions. Our discovery of $Pb_7I_6(CN_2)_4$ is the result of a solid-state reaction of $PbCN_2$ with PbI_2 at 420 °C. Its crystal structure was solved and refined from X-ray diffraction data based on a single crystal with the space group $P6_3/mmc$. The crystal structure is based on a network of lead tetrahedra, lead trigonal bipyramids and lead octahedra interconnected by $[NCN]^{2-}$ and iodide. Properties of the material were investigated by diffuse reflection measurement, photoluminescence measurements, and electronic band structure calculations demonstrating that this material is a semiconductor.

Open Access Article. Published on 20 March 2024. Downloaded on 10/1/2025 9:04:04 AM. This article is licensed under a Creative Commons Attribution 3.0 Unported Licence.

Introduction

The development of metal dinitridocarbonate compounds is advancing, with many compounds remaining to be discovered. The dinitridocarbonate ion is isolobal to oxygen and thus in some ways analogous to the oxide ion. Generally, the dinitridocarbonate ion can appear as carbodiimide $[N{=}C{=}N]^{2-}$ or cyanamide $[N{\equiv}C{-}N]^{2-}$, depending on the nature and surrounding with cations.

Within the last decades, a remarkable number of metal dinitridocarbonates have been described, most of them having been developed by solid-state metathesis reactions.[1] Many kinds of cations ranging from alkali[2–4] and alkaline earth,[5] transition metal,[6] and a large number of rare earth metals[7,8] have been incorporated; the resulting materials have been studied in terms of their luminescence,[9] magnetism,[10] electrical conductivity,[11,12] and electrochemistry.[13]

Furthermore, complex compounds such as tetracyanamidometallates $[T(NCN)_4]^{n-}$ with T being aluminium,[14] gallium,[15] silicon[16] and germanium[17] have been developed. These materials have shown remarkable photoluminescence properties when combined with a rare earth activator; non-centrosymmetric structures have shown good second harmonic generation (SHG) properties.[16,18] Excellent photoluminescence properties were reported for doped pseudo-binary rare earth (RE) carbodiimides $RE_2(CN_2)_3$,[7,19] such as $RE_2(CN_2)_3$:Ce.[18,20] The structure of the oxide-carbodiimide $Y_2O_2(CN_2)$ is similar to that of the oxide-sulfide Y_2O_2S, which is a well-known host lattice material for photoluminescence.[21] The formal substitution of a chalcogenide *versus* $(CN_2)^{2-}$ is very interesting from a chemical point of view, because it demonstrates that a metal oxide or metal sulfide may serve as a template for the composition of a yet-unknown metal dinitridocarbonate.

The recently discovered compounds $Sn(CN_2)$ and $Sn_2O(CN_2)$ were described as semiconductors with band gaps in the order of 2.0 eV, according to band structure calculations and optical measurements. They have been investigated as a negative electrode material in so-called conversion batteries. Like other transition-metal compounds, carbodiimides $M_x(NCN)_y$ with M = Mn, Cr, Zn have been successfully cycled *versus* lithium and sodium ions.[22]

The diversity of the reported dinitridocarbonate compounds includes several lead-based compounds, such as $Pb(CN_2)$,[23,24] $APb_2Cl_3(CN_2)$ (A = Li, Na, Ag), $LiPb_2Br_3(CN_2)$, $LiPbCl(CN_2)$,[25] $K_{12}Pb_{51}Cl_{54}(CN_2)_{30}$ [26] and $Pb_{14.66}Sn_{7.34}Br_{26}(CN_2)_7O_2$.[27]

In addition, some lead compounds have received special attention over recent years. $CsPbI_3$ can be considered as the archetype for perovskite solar cells following the well-known substitution $(MA)PbI_3$ (MA = CH_3NH_3). $CsPbI_3$ has a bandgap of 1.6–1.8 eV, which is favorable for photovoltaic applications.[28] Other derivatives like $(MA)_2Pb(SCN)_2I_2$, have also been reported.[29] In light of these interesting issues, we herein describe the structure and properties of the new lead carbodiimide iodide $Pb_7I_6(CN_2)_4$.

[a]*Section for Solid State and Theoretical Inorganic Chemistry, Institute of Inorganic Chemistry, University of Tübingen, Auf der Morgenstelle 18, 72076 Tübingen, Germany. E-mail: juergen.meyer@uni-tuebingen.de*
[b]*Department of Materials, ETH Zürich, Wolfgang-Pauli-Str.27, 8093 Zürich, Switzerland*
[c]*Department of Chemical Engineering, FH Münster University of Applied Science, Stegerwaldstraße 39, 48565 Steinfurt, Germany*

†Electronic supplementary information (ESI) available. CCDC 2211751. For ESI and crystallographic data in CIF or other electronic format see DOI: https://doi.org/10.1039/d4dt00369a

This journal is © The Royal Society of Chemistry 2024

Open Access Article. Published on 20 March 2024. Downloaded on 10/1/2025 9:04:04 AM.
This article is licensed under a Creative Commons Attribution 3.0 Unported Licence.

Results and discussion

Synthesis

The preparation of crystalline $Pb_7I_6(CN_2)_4$ was performed in a straightforward manner from appropriate (3 : 4) proportions of PbI_2 and $Pb(CN_2)$ heated in fused silica tubes at 420 °C for 5 days (1). This procedure appears to be more efficient than solid-state metathesis, which was used in syntheses of the vast majority of dinitridocarbonate compounds (2). The procedure (1) removes the possibility of incorporation of lithium in the product and avoids the need for leaching significant amounts of the metathesis salt (LiI).

$$3PbI_2 + 4Pb(CN_2) \rightarrow Pb_7I_6(CN_2)_4 \quad (1)$$

$$7PbI_2 + 4Li_2(CN_2) \rightarrow Pb_7I_6(CN_2)_4 + 8LiI \quad (2)$$

$Pb_7I_6(CN_2)_4$ was obtained as a dark yellow crystalline material in high yield, with small amounts of lead being obtained as side phase in the X-ray powder diffraction pattern (Fig. 1).

The side-phase could be a result of the reducing nature of the $(NCN)^{2-}$ ion.[25] EDX measurements on nine different spots on several single crystals revealed a lead to iodine ratio of 7 : 5.96(5), verifying the Pb : I ratio in $Pb_7I_6(CN_2)_4$ that was found in the structure refinement.

Crystal structure of $Pb_7I_6(CN_2)_4$

The crystal structure of $Pb_7I_6(CN_2)_4$ was solved and refined by X-ray diffraction based on recorded single-crystal data. The structure refinement yielded the hexagonal space group $P6_3/mmc$. Some crystal structure and refinement data are given in Table 1.

The crystal structure refinement revealed five crystallographically distinct sites for the lead atoms, with Wyckoff positions, site occupation factors, and atomic coordinates presented in the Table S1.† Pb1 is surrounded by five iodides and three carbodiimide ions, $[NCN]^{2-}$. The environment of Pb2 appears similar to that of Pb1, with one more iodide, forming a coordination pattern derived from a tricapped trigonal antiprism. The third lead site (Pb3) represents a coordination environment with four iodides and three carbodiimide ions. Pb4 is coordinated by three iodine atoms and three $[NCN]^{2-}$ units. Pb5, with a site-occupation factor of 0.75 (see Table S1†), is surrounded by six iodide ions in distorted octahedral formation. Pb–I distances of the distorted octahedron range from 3.0528(6)–3.2555(6) Å. All other Pb–I distances in the drawings outlined in Fig. 2 range from 3.4423(4) Å to 3.7114(8) Å.

Table 1 Selected crystal and structure refinement data for $Pb_7I_6(CN_2)_4$, recorded at 150 K

Empirical formula	$Pb_7I_6(CN_2)_4$
CCDC code	2211751†
Formula weight (g mol^{-1})	5929.62
Wavelength (Mo-K$_\alpha$) (Å)	0.71073
Crystal system	Hexagonal
Space group	$P6_3/mmc$
Unit cell dimensions (Å)	$a = b = 10.7144(1)$
	$c = 29.4426(4)$
Volume (Å^3)	2927.13(7)
Z	5
Density (calculated) (g cm^{-3})	6.728
Absorption coefficient (mm^{-1})	58.057
Final R indices ($I > 2\sigma(I)$)	$R_1 = 0.0212$, w$R_2 = 0.0432$
R indices (all data)	$R_1 = 0.0220$, w$R_2 = 0.0436$
GOOF	1.113

The coordination environments of the three crystallographically distinct $[NCN]^{2-}$ units in $Pb_7I_6(CN_2)_4$ are similar to those in the previously reported compound $Pb_{14.66}Sn_{7.34}Br_{26}(CN_2)_7O_2$.[27] Two $[NCN]^{2-}$ units (centred by C1 and C2) are surrounded by six lead ions forming a trigonal antiprismatic arrangement. The third (C3) is surrounded by lead in a trigonal prismatic fashion. A detailed view is shown in Fig. 3.

The Pb–N bond distances range between 2.478(4) and 2.606(4) Å, and are similar to those in the related lead compounds $Pb(CN_2)$ (2.31–2.62 Å),[23] $LiPb_2Cl_3(CN_2)$ (2.54 Å) and $LiPbCl(CN_2)$ (2.39–2.70 Å).[25] The C–N bond lengths of the three crystallographically distinct $[NCN]^{2-}$ units are given in Fig. 3 and appear quite uniform. The C–N lengths around C1 are only slightly different, but the remaining two $[NCN]^{2-}$ are symmetrical, as a result of the a two-fold rotation axis (through C_2) and a mirror plane (cutting C3). Despite minor

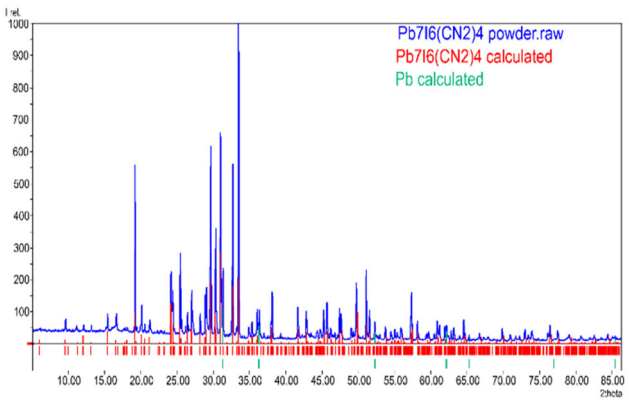

Fig. 1 XRD measurement of compound $Pb_7I_6(CN_2)_4$.

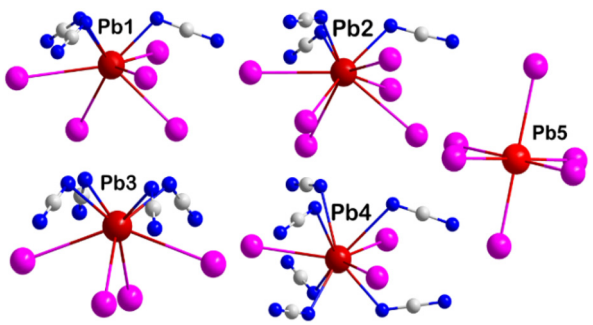

Fig. 2 Different coordination environments of lead atoms in $Pb_7I_6(CN_2)_4$. Iodine is shown in purple, carbon in white and nitrogen in blue.

Open Access Article. Published on 20 March 2024. Downloaded on 10/1/2025 9:04:04 AM.
This article is licensed under a Creative Commons Attribution 3.0 Unported Licence.

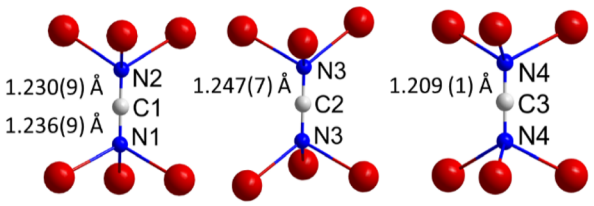

Fig. 3 Three crystallographically distinct $[NCN]^{2-}$ units; two are coordinated nearly trigonal antiprismatic and the third pseudo- octahedrally by lead (red).

differences in length, all three $[NCN]^{2-}$ units can be safely described as carbodiimide ions. An infrared (IR) spectroscopic measurement recorded on a sample of $Pb_7I_6(CN_2)_4$ reveals the presence of three quite similar $[NCN]^{2-}$ units, by showing an asymmetric stretching vibration of the $[NCN]^{2-}$ unit at 1900 cm^{-1} and a C–N bending vibration at 630 cm^{-1} (see Fig. S1†).

An interesting feature in the crystal structure of $Pb_7I_6(CN_2)_4$ is the clustering of lead atoms. A section of the structure showing all five lead atoms is presented in Fig. 4.

The arrangement of lead atoms in the structure may be described as a triple-Pb_4-tetrahedra cluster, composed of three tetrahedra in a face-sharing and edge-sharing fashion, for Pb1–Pb4, or as a trigonal bipyramid with a tetrahedron. All trigonal faces are capped by a nitrogen atom of $[NCN]^{2-}$ (except for the shared one). Pb5 is situated in an octahedral environment of iodide ions. The structure section shown in Fig. 4 is interconnected *via* iodide and carbodiimide ions to form the crystal structure of $Pb_7I_6(CN_2)_4$, as displayed in Fig. 5. Interatomic distances between lead atoms in and between adjacent Pb_4 tetrahedra and with Pb5 range between 3.92(3)–4.23(7) Å. These distances between lead atoms give rise to define block layers within the *ab*-plane in the structure. The given distances are essentially nonbonding distances of Pb^{2+}. However, the distances are significantly shorter than interatomic distances between lead atoms in cubic perovskite structure of $CsPbI_3$, which correspond with the lattice parameter a = 6.2894(2) Å of $CsPbI_3$. This distance resembles the arrangement of edge-shared $[PbI_6]$ octahedra, and is similar with twice the average Pb–I distance (2 × 3.154(1) Å) in the $[PbI_6]$ octahedron of $Pb_7I_6(CN_2)_4$. The surroundings of Pb^{2+} ions in the structure of $Pb_7I_6(CN_2)_4$ do not indicate a lone-pair effect from Pb^{2+}, and the clustering of lead atoms in layers in the structure ultimately suggests some interesting properties.

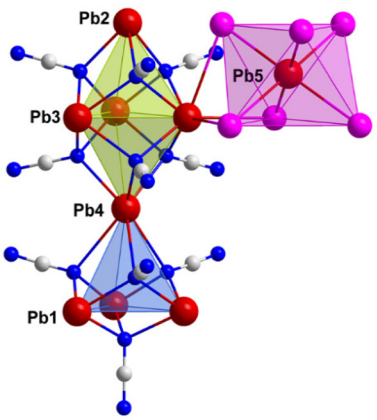

Fig. 4 Face-shared and edge-shared triple-Pb_4-tetrahedra fragment with face-capping carbodiimide ions and an associated $[PbI_6]$ octahedron (purple).

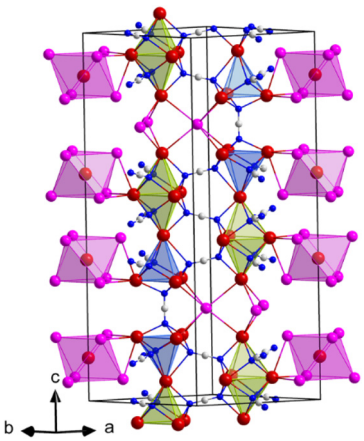

Fig. 5 Section of the crystal structure of $Pb_7I_6(CN_2)_4$. Iodide atoms are shown in purple, lead in red, carbon in white and nitrogen in blue.

Electronic structure

The DFT-calculated electronic band structure of $Pb_7I_6(CN_2)_4$ is shown in Fig. 6. The calculations reveal that the material is an

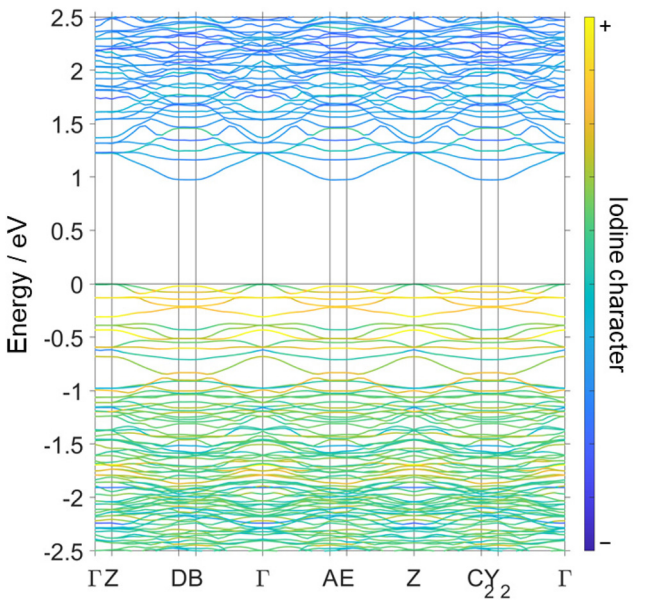

Fig. 6 The electronic band structure of $Pb_7I_6(CN_2)_4$, with bands coloured by their I character. Special points in the Brillouin zone are labelled Γ (0 0 0), Z (0 0 0.5), D (0 0.5 0.5), B (0 0.5 0), A (–0.5 0.5 0), E (–0.5 0.5 0.5), C_2 (–0.5 0.5 0), and Y_2 (–0.5 0 0) and were chosen following literature.[51]

This journal is © The Royal Society of Chemistry 2024

Open Access Article. Published on 20 March 2024. Downloaded on 10/1/2025 9:04:04 AM.
This article is licensed under a Creative Commons Attribution 3.0 Unported Licence.

indirect band gap semiconductor, with a gap of about 1 eV. The valence band maximum is close to degenerate (within 0.05 eV) at all special points in reciprocal space; the conduction band minimum is similarly close to degenerate at D (0 0.5 0.5), B (0 0.5 0), A (−0.5 0.5 0), E (−0.5 0.5 0.5), C_2 (−0.5 0.5 0), and Y_2 (−0.5 0 0) points. This result suggests the correct interpretation of the Tauc plot corresponds to an indirect allowed transition with an energy of 2.38 eV (Fig. S2†) rather than a direct allowed transition of 2.47 eV (Fig. S3†). The underestimation of experimental band gaps in DFT is a well-known phenomenon.[30] This problem can be alleviated by the use of hybrid exchange–correlation functionals,[30] however these are significantly more computationally expensive and their use was unfortunately precluded by the large size and low symmetry of the unit cell.

The valence bands near the Fermi energy were found to have significant iodine character (Fig. 6); as in lead halide perovskites.[31] However, the addition of carbodiimide ligands leads to some hybridization of the iodine states with those of nitrogen (Fig. S4†). The complexity of the crystal structure leads to flattening of the electronic bands and, consequently, increased electron localization. It is important to note that, due to this structural complexity and the presence of vacancies, it was not possible to relax the crystal structure in DFT prior to calculating the electronic band structure. This is important as the vacancies would be expected to cause rotation of the coordination polyhedra, which can play an important role in the electronic properties.[32]

Photoluminescence properties

Pb^{2+} comprising compounds are well known for their photoluminescent properties.[33–36] Therefore, an investigation of the photoluminescence properties was carried out, while the excitation and emission spectra of $Pb_7I_6(CN_2)_4$ at 77 K are shown in Fig. 7.

As shown in Fig. 7, the excitation spectrum was observed for monitoring the 525 nm emission and results from the superposition of several sub-bands. More precisely, the spectrum could be resolved into three sub-bands peaking at 302 nm (4.11 eV), 333 nm (3.72 eV), and 378 nm (3.28 eV). As Pb^{2+} is an ns^2 type impurity ion, for the free ion the ground state ($^1S_0$ RS term) arises from the electronic configuration $6s^2$ and the first excited state from the $6s^16p^1$ configuration, consisting of triplet $^3P_{0,1,2}$ and singlet $^1P_1$ states (Fig. 8).[37–39]

Comparison of the measured data with the literature[33,40] suggests that the excitation bands at 302 nm, 333 nm and 382 nm correspond to the transitions from the ground state $^1S_0$ to the excited states $^1P_1$, $^3P_2$ and $^3P_1$ respectively.

The room temperature emission spectra of Pb^{2+}-comprising materials is dominated by a broad emission band, which is typically assigned to the $^3P_1$–$^1S_0$ transition,[37,41] although at low temperatures the strongly forbidden $^3P_0$–$^1S_0$ emission is also observed.[39] The emission spectrum of $Pb_7I_6(CN_2)_4$ at 77 K shows a single broad band peaking at 525 nm (2.36 eV), while the luminescence process is almost completely quenched at 150 K (Fig. 9).

The decay curve of the photoluminescence at 525 nm is almost perfectly monoexponential and yields a decay time of about $\tau_{1/e}$ = 356 ns (Fig. 10).

Since the luminescence of compounds containing the s^2 ion Pb^{2+} is rather diverse, it is useful to compare the found PL data of $Pb_7I_6(CN_2)_4$ with those reported for other Pb^{2+} comprising materials with low and high alkalinity (Table 2).

According to the work of Duffy,[45] the optical alkalinity Λ of Pb^{2+} comprising compounds can be calculated by

$$\Lambda = (60\,700\ \mathrm{cm}^{-1} - \nu)/31\,000\ \mathrm{cm}^{-1}$$

where ν is the energy of the first absorption band in wavenumbers. By definition, this equation yields a Λ value of 1.00 for calcium oxide (CaO). The Λ value of $Pb_7I_6(CN_2)_4$ is found to be 1.10, which points to an optical alkalinity comparable to SrO, which is consistent with the presence of the highly polarizable anions I^- and $(CN_2)^{2-}$ in this compound.

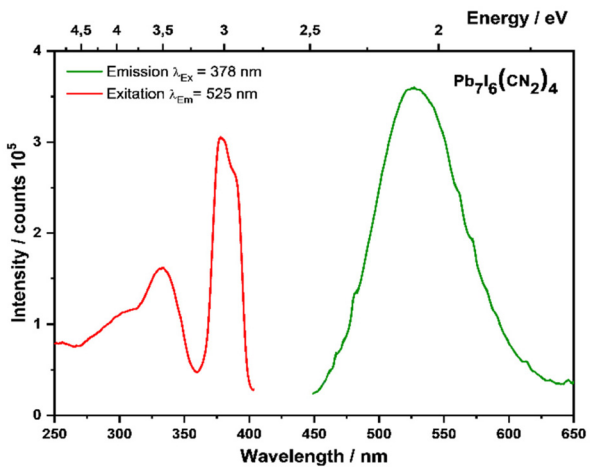

Fig. 7 Excitation and emission spectra of $Pb_7I_6(CN_2)_4$ at 77 K.

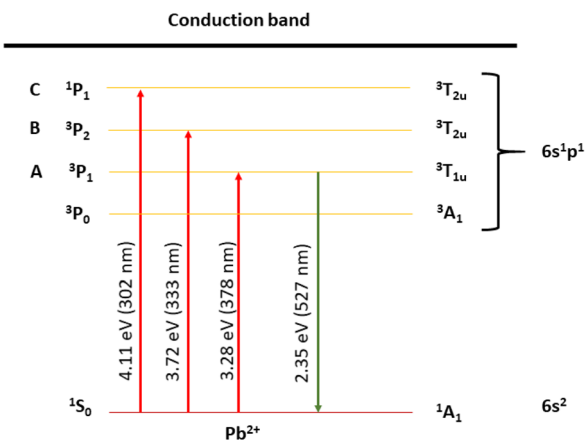

Fig. 8 Energy level scheme of a free Pb^{2+} ion, while the emission occurs from the $^3P_1$ state resulting in a single broad emission band.

Open Access Article. Published on 20 March 2024. Downloaded on 10/1/2025 9:04:04 AM.
This article is licensed under a Creative Commons Attribution 3.0 Unported Licence.

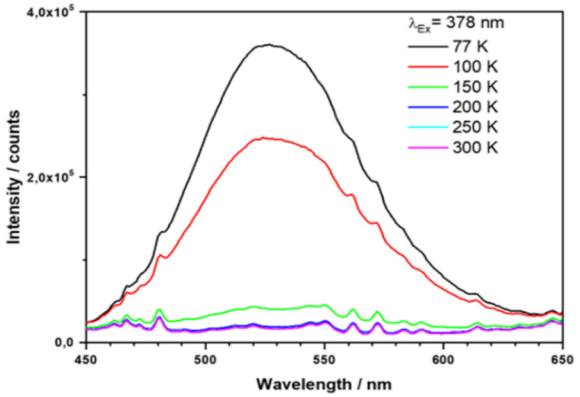

Fig. 9 Temperature dependent emission spectra of $Pb_7I_6(CN_2)_4$ upon 378 nm excitation between 77 and 300 K.

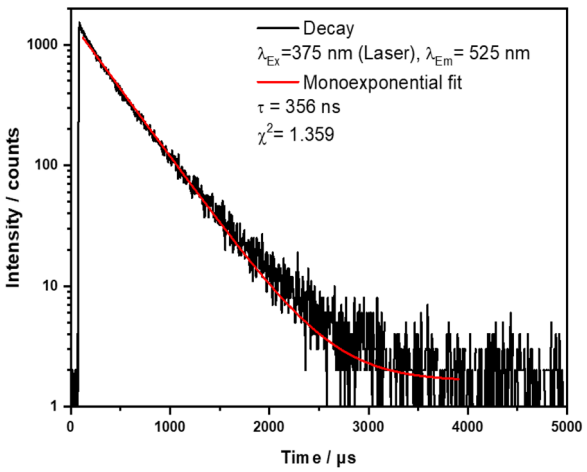

Fig. 10 Decay curve of the 525 nm emission of $Pb_7I_6(CN_2)_4$ at 77 K after excitation at 375 nm.

Table 2 PL data of $Pb_7I_6(CN_2)_4$ and selected lead compounds recorded at low temperature

Composition	Exc. [nm]	Emis. [nm]	Stokes shift [cm^{-1}]	Ref.
$PbSO_4$	235	340	13 000	42
Pb_2OMoO_4	345	525	10 000	43
$Pb_7I_6(CN_2)_4$	378	525	7500	This work
Pb_2OWO_4	340	560	11 500	44

Conclusions

Reactions between lead carbodiimide and lead iodine led to the formation of the previously unknown lead iodine carbodiimide $Pb_7I_6(CN_2)_4$, as confirmed by EDX analysis. Single-crystal X-ray diffraction revealed a complex coordination pattern in the crystal structure, resulting in semiconducting behaviour. Lead atoms form tetrahedral motifs, with an edge-bridging connectivity to a trigonal bipyramid; they can be alternatively viewed as a triple-Pb_4-tetrahedron, with all unoccupied trigonal faces capped by terminally bond carbodiimide ions. Relatively short but nonbonding Pb–Pb distances within these Pb^{2+} clusters give rise to semiconducting behaviour, as determined by band structure calculations. Further electronic properties, such as an evaluation of the photoelectric properties in comparison to the well-known material $(MA)PbI_3$ have not yet been established.

Photoluminescence measurements show the presence of a single broad emission band in the green spectral range with a short decay time of 356 ns at 77 K. The complete quenching at room temperature is likely caused by the large Stokes Shift, which is in line with observations from literature. An emission band of Pb^{2+} at 525 nm points to a highly alkaline environment, which is in good agreement with the high polarizability of the anions of the novel $Pb_7I_6(CN_2)_4$.

Experimental section and calculation details

Synthesis of $Pb_7I_6(CN_2)_4$

Powders of PbI_2 (Sigma-Aldrich, 99.999%) and $PbCN_2$ (synthesized as described in[23]) were mixed and pestled in a glove box under dry argon atmosphere in a 3 : 4 molar ratio. The reaction powder was filled into a silica ampoule and sealed under vacuum. The ampoule was heated in a crucible furnace at 420 °C at a heating and cooling rate of 2 K min^{-1} for 5 d. The reaction product was obtained as a dark yellowish powder with an estimated yield of 90% and lead as a side-phase.

Powder X-ray diffraction

The powder X-ray diffraction pattern was recorded on a well-ground powder in the range $5° < 2\theta < 120°$ using a StadiP diffractometer (Stoe, Darmstadt) with Ge-monochromated Cu-$K_{\alpha1}$ radiation and a Mythen 1 Detector.

Single-crystal X-ray diffraction

Intensity data of single crystals of $Pb_7I_6(CN_2)_4$ were recorded on a Rigaku XtalLAP Synergy-S single-crystal diffractometer, equipped with a HyPix-6000HE detector and monochromatic Mo-Kα radiation. The measurement was performed under N_2 cooling at 150 K. Corrections for absorption effects of the X-ray intensities were applied with a numerical method using CrysAlisPro 1.171.42.64a (Rigaku Oxford Diffraction, 2022). The structure was solved by SHelXL 2018/3 (Sheldrick, 2018) using dual methods and full-matrix least-squares structure refinements implemented in Olex2 1.5-ac5-024.

UV-Vis in diffuse reflectance

The reflectance spectra were recorded on an OceanOptics Maya 2000 Pro spectrometer equipped with a Harrick praying mantis sample chamber. A deuterium tungsten lamp (DH 200 BAL) from OceanOptics was used as the light source. The measurement was performed with the following settings: scan to average = 100, boxcar width = 10 and integration time = 300 ms using OceanView 1.6.7 (lite) software from

This journal is © The Royal Society of Chemistry 2024

Open Access Article. Published on 20 March 2024. Downloaded on 10/1/2025 9:04:04 AM.
This article is licensed under a Creative Commons Attribution 3.0 Unported Licence.

OceanOptics. To determine the optical band gap E_g, the Tauc equation was used: $(\alpha \cdot h\nu)^{1/r} = A(h\nu - E_g)$, where α is the absorption coefficient, h is the Planck constant, A is a material related constant and $h\nu$ is the photon energy. For a direct allowed bandgap transition, r = 1/2, and for an indirect allowed bandgap transition, r = 2.

EDX measurements

The energy dispersive X-ray spectroscopy (EDX) were performed with a Hitachi SU8030 scanning electron microscope equipped with a Bruker QUANTAX 6G EDX detector.

Density functional theory (DFT)

Density functional theory (DFT) calculations were performed using the Abinit software package (v. 9)[46] and the Perdew–Burke–Ernzerhof exchange–correlation functional.[47] The electronic structure calculations used the projector-augmented wave (PAW) method[48] with an energy cutoff of 25 Ha outside of the PAW spheres and a 125 Ha cutoff inside them. A 3 × 3 × 2 Monkhorst–Pack grid of k-points was used to sample reciprocal space.[49] Methfessel–Paxton cold smearing of the electronic occupation was included in the calculations.[50] To model the partial occupation of the Pb5 site and respect stoichiometry within the DFT calculations, a Pb5 vacancy was included in the unit cell. The inclusion of this vacancy, along with the structural complexity of the material, precluded structural optimization prior to calculation of the electronic band structure. Special points in and paths through the Brillouin Zone were chosen following Hinuma *et al.*[51]

Photoluminescence

Excitation and emission spectra of $Pb_7I_6(CN_2)_4$ samples were recorded using a fluorescence spectrometer FLS920 (Edinburgh Instruments) equipped with a 450 W xenon discharge lamp (OSRAM) as the radiation source. For powder samples a mirror optic was mounted inside the sample chamber. For the collection of data, a R2658P single-photon-counting photomultiplier tube from Hamamatsu was used. For temperature adjustment a cryostat "MicrostatN" from the company Oxford Instruments had been applied to the present spectrometer. Liquid nitrogen was used as a cooling agent. The photoluminescence decay curve was also measured on the FLS920 spectrometer, while a 375 nm ps laser diode from Edinburgh Instruments was used as an excitation source.

Infrared spectra

Vibrational spectra were recorded with a Bruker Vertex 70 spectrometer within the spectral range from 400to 4000 cm^{-1}; sample were prepared using KBr pellets.

Conflicts of interest

The authors declare no conflict of interest.

Acknowledgements

Support of this research by the Deutsche Forschungsgemeinschaft (DFG-Bonn) through the project ME 914/34-1 is gratefully acknowledged. C. P. R. was supported by ETH Zurich and by the European Union and Horizon 2020 through a Marie Sklodowska-Curie Fellowship, Grant Agreement No. 101030352. Computational resources were provided by ETH Zurich and by the Swiss National Supercomputing Center (CSCS) under project IDs s1128 and eth3.

References

1 H.-J. Meyer, *Dalton Trans.*, 2010, **39**, 5973–5982.
2 M. G. Down, M. J. Haley, P. Hubberstey, R. J. Pulham and A. E. Thunder, *Dalton Trans.*, 1978, 1407–1411.
3 M. Becker, J. Nuss and M. Jansen, *Z. Anorg. Allg. Chem.*, 2000, **626**, 2505.
4 M. G. Down, M. J. Haley, P. Hubberstey, R. J. Pulham and A. E. Thunder, *Dalton Trans.*, 1978, 1407.
5 U. Berger and W. Schnick, *J. Alloys Compd.*, 1994, **206**, 179–184.
6 X. Liu, M. Krott, P. Müller, C. Hu, H. Lueken and R. Dronskowski, *Inorg. Chem.*, 2005, **44**, 3001–3003.
7 M. Neukirch, S. Tragl and H.-J. Meyer, *Inorg. Chem.*, 2006, **45**, 8188–8193.
8 L. Unverfehrt, M. Ströbele, J. Glaser and H.-J. Meyer, *Z. Anorg. Allg. Chem.*, 2009, **635**, 1947–1952.
9 D. Dutczak, A. Siai, M. Ströbele, D. Enseling, T. Jüstel and H.-J. Meyer, *Eur. J. Inorg. Chem.*, 2020, **2020**, 3954–3958.
10 X. Tang, H. Xiang, X. Liu, M. Speldrich and R. Dronskowski, *Angew. Chem., Int. Ed.*, 2010, **49**, 4738–4742.
11 K. Dolabdjian, A. L. Görne, R. Dronskowski, M. Ströbele and H.-J. Meyer, *Dalton Trans.*, 2018, **47**, 13378–13383.
12 M. Löber, K. Dolabdjian, M. Ströbele, C. P. Romao and H.-J. Meyer, *Inorg. Chem.*, 2019, **58**, 7845–7851.
13 Z. Chen, M. Löber, A. Rokicińska, Z. Ma, J. Chen, P. Kuśtrowski, H.-J. Meyer, R. Dronskowski and A. Slabon, *Dalton Trans.*, 2020, **49**, 3450–3456.
14 L. Unverfehrt, M. Kalmutzki, M. Ströbele and H.-J. Meyer, *Dalton Trans.*, 2011, **40**, 9921–9924.
15 M. Kalmutzki, M. Ströbele, S. Kroeker, J. E. C. Wren and H. J. Meyer, *Eur. J. Inorg. Chem.*, 2013, **2013**, 6091–6096.
16 J. Glaser, H. Bettentrup, T. Jüstel and H.-J. Meyer, *Inorg. Chem.*, 2010, **49**, 2954–2959.
17 M. Kalmutzki, D. Enseling, J. E. C. Wren, S. Kroeker, V. V. Terskikh, T. Jüstel and H. J. Meyer, *Inorg. Chem.*, 2013, **52**, 12372–12382.
18 K. Dolabdjian, C. Schedel, D. Enseling, T. Jüstel and H.-J. Meyer, *Z. Anorg. Allg. Chem.*, 2017, **643**, 488–494.
19 J. Glaser, L. Unverfehrt, H. Bettentrup, G. Heymann, H. Huppertz, T. Jüstel and H.-J. Meyer, *Inorg. Chem.*, 2008, **47**, 10455–10460.

Open Access Article. Published on 20 March 2024. Downloaded on 10/1/2025 9:04:04 AM.
This article is licensed under a Creative Commons Attribution 3.0 Unported Licence.

20 Y.-C. Wu, T.-M. Chen, C.-H. Chiu and C.-N. Mo, *J. Electrochem. Soc.*, 2010, **157**, J342.
21 J. Sindlinger, J. Glaser, H. Bettentrup, T. Jüstel and H.-J. Meyer, *Z. Anorg. Allg. Chem.*, 2007, **633**, 1686–1690.
22 M. T. Sougrati, A. Darwiche, X. Liu, A. Mahmoud, R. P. Hermann, S. Jouen, L. Monconduit, R. Dronskowski and L. Stievano, *Angew. Chem., Int. Ed.*, 2016, **55**, 5090–5095.
23 X. Liu, A. Decker, D. Schmitz and R. Dronskowski, *Z. Anorg. Allg. Chem.*, 2000, **626**, 103–105.
24 X. Qiao, Z. Ma, D. Luo, A. J. Corkett, A. Slabon, A. Rokicinska, P. Kuśtrowski and R. Dronskowski, *Dalton Trans.*, 2020, **49**, 14061–14067.
25 K. Dolabdjian and H.-J. Meyer, *Z. Anorg. Allg. Chem.*, 2017, **643**, 1898–1903.
26 X. Meng, F. Liang, W. Yin, Z. Lin and M. Xia, *New J. Chem.*, 2019, **43**, 9766–9770.
27 M. Löber, M. Ströbele and H.-J. Meyer, *Z. Anorg. Allg. Chem.*, 2021, **647**, 1973–1977.
28 L. Duan, H. Zhang, M. Liu, M. Grätzel and J. Luo, *ACS Energy Lett.*, 2022, **7**, 2911–2918.
29 M. Daub and H. Hillebrecht, *Angew. Chem., Int. Ed.*, 2015, **54**, 11016–11017.
30 T. Das, G. Di Liberto and G. Pacchioni, *J. Phys. Chem. C*, 2022, **126**, 2184–2198.
31 J. Kaczkowski and I. Płowaś-Korus, *J. Phys. Chem. Lett.*, 2021, **12**, 6613–6621.
32 Y. Huang, W.-J. Yin and Y. He, *J. Phys. Chem. C*, 2018, **122**, 1345–1350.
33 J. Chen, S. Wang, Y. Du and L. Chen, *J. Alloys Compd.*, 2014, **597**, 249–257.
34 W. C. Collins and J. H. Crawford, *Solid State Commun.*, 1971, **9**, 853–856.
35 P. Yang, M. K. Lü, C. F. Song, S. W. Liu, F. Gu and S. F. Wang, *Inorg. Chem. Commun.*, 2004, **7**, 268–270.
36 M. Yılmaz and E. Erdoğmuş, *J. Lumin.*, 2020, **218**, 116868.
37 H. F. Folkerts and G. Blasse, *J. Mater. Chem.*, 1995, **5**, 273–276.
38 H. F. Folkerts and G. Blasse, *J. Phys. Chem. Solids*, 1996, **57**, 303–306.
39 C. P. Joshi and S. V. Moharil, *Phys. Status Solidi B*, 2000, **220**, 985–989.
40 N. Yamashita, T. Ohira, H. Mizuochi and S. Asano, *J. Phys. Soc. Jpn.*, 1984, **53**, 419–426.
41 C. Fouassier, *Curr. Opin. Solid State Mater. Sci.*, 1997, **2**, 231–235.
42 H. F. Folkerts, M. A. Hamstra and G. Blasse, *Chem. Phys. Lett.*, 1995, **246**, 135–138.
43 H. F. Folkerts, J. Zuidema and G. Blasse, *Solid State Commun.*, 1996, **99**, 655–658.
44 R. Alexey, R. Mariana and G. Veronika, *Optik*, 2021, **226**, 165912.
45 J. A. Duffy, *J. Chem. Educ.*, 1996, **73**, 1138.
46 X. Gonze, B. Amadon, G. Antonius, F. Arnardi, L. Baguet, J.-M. Beuken, J. Bieder, F. Bottin, J. Bouchet, E. Bousquet, N. Brouwer, F. Bruneval, G. Brunin, T. Cavignac, J.-B. Charraud, W. Chen, M. Côté, S. Cottenier, J. Denier, G. Geneste, P. Ghosez, M. Giantomassi, Y. Gillet, O. Gingras, D. R. Hamann, G. Hautier, X. He, N. Helbig, N. Holzwarth, Y. Jia, F. Jollet, W. Lafargue-Dit-Hauret, K. Lejaeghere, M. A. L. Marques, A. Martin, C. Martins, H. P. C. Miranda, F. Naccarato, K. Persson, G. Petretto, V. Planes, Y. Pouillon, S. Prokhorenko, F. Ricci, G.-M. Rignanese, A. H. Romero, M. M. Schmitt, M. Torrent, M. J. van Setten, B. Van Troeye, M. J. Verstraete, G. Zérah and J. W. Zwanziger, *Comput. Phys. Commun.*, 2020, **248**, 107042.
47 J. P. Perdew, K. Burke and M. Ernzerhof, *Phys. Rev. Lett.*, 1996, **77**, 3865–3868.
48 M. Torrent, N. A. W. Holzwarth, F. Jollet, D. Harris, N. Lepley and X. Xu, *Comput. Phys. Commun.*, 2010, **181**, 1862–1867.
49 H. J. Monkhorst and J. D. Pack, *Phys. Rev. B: Solid State*, 1976, **13**, 5188–5192.
50 M. Methfessel and A. T. Paxton, *Phys. Rev. B: Condens. Matter Mater. Phys.*, 1989, **40**, 3616–3621.
51 Y. Hinuma, G. Pizzi, Y. Kumagai, F. Oba and I. Tanaka, *Comput. Mater. Sci.*, 2017, **128**, 140.

This journal is © The Royal Society of Chemistry 2024

Electronic Supplementary Material (ESI) for Dalton Transactions.
This journal is © The Royal Society of Chemistry 2024

The Luminescent Semiconductor $Pb_7I_6(CN_2)_4$

Albert T. Schwarz [a], Markus Ströbele [a], Carl P. Romao [b], David Enseling [c], Thomas Jüstel [c] and H.-Jürgen Meyer *[a]

Supporting Information:

Table S 1: Wyckoff position, site occupation factors and atomic coordinates of $Pb_7I_6(CN_2)_4$

Atom	Wyck.	Site	S.O.F.	x/a	y/b	z/c
Pb1	12k	.m.		-0.21139(2)	0.21139(2)	0.67292(2)
Pb2	4f	3m.		-2/3	-1/3	0.67125(2)
Pb3	12k	.m.		-0.41586(3)	-0.20793(2)	0.56014(2)
Pb4	4f	3m.		-1/3	1/3	0.55141(2)
Pb5	4e	3m.	0.75	0	0	0.61669(2)

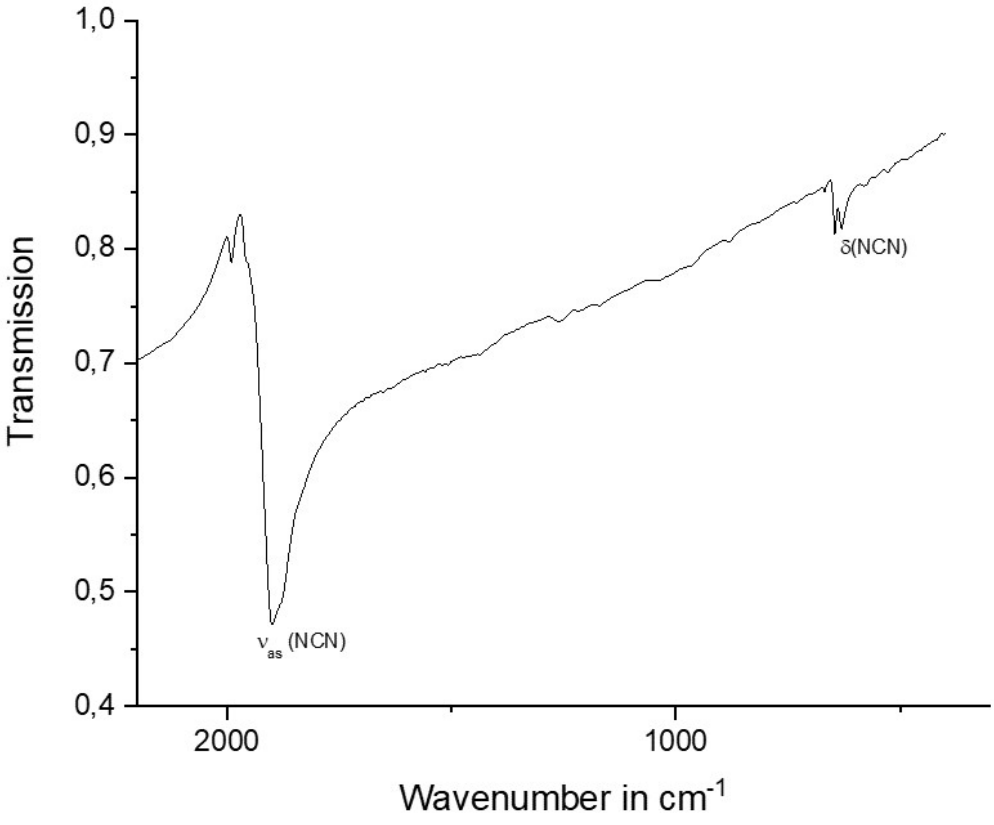

Figure S 1: Infrared spectrum of $Pb_7I_6(CN_2)_4$

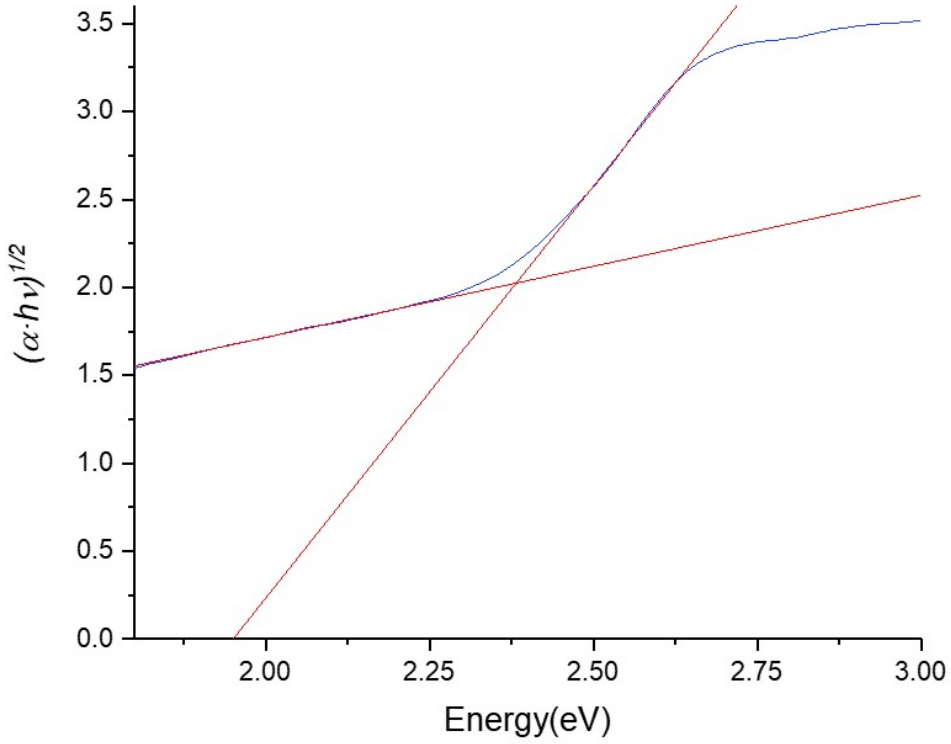

Figure S 2: Tauc plot for indirect allowed transition of $Pb_7I_6(CN_2)_4$

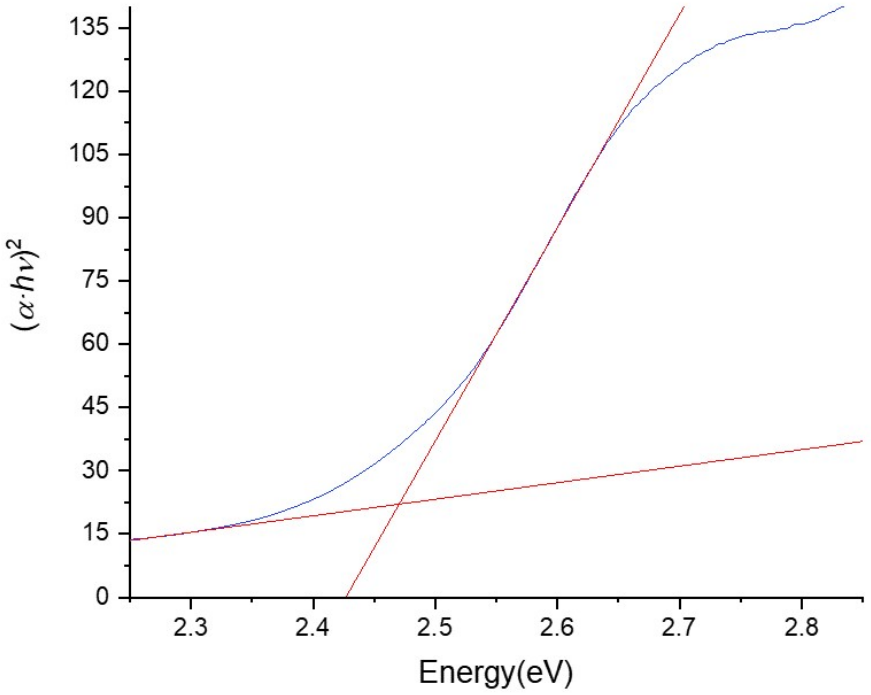

Figure S 3: Tauc plot for direct allowed transition of $Pb_7I_6(CN_2)_4$

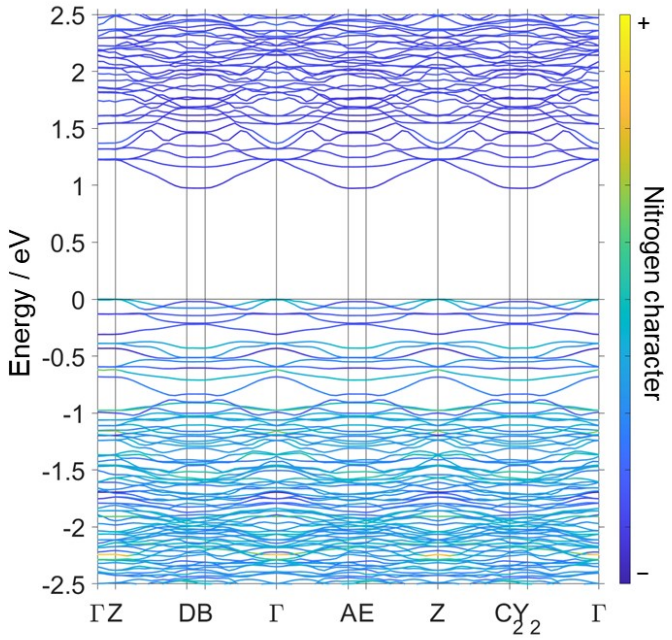

Figure S 4: The electronic band structure of $Pb_7I_6(CN_2)_4$, with bands coloured by their N character, on the same scale as Figure 5. Special points in and paths through the Brillouin Zone were chosen following literature.

Publication 2

The Mixed-Anion Compound $La_2S_2(CN_2)$

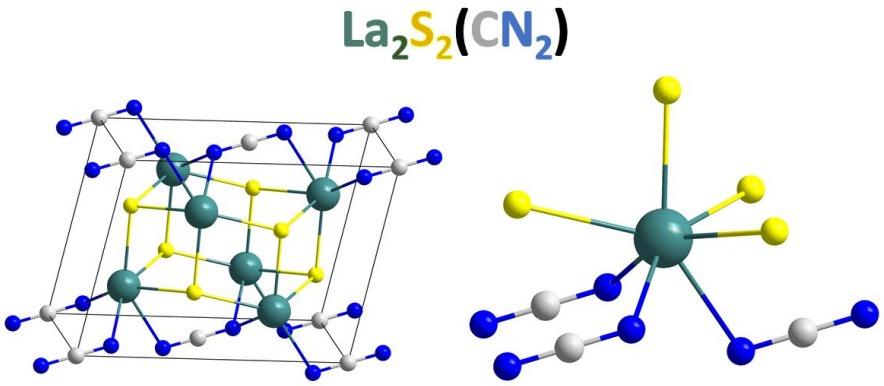

https://doi.org/10.1002/zaac.202400038

Reprinted from

Z. Anorg. Allg. Chem. **2024**, *650,* e202400038

with permission from

Copyright © 2024 Wiley-VCH GmbH

Journal of Inorganic and General Chemistry
ZAAC
Zeitschrift für anorganische und allgemeine Chemie
www.zaac.wiley-vch.de
RESEARCH ARTICLE
Check for updates
DOI: 10.1002/zaac.202400038

The Mixed-Anion Compound $La_2S_2(CN_2)$

Albert T. Schwarz,[a] Markus Ströbele,[a] and H.-Jürgen Meyer*[a]

Dedicated to Professor Martin Jansen on the occasion of his 80th Birthday

The new binary metal carbodiimide $La_2S_2(CN_2)$ was synthesized via a solid-state metathesis reaction. The crystal structure was solved and refined on the basis of single-crystal X-ray diffraction data with space group *C*2/*m*. The structure is represented by a layered arrangement, based on alternating layers of lanthanum, sulfide, and carbodiimide units. A close resemblance of the structure with that of $La_2O_2C_2$ is discussed, as well as the less-common coordination number seven of the lanthanum atom.

Introduction

Increasing interest in solids is based on the expectation to develop new materials which will make significant contributions to relevant fields related to energy, electronic, or optical devices, catalysis, and so on. To this end, functional solid-state materials, such as borides, carbides, pnictides, and chalcogenides have been successfully developed. Derived from metal chalcogenide, another avenue of compounds with less-common inorganic molecular anions such as metal dinitridocarbonates have emerged. The number of metal dinitridocarbonates, commonly referred as carbodiimides $(N{=}C{=}N)^{2-}$ or cyanamides $(N{-}C{\equiv}N)^{2-}$, has been considerably growing during the past 20 years. The vast majority of these compounds can be assigned as carbodiimides, with the $(N{=}C{=}N)^{2-}$ being isolobal with the chalcogenide anions O^{2-} and S^{2-}.

The preparation of compounds containing a complex anion like $(N{=}C{=}N)^{2-}$ can be hardly controlled in reactions when departing from a nitride (or azide) and carbide (or carbon) in classical solid-state reactions, therefore, another method has been successfully employed to develop a broader chemistry of this class of compounds.

The solid-state metathesis reaction (SSM)[1] is a highly effective preparation technique beyond high-temperature solid-state reactions (or ceramic methods). This method involves the direct reaction of two or more solid reaction partners to form a new compound and a metathesis salt. Following this method, a salt-like carbodiimide ($Li_2(CN)_2$ or $Na_2(CN_2)$, etc.) is reacted with a metal halide to form a metal carbodiimide and a metathesis salt. This reaction strategy has delivered several compounds with 16 electron anions like $(NCN)^{2-}$ or $(NBN)^{3-}$ that are reported in the literature.[2–6]

From a strategic point of view, the field of binary metal carbodiimides can be extended to mixed-metal compounds and mixed-anion compounds. The largest field of hitherto developed metal carbodiimides refers to rare earth (RE) elements. Among them the mixed-anion compounds $RE_2O_2(CN_2)$,[7–9] $RE_2O(CN_2)_2$,[10] $RE_2(SiO_4)(CN_2)$,[11] $RE_3N(CN_2)_3$,[12,13] $RE_2X(CN_2)N$[14] and $REX(CN_2)$[14–16] (X = halide) are prominent examples.

As oxides and sulfides are important materials in various applications, we successfully attempted the preparation of $La_2S_2(CN_2)$, that to our knowledge, represents the first example of a sulfide-carbodiimide compound.

Results and Discussion

Synthesis

Rare earth carbodiimides are usually prepared by SSM reaction via thermal conversion of a rare earth trihalide with an alkali metal carbodiimide. Typical ignition temperatures that initiate the conversion reaction can be observed as an exothermic effect in a thermoanalytical study, typically ranging between 400 °C and 600 °C.[4,17–19] Preparations aiming for homogeneous and well-crystalline material are often performed at somewhat higher temperatures. This concept of SSM reactions can be extended to include three or more reaction partners, as has been demonstrated for the synthesis of rare earth oxycarbodiimides (or oxide carbodiimides). The preparation of $RE_2O_2(CN_2)$ can be successfully performed with diverse oxide sources, which may be an alkali metal oxide (1) or a rare earth sesquioxide (2).[20]

$$2RECl_3 + Li_2(CN_2) + 2Li_2O \rightarrow RE_2O_2(CN_2) + 6LiCl \quad (1)$$

$$2RECl_3 + 3Li_2(CN_2) + 2RE_2O_3 \rightarrow 3RE_2O_2(CN_2) + 6LiCl \quad (2)$$

Based on the synthesis described above, many reactions of mixed-metal carbodiimides can be envisioned, reaching for new compounds. It is interesting to note that generally, even inert

[a] A. T. Schwarz, Dr. M. Ströbele, Prof. Dr. H.-J. Meyer
Section for Solid State and Theoretical Inorganic Chemistry
Institute of Inorganic Chemistry, Eberhard Karls University Tübingen Auf der Morgenstelle18, D-72076 Tübingen, Germany
E-mail: juergen.meyer@uni-tuebingen.de

Supporting information for this article is available on the WWW under https://doi.org/10.1002/zaac.202400038

© 2024 The Author(s). Zeitschrift für anorganische und allgemeine Chemie published by Wiley-VCH GmbH. This is an open access article under the terms of the Creative Commons Attribution License, which permits use, distribution and reproduction in any medium, provided the original work is properly cited.

15213749, 2024, 15, Downloaded from https://onlinelibrary.wiley.com/doi/10.1002/zaac.202400038 by Universitatsbibliothek Tübingen, Wiley Online Library on [27/09/2025]. See the Terms and Conditions (https://onlinelibrary.wiley.com/terms-and-conditions) on Wiley Online Library for rules of use; OA articles are governed by the applicable Creative Commons License

reactants (RE_2O_3, RE_2S_3) can be employed in reactions due to the internal heat production of exothermic SSM reactions.[1] The employment of an appropriate sulfur source, as demonstrated in reactions (3) and (4), leads to the title compound $La_2S_2(CN_2)$. A well-crystalline product of $La_2S_2(CN_2)$ was obtained by reacting appropriate mixtures corresponding to (4) for three days at 670 °C (Figure 1). Despite the dominance of the desired product and the accompanied metathesis salt (LiCl), there is a small amount of an unknown side-phase present.

$$2LaCl_3 + Li_2(CN_2) + 2Na_2S \rightarrow La_2S_2(CN_2) + 2LiCl + 4NaCl \quad (3)$$

$$2LaCl_3 + 3Li_2(CN_2) + 2La_2S_3 \rightarrow 3La_2S_2(CN_2) + 6LiCl \quad (4)$$

Crystal Structure of $La_2S_2(CN_2)$

The crystal structure of $La_2S_2(CN_2)$ was solved and refined by X-ray diffraction based on recorded single-crystal data. The refinement led to the monoclinic space group (*C*2/*m*), with some selected crystal structure and refinement data summarized in Table 1.

The structure of $La_2S_2(CN_2)$ is very simple from a crystallographic point of view, being defined by only one crystallographic position for each atom type. The overall crystal structure of $La_2S_2(CN_2)$ shows a close resemblance to that of $La_2O_2C_2$[3], also crystallizing in the space group *C*2/*m*[21]. The relationship between both structures is dominated by the fact that the $(C_2)^{2-}$ unit in $La_2O_2C_2$ is substituted for $[N{=}C{=}N]^2$ in $La_2S_2(CN_2)$, as displayed in Figure 2.

The structure of $La_2S_2(CN_2)$ can be described by a layered arrangement following the sequence –(NCN)–La–S–S–La–, stacked along the [001] direction, as can be seen in Figure 3. This layer arrangement is typical for many metal carbodiimides such as $RE_2(CN_2)_3$ (*RE*=Y, Ce–Nd and Sm–Tm)[22,23] or $La_2O_2(CN_2)$,[7] $Y_2O_2(CN_2)$[20] and $Bi_2O_2(CN_2)$.[24]

As shown in Figure 3, the lanthanum sulfide layer consists of corner sharing [La_4S] tetrahedra. The sulfur atom is surrounded by four lanthanum atoms, with La–S distances ranging between 2.8676(2) Å and 2.9026 (2) Å. The distances between La and N of the carbodiimide ions range between 2.6623(5) Å and 2.6711(8) Å. The C–N distance within the $[N{=}C{=}N]^{2-}$ ion is 1.2317(8) Å, with a N–C–N bond angle of 180°. The carbodiimide character is supported not only through the crystal structure refinement but also by DRIFT spectroscopy

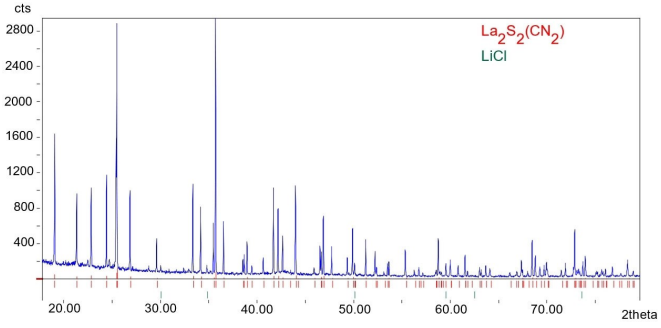

Figure 1. Powder XRD pattern of $La_2S_2(CN_2)$ and the metathesis salt (LiCl) in comparison to the position of the calculated Bragg reflections from single-crystal XRD.

Table 1. Selected crystal and structure refinement data for $La_2S_2(CN_2)$, recorded at 100 K.

Empirical Formula	$La_2S_2(CN_2)$
CCDC code	2284703
Formula weight (g/mol)	381.97
Wavelength (Mo-K_α) (Å)	0.71073
Crystal system	monoclinic
Space group	*C*2/*m*
Unit cell dimensions (Å)	$a = 9.40083(2)$ $b = 4.27512(7)$ $c = 7.06013(1)$ $\beta = 98.3161(2)$
Volume (Å^3)	280.761(8)
Z	2
Density (calculated) (g/cm^3)	4.518
Absorption coefficient (mm^{-1})	15.611
Final R indices ($I > 2\sigma(I)$)[a]	R1 = 0.0077, wR2 = 0.0185
R indices (all data)	R1 = 0.0083, wR2 = 0.0186
GOOF	1.180

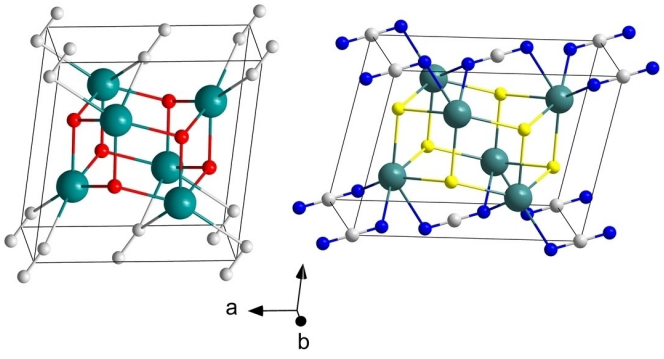

Figure 2. Comparison of unit cells of $La_2O_2C_2$ (left) and $La_2S_2(CN_2)$ (right). Lanthanum atoms are shown in dark turquoise, sulfur in yellow, oxygen in red, nitrogen in blue, and carbon in grey.

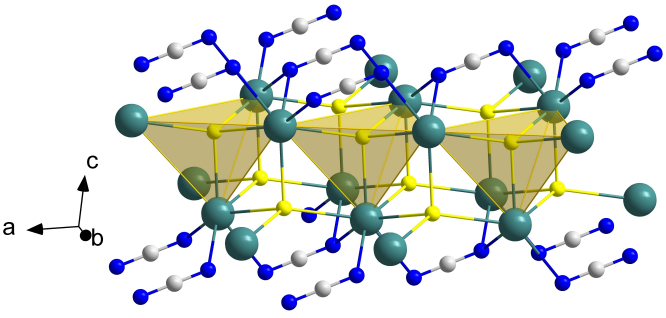

Figure 3. A section of the layered arrangement in the structure of $La_2S_2(CN_2)$. Environments of sulfur atoms are highlighted as yellow tetrahedra.

 © 2024 The Author(s). Zeitschrift für anorganische und allgemeine Chemie published by Wiley-VCH GmbH

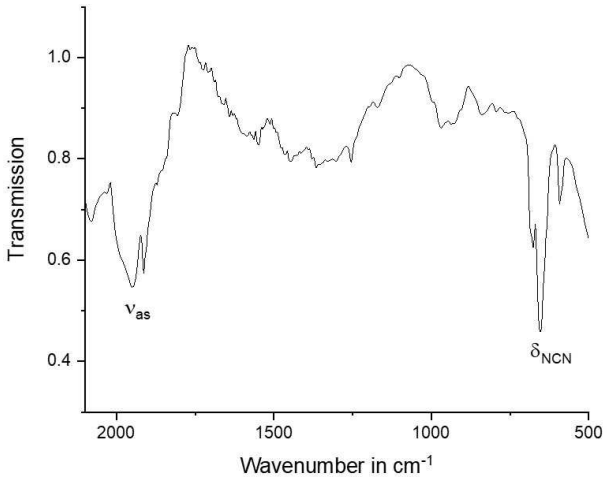

Figure 4. DRIFT measurement of $La_2S_2(CN_2)$.

measurement, which showed asymmetric stretching of the $[N{=}C{=}N]^{2-}$ unit at 1951 cm^{-1} and the bending vibration peaking at 653 cm^{-1}. The presence of smaller side-peaks is likely due to a side-phase indicating the presence of another carbodiimide species in the measured sample (Figure 4) that is not clearly detectable in the XRD pattern (Figure 1).

For completeness, we have a look at local atom environments, shown in Figure 5. Lanthanum atoms are surrounded by four sulfide ions and three carbodiimide ions in a sevenfold environment. A similar environment is seen for lanthanum in the structure of a modification of lanthanum sesquioxide. A–type La_2O_3 crystallizes in a hexagonal space group ($P\bar{3}m1$) and shows a close relationship with the given structure because atoms in A–La_2O_3 and $La_2S_2(CN_2)$ occupy similar centers of gravity, although carbodiimide ions have different space requirements. This analogy points out once more the resemblance between carbodiimide and chalcogenide ions.

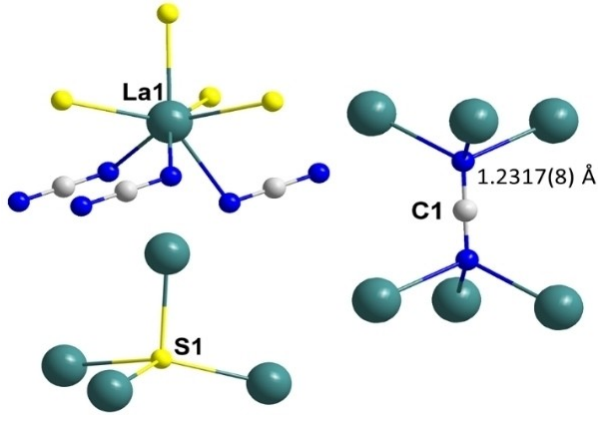

Figure 5. Coordination environments in $La_2S_2(CN_2)$.

Conclusions

Research on binary metal carbodiimides can be expanded to the vast majority of metals of the PSE. Some limitations appear for 3d carbodiimides, which tend to be unstable at elevated temperatures. Additionally, for 4d and 5d elements, because they can be reduced by $[N{=}C{=}N]^{2-}$, sometimes resulting in the formation of nitride compounds. There is already a large number of compounds with $[N{=}C{=}N]^{2-}$ ions (mostly carbodiimides) known and still many to be discovered when this chemistry is extended to mixed-metal compounds and to mixed-anion compounds. The new $La_2S_2(CN_2)$ represents the first mixed-anion compound based on a sulfide-carbodiimide that has been successfully synthesized through a conventional and straightforward solid-state metathesis reaction of lanthanum chloride, lanthanum sulfide, and $Li_2(CN_2)$. The structure resembles alternating layers, typical for the majority of carbodiimides, and shows a close relationship to the structure of $La_2O_2C_2$ when substituting $(C_2)^{2-}$ by $[N{=}C{=}N]^{2-}$.

Experimental Section

Synthesis

$La_2S_2(CN_2)$ was prepared from $LaCl_3$ (Sigma Aldrich 99,99%), $Li_2(CN_2)$, and La_2S_3 (Alfa Aesar, 99%) in 2:3:2 molar ratio (see eq. (4)) with a total mass of approx. 250 mg. $Li_2(CN_2)$ was prepared according to a previously reported synthesis.[13] The reactants were ground under argon in an argon-filled glove box and filled into silica ampoules which were flame-sealed under vacuum. The ampoule was heated to 670 °C and remained at this temperature for 72 h. After cooling to room temperature, the ampoules were opened in the glove box. The metathesis salt (LiCl) was washed out with dry ethanol under an argon atmosphere, leaving behind a dark brownish crystalline powder. The X-ray powder pattern indicates a high-yield product (>85%) after superposition with the calculated pattern. Single crystals of $La_2S_2(CN_2)$ were obtained by heating the reaction mixture with a LiCl/KCl flux (59:41) at a rate of 2 K/min to 650 °C and maintaining the temperature for 200 hours, followed by a cooling rate of 0.1 K/min. $La_2S_2(CN_2)$ behaves sensitively in moist air.

Powder X-Ray Diffraction

The powder X-ray diffraction pattern was recorded on a well-ground powder in the range $5 < 2\theta < 120$ using a StadiP diffractometer (Stoe, Darmstadt) with Ge-monochromated Cu-$K_{\alpha 1}$ radiation and a Mythen 1 Detector.

Single-Crystal X-Ray Diffraction

Intensity data of single crystals of $La_2S_2(CN_2)$ were recorded on a Rigaku XtalLAP Synergy-S single-crystal diffractometer, equipped with a HyPix-6000HE detector and monochromatic Mo–Kα radiation. The measurement was performed under N_2 cooling at 100 K. Corrections for absorption effects of the X-ray intensities were applied with a numerical method using CrysAlisPro 1.171.42.70a (Rigaku Oxford Diffraction, 2022).[25] The structure was solved by ShelXS (Sheldrick, 2008)[26] The model was refined with ShelXT 2018/3 (Sheldrick, 2015)[27] using full matrix least squares implemented in Olex2 1.5-ac5-024 (Dolomanov et al., 2009).[28]

 © 2024 The Author(s). Zeitschrift für anorganische und allgemeine Chemie published by Wiley-VCH GmbH

15213749, 2024, 15, Downloaded from https://onlinelibrary.wiley.com/doi/10.1002/zaac.202400038 by Universitatsbibliothek Tubingen, Wiley Online Library on [27/09/2025]. See the Terms and Conditions (https://onlinelibrary.wiley.com/terms-and-conditions) on Wiley Online Library for rules of use; OA articles are governed by the applicable Creative Commons License

DRIFT (Diffuse Reflectance Infrared Fourier Transform) Spectroscopy

Samples of $La_2S_2(CN_2)$ were measured at room temperature using a Bruker Vertex 70 infrared spectrophotometer with a deuterated triglycine sulfate (DTGS) detector and KBr beamsplitter. Diffuse reflectance was employed with a Harrick Praying Mantis attachment. The background spectra were collected using pure dried KBr in powder form.

Acknowledgements

Funding by the Deutsche Forschungsgemeinschaft through grant ME 914/34-1 is gratefully acknowledged. Open Access funding enabled and organized by Projekt DEAL.

Conflict of Interest

The authors declare no conflict of interest.

Data Availability Statement

The data that support the findings of this study are available from the corresponding author upon reasonable request.

Keywords: Carbodiimide · Crystal structure · Lanthanum · Sulfur

[1] H.-J. Meyer, *Dalton Trans.* **2010**, *39*, 5973–5982.
[2] K. Dolabdjian, H.-J. Meyer, *Z. Anorg. Allg. Chem.* **2017**, *643*, 1898–1903.
[3] K. Dolabdjian, C. Castro, H.-J. Meyer, *Eur. J. Inorg. Chem.* **2018**, *2018*, 1624–1630.
[4] K. Dolabdjian, A. Kobald, C. P. Romao, H.-J. Meyer, *Dalton Trans.* **2018**, *47*, 10249–10255.
[5] C.-D. Brand, M. Ströbele, D. Enseling, T. Jüstel, H.-J. Meyer, *J. Cluster Sci.* **2024**, *35*, 101–107.
[6] D. Dutczak, K. M. Wurst, M. Ströbele, D. Enseling, T. Jüstel, H.-J. Meyer, *Eur. J. Inorg. Chem.* **2016**, *2016*, 861–866.
[7] Y. Hashimoto, M. Takahashi, S. Kikkawa, F. Kanamaru, *J. Solid State Chem.* **1995**, *114*, 592–594.
[8] Y. Hashimoto, M. Takahashi, S. Kikkawa, F. Kanamaru, *J. Solid State Chem.* **1996**, *125*, 37–42.
[9] M. Li, W. Yuan, J. Wang, C. Gu, H. Zhao, *Powder Diffr.* **2007**, *22*, 59–63.
[10] R. Srinivasan, S. Tragl, H.-J. Meyer, *Z. Anorg. Allg. Chem.* **2005**, *631*, 719–722.
[11] M. Kubus, J. Glaser, A. Kłonkowski, H.-J. Meyer, *Z. Anorg. Allg. Chem.* **2010**, *636*, 991–995.
[12] B. Jürgens, E. Irran, W. Schnick, *J. Solid State Chem.* **2005**, *178*, 72–78.
[13] L. Unverfehrt, M. Ströbele, J. Glaser, H.-J. Meyer, *Z. Anorg. Allg. Chem.* **2009**, *635*, 1947–1952.
[14] D. Dutczak, A. Siai, M. Ströbele, D. Enseling, T. Jüstel, H.-J. Meyer, *Eur. J. Inorg. Chem.* **2020**, *2020*, 3954–3958.
[15] R. Srinivasan, J. Glaser, S. Tragl, H.-J. Meyer, *Z. Anorg. Allg. Chem.* **2005**, *631*, 479–483.
[16] L. Unverfehrt, J. Glaser, M. Ströbele, S. Tragl, K. Gibson, H.-J. Meyer, *Z. Anorg. Allg. Chem.* **2009**, *635*, 479–483.
[17] K. D. Röseler, K. Eichele, M. Ströbele, H.-J. Meyer, *Eur. J. Inorg. Chem.* **2024**, *27*, e202300713.
[18] M. Kubus, D. Enseling, T. Jüstel, H.-J. Meyer, *Eur. J. Inorg. Chem.* **2013**, *2013*, 3195–3199.
[19] M. Löber, C. S. Geißenhöner, M. Ströbele, S. Indris, C. P. Romao, H.-J. Meyer, *Inorg. Chem.* **2019**, *58*, 14560–14567.
[20] J. Sindlinger, J. Glaser, H. Bettentrup, T. Jüstel, H.-J. Meyer, *Z. Anorg. Allg. Chem.* **2007**, *633*, 1686–1690.
[21] R. L. Seiver, H. A. Eick, *J. Less-Common Met.* **1976**, *44*, 1–9.
[22] M. Neukirch, S. Tragl, H.-J. Meyer, *Inorg. Chem.* **2006**, *45*, 8188–8193.
[23] J. Glaser, L. Unverfehrt, H. Bettentrup, G. Heymann, H. Huppertz, T. Jüstel, H.-J. Meyer, *Inorg. Chem.* **2008**, *47*, 10455–10460.
[24] A. J. Corkett, Z. Chen, D. Bogdanovski, A. Slabon, R. Dronskowski, *Inorg. Chem.* **2019**, *58*, 6467–6473.
[25] CrysAlisPro, Rigaku, V1.171.42.70a, 2022.
[26] G. M. Sheldrick, *Acta Crystallogr. Sect. A* **2008**, *64*, 112–122.
[27] G. M. Sheldrick, *Acta Crystallogr. C Struct Chem.* **2015**, *71*, 3–8.
[28] O. V. Dolomanov, L. J. Bourhis, R. J. Gildea, J. A. K. Howard, H. Puschmann, *J. Appl. Crystallogr.* **2009**, *42*, 339–341.

 © 2024 The Author(s). Zeitschrift für anorganische und allgemeine Chemie published by Wiley-VCH GmbH

15213749, 2024, 15, Downloaded from https://onlinelibrary.wiley.com/doi/10.1002/zaac.202400038 by Universitatsbibliothek Tübingen, Wiley Online Library on [27/09/2025]. See the Terms and Conditions (https://onlinelibrary.wiley.com/terms-and-conditions) on Wiley Online Library for rules of use; OA articles are governed by the applicable Creative Commons License

Publication 3

Characterizing Gallium Dinitridocarbonates: A Focus on $LiGa(CN_2)_2$, $Li_{13.6}Ga_{2.8}(CN_2)_{10}I_2$, and $SrGa_2(CN_2)_4$

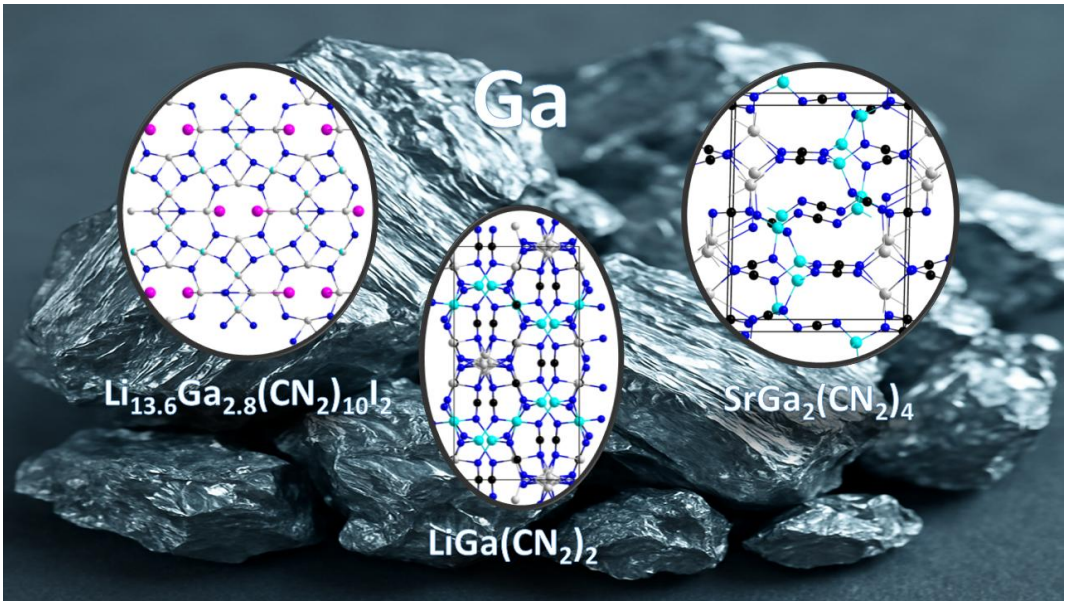

https://doi.org/10.1002/zaac.202500085

Reprinted from

Z. Anorg. Allg. Chem. **2025**, *0,* e202500085

with permission from

Copyright © 2025 Wiley-VCH GmbH

Journal of Inorganic and General Chemistry
ZAAC
Zeitschrift für anorganische und allgemeine Chemie
www.zaac.wiley-vch.de
RESEARCH ARTICLE
Check for updates
DOI: 10.1002/zaac.202500085

Characterizing Gallium Dinitridocarbonates: A Focus on $LiGa(CN_2)_2$, $Li_{13.6}Ga_{2.8}(CN_2)_{10}I_2$, and $SrGa_2(CN_2)_4$

Albert T. Schwarz, Oleksander Kysliak, Klaus Eichele, Markus Ströbele, and H.-Jürgen Meyer*

This study describes the synthesis and characterization of three new gallium dinitridocarbonates: $LiGa(CN_2)_2$, $Li_{13.6}Ga_{2.8}(CN_2)_{10}I_2$, and $SrGa_2(CN_2)_4$. These compounds are obtained through solid-state metathesis reactions, demonstrating an efficient route for the formation of dinitridocarbonate-based materials. The crystal structures of $LiGa(CN_2)_2$ and $Li_{13.6}Ga_{2.8}(CN_2)_{10}I_2$ are solved and refined in the orthorhombic space groups $I2_12_12_1$ and *Imma*, respectively. The single-crystal diffraction study of $SrGa_2(CN_2)_4$ revealed the monoclinic space group $P2_1/c$. All the compounds under consideration feature networks based on metal-centered tetrahedral arrangements. The presence of lithium in the compounds $LiGa(CN_2)_2$ and $Li_{13.6}Ga_{2.8}(CN_2)_{10}I_2$ is confirmed by ^{7}Li magic-angle spinning nuclear magnetic resonance (MAS NMR) spectroscopy. Infrared spectroscopy measurements indicate the presence of carbodiimide and cyanamide units within the compounds. Furthermore, the optical reflectance of the air-stable compound $SrGa_2(CN_2)_4$ has shown to be a wide gap semiconductor.

1. Introduction

Group 13 nitride (III–V) semiconductors have emerged as strong candidates in a multitude of electronic and optoelectronic applications.[1] For example, $In_xGa_{1-x}N$ alloys span band gaps ranging from approximately 0.7 eV (InN)[2] to 3.4 eV (GaN),[3] making this material useful for light-emitting diodes and laser diodes.[4]

Metal dinitridocarbonates, which are more commonly referred to as carbodiimides $(N{=}C{=}N)^{2-}$ or cyanamides $(N{\equiv}C{-}N)^{2-}$ have been successfully established as salt-like compounds with a wide range of metal atoms throughout the periodic table. The discovery of new compounds in this class continues to expand. The synthesis of group 13 metal carbodiimides has been demonstrated in previous studies. In 1995, the synthesis of $NaIn(CN_2)_2$ was achieved through a reaction of InBr and NaCN at 400 °C.[5] With the exception of $In_{2.24}(CN_2)_3$[5] and $Tl_2(CN_2)$,[6] no other binary carbodiimide comprising a group 13 metal has been reported to this date. However, reactions also resulted in the formation of multinary compounds, exemplified by ternary $LiAl(CN_2)_2$.[7] Another particularly appealing category of compounds in the chemistry of $(NCN)^{2-}$ ions are tetracyanamidometallates, exemplified by $LiSr_2[Ga(CN_2)_4]$.[8] The structure of the $[T(CN_2)_4]^{n-}$ ion, where *T* represents a main group element including Al or Ga, can be derived from the orthosilicate ion.[8,9] Additionally, compounds comprising a group 14 element, namely silicon or germanium, have been identified: Tetracyanamidosilicate compounds $ARE[Si(CN_2)_4]$ (A = K, Rb, Cs; RE = rare-earth element) are reported to possess exemplary optical characteristics, including photoluminescence and/or second harmonic generation, as well as remarkable good stability in air.[10] The synthesis of these compounds has previously involved the preparation of suitable mixtures of hexafluorometallate salts, such as $K_2(SiF_6)$ with $RECl_3$ and $Li_2(CN_2)$, which then undergo a reaction to produce $KRE[Si(CN_2)_4]$. Recently, the fundamental compounds $Li_4[Si(CN_2)_4]$ and $Li_4[Ge(CN_2)_4]$ were presented from reactions of SiI_4 or GeI_4 with $Li_2(CN_2)$ at 500 °C.[11] Given the existence of tetracyanamidometallates with Al and Ga, it seems reasonable to posit that the basic form of the respective metallates, such as $Li_5[Ga(CN_2)_4]$ or $Li_5[Al(CN_2)_4]$, could also exist. To this end, a series of reactions were conducted in the area, resulting in the synthesis of the three ternary gallium carbodiimides presented in this work.

2. Results and Discussion

2.1. Synthesis of $LiGa(CN_2)_2$, $Li_{13.6}Ga_{2.8}(CN_2)_{10}I_2$, and $SrGa_2(CN_2)_4$

Solid-state metathesis (SSM) reactions have been demonstrated to be an efficient method for the synthesis of several metal dinitridocarbonates.[12] This approach offers numerous advantages, including a rapid reaction, moderate heating requirements, and an option to prepare thermally labile compounds or even refractive materials. Hence, a diverse range of new compounds and materials may be prepared using this way of synthesis.[13] The majority of metal carbodiimides were synthesized through the reaction of metal trihalides with $Li_2(CN_2)$. $Li_2(CN_2)$ is a good carbodiimide

A. T. Schwarz, O. Kysliak, M. Ströbele, H.-J. Meyer
Section for Solid State and Theoretical Inorganic Chemistry, Institute of Inorganic Chemistry, Eberhard Karls University, Auf der Morgenstelle 18, D-72076 Tübingen, Germany
E-mail: juergen.meyer@uni-tuebingen.de
K. Eichele
Institute of Inorganic Chemistry, Eberhard Karls University, Auf der Morgenstelle 18, D-72076 Tübingen, Germany

© 2025 The Author(s). Zeitschrift für anorganische und allgemeine Chemie published by Wiley-VCH GmbH. This is an open access article under the terms of the Creative Commons Attribution License, which permits use, distribution and reproduction in any medium, provided the original work is properly cited.

source having a high thermal stability. However, other carbodiimide sources like $Na_2(CN_2)$ or $K_2(CN_2)$ may be used instead.[7,14],[15] The new compounds $LiGa(CN_2)_2$ and $Li_{13.6}Ga_{2.8}(CN_2)_{10}I_2$ were synthesized by SSM reactions from mixtures of $GaCl_3$ or GaI_3 and $Li_2(CN_2)$ following Equation ((1) and (2)). $SrGa_2(CN_2)_4$ was obtained from a mixture of $SrCl_2$, $GaCl_3$, and $Na_2(CN_2)$ following Equation (3). See the experimental section for more details.

$$GaCl_3 + 2\,Li_2(CN_2) \rightarrow LiGa(CN_2)_2 + 3\,LiCl \quad (1)$$

$$2.8\,GaI_3 + 10\,Li_2(CN_2) \rightarrow Li_{13.6}Ga_{2.8}(CN_2)_{10}I_2 + 6.4\,LiI \quad (2)$$

$$2\,GaCl_3 + SrCl_2 + 4\,Na_2(CN_2) \rightarrow SrGa_2(CN_2)_4 + 8\,NaCl \quad (3)$$

The compound $LiGa(CN_2)_2$ was obtained as a white powder. $Li_{13.6}Ga_{2.8}(CN_2)_{10}I_2$ was synthesized as a white-grayish powder with the presence of an unknown side-phase. It was observed that both compounds exhibit a high degree of sensitivity to moist air. $SrGa_2(CN_2)_4$ was successfully synthesized by SSM and obtained as a crystalline, grayish-white powder. Following a five-day exposure to air and subsequent inspection via X-ray diffraction, it was observed that the compound remained unchanged in the presence of air. All three compounds were obtained as crystalline powder in high yields, as represented with their X-ray powder-diffraction patterns displayed in **Figure 1**–**3**. Some crystallographic data are summarized in **Table 1**. Further details of the crystal-structure investigations may be obtained from the Fachinformationzentrum Karlsruhe, D-76,344 Eggenstein-Leopoldshafen, Germany, on quoting the depository numbers given in Table 1.

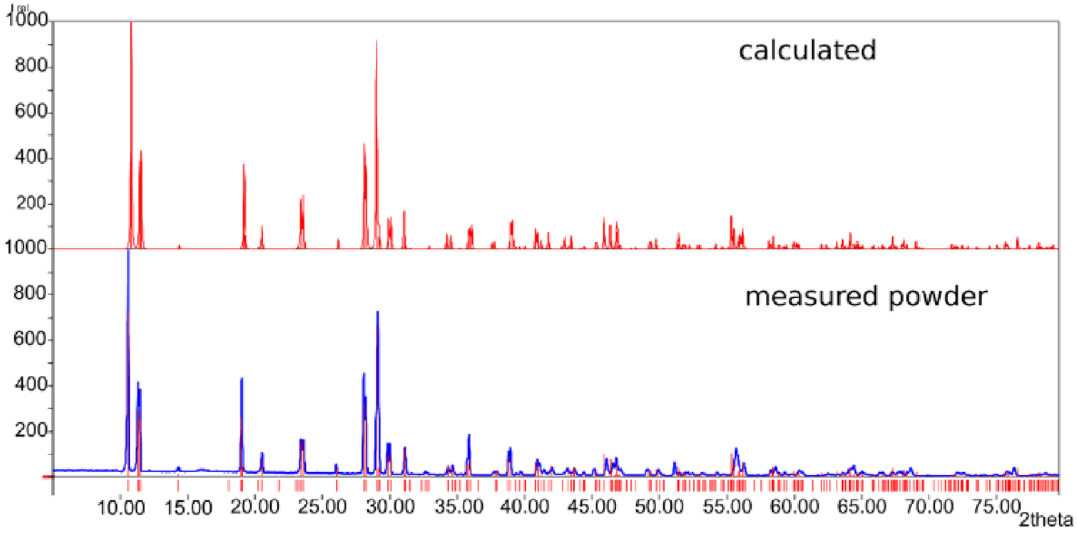

Figure 1. X-ray powder diffraction pattern of $LiGa(CN_2)_2$ (blue) in comparison to the calculated pattern and Bragg reflections (both red) from single-crystal refinement data.

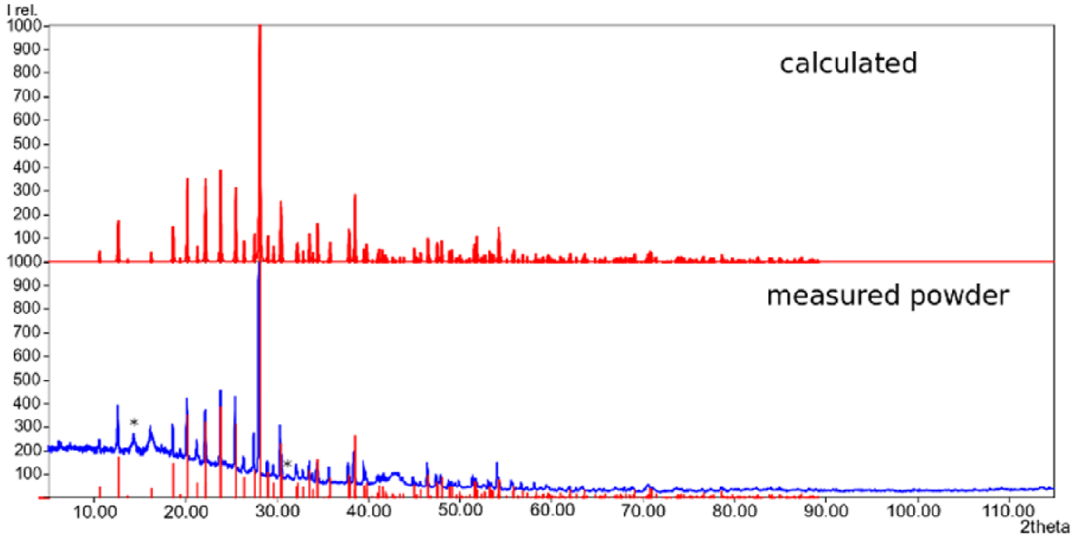

Figure 2. X-ray powder diffraction pattern of the compound $Li_{13.6}Ga_{2.8}(CN_2)_{10}I_2$ in comparison to the calculated pattern and Bragg reflections (both red) from single-crystal refinement data.

 © 2025 The Author(s). Zeitschrift für anorganische und allgemeine Chemie published by Wiley-VCH GmbH

15213749, 0, Downloaded from https://onlinelibrary.wiley.com/doi/10.1002/zaac.202500085 by Universitatsbibliothek Tubingen, Wiley Online Library on [27/09/2025]. See the Terms and Conditions (https://onlinelibrary.wiley.com/terms-and-conditions) on Wiley Online Library for rules of use; OA articles are governed by the applicable Creative Commons License

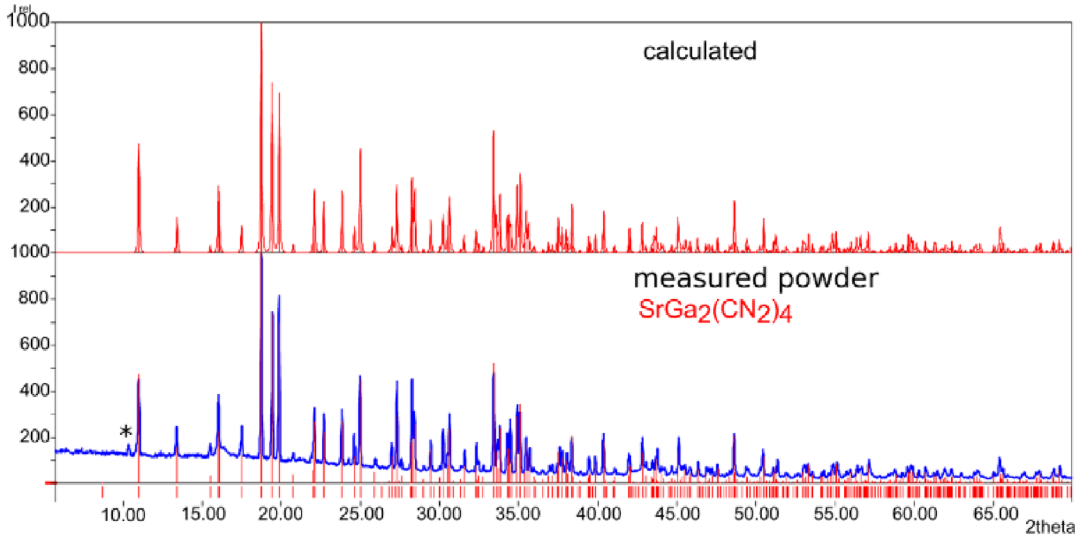

Figure 3. X-ray powder diffraction pattern of the compound $SrGa_2(CN_2)_4$ in comparison to the calculated pattern and Bragg reflections (both red) from single-crystal refinement data.

Table 1. Crystal and structure refinement data.

Empirical formula	$Li_{13.6}Ga_{2.8}(CN_2)_{10}I_2$	$SrGa_2(CN_2)_4$	$LiGa(CN_2)_2$
CCDC code	2250452	2321110	2245222
Formula weight [g mol^{-1}]	942.76	387.18	156.68
Crystal system	orthorhombic	monoclinic	orthorhombic
Space group	*Imma*	$P2_1/c$	$I2_12_12_1$
Unit cell dimensions [Å]	$a = 9.1235(3)$	$a = 10.4444(5)$	$a = 8.7490(3)$
	$b = 12.9465(4)$	$b = 13.1942(5)$	$b = 16.3146(5)$
	$c = 10.8785(3)$	$c = 6.5215(2)$	$c = 8.6435(3)$
Volume [Å^3]	1284.94(7)	872.52(6)	1233.75(7)
Z	2	4	12
Wavelength [Å]	1.54184	0.71073	0.71073
Radiation type	Cu-K_α	Mo-K_α	Mo-K_α
T/K	150	200	130
Density (calculate [g cm^{-3}])	2.437	2.947	2.531
Absorption coefficient [mm^{-1}]	22.703	12.196	6.520
Final *R* indices ($I > 2\sigma(I)$)	$R_1 = 0.0287$, $wR_2 = 0.0694$	$R_1 = 0.0476$, $wR_2 = 0.1188$	$R_1 = 0.0140$, $wR_2 = 0.0391$
R indices (all data)	$R_1 = 0.0289$, $wR_2 = 0.0695$	$R_1 = 0.0490$, $wR_2 = 0.1192$	$R_1 = 0.0144$, $wR_2 = 0.0393$
GooF	1.272	1.409	1.082
Flack	–	–	0.01(2)
Largest Peak	0.936	1.695	0.397

2.2. Crystal Structures

2.2.1. $LiGa(CN_2)_2$

The crystal structure of $LiGa(CN_2)_2$ was solved and refined by single-crystal X-ray diffraction with the orthorhombic space group $I2_12_12_1$ and contains two crystallographically distinct Ga, four Li positions and, four carbodiimide groups. The asymmetric unit contains 1 1/2 formula units. The lithium position Li1 is fully occupied, while the other positions show partial occupancies (Li2 = 34.3%, Li3 = 28.7%, and Li4 = 17.6%), revealing a lithium disordering within channels of the structure along the *c*-axis (see **Figure 4**). All lithium positions (including Li1) were restraint to yield one lithium ion per formula unit. In contrast to the previously published compound $LiSr_2[Ga(CN_2)_4]$,[8] no evidence of mixing between lithium and gallium positions was found. The overall crystal structure of $LiGa(CN_2)_2$ includes a network of Ga- or Li-centered tetrahedra, some of which are corner-linked via nitrogen atoms of $(NCN)^{2-}$ units (**Figure 5**) with Ga—N bond lengths ranging from 1.883(2) to 1.930(2) Å and Li—N bond lengths ranging from 1.93(2) to 2.30(2) Å. Furthermore, the network contains four distinct $(NCN)^{2-}$ units, which are surrounded by lithium and gallium ions in different ways (**Figure 6**). It is well known in the chemistry of dinitridocarbonates that the geometry of the $(NCN)^{2-}$ ion very much depends on whether it is coordinated symmetrically to appear as carbodiimide, or asymmetrical to appear as cyanamide. The carbon atoms C1 and C2 are situated on a twofold rotation axis and represent the carbodiimide unit

 © 2025 The Author(s). Zeitschrift für anorganische und allgemeine Chemie published by Wiley-VCH GmbH

15213749, 0, Downloaded from https://onlinelibrary.wiley.com/doi/10.1002/zaac.202500085 by Universitatsbibliothek Tubingen, Wiley Online Library on [27/09/2025]. See the Terms and Conditions (https://onlinelibrary.wiley.com/terms-and-conditions) on Wiley Online Library for rules of use; OA articles are governed by the applicable Creative Commons License

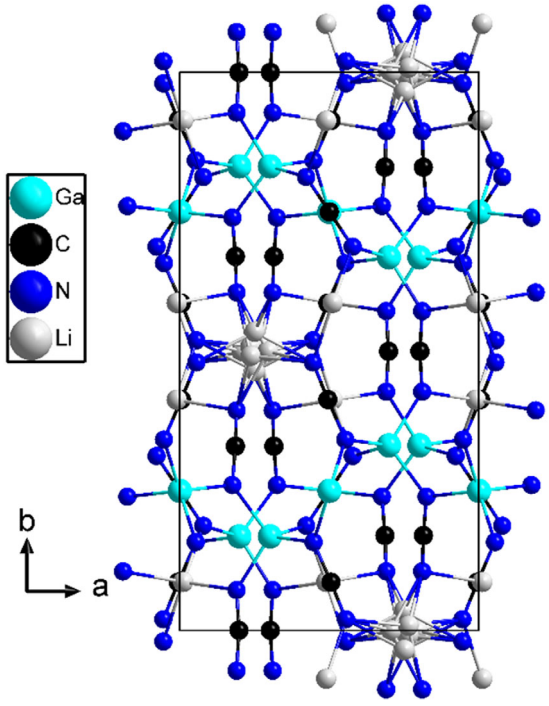

Figure 4. The unit cell of the $LiGa(CN_2)_2$ with the disordered lithium ions in channels along the *c*-axis.

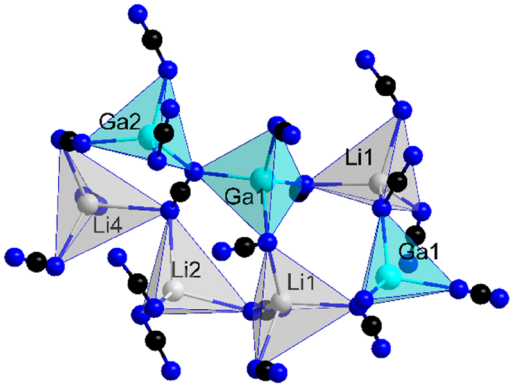

Figure 5. Section of the structure of $LiGa(CN_2)_2$, showing the tetrahedral environments of the lithium and gallium atoms. Here Li is gray, Ga turquoise, C black, and N blue.

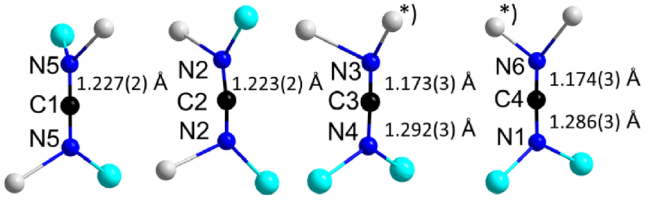

Figure 6. Coordination environments and C—N bond lengths of four distinct $(NCN)^{2-}$ ions in the structure of $liGa(CN_2)_2$. Lithium ion positions (gray spheres) marked with *) represent average positions of disordered lithium ions (Li2, Li3, and Li4).

with their respective nitrogen atoms (see Figure 6). Conversely, the dinitridocarbonate groups based on C3 an C4 are surrounded by lithium atoms and gallium on opposite N-atoms of the $(NCN)^{2-}$ ion and represent the cyanamide unit. To facilitate comprehension, one of the respective lithium positions (marked with *) is shown as an average of the respective Li2, Li3, and Li4 positions. The carbodiimide units (C1 and C2) with NCN bond angles of 179.7(3)° and 173.7(4)° are showing bond lengths of $d_{C1-N5} = 1.227(2)$ and $d_{C2-N2} = 1.223(2)$ Å. The two $(NCN)^{2-}$ units (C3 and C4) include NCN bond angles of 177.1(3)° for (N4–C3–N3) and 177.6(3)° for (N6–C4–N1) and exhibit bond lengths of $d_{C3-N4} = 1.292(3)$ Å; $d_{C3-N3} = 1.173(3)$ and $d_{C4-N1} = 1.286(3)$ Å and $d_{C4-N6} = 1.174(3)$ Å, close to the cyanamide shape in H_2CN_2 (1.15 and 1.31 Å).[16]

2.2.2. $SrGa_2(CN_2)_4$

$SrGa_2(CN_2)_4$ appears as colorless crystals that crystallize in the monoclinic space group $P2_1/c$, with relevant crystal data presented in Table 1. The structure contains one crystallographically independent Sr and two different sites for Ga ions. Coordination numbers of the strontium ions are seven, and of the gallium ions are four, represented by a trigonal prism ($d_{Sr-N} = 2.621(9)$–$2.697(9)$ Å) mono-capped by one nitrogen atom ($d_{Sr-N} = 2.97(1)$ Å) and a tetrahedral environment with nitrogen atoms of $(NCN)^2$ units ($d_{Ga-N} = 1.81(1)$–$1.936(8)$ Å) shown in **Figure 7**.

Metal ions in the network structure of $SrGa_2(CN_2)_4$ are connected through five crystallographically independent $(NCN)^{2-}$ units. The $(NCN)^{2-}$ units including N1–C1–N2, N3–C2–N4 and N5–C3–N6 are coordinated by two Ga^{3+} on one end and two Sr^{2+} cations on the other, introducing a cyanamide-like pattern of $(NCN)^{2-}$ ions. The units N7–C4–N7 and N8–C5–N8 are surrounded symmetrically by one Ga^{3+} and one Sr^{2+} on each nitrogen atom (**Figure 8**). The respective $(NCN)^{2-}$ units can be referred to as three cyanamide ions with C—N bond lengths ranging from

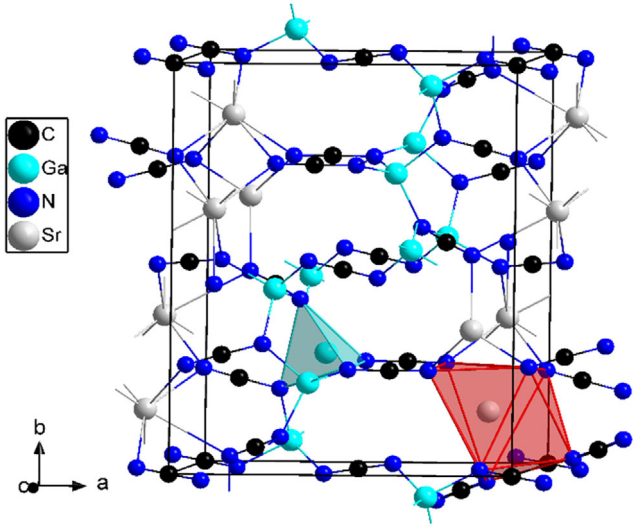

Figure 7. Unit cell of $SrGa_2(CN_2)_4$ showing network of Ga^{3+} and Sr^{2+} cations interconnected via carbodiimide bridges.

© 2025 The Author(s). Zeitschrift für anorganische und allgemeine Chemie published by Wiley-VCH GmbH

15213749, 0, Downloaded from https://onlinelibrary.wiley.com/doi/10.1002/zaac.202500085 by Universitatsbibliothek Tubingen, Wiley Online Library on [27/09/2025]. See the Terms and Conditions (https://onlinelibrary.wiley.com/terms-and-conditions) on Wiley Online Library for rules of use; OA articles are governed by the applicable Creative Commons License

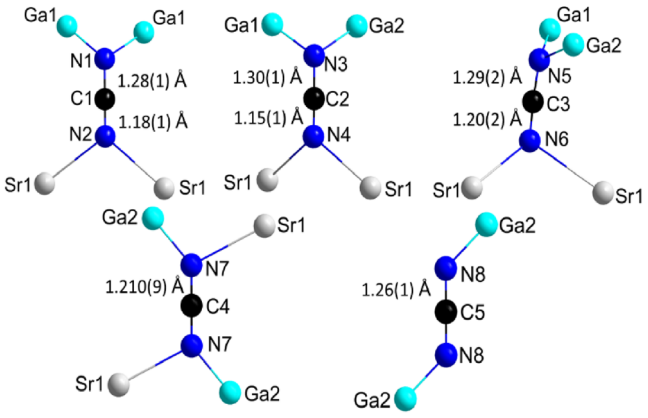

Figure 8. Coordination environments of each crystallographically independent $(CN_2)^{2-}$ ion in the structure of $SrGa_2(CN_2)_4$.

1.18(1) to 1.30(2) Å and two carbodiimide ions exhibiting typical N=C=N bond lengths of 1.210(9) and 1.26(1) Å.[17] The bond angle of the cyanamide units include a range from 175.4(1)° to 178.6(1)°. Bond angles of the carbodiimide units are at 180°.

The crystal structure of $SrGa_2(CN_2)_4$ is based on tetracyanamidometallate units which have been described in the introduction part. The crystal structure of $LiBa_2[Al(CN_2)_4]$ contains isolated tetracyanamidoaluminate ions, whereas the structure of $SrGa_2(CN_2)_4$ is based on chains of condensed tetracyanamidogallate ions of the type -Ga-NCN-Ga-NCN- running through the structure (Figure 7).[8,9]

2.2.3. $Li_{13.6}Ga_{2.8}(CN_2)_{10}I_2$

The crystal structure of $Li_{13.6}Ga_{2.8}(CN_2)_{10}I_2$ was solved and refined on a colorless single crystal by single-crystal X-ray diffraction with the orthorhombic space group *Imma*, with relevant crystallographic data presented in Table 1.

The structure contains five distinct cation positions, all linked via carbodiimide units. Two of these positions are refined as shared Li1/Ga1 and Li2/Ga2 positions (with 24% Li for position Li1 and 46% Li for position Li2), and the remaining three positions are occupied by lithium ions (Li3, Li4, Li5). In order to ensure charge neutrality, lithium positions Li3 and Li4 are partially occupied with 95% and 32%. It is evident that the ionic radii (Shannon)[18] of the Li/Ga couple (59/47 pm for coordination number 4) are close, and that they share the same preference for a tetrahedral coordination environment. Consequently, a mixed occupation between lithium and gallium is observed in the compound. A corresponding mixed occupation for lithium and gallium was also described in $LiSr_2[Ga(CN_2)_4]$.[8] The overall structure of $Li_{13.6}Ga_{2.8}(CN_2)_{10}I_2$ can be described as a layered arrangement in which a layer of $(NCN)^{2-}$ ions alternates with a layer of metal ions (**Figure 9**) which is very common for the majority of metal dinitridocarbonates. Three out of five lithium positions in the structure (Li1-Li3) are surrounded by $(NCN)^{2-}$ ions in tetrahedral arrangements with Li–N distances ranging from 1.968(4) to 2.079(5) Å. The environment of Li4 and Li5 is different: Li5 has only three nitrogen neighbors (d_{Li-N} = 2.07(1)–2.104(7) Å)

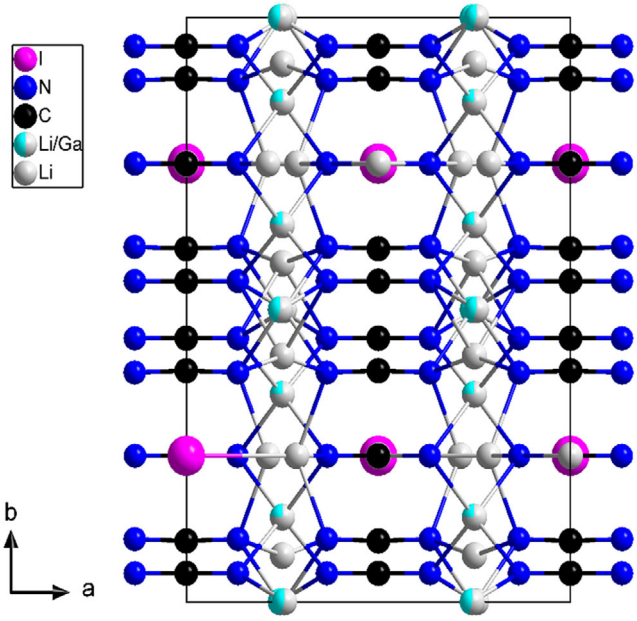

Figure 9. Layered arrangement in the crystal structure of $Li_{13.6}Ga_{2.8}(CN_2)_{10}I_2$.

and Li4 is situated in a side-on coordination to a cyanamide ion at a longer distance (d_{Li-N} = 2.46(5) Å) due to the repulsive interactions with the central carbon atom. (**Figure 10**). Furthermore, the Li-I distances range from 2.804(1) to 2.85(5) Å.

The crystal structure refinement revealed three independent carbodiimide units surrounded by lithium and gallium in a nearly trigonal prismatic coordination environments (**Figure 11**). Due to the symmetrical arrangement imposed by the symmetry elements (mirror plane cutting through C1 and C2 and a twofold rotation-axis in C3), all three $(NCN)^{2-}$ units are showing identical C—N bond lengths, ranging between 1.219(6) Å and 1.227(4) Å, including bond angles for N1–C1–N1 of 176.0(7)°, N2–C2–N2 of 179.0(1)°, and N3–C3–N3 of 176.0(1)°.

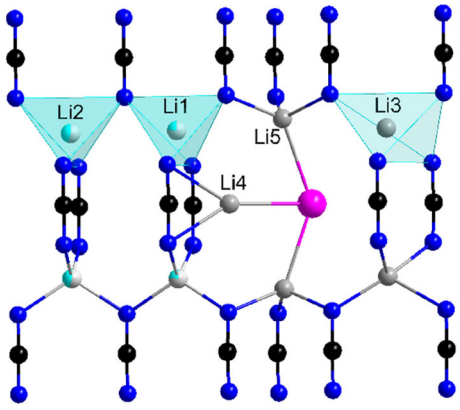

Figure 10. A section of the metal carbodiimide layer in the structure of $Li_{13.6}Ga_{2.8}(CN_2)_{10}I_2$ with highlighted Li1/Ga1, Li2/Ga2, and Li3 tetrahedra, with lithium ions shown in gray color and iodide in violet.

© 2025 The Author(s). Zeitschrift für anorganische und allgemeine Chemie published by Wiley-VCH GmbH

15213749, 0, Downloaded from https://onlinelibrary.wiley.com/doi/10.1002/zaac.202500085 by Universitatsbibliothek Tubingen, Wiley Online Library on [27/09/2025]. See the Terms and Conditions (https://onlinelibrary.wiley.com/terms-and-conditions) on Wiley Online Library for rules of use; OA articles are governed by the applicable Creative Commons License

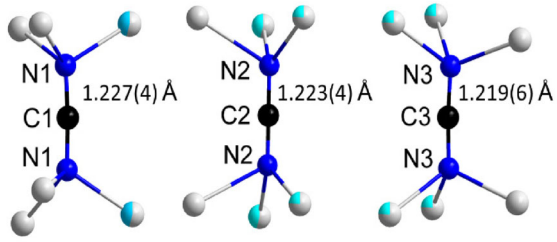

Figure 11. Three crystallographically independent carbodiimide units in the compound $Li_{13.6}Ga_{2.8}(CN_2)_{10}I_2$.

2.3. Infrared Studies

The infrared spectrum of $LiGa(CN_2)_2$ (**Figure 12**) displays the characteristic features of both, carbodiimide and cyanamide units. The asymmetric stretching of the units is divided into two signals, with their center at 2035 and 2148 cm^{-1}, respectively. The symmetrical stretching vibrations in the range of 1249 and 1181 cm^{-1} can be assigned to the cyanamide units present in the compound. The bending vibrations of the units are in a range from 754 to 598 cm^{-1}. In the crystal structure of $Li_{13.6}Ga_{2.8}(CN_2)_{10}I_2$, three crystallographically distinct carbodiimide units are observed. In accordance with the symmetry description provided in the crystallographic section, the infrared spectrum (**Figure 13**) exhibits the anticipated asymmetric vibrations at 2122 and 2033 cm^{-1}, the deformation vibrations at 708 and 637 cm^{-1} which are characteristic of such carbodiimide units. The presence of additional bands can be attributed to the commencement of hydrolysis of the compound, a process that occurred during the measurement due to the presence of relative humidity and an as yet unidentified secondary phase, indicating the presence of other cyanamide.

The IR spectrum of $SrGa_2(CN_2)_4$ (**Figure 14**) exhibits a prominent band at 2125 cm^{-1}, which can be attributed to the stretching vibrations of the $(NCN)^{2-}$ units. Additionally, there are several bands at 1275, 1246, and 1194 cm^{-1} which can be assigned to the

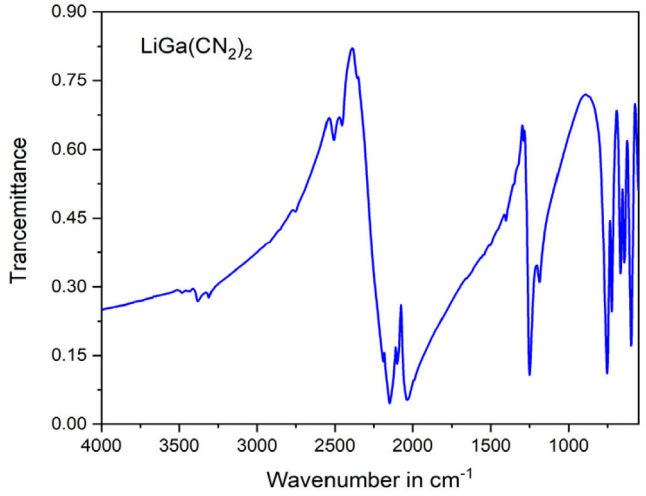

Figure 12. Infrared spectrum of the compound $LiGa(CN_2)_2$.

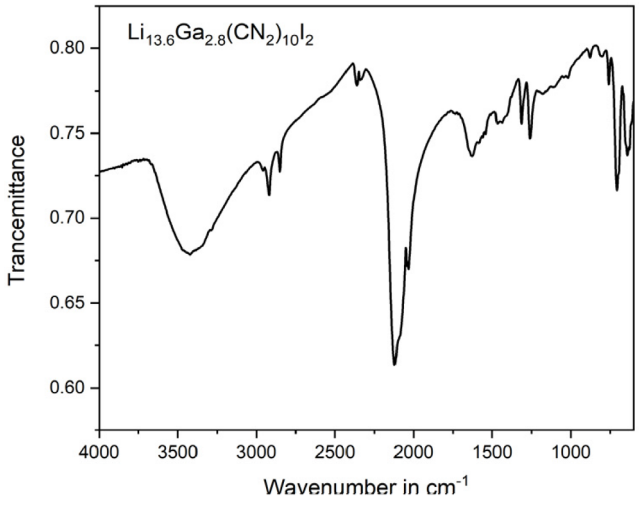

Figure 13. Infrared spectrum of the compound $Li_{13.6}Ga_{2.8}(CN_2)_{10}I_2$.

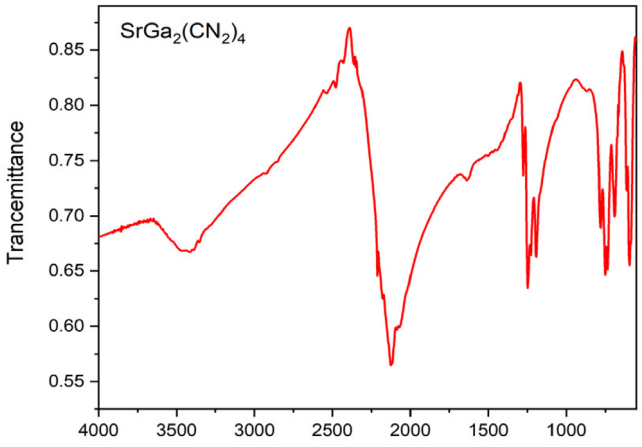

Figure 14. Infrared spectrum of the compound $SrGa_2(CN_2)_4$.

symmetrical stretching vibrations for the three independent crystallographic cyanamide units in the compound. The bands at 781, 750, 737, and 692 cm^{-1} are indicative of bending vibrations of the $(NCN)^{2-}$ units. **Table 2** offers a summary of relevant vibration frequencies of the reported compounds in comparison with other cyanamide and carbodiimide compounds.

2.4. Solid-State NMR

The ^7Li MAS nuclear magnetic resonance (NMR) spectrum of $LiGa(CN_2)_2$ consists of one relatively sharp ($\Delta\nu = 390$ Hz) and intense isotropic peak at 0.3 ppm, flanked by weaker spinning sidebands spaced at integral multiples of the spinning frequency (**Figure 15**, upper trace). While the strong isotropic peak arises mainly from the central transition of the spin-3/2 ^7Li nucleus, the spinning sidebands are associated with the satellite transitions and reflect the quadrupole interaction of the ^7Li nuclear quadrupole moment with the electric field gradient (EFG) at the lithium site.[19] An exception are the first-order spinning

 © 2025 The Author(s). Zeitschrift für anorganische und allgemeine Chemie published by Wiley-VCH GmbH

15213749, 0, Downloaded from https://onlinelibrary.wiley.com/doi/10.1002/zaac.202500085 by Universitatsbibliothek Tubingen, Wiley Online Library on [27/09/2025]. See the Terms and Conditions (https://onlinelibrary.wiley.com/terms-and-conditions) on Wiley Online Library for rules of use; OA articles are governed by the applicable Creative Commons License

15213749, 0, Downloaded from https://onlinelibrary.wiley.com/doi/10.1002/zaac.202500085 by Universitatsbibliothek Tubingen, Wiley Online Library on [27/09/2025]. See the Terms and Conditions (https://onlinelibrary.wiley.com/terms-and-conditions) on Wiley Online Library for rules of use; OA articles are governed by the applicable Creative Commons License

Table 2. Overview of vibrational frequencies of the described compounds in comparison to selected carbodiimides and cyanamides.

Compound	ν_{as} [cm^{-1}]	ν_s [cm^{-1}]	δ [cm^{-1}]
$LiGa(CN_2)_2$	2035, 2148	1249, 1181	754, 722, 668, 641, 598
$Li_{13.6}Ga_{2.8}(CN_2)_{10}I_2$	2122, 2033	–	708, 637
$SrGa_2(CN_2)_4$	2125	1275, 1246, 1194	781, 750, 737, 692
$Pb_7I_6(CN_2)_4$[28]	1900	–	630
$Pb(CN_2)$[29]	2000	1215, 1305	643
$Tl_2(CN_2)$[6]	1851	–	632
$Li_4[Si(CN_2)_4]$[11]	2102, 2193	1310	621

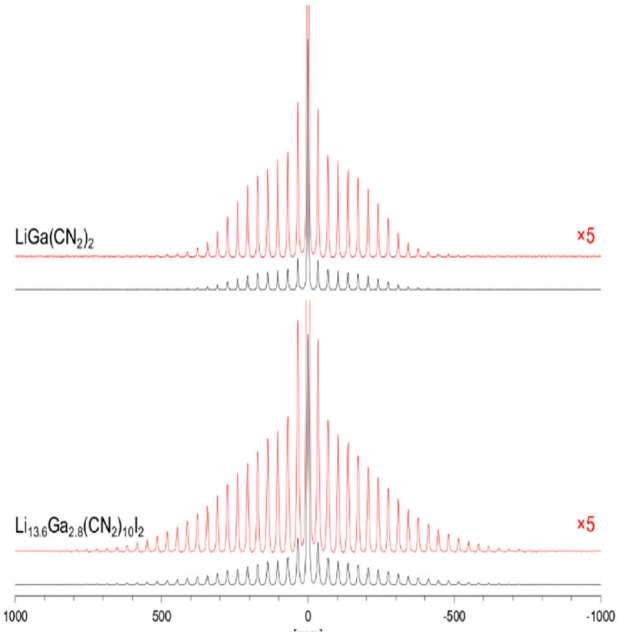

Figure 15. Lithium-7 MAS NMR spectra of $LiGa(CN_2)_2$ and $Li_{13.6}Ga_{2.8}(CN_2)_{10}I_2$ obtained at 7.05 T and a spinning rate of 4 kHz.

sidebands, which are also affected by direct dipolar interactions, mostly of the homonuclear kind.[20]

The ^{7}Li MAS NMR spectrum of $Li_{13.6}Ga_{2.8}(CN_2)_{10}I_2$ is similar (Figure 15, lower trace), but the spinning sidebands cover a wider range around the isotropic peak at 0.0 ppm ($\Delta\nu = 810$ Hz). For both compounds, the envelope of spinning sideband intensities is close to a Gaussian distribution, indicating that several lithium sites contribute to the ^{7}Li MAS NMR spectrum, in agreement with the results of the X-ray diffraction results. In the case of $LiGa(CN_2)_2$, the Li1 position is fully occupied and contributes most (67%) to the ^{7}Li MAS NMR spectrum. Independent of the asymmetry parameter of the EFG tensor, the separation of the outermost spinning sidebands corresponds for a spin-3/2 nucleus to the greatest quadrupolar coupling, $\chi = 140$ kHz. The situation is more complicated for $Li_{13.6}Ga_{2.8}(CN_2)_{10}I_2$, because there are five different lithium positions with different occupation numbers and multiplicities, so that five different positions with relative contributions of 5%–30% contribute almost equally to the ^{7}Li NMR spectrum. The separation between the outermost spinning sidebands amounts to $\chi = 196$ kHz. Both compounds demonstrate with their very similar chemical shifts that the ^{7}Li nucleus is not very sensitive to the chemical environment but differ clearly from LiI, $\delta(^7\text{Li}) = -4.3$ ppm, a potential contaminant.[21] For that purpose we also acquired the ^{127}I MAS NMR spectrum of $Li_{13.6}Ga_{2.8}(CN_2)_{10}I_2$, because the ^{127}I NMR signal of LiI at 411 ppm is very easy to detect. However, no signal was observed. The observation of ^{127}I NMR signals for iodine in noncubic situations succeeds rarely, because the ^{127}I quadrupole coupling constant can amount to several hundreds of MHz.[22]

2.5. Band Gap Determination

In the pursuit of predicting the photophysical and photochemical properties exhibited by a material, the determination of its band gap constitutes a pivotal point. This parameter is frequently cited in discourse pertaining to the photocatalytic properties of semiconductors. The stability of $SrGa_2(CN_2)_4$ in air, in conjunction with its straightforward synthesis, positions this compound as a promising candidate for wide band gap semiconductor material. Consequently, the Tauc plot formalism was employed for the experimental determination of the band gap. The absorption coefficient was obtained from the Kubelka-Munk relation.

$$F(R_\infty) = \frac{\alpha}{S} = \frac{(1 - R_\infty)^2}{2R_\infty} \tag{4}$$

R_∞ is defined as the reflectance of an infinitely thick sample, while α is the absorption coefficient and S is the scattering coefficient. In the case of particle sizes that exceed the wavelengths employed in the measurement process, the scattering coefficient is regarded as being approximately frequency-independent and therefore the $F(R_\infty) \approx \alpha$. Consequently, $F(R_\infty)$ can be utilized as a 'pseudo-absorption coefficient'.[23]

The optical band gap was determined by employing the Tauc method in accordance with the following relationship:

$$(\alpha \cdot h\nu)^{\frac{1}{\beta}} = A(h\nu - E_g) \tag{5}$$

where α is the absorption coefficient, $h\nu$ is the photon energy, h is the Planck constant, and A is a material-related constant. In the case of a direct allowed bandgap transition, $\beta = 1/2$; for an indirect allowed bandgap transition $\beta = 2$. Substituting the previously derived relationship for the absorption coefficient in this particular equation results in the subsequent equation[24]

$$(F(R_\infty) \cdot h\nu)^{\frac{1}{\beta}} = A(h\nu - E_g) \tag{6}$$

 © 2025 The Author(s). Zeitschrift für anorganische und allgemeine Chemie published by Wiley-VCH GmbH

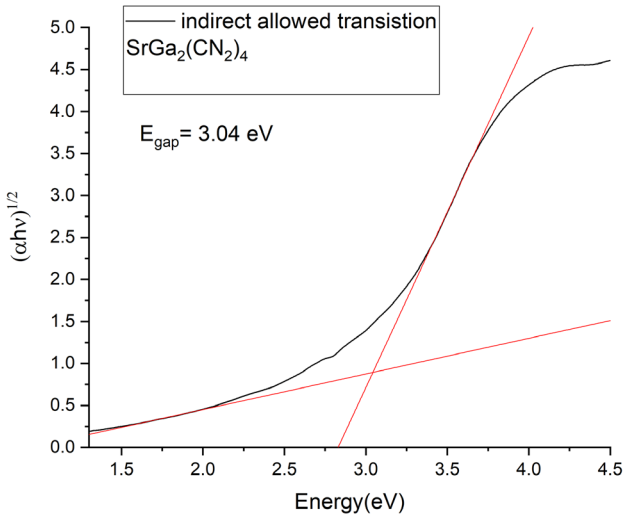

Figure 16. Tauc plot of $SrGa_2(CN_2)_4$ for indirect band gap fitting (black) along with the linear extrapolation (red) for the determination of the optical band gap.

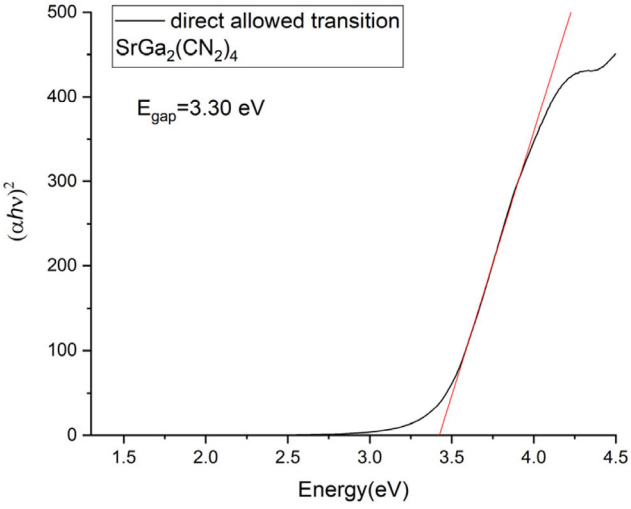

Figure 17. Tauc plot of $SrGa_2(CN_2)_4$ for direct band gap fitting (black) along with the linear extrapolation (red) for the determination of the optical band gap.

The value of the band gap was determined by the intersection between the energy axis at the absorption offset and the line extrapolated from the linear part of the absorption edge in the diagram of $(F(R_\infty) \cdot h\nu)^{\frac{1}{\beta}}$ against E. The Tauc plot analysis resulted in an indirect band gap of 3.04 eV and a direct band gap of 3.30 eV for $SrGa_2(CN_2)_4$. (**Figure 16** and **17**).

3. Conclusions

This study presents the synthesis and characterization of three ternary gallium carbodiimides. The formation of these compounds was enabled by SSM reactions under optimized conditions, thereby demonstrating the efficacy of this approach. Structural analysis through single-crystal XRD revealed distinct crystallographic arrangements, including tetrahedral and layered configurations, thus highlighting the diverse bonding environments of strontium, gallium, and lithium in carbodiimide frameworks. Infrared spectroscopy (IR) confirmed the presence of characteristic carbodiimide and cyanamide units. One compound prepared is $SrGa_2(CN_2)_4$, which has been shown to behave stable under ambient conditions and is showing a band gap in the order of 3 eV.

This study contributes to the expanding field of main group metal carbodiimides and opens up further opportunities to explore their optical and electronic properties. The development is still ongoing. Generally, metal dinitridocarbonates have demonstrated the capacity to act as semiconductors, exhibiting the potential for luminescence, function in lithium batteries, or display photocatalytic properties.

4. Experimental Section

Preparation of $LiGa(CN_2)_2$: $Li_2(CN_2)$[25] and $GaCl_3$ (Alfa Aeser 99.999%) were mixed in a molar ratio of 2:1 within an argon atmosphere (total mass ca. 200 mg) and subsequently filled in an evacuated quartz glass ampoule. The reaction mixture was heated at a rate of 2 K min^{-1} to a temperature of 525 °C. Following a holding period of 15 h, the mixture was cooled again at the same rate to room temperature. The resulting powder was white in color and contained both the novel compound $LiGa(CN_2)_2$ with a yield of over 95% (with respect to Ga) and the metathesis salt, LiCl, which was removed from the crude product by washing it with dry methanol using the standard Schlenk technique.

Preparation of $Li_{13.6}Ga_{2.8}(CN_2)_{10}I_2$: A molar ratio of 2.8:10 of GaI_3 (Sigma–Aldrich, 99.99%) and $Li_2(CN)_2$[25] was prepared and sealed in a dry box under argon. The mixture was then charged with a total mass of 200 mg into a quartz tube and flame-sealed under vacuum. The quartz ampule was placed vertically in a carbolite chamber oven and heated to 470 °C at a rate of 2 K min^{-1}, where it was maintained for 20 h. The oven was then cooled to 25 °C at a same rate resulting in the formation of the compound as a grayish powder with a yield of 90% (with respect to Ga). LiI, which is formed as a by-product, was removed by washing the crude product with acetonitrile using the standard Schlenk technique.

Preparation of $SrGa_2(CN_2)_4$: A mixture of $SrCl_2$ (Alfa Aesar, 99.5%), $GaCl_3$(Alfa Aeser 99.999%), and $Na_2(CN_2)$[26] in a molar ratio of 1:2:4 was prepared by grinding the components together. The resulting homogeneous mixture (total mass ca. 200 mg) was transferred into a quartz ampoule and sealed under vacuum. The ampoule was placed into the oven and heated at 550 °C for 72 h, with a heating and cooling rate of 1 K min^{-1}. Subsequently, the ampoule was opened in the glove box, and the product was analyzed by X-ray powder diffraction. The yield of the product is 95% (with respect to Ga). The metathesis salt NaCl was removed by washing the crude product with dry methanol.

Single-Crystal X-Ray Diffraction (XRD): Single-crystal XRD studies were performed using a Rigaku XtaLab Synergy-S diffractometer with monochromatic Cu−Kα ($\lambda = 154.0598$ pm) and Mo Kα ($\lambda = 71.073$ pm) radiation and a mirror monochromator. Measurements were conducted under N_2 cooling. Crystal structure refinements and solutions were performed with direct methods (SHELXS) and least square refinements of F^2.

© 2025 The Author(s). Zeitschrift für anorganische und allgemeine Chemie published by Wiley-VCH GmbH

15213749, 0, Downloaded from https://onlinelibrary.wiley.com/doi/10.1002/zaac.202500085 by Universitatsbibliothek Tubingen, Wiley Online Library on [27/09/2025]. See the Terms and Conditions (https://onlinelibrary.wiley.com/terms-and-conditions) on Wiley Online Library for rules of use; OA articles are governed by the applicable Creative Commons License

15213749, 0, Downloaded from https://onlinelibrary.wiley.com/doi/10.1002/zaac.202500085 by Universitatsbibliothek Tübingen, Wiley Online Library on [27/09/2025]. See the Terms and Conditions (https://onlinelibrary.wiley.com/terms-and-conditions) on Wiley Online Library for rules of use; OA articles are governed by the applicable Creative Commons License

Powder XRD: The powder samples were analyzed using an X-ray powder diffractometer (STOE Darmstadt, STADI-P, Ge-monochromator) with Cu-Kα_1 radiation ($\lambda = 154.0598$ pm) in the 2θ range of 5°–120°.

Infrared Spectroscopy: IR spectra were recorded using a VERTEX 70 FT-IR Spectrometer in the range of 400–4000 cm^{-1} using KBr pellets. Samples were prepared in a glove-box under argon atmosphere (SI).

Solid-State NMR: Solid-state magic-angle spinning (MAS) NMR spectra were obtained at 7.05 T on a Bruker Avance III HD spectrometer with a 300 MHz wide-bore magnet equipped with a double-bearing broad-band cross-polarization/MAS probe head, operating at 116.642 MHz for ^{7}Li and 60.048 MHz for ^{127}I. Powdered samples were packed in a glove box into 4 mm (o.d.) zirconia rotors and spun at the magic angle at a spinning rate of 4000 Hz. Spectra were acquired after single-pulse excitation for ^{7}Li using a 1.0 µs pulse (solution 30°). The ^{7}Li MAS NMR spectra were simulated using the sola module of Bruker TopSpin 4.4.1. Referencing against 38.863796% (^{7}Li) or 20.007486% (^{127}I)[27] was achieved by the substitution method: an external sample of $CHCl_3$ in acetone in a zirconia rotor was spun at 1.5 kHz and the external magnetic field was adjusted such that the ^{1}H chemical shift of $CHCl_3$ matched a predetermined chemical shift wrt. external 1% TMS in $CHCl_3$.

UV–Vis in Diffuse Reflectance: The reflectance spectra were recorded on an OceanOptics Maya 2000 Pro spectrometer equipped with a Harrick praying mantis sample chamber. The light source employed was a deuterium tungsten lamp (DH 200 BAL) from OceanOptics. The measurement was carried out with the following settings: scan to average = 80, boxcar width = 10 and integration time = 300 milli s, using OceanView 1.6.7 (lite) software from OceanOptics.

Acknowledgements

The authors gratefully acknowledge the support provided by the Deutsche Forschungsgemeinschaft (DFG-Bonn) for this research project (ME 914/34-1).

Open Access funding enabled and organized by Projekt DEAL.

Conflict of Interest

The authors declare no conflict of interest.

Data Availability Statement

The data that support the findings of this study are available from the corresponding author upon reasonable request.

Keywords: band gap · carbodiimide · crystal structure · gallium · solid-state metathesis

[1] a) S. Patwal, M. Agrawal, K. Radhakrishnan, T. L. A. Seah, N. Dharmarasu, *Phys. Status Solidi A* **2020**, *217*, 1900818; b) A. M. Bhat, R. Poonia, A. Varghese, N. Shafi, C. Periasamy, *Micro Nanostruct.* **2023**, *176*, 207528.
[2] T. Matsuoka, H. Okamoto, M. Nakao, H. Harima, E. Kurimoto, *Appl. Phys. Lett.* **2002**, *81*, 1246.
[3] J. I. Pankove, *Mater. Sci. Eng. B* **1999**, *61–62*, 305.
[4] a) V. Wang, Z. Q. Wu, Y. Kawazoe, W. T. Geng, *J. Phys. Chem. C* **2018**, *122*, 6930; b) J. Orton, C. Foxon, *Rep. Prog. Phys.* **1998**, *61*, 1; c) J. Wu, W. Walukiewicz, K. Yu, W. Shan, J. A. Iii, E. Haller, H. Lu, W. J. Schaff, W. Metzger, S. Kurtz, *J. Appl. Phys.* **2003**, *94*, 6477.
[5] R. Dronskowski, *Z. Naturforsch. B* **1995**, *50*, 1245.
[6] L. Stork, X. Liu, B. P. T. Fokwa, R. Dronskowski, *Z. Anorg. Allg. Chem.* **2007**, *633*, 1339.
[7] M. Kubus, R. Heinicke, M. Ströbele, D. Enseling, T. Jüstel, H.-J. Meyer, *Mater. Res. Bull.* **2015**, *62*, 37.
[8] M. Kalmutzki, M. Ströbele, S. Kroeker, J. E. C. Wren, H.-J. Meyer, *Eur. J. Inorg. Chem.* **2013**, *2013*, 6091.
[9] L. Unverfehrt, M. Ströbele, H.-J. Meyer, *Z. Anorg. Allg. Chem.* **2013**, *639*, 1722.
[10] a) D. Dutczak, M. Ströbele, D. Enseling, T. Jüstel, H.-J. Meyer, *Eur. J. Inorg. Chem.* **2016**, *2016*, 4011; b) J. Glaser, H.-J. Meyer, *Angew. Chem.* **2008**, *120*, 7658; c) J. Glaser, H. Bettentrup, T. Jüstel, H.-J. Meyer, *Inorg. Chem.* **2010**, *49*, 2954.
[11] K. D. Röseler, K. Eichele, M. Ströbele, H.-J. Meyer, *Eur. J. Inorg. Chem.* **2024**, *27*, e202300713.
[12] H.-J. Meyer, *Dalton Trans.* **2010**, *39*, 5973.
[13] I. P. Parkin, *Chem. Soc. Rev.* **1996**, *25*, 199.
[14] K. Dolabdjian, C. Castro, H.-J. Meyer, *Eur. J. Inorg. Chem.* **2018**, *2018*, 1624.
[15] M. Ströbele, E. Bayat, H.-J. Meyer, *Inorg. Chem.* **2024**, *63*, 16565.
[16] L. Unverfehrt, M. Kalmutzki, M. Ströbele, H. J. Meyer, *Dalton Trans.* **2011**, *40*, 9921.
[17] L. Unverfehrt, M. Ströbele, H.-J. Meyer, *Inorg. Chem.* **2012**, *51*, 12925.
[18] R. Shannon, *Acta Crystallogr. A* **1976**, *32*, 751.
[19] R. W. Schurko, M. J. Jaroszewicz, in *Encyclopedia of Inorganic and Bioinorganic Chemistry*, John Wiley & Sons, Ltd. **2015**, pp. 117–172.
[20] a) M. Feuerstein, R. Lobo, *Chem. Mater.* **1998**, *10*, 2197; b) R. Schmidt, M. Ströbele, K. Eichele, H.-J. Meyer, *Z. Anorg. Allg. Chem.* **2019**, *645*, 461.
[21] M. Löber, M. Ströbele, K. Eichele, C. P. Romao, H.-J. Meyer, *Eur. J. Inorg. Chem.* **2021**, *2021*, 4929.
[22] a) K. Yamada, T. Matsui, T. Tsuritani, T. Okuda, S. Ichiba, *Z. Naturforsch. A* **1990**, *45*, 307; b) C. M. Widdifield, D. L. Bryce, *J. Phys. Chem. A* **2010**, *114*, 10810; c) D. L. Bryce, C. M. Widdifield, R. P. Chapman, R. J. Attrell, *Chlorine, Bromine, and Iodine Solid-State NMR*, John Wiley and Sons Ltd., Chichester, UK **2011**.
[23] W. W. Wendlandt, H. G. Hecht, *Reflectance Spectroscopy*, Wiley, New York, NY **1966**, p. 298.
[24] P. Makuła, M. Pacia, W. Macyk, *J. Phys. Chem. Lett.* **2018**, *9*, 6814.
[25] R. Srinivasan, M. Ströbele, H.-J. Meyer, *Inorg. Chem.* **2003**, *42*, 3406.
[26] L. Unverfehrt, *Dissertation*, Eberhard Karls Universität Tübingen **2011**.
[27] R. K. Harris, E. D. Becker, S. M. C. de Menezes, R. Goodfellow, P. Granger, *Pure Appl. Chem.* **2001**, *73*, 1795.
[28] A. T. Schwarz, M. Ströbele, C. P. Romao, D. Enseling, T. Jüstel, H.-J. Meyer, *Dalton Trans.* **2024**, *53*, 6416.
[29] M. Löber, M. Ströbele, H.-J. Meyer, *Z. Anorg. Allg. Chem.* **2021**, *647*, 1973.

Manuscript received: May 12, 2025
Revised manuscript received: July 15, 2025
Version of record online:

 © 2025 The Author(s). Zeitschrift für anorganische und allgemeine Chemie published by Wiley-VCH GmbH

Supporting Information for

Characterizing Gallium Dinitridocarbonates: A Focus on $LiGa(CN_2)_2$, $Li_{13.6}Ga_{2.8}(CN_2)_{10}I_2$, and $SrGa_2(CN_2)_4$

*Albert T. Schwarz[a], Oleksander Kysliak[a], Klaus Eichele[b], Markus Ströbele[a] and H.-Jürgen Meyer[*a]*

Section for Solid State and Theoretical Inorganic Chemistry, Institute of Inorganic Chemistry, Eberhard Karls University, Auf der Morgenstelle18, D-72076 Tübingen, Germany.

Table of contents

Table S2: Fractional Atomic Coordinates (×10⁴) and Equivalent Isotropic Displacement Parameters (Å²×10³) for **$Li_{13.6}Ga_{2.8}(CN_2)_{10}I_2$.** U_{eq} is defined as 1/3 of the trace of the orthogonalised U_{ij}.

Atom	x	y	z	U_{eq}
I1	½	¾	0.61397(6)	20.7(2)
Ga1	¾	0.6449(2)	¼	11.8(8)
Ga2	0.7556(2)	½	½	10.6(5)
N1	0.8656(4)	0.6074(3)	0.5887(3)	18.3(8)
N2	0.6341(5)	0.5489(3)	0.3564(4)	26(1)
N3	0.8665(6)	¾	0.3446(5)	21(1)
C1	0	0.6043(5)	0.5872(5)	13(1)
C2	½	0.5488(5)	0.3574(5)	13(1)
C3	0	¾	0.341(1)	31(3)
Li1	¾	6449(2)	¼	11.8(8)
Li2	0.7556(2)	½	½	10.6(5)
Li3	¾	0.579(1)	¾	40(3)
Li4	0	¾	0.148(5)	21(9)
Li5	0.788(1)	¾	0.523(1)	21(2)

Table S2: Fractional Atomic Coordinates (×10⁴) and Equivalent Isotropic Displacement Parameters (Å²×10³) for **$SrGa_2(CN_2)_4$**. U_{eq} is defined as 1/3 of the trace of the orthogonalised U_{ij}.

Atom	x	y	z	U_{eq}
Sr1	-0.1159(1)	0.35648(8)	0.0682(1)	20.8(3)
Ga1	0.3926(1)	0.27877(8)	0.4136(2)	11.7(3)
Ga2	0.2703(1)	0.44189(8)	0.6940(2)	14.8(3)
N1	0.4861(8)	0.2528(7)	0.199(1)	17(2)
N2	0.7280(9)	0.2518(8)	0.268(1)	27(2)
N3	0.2490(8)	0.1879(6)	0.318(1)	16(2)
N4	0.0300(9)	0.2385(8)	0.354(1)	28(2)
N5	0.3167(9)	0.4098(7)	0.431(1)	21(2)
N6	0.138(1)	0.4671(9)	0.129(2)	41(3)
N7	0.1064(9)	0.5107(7)	0.622(1)	22(2)
N8	0.387(1)	0.5165(9)	0.884(2)	56(3)
C1	0.612(1)	0.2535(7)	0.237(1)	15(2)
C2	0.132(1)	0.2138(8)	0.336(2)	19(2)
C3	0.228(2)	0.4405(9)	0.271(2)	36(3)
C4	0	½	½	16(3)
C5	½	½	0	36(4)

Table S3: Fractional Atomic Coordinates (×10^4) and Equivalent Isotropic Displacement Parameters (Å^2×10^3) for **$Li_4Ga(CN_2)_4$**. U_{eq} is defined as 1/3 of the trace of the orthogonalised U_{ij}.

Atom	x	y	z	U_{eq}
Ga1	0.3010.9(3)	0.83158(2)	0.74440(3)	7.53(7)
Ga2	0	¾	0.55113(4)	4.89(8)
N1	0.4468(3)	0.8419(1)	0.5746(3)	7.8(4)
N2	0.1898(3)	0.9278(1)	0.7871(3)	10.6(4)
N3	0.1898(3)	0.6056(1)	0.8153(3)	12.5(4)
N4	0.1756(2)	0.7396(1)	0.6845(2)	7.8(4)
N5	0.4221(3)	0.8125(1)	0.9264(2)	8.6(4)
N6	-0.0552(3)	0.0198(1)	0.0460(3)	14.5(5)
C1	½	¾	0.9268(3)	4.2(5)
C2	0.1976(3)	0	¾	3.6(5)
C3	0.1857(2)	0.6700(1)	0.7552(3)	5.8(4)
C4	0.5053(3)	0.9137(1)	0.5574(3)	6.7(4)
Li1	0.0108(7)	0.9132(3)	0.9481(7)	18(1)
Li2	0.294(2)	½	¾	4(2)
Li3	-¼	0.965(1)	0	4(2)
Li4	0.236(2)	0.508(2)	0.646(3)	4(2)

Picture S1: Drawing of the anisotropic displacement parameters of the N5-C1-N5 unit in $LiGa(CN_2)_2$. Ellipsoids drawn with 99 % probability.

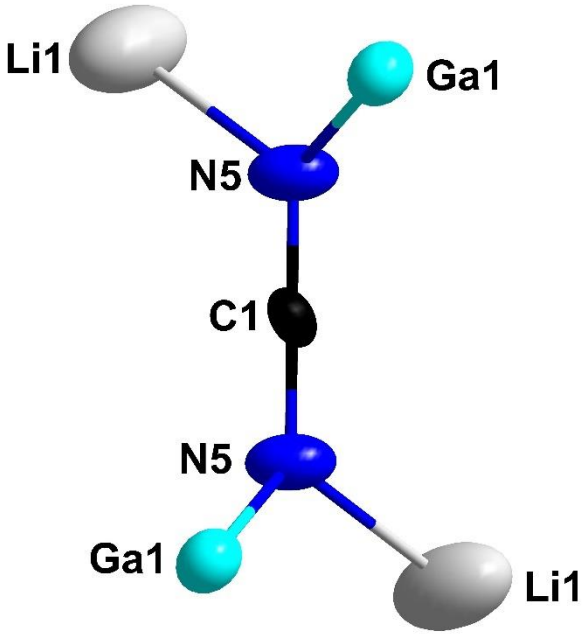

Picture S2: Drawing of the anisotropic displacement parameters of the N2-C2-N2 unit in $LiGa(CN_2)_2$. Ellipsoids drawn with 99 % probability.

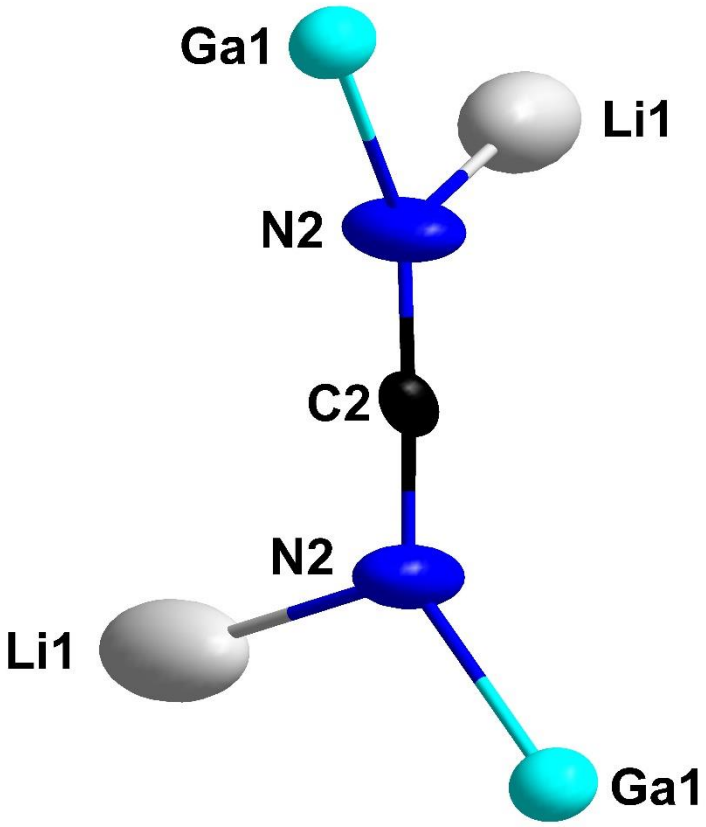

Picture S3: Drawing of the anisotropic displacement parameters of the N3-C3-N4 unit in $LiGa(CN_2)_2$. Ellipsoids drawn with 99 % probability.

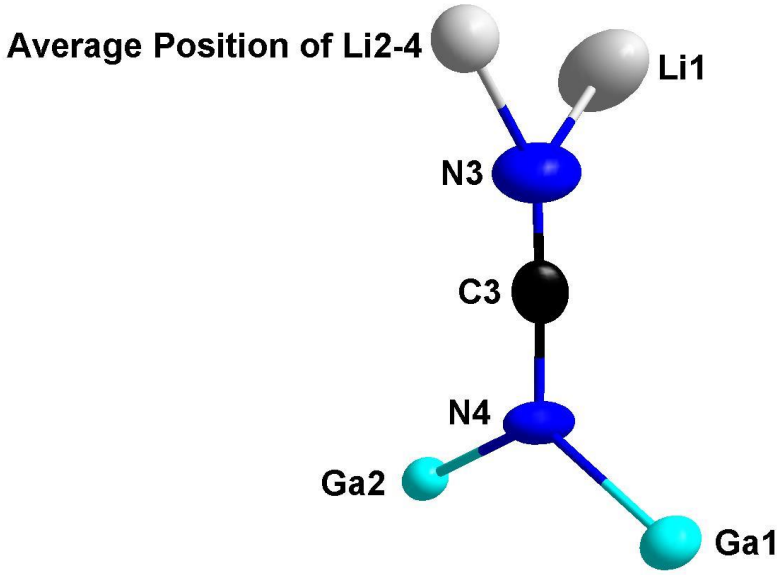

Picture S4: Drawing of the anisotropic displacement parameters of the N1-C4-N6 unit in $LiGa(CN_2)_2$. Ellipsoids drawn with 99 % probability.

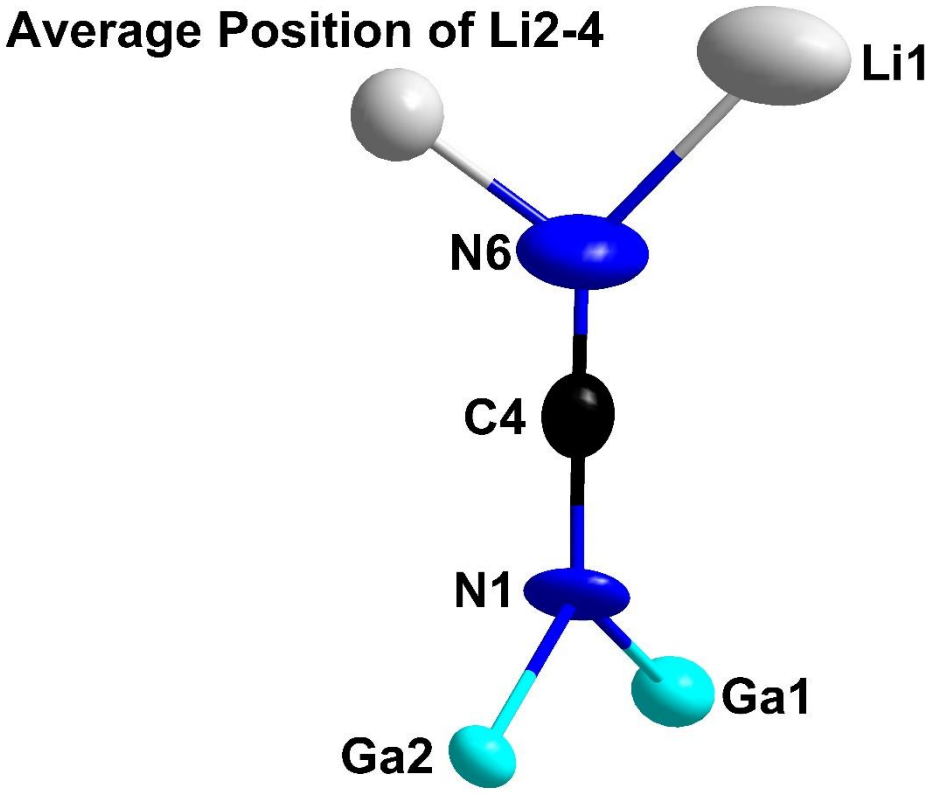

Picture S5: Drawing of the anisotropic displacement parameters of the N1-C1-N2 unit in $SrGa_2(CN_2)_4$. Ellipsoids drawn with 75 % probability.

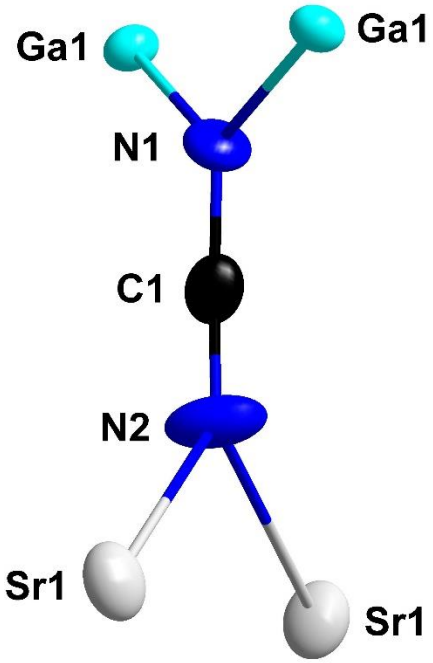

Picture S6: Drawing of the anisotropic displacement parameters of the N3-C2-N4 unit in $SrGa_2(CN_2)_4$. Ellipsoids drawn with 75 % probability.

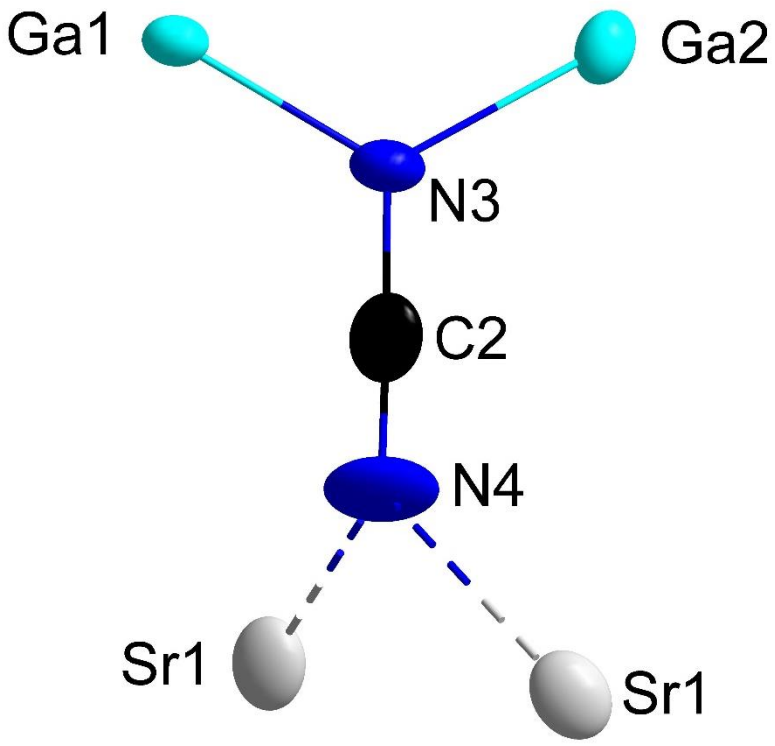

Picture S7: Drawing of the anisotropic displacement parameters of the N5-C3-N6 unit in $SrGa_2(CN_2)_4$. Ellipsoids drawn with 75 % probability.

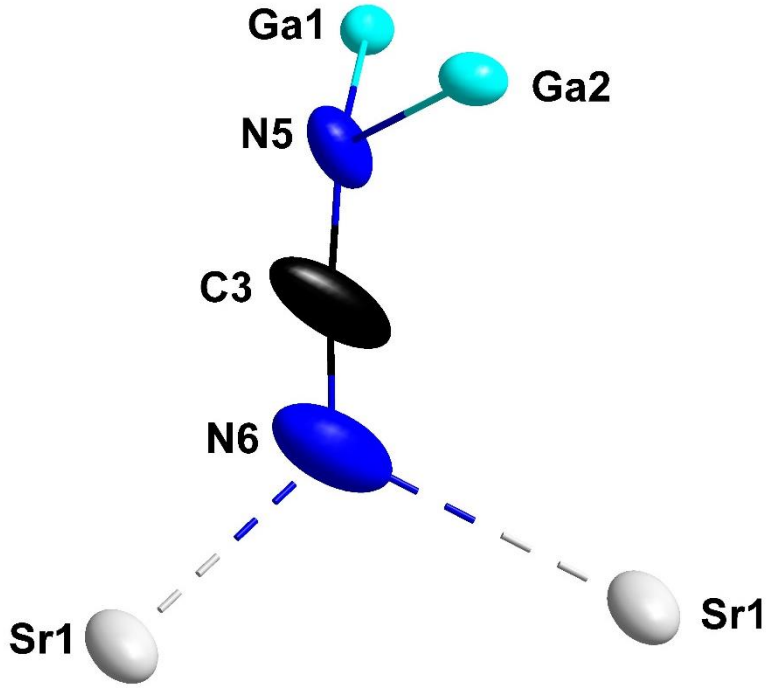

Picture S8: Drawing of the anisotropic displacement parameters of the N7-C4-N7 unit in $SrGa_2(CN_2)_4$. Ellipsoids drawn with 75 % probability.

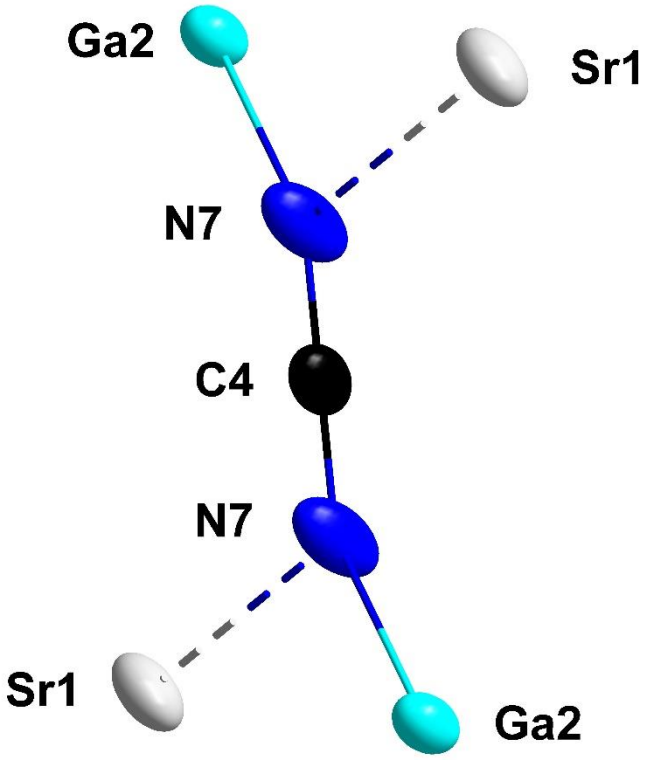

Picture S9: Drawing of the anisotropic displacement parameters of the N8-C5-N8 unit in $SrGa_2(CN_2)_4$. Ellipsoids drawn with 75 % probability.

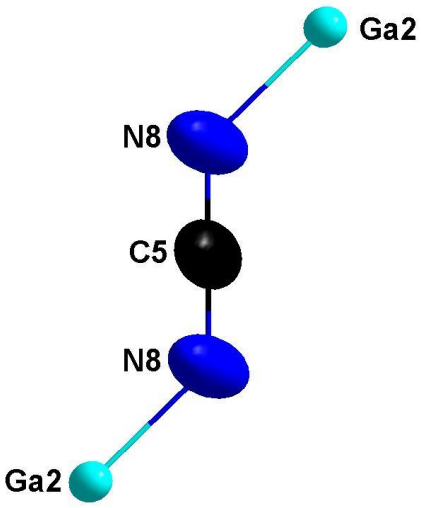

Picture S10: Drawing of the anisotropic displacement parameters of the N1-C1-N1 unit in $Li_{13.6}Ga_{2.8}(CN_2)_{10}I_2$. Ellipsoids drawn with 75 % probability.

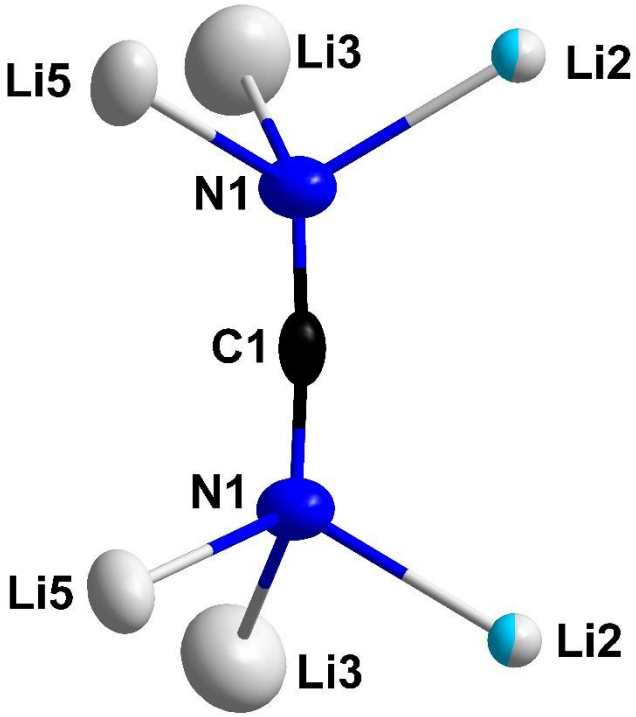

Picture S11: Drawing of the anisotropic displacement parameters of the N2-C2-N2 unit in $Li_{13.6}Ga_{2.8}(CN_2)_{10}I_2$. Ellipsoids drawn with 75 % probability.

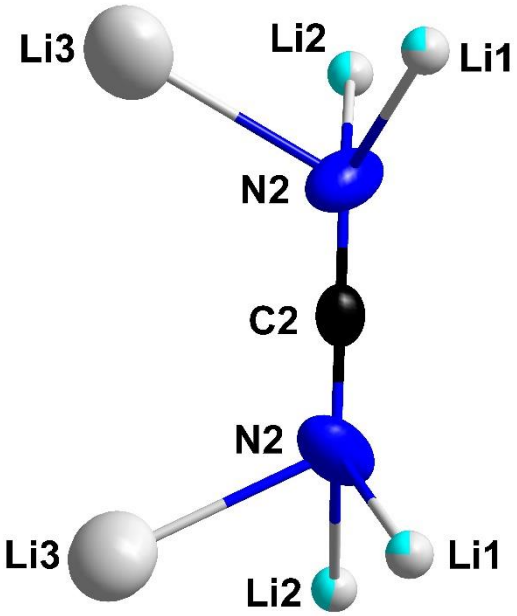

Picture S12: Drawing of the anisotropic displacement parameters of the N3-C3-N3 unit in $Li_{13.6}Ga_{2.8}(CN_2)_{10}I_2$. Ellipsoids drawn with 75 % probability.

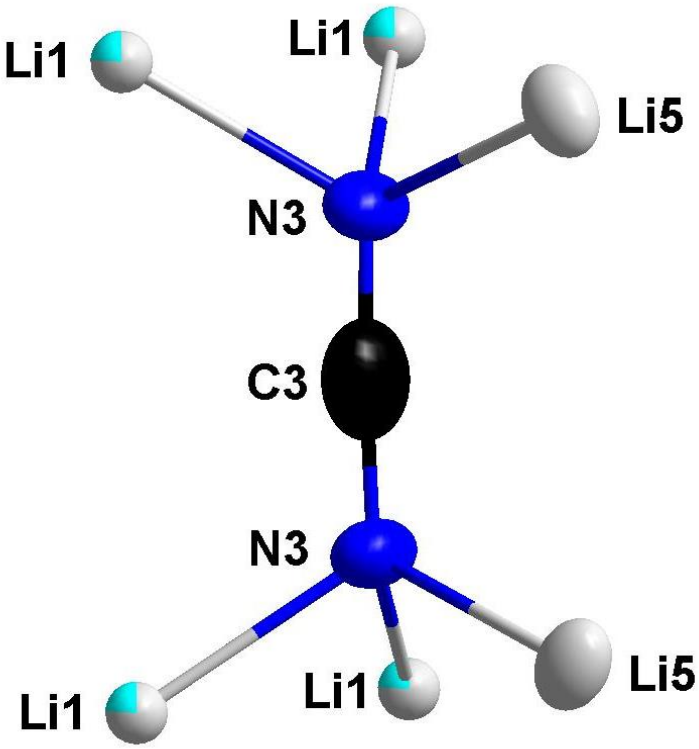

Publication 4

A Mixed-Anion Compound Based Upon a $[Pb_4O_4]$ Heterocubane Unit: Synthesis, Structure and Electronic Properties of $Pb_8O_4I_6(CN_2)$

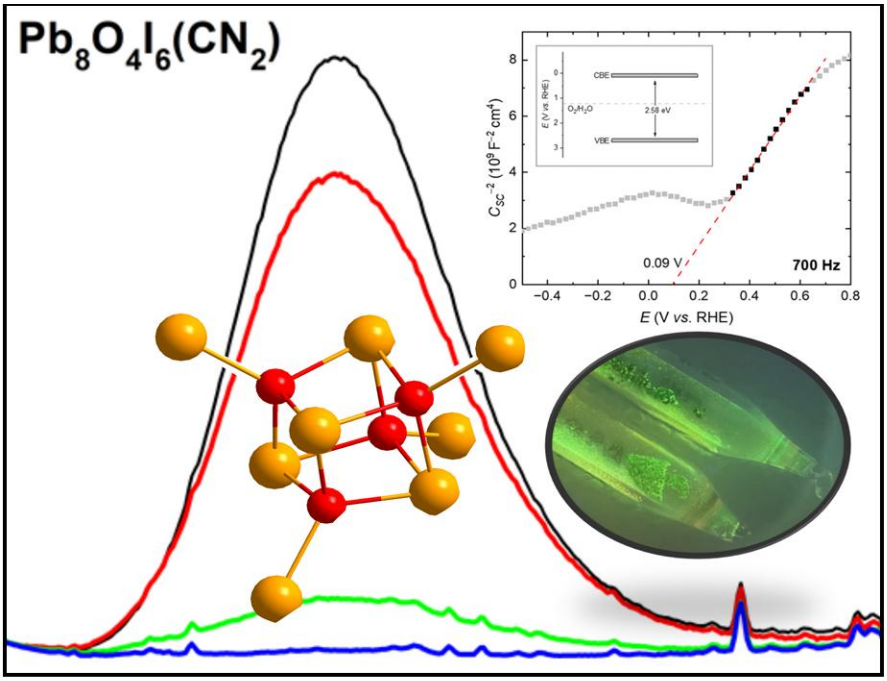

https://doi.org/10.1039/D5DT01979F

Reproduced from

Dalton Trans., **2025**, *54*, 15169-15175

with permission from

Copyright © 2025 The Royal Society of Chemistry

Dalton Transactions

ROYAL SOCIETY OF CHEMISTRY

PAPER

View Article Online
View Journal

Check for updates

Cite this: DOI: 10.1039/d5dt01979f

A mixed-anion compound based upon a $[Pb_4O_4]$ heterocubane unit: synthesis, structure and electronic properties of $Pb_8O_4I_6(CN_2)$

Albert T. Schwarz,[a] Nele Petersen,[c] Markus Ströbele,[a] David Enseling,[b] Thomas Jüstel,[b] Adam Slabon[c] and H.-Jürgen Meyer*[a]

Received 19th August 2025,
Accepted 8th September 2025

DOI: 10.1039/d5dt01979f

rsc.li/dalton

The present study reports the synthesis, crystal structure, and electronic properties of the lead–oxide–iodide–carbodiimde $Pb_8O_4I_6(CN_2)$. The n-type semiconducting compound was obtained *via* ceramic method from PbI_2, PbO and $Pb(CN_2)$, yielding an air stable, dark yellow crystalline material. Single-crystal X-ray diffraction revealed the monoclinic space group *C*2/*c* featuring a heterocubane-type $[Pb_4O_4]$ motif interconnected by iodide bridges and $(NCN)^{2-}$ units. The optical properties were characterized by diffuse reflectance UV-Vis spectroscopy, Mott–Schottky analysis, and photoluminescence spectroscopy, providing insights into the electronic structure.

Open Access Article. Published on 23 September 2025. Downloaded on 10/1/2025 9:03:17 AM.
This article is licensed under a Creative Commons Attribution 3.0 Unported Licence.

Introduction

Over the past decades, the chemistry of metal dinitridocarbonates—commonly referred to as carbodiimides ($(N{=}C{=}N)^{2-}$) or cyanamides ($(N{-}C{\equiv}N)^{2-}$)—has become a dynamic field in solid-state chemistry. This interest is driven by the discovery of structurally diverse compounds exhibiting notable luminescent,[1–6] magnetic,[7–10] and electronic properties.[11–13] Due to their isolobal relationship with chalcogenide anions (O^{2-}, S^{2-}), dinitridocarbonate units can be considered to replace oxide and sulfide anions, enabling the rational design of carbodiimide or cyanamide-based analogues of established oxide and sulfide structures. The electron distribution within the $(NCN)^{2-}$ unit is strongly influenced by the nature and arrangements of surrounding metal atoms. The carbodiimide shape is preferred by hard cations, while the cyanamide form is typically stabilized by softer cations, as anticipated by Pearson's HSAB concept.[14] Dinitridocarbonates based on group 14 elements—including silicon, germanium, tin, and lead—display a wide range of structural patterns and functional properties. These compounds often form extended frameworks composed of tetrahedral or octahedral coordination polyhedra, with the $(NCN)^{2-}$ ligand connecting multiple metal centres.[15–18] Tetracyanamidometallates of the type $[M(CN_2)_4]^{n-}$ (M = Si, Ge) resemble a tetrahedral environment of M atoms, as can be derived from the orthosilicate ion. These compounds are notable for their pronounced photoluminescent properties, second-harmonic generation (SHG) activity, and exceptional thermal as well as hydrolytic stability.[19–23] Tin-based carbodiimides such as $Sn(CN_2)$ and $Sn_2O(CN_2)$ exhibit semiconducting behavior with band gaps near 2.0 eV, and have been investigated as potential materials for energy storage applications, including as electrodes in conversion-type batteries.[24–26] Lead-based carbodiimides display even greater structural complexity. Compounds such as $Pb(CN_2)$, $APb_2Cl_3(CN_2)$ (A = Li, Na, Ag) form extended three-dimensional frameworks consisting of Pb-polyhedra—ranging from trigonal bipyramids and octahedral to more complex arrangements—interconnected by halide and carbodiimide ligands.[1,27,28] In $Pb_7I_6(CN_2)_4$, several Pb-based structural motifs coexist within a layered crystal structure, giving rise to semiconducting behavior with an indirect optical band gap of approximately 2.4 eV. Furthermore, this compound exhibits green photoluminescence at 77 K. Such mixed-anion compounds provide an additional degree of freedom in materials design. In a recent review, Kageyama *et al.* summarized the progress on the synthesis and electronic structure for this class of compounds.[29] Interestingly, the $6s^2$ lone-pair of Pb^{2+} in many carbodiimide-containing compounds appears to be stereochemical inactive or structurally suppressed. By contrast, the influence of the $6s^2$ lone pair becomes prominent in Pb–O-based cluster-like or oxide halide compounds,[30] where low coordination numbers allow its expression. In such systems, Pb^{2+} often adopts pyramidal $[PbO_3]$ coordination, resulting in distinct distortions from ideal geometries. A characteristic example is the occurrence of heterocubane-type $[Pb_4O_4]$ units

[a]*Section for Solid State and Theoretical Inorganic Chemistry, Institute of Inorganic Chemistry, University Tübingen, Auf der Morgenstelle 18, 72076 Tübingen, Germany. E-mail: juergen.meyer@uni-tuebingen.de*
[b]*Department of Chemical Engineering, FH Münster University of Applied Science, Stegerwaldstraße 39, 48565 Steinfurt, Germany*
[c]*Chair of Inorganic Chemistry, University of Wuppertal, Gaußstraße 20, 42119 Wuppertal, Germany*

Open Access Article. Published on 23 September 2025. Downloaded on 10/1/2025 9:03:17 AM. This article is licensed under a Creative Commons Attribution 3.0 Unported Licence.

—comprised of four Pb^{2+} cations and four bridging oxide ions —found in various oxide halides. These building units, characterized by pseudo-tetrahedral geometries and lone-pair-induced distortions, constitute a structurally versatile motif within Pb^{2+} coordination chemistry. In this context, $Pb_8O_4I_6(CN_2)$ represents the first structurally characterized dinitridocarbonate compound with a heterocubane-type $[Pb_4O_4]$ unit, wherein the stereochemically active $6s^2$ lone pair of Pb^{2+} exerts an influence on the local coordination environment.

Results and discussion

Synthesis of $Pb_8O_4I_6(CN_2)$

Although solid-state metathesis (SSM) reactions involving $Li_2(CN_2)$ or $Na_2(CN_2)$ have proven to be efficient and effective methods for the synthesis of a wide range of dinitridocarbonates,[31] the ceramic method,[32] was employed for the preparation of $Pb_8O_4I_6(CN_2)$. This approach involves the homogenization and mechanical grinding of the starting materials PbI_2, PbO, and $Pb(CN_2)$ in a stoichiometric ratio of 3 : 4 : 1 according to reaction (1). The resulting mixture is then subjected to elevated temperatures, yielding $Pb_8O_4I_6(CN_2)$ as a dark yellow powder in high yield. Minor amounts of elemental lead were detected as a side-phase (Fig. 1). Powder XRD confirmed the compound's stability under ambient air and humidity after five days.

$$3PbI_2 + 4PbO + Pb(CN_2) \rightarrow Pb_8O_4I_6(CN_2) \quad (1)$$

An analysis by energy-dispersive X-ray spectroscopy (EDX) on seven distinct points on different single crystals resulted in a lead to iodine ratio of 8 : 5.92(2), thus confirming the Pb : I ratio of $Pb_8O_4I_6(CN_2)$ determined by single-crystal XRD.

Crystal structure

The crystal structure of $Pb_8O_4I_6(CN_2)$ was solved and refined by single-crystal X-ray diffraction (XRD) with monoclinic space group $C2/c$. Some selected crystal structure and refinement data are given in Table 1.

The single-crystal refinement revealed the presence of four crystallographically distinct lead positions with unique environments. As demonstrated in Fig. 2, the lead sites Pb1 and Pb2 are surrounded by three oxygen and two iodine atoms for Pb1, and by three iodine atoms for Pb2. The position of Pb3 represents a surrounding with five iodine atoms, one oxygen atom and one $(NCN)^{2-}$ unit. Moreover, the coordination environment of Pb4 comprises four iodine atoms, one oxygen atom, and one $(NCN)^{2-}$ unit. There is one crystallographic $(NCN)^{2-}$ unit present in the structure, where both nitrogen atoms in the $(NCN)^{2-}$ unit are surrounded by two lead atoms (Pb3 and Pb4) each, including Pb–N bond lengths of d_{Pb3-N} = 2.583(4) Å and d_{Pb4-N} = 2.493(4) Å, which are comparable to corresponding Pb–N distances in related lead compounds $Pb_7I_6(CN_2)_4$,[1] $PbCN_2$,[27] $LiPb_2Cl_3(CN_2)$ and LiPbCl (CN_2).[28] The $(NCN)^{2-}$ unit adopts a nearly linear geometry with an N–C–N angle of 179.4(7)° with an identical C–N bond

Table 1 Selected crystal and structure refinement data for $Pb_8O_4I_6(CN_2)$ measured at 150 K

Empirical formula	$Pb_8O_4I_6(CN_2)$
CCDC code	2389167
Formula weight (g mol^{-1})	2522.95
Wavelength (Mo-K$_\alpha$)	0.71073
Crystal system	Monoclinic
Space group	$C2/c$
Unit cell dimensions (Å)	a = 18.8050(5)
	b = 8.13080(1)
	c = 16.1378(4)
	β = 114.053(3)
Volume (Å^3)	2253.21(1)
Z	4
Calculated density (g cm^{-3})	7.437
Absorption coefficient (mm^{-1})	67.772
Final R indices ($I > 2\sigma(I)$)	R_1 = 0.0108, wR_2 = 0.0214
R indices (all data)	R_1 = 0.0113, wR_2 = 0.0215
GooF	1.222

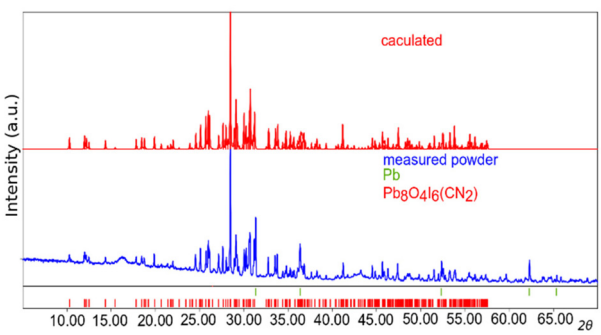

Fig. 1 Recorded powder X-ray diffraction pattern of $Pb_8O_4I_6(CN_2)$ (blue) in comparison with the calculated pattern from the single-crystal refinement (red) and the Bragg positions of the compound (red). Elemental lead appears as a side-phase, shown with its Bragg positions with green color.

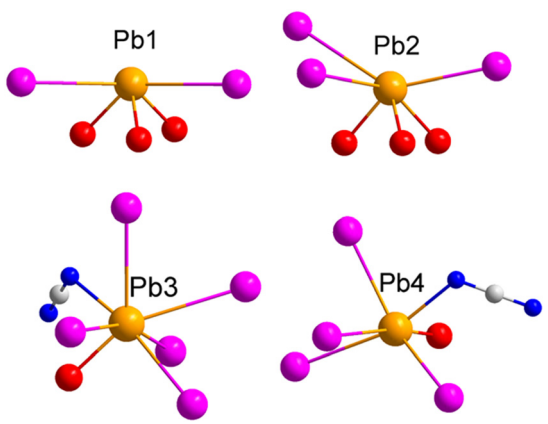

Fig. 2 Coordination environments of four distinct lead positions in $Pb_8O_4I_6(CN_2)$. Iodine atoms are shown in purple, oxygen in red, carbon in white, and nitrogen in blue.

This journal is © The Royal Society of Chemistry 2025

Open Access Article. Published on 23 September 2025. Downloaded on 10/1/2025 9:03:17 AM. This article is licensed under a Creative Commons Attribution 3.0 Unported Licence.

lengths of 1.223(4) Å as a result of a crystallographic twofold rotation axis passing through the central carbon atom. Infrared spectroscopic data (Fig. S1) further confirm the symmetric nature of the carbodiimide unit, revealing the characteristic deformation vibration at 638 cm^{-1} and the asymmetric stretching vibration at 1908 cm^{-1}. A notable feature in the crystal structure of $Pb_8O_4I_6(CN_2)$ is the presence of $[Pb_4O_4]$ unit, resembling the motif of carbon atoms in the cubane structure (C_8H_8) (Fig. 3). In the heterocubane arrangement, each oxygen atom adopts a tetrahedral coordination environment with four lead atoms, including the Pb3 and Pb4 atoms, exhibiting Pb–O bond distances between 2.272(3) Å and 2.382 (3) Å. The Pb positions Pb1 and Pb2 at the corners of the heterocubane adopts pyramidal (PbO_3) geometries, suggesting a localization of the $6s^2$ lone pair of Pb^{2+}. The described Pb–O motif is connected through iodide bridges and $(NCN)^{2-}$ units, with the iodide-bridged heterocubane units being related by a center of symmetry ($\bar{1}$) (Fig. 4 and 5). Such $[Pb_4O_4]$ motifs and coordination patterns have also been observed in lead oxide halide alcoholates[30] and tin oxide halides.[33] In these lead oxide halide alcoholates, however, the heterocubane cores consist of four oxygen atoms, two of which two are from alkoxide groups (OR^-). In contrast, the heterocubane units in $Pb_8O_4I_6(CN_2)$ are composed exclusively of oxide ions.

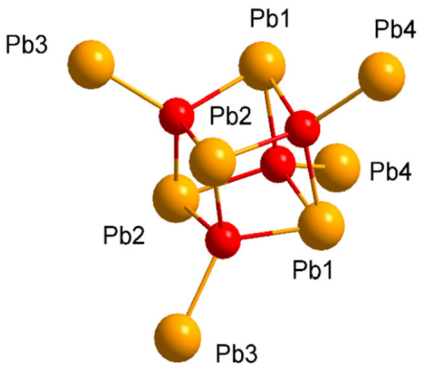

Fig. 3 The heterocubane motif with surrounding lead atoms (Pb3 and Pb4) in the structure of $Pb_8O_4I_6(CN_2)$.

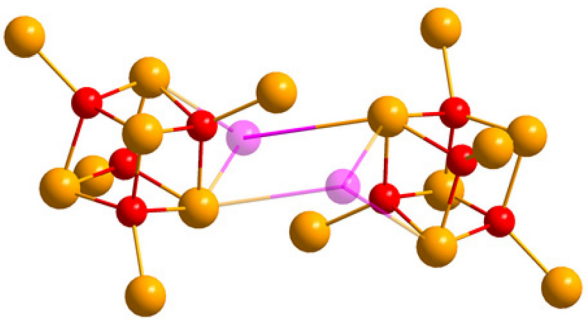

Fig. 4 Section of two iodine-bridged heterocubanes, interconnected by a center of symmetry ($\bar{1}$).

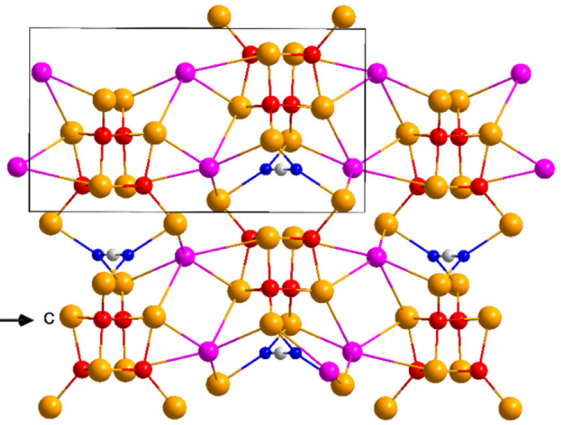

Fig. 5 Representation of the atomic arrangement within a single layer of the $Pb_8O_4I_6(CN_2)$ structure.

Notably, in α-$Pb_6(C_4H_8O_3)O_2I_6$ a comparable arrangement is observed, where the heterocubane units are linked by two diethylene glycolate ligands instead and exhibit an analogous symmetrical relationship ($\bar{1}$). In the aforementioned lead oxide alcoholates, the lead atoms predominantly adopt pyramidal PbO_3 coordination geometries, with an average Pb–O bond length of 2.318 Å, which aligns well with the values observed in $Pb_8O_4I_6(CN_2)$. A comparison of the overall structures of α-$Pb_6(C_4H_8O_3)O_2I_6$ and $Pb_8O_4I_6(CN_2)$ reveals distinct differences in the connectivity of the $[Pb_4O_4]$ units. In the lead alcoholate compound, the $[Pb_4O_4]$ units are arranged in one-dimensional chain-like assemblies that extend into layers within the unit cell. In the crystal structure of $Pb_8O_4I_6(CN_2)$, one type of layer extends within the *bc*-plane and consists of chains running along the *b*-axis, composed of alternating $[Pb_4O_4]$ units and $(NCN)^{2-}$ ligands. Along the *c*-axis, these $[Pb_4O_4]$ units are interconnected by iodide bridges, forming a two-dimensional heterocubane-based network (Fig. 5). Alternating with these layers are planes composed exclusively

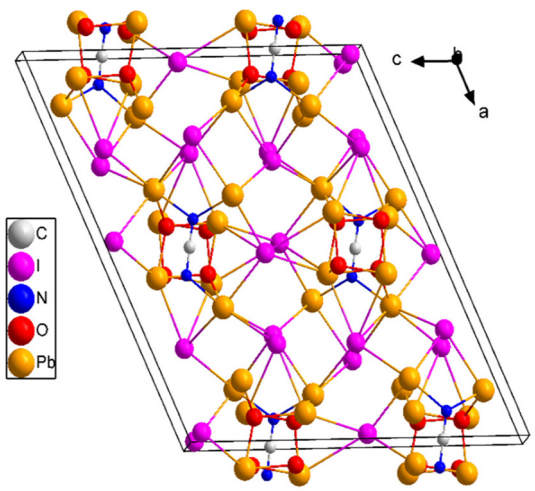

Fig. 6 Unit cell of the compound $Pb_8O_4I_6(CN_2)$.

Open Access Article. Published on 23 September 2025. Downloaded on 10/1/2025 9:03:17 AM.
This article is licensed under a Creative Commons Attribution 3.0 Unported Licence.

of iodide ions. Together, these two types of layers stack along the *a*-axis to form the overall layered structure of the compound (Fig. 6). Heterocubane clusters of the type $[Pb_4(OH)_4]^{4+}$ are quite common in aqueous lead(II) chemistry. They appear in the presence of weakly coordinating ligands, for example in $[Pb_4(OH)_4][NO_3]_4$,[34] whereas neutral $[Pb_4O_4]$ species, as in $[Pb_4O_4]Pb_4I_6(CN_2)$ remain less common.

Electronic structure and photoelectrochemistry

In order to determine the band gap of $Pb_8O_4I_6(CN_2)$, the Tauc method was employed in accordance with the following equation:

$$(\alpha \cdot h\nu)^{1/\beta} = A(h\nu - E_g)$$

where α is the absorption coefficient, E_g is the optical band gap, $h\nu$ is the photon energy with the frequency ν, h is the Planck constant, and A is a material-related constant.[35] The Kubelka Munk relation was used to determine the absorption coefficient α.[36] The material exhibits indirect and direct band gaps of 2.58 eV and 2.63 eV, respectively (Fig. S2 and S3). This would render the compound a candidate for use as photoanode in the water oxidation process. Therefore, Mott–Schottky (MS) experiments were conducted to ascertain the semiconducting type and the band edge positions. It is evident from the measured curves (Fig. S4) that they all exhibit a positive slope, thus indicating that $Pb_8O_4I_6(CN_2)$ is an n-type semiconductor. The semiconductor type and the photoactivity was further confirmed by interrupted AM 1.5G illumination (quantum design), as irradiation led to an increase of the measured current density with subsequent decrease to the baseline after switching off the irradiation (Fig. S5). The dark current contribution originates most likely from the photocorrosion, because no passivating layer, *e.g.* amorphous sub-stoichiometric titania, has been applied; a phenomenon known for nitrogen-containing photoanodes.[37,38] The extrapolation of the measured data recorded at 700 Hz yields a flat-band potential of 0.09 V *vs.* reversible hydrogen electrode (RHE) (Fig. 7). For n-type semiconductors, the given potential is close to the conduction band edge (CBE) position. Considering the determined band gaps, the valence band edge (VBE) is positions at 2.67 eV (indirect) and 2.72 eV (direct). The compound exhibits a VBE that is more positive than 1.23 V *vs.* RHE, suggesting its potential as a photoanode for the oxygen evolution reaction (OER).[24,39] The stability of the material under electrochemical conditions was confirmed by cyclic voltammetry before and after the MS measurements. The resulting cyclic voltammogram displays a stable hysteresis, thus confirming the compound's stability (Fig. S6).

Photoluminescence properties

Compounds comprising Pb^{2+} are well known for their intense and long-term stable photoluminescence.[40–44] The high stability of $Pb_8O_4I_6(CN_2)$ in air and against relative humidity, in combination with the straightforward synthesis of the compound, leads to its consideration as a promising material for application in fluorescent light sources or optical marker. Therefore, an investigation of its photoluminescence properties was carried out.

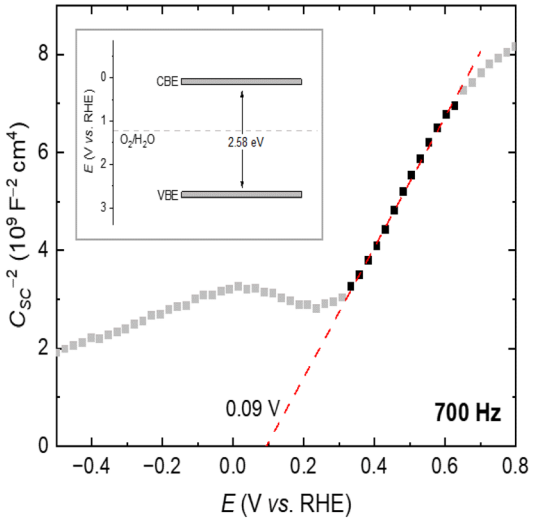

Fig. 7 Mott–Schottky plot of $Pb_8O_4I_6(CN_2)$ on FTO substrate in 0.1 M KPi–electrolyte (Sørensen) with pH 7.0 at a frequency of 700 Hz. Inserted is a schematic representation of the energy levels for $Pb_8O_4I_6(CN_2)$.

As demonstrated in Fig. 8, the emission spectrum was observed for the purposes of monitoring the 377 nm excitation at 80 K, resulting in a broad band peaking at 520 nm (19 200 cm^{-1}). The excitation spectrum was observed for monitoring the 520 nm emission at 80 K. As was the case in the preceding research, including the compound $Pb_7I_6(CN_2)_4$,[1] the excitation spectrum is a superposition of three sub-bands peaking at 310 nm (32 300 cm^{-1}), 333 (30 000 cm^{-1}) nm and 376 nm (26 600 cm^{-1}). In order to interpret the excitation and emission spectrum, it is necessary to understand that Pb^{2+} is considered to be an impurity ion of the ns^2 type, with the ground state ($^1S_0$) in the $6s^2$ electronic configuration and the

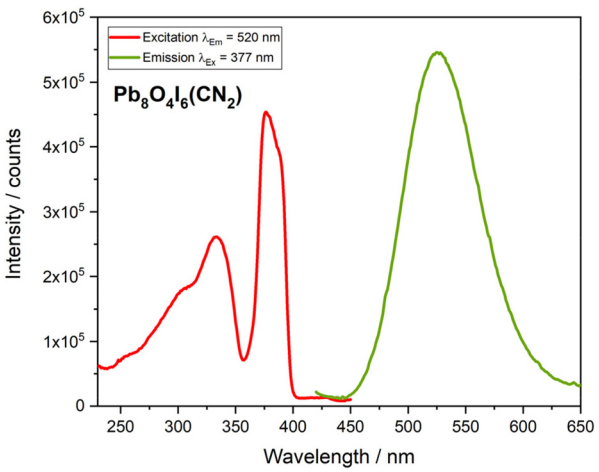

Fig. 8 Excitation and emission spectra of $Pb_8O_4I_6(CN_2)$ at 80 K.

This journal is © The Royal Society of Chemistry 2025

Open Access Article. Published on 23 September 2025. Downloaded on 10/1/2025 9:03:17 AM.
This article is licensed under a Creative Commons Attribution 3.0 Unported Licence.

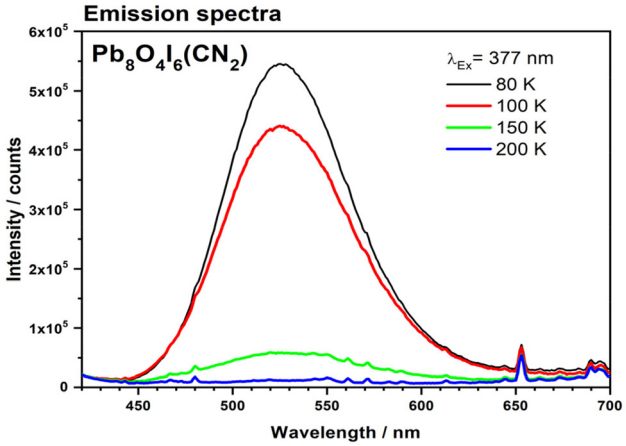

Fig. 9 Temperature dependent emission spectra of $Pb_8O_4I_6(CN_2)$ upon 377 nm excitation between 80 and 200 K.

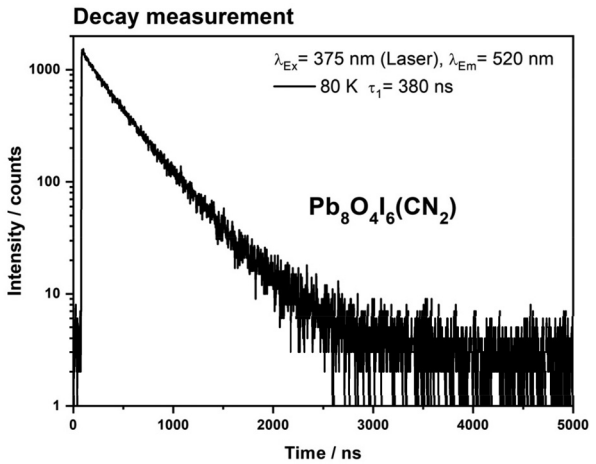

Fig. 10 Decay curve monitored for the 525 nm emission of $Pb_8O_4I_6(CN_2)$ upon 375 nm excitation at 80 K.

first excited state in the $6s^1p^1$ electronic configuration. The first excited state splits into four states consisting of three triplet ($^3P_0$, $^3P_1$, $^3P_2$) and a single state ($^1P_1$). The excitation band observed in the spectrum peaking at 310 nm, 333 nm, and 376 nm can be assigned to the transitions from the ground state $^1S_0$ to the three excited states $^3P_0$, $^3P_1$, $^3P_2$ of Pb^{2+} The emission band can be assigned to the $^3P_1$–$^1S_0$ transition, which is almost completely quenched at 150 K (Fig. 9). The decay curve of the photoluminescence at 80 K (Fig. 10) shows a mono-exponential behavior with a decay time of about $\tau_{1/c}$ = 380 ns.

Conclusions

The reaction between lead cyanamid, lead oxide and lead iodide resulted in the formation of the new $Pb_8O_4I_6(CN_2)$, as confirmed by PXRD and EDX analysis. The compound features a heterocubane-like $[Pb_4O_4]$ motif interconnected *via* iodide bridges and carbodiimide units. The material demonstrates chemical and structural stability under ambient conditions. Optical and electrochemical measurements reveal an indirect band gap of 2.58 eV, a direct band gap of 2.63 eV, and n-type semiconducting behavior with a flat-band potential conducive to water oxidation. Moreover, photoluminescence of $Pb_8O_4I_6(CN_2)$ at low temperatures was confirmed by photoluminescence spectroscopy. The straight forward synthesis and the air-stability of $Pb_8O_4I_6(CN_2)$ emphasize its potential as a photoactive material for photoelectrochemical applications and as a luminescent compound for optical technologies.

Experimental section and calculation details

Preparation of $Pb_8O_4I_6(CN_2)$

Crystalline powders of $PbCN_2$ (synthesized as described in the literature[45]), PbI_2 (purchased from Sigma-Aldrich, 99.999% purity) and PbO (purchased from Sigma-Aldrich, 99.999% purity) were mixed in a glove box under dry argon atmosphere in a 3 : 1 : 4 molar ratio. The reaction mixture was then transferred into a silica ampoule and sealed under vacuum. The ampoule was then heated in a crucible furnace at 420 °C at a heating and cooling rate of 2 K min^{-1} for a duration of five days. The reaction product was obtained as a dark yellowish powder, with an estimated yield of 90%, and elemental lead as a side phase.

Synthesis of $Pb_8O_4I_6(CN_2)$ thin film on FTO

The FTO glass was first thoroughly washed with water and acetone. For EPD, a suspension was prepared by dissolving 20 mg of iodine in 20 mL of acetone. Subsequently, approx. 100 mg of $Pb_8O_4I_6(CN_2)$ powder was added to the solution. The mixture was sonicated for 60 min at room temperature to obtain small particles and ensure homogeneity of the suspension. The EPD cell consisted of FTO glass as conductive substrate connected as the working electrode (negative terminal) and a platinum wire as the counter electrode (positive terminal). The electrodes were positioned parallel to each other at a fixed distance. A voltage of 45 V was applied to the system using a Voltcraft HPS-16010 power supply. The resulting coated FTO glass was gently rinsed with water and acetone to remove loose particles and the electrode was dried at room temperature overnight.

Single-crystal XRD

Single-crystal XRD studies were performed using a Rigaku XtaLab Synergy-S diffractometer with monochromatic Mo-Kα (λ = 0.71073 Å) radiation and a mirror monochromator. Measurements were conducted under N_2 cooling at 150 K. Corrections for absorption effects of the X-ray intensities were applied with a numerical method using CrysAlisPro 1.171.43.121 (Rigaku Oxford Diffraction, 2024).[46] The structure was solved by ShelXT (Sheldrick, 2008)[47] The model was refined with ShelXL 2019/3 (Sheldrick, 2015)[48] using full

Open Access Article. Published on 23 September 2025. Downloaded on 10/1/2025 9:03:17 AM. This article is licensed under a Creative Commons Attribution 3.0 Unported Licence.

matrix least squares implemented in Olex2 1.5-ac5-024 (Dolomanov *et al.*, 2009).[49]

Powder XRD

The powder samples were analysed using an X-ray powder diffractometer (STOE Darmstadt, STADI-P, Ge-monochromator) with Cu-Kα_1 radiation (λ = 154.0598 pm) in the 2θ range between 5° to 70°.

IR-spectroscopy

Infrared spectra were recorded using a VERTEX 70 FT-IR Spectrometer in the range of 400 cm^{-1} to 4000 cm^{-1} using KBr pellets of $Pb_8O_4I_6(CN_2)$. Samples were prepared in a glove-box under Argon atmosphere.

Photoluminescence spectroscopy

Excitation and emission spectra of $Pb_8O_4I_6(CN_2)$ sample were recorded using a fluorescence spectrometer FLS920 (Edinburgh Instruments) equipped with a 450 W xenon discharge lamp (OSRAM) as the radiation source. For powder samples a mirror optic was mounted inside the sample chamber. For the collection of data, a R2658P single-photon-counting photomultiplier tube from Hamamatsu was used. For temperature adjustment a cryostat "MicrostatN" from the company Oxford Instruments had been applied to the present spectrometer. Liquid nitrogen was used as a cooling agent. The photoluminescence decay curve was also measured on the FLS920 spectrometer, while a 375 nm ps laser diode from Edinburgh Instruments was used as an excitation source.

UV-Vis in diffuse reflectance

The reflectance spectra were recorded on an OceanOptics Maya 2000 Pro spectrometer equipped with a Harrick praying mantis sample chamber. A deuterium tungsten lamp (DH 200 BAL) from OceanOptics was used as the light source. The measurement was performed with the following settings: scan to average = 100, boxcar width = 10 and integration time = 300 ms using OceanView 1.6.7 (lite) software from OceanOptics. To determine the optical band gap E_g, the Tauc equation was used: $(\alpha \cdot h\nu)^{1/r} = A(h\nu - E_g)$, where α is the absorption coefficient, h is the Planck constant, A is a material related constant and $h\nu$ is the photon energy. For a direct allowed bandgap transition, r = 1/2, and for an indirect allowed bandgap transition, r = 2.

EDX measurements

The energy dispersive X-ray spectroscopy (EDX) was performed with a Hitachi SU8030 scanning electron microscope equipped with a Bruker QUANTAX 6G EDX detector.

Photoelectrochemistry

Mott–Schottky (MS) measurements were performed with a BioLogic SP-300 potentiostat using a three-electrode setup and floating ground. The prepared electrode was used as working electrode, a platinum wire was used as counter electrode and an Ag/AgCl electrode in saturated KCl was used as reference electrode. The measured potential was recorded *vs.* $E_{Ag/AgCl\ (KCl\ sat.)}$ (V) and then converted to the reversible hydrogen electrode (RHE) E_{RHE} (V) according to E_{RHE} (V) = 0.197 + $E_{Ag|AgCl|KCl\ sat}$ + (0.059·pH) at 25 °C. The measurements were performed in a potassium phosphate buffer (0.1 M KPi) as electrolyte pH 7 in the dark at an AC amplitude of 10 mV with frequencies in the decadic distant range of 0.7 Hz to 700 Hz, to determine the band edge E_{FB}.

Chronoamperometry (CA) was performed at 0 V *vs.* RHE to again determine whether $Pb_8O_4I_6(CN_2)$ exhibits p-type or n-type behaviour by applying an AM 1.5G illumination at 100 mW cm^{-2} to the electrode and interrupting the illumination every 30 seconds for 30 seconds. The measurement was started in the dark.

Capacitance measurement according to the MS function

$$\frac{1}{{C_{sc}}^2} = \frac{2}{A^2 \varepsilon \varepsilon_0 q N_D}\left(E - E_{FB} - \frac{k_b T}{q}\right)$$

In the equation, C_{SC} is determined to be the capacitance in the space-charge-layer, ε is the dielectric constant of the material, A is the interfacial area of electrode and electrolyte, the permittivity of free space is ε_0, q is the electronic charge, N_D is the donor density, E is the potential that is applied, k_b the Boltzmann's constant, T is the absolute temperature, and E_{FB} is the flat-band potential. E_{FB} and $2/(A^2\varepsilon\varepsilon_0 q N_D)$ can be determined using a plot of $1/{C_{SC}}^2$ against E from the x-axis intercept and the slope of the linear region, respectively. The type of semiconductor can be identified by the slope of $2/(A^2\varepsilon\varepsilon_0 q N_D)$ being positive for an n-type or negative for a p-type. The obtained results for E_{FB} correspond approximately to the conducting band edge, E_{CB}, of an n-type or to the valence band edge, E_{VB}, of a p-type semiconductor respectively. When one of the potentials (E_{VB} or E_{CB}) is defined, the respective other potential can be deduced based on $E_g = E_{VB} - E_{CB}$.

Conflicts of interest

The authors declare no conflict of interest.

Data availability

The data that support the findings of this study are available in the SI. Supplementary information is available. See DOI: https://doi.org/10.1039/d5dt01979f.

CCDC 2389167 contains the supplementary crystallographic data for this paper.[50]

Acknowledgements

We gratefully acknowledge the support provided by the Deutsche Forschungsgemeinschaft (DFG-Bonn) for this research project (ME 914/34-1).

This journal is © The Royal Society of Chemistry 2025

Open Access Article. Published on 23 September 2025. Downloaded on 10/1/2025 9:03:17 AM. This article is licensed under a Creative Commons Attribution 3.0 Unported Licence.

References

1 A. T. Schwarz, M. Ströbele, C. P. Romao, D. Enseling, T. Jüstel and H.-J. Meyer, *Dalton Trans.*, 2024, **53**, 6416–6422.
2 D. Dutczak, A. Siai, M. Ströbele, D. Enseling, T. Jüstel and H.-J. Meyer, *Eur. J. Inorg. Chem.*, 2020, **2020**, 3954–3958.
3 C.-D. Brand, M. Ströbele, D. Enseling, T. Jüstel and H.-J. Meyer, *J. Cluster Sci.*, 2024, **35**, 101–107.
4 A. Siai, C.-D. Brand, M. Ströbele, D. Enseling, T. Jüstel and H.-J. Meyer, *J. Cluster Sci.*, 2023, **34**, 1001–1008.
5 Y.-C. Wu, T.-M. Chen, C.-H. Chiu and C.-N. Mo, *J. Electrochem. Soc.*, 2010, **157**, J342.
6 M. Krings, G. Montana, R. Dronskowski and C. Wickleder, *Chem. Mater.*, 2011, **23**, 1694–1699.
7 M. Li, P. Zhang and X. Wei, *J. Phys. Chem. Solids*, 2016, **98**, 123–127.
8 X. Liu, M. Krott, P. Müller, C. Hu, H. Lueken and R. Dronskowski, *Inorg. Chem.*, 2005, **44**, 3001–3003.
9 M. Krott, X. Liu, B. P. T. Fokwa, M. Speldrich, H. Lueken and R. Dronskowski, *Inorg. Chem.*, 2007, **46**, 2204–2207.
10 X. Liu, L. Stork, M. Speldrich, H. Lueken and R. Dronskowski, *Chem. – Eur. J.*, 2009, **15**, 1558–1561.
11 M. Löber, C. S. Geißenhöner, M. Ströbele, S. Indris, C. P. Romao and H.-J. Meyer, *Inorg. Chem.*, 2019, **58**, 14560–14567.
12 X. Qiao, Z. Ma, D. Luo, A. J. Corkett, A. Slabon, A. Rokicinska, P. Kuśtrowski and R. Dronskowski, *Dalton Trans.*, 2020, **49**, 14061–14067.
13 M. Davi, M. Mann, Z. Ma, F. Schrader, A. Drichel, S. Budnyk, A. Rokicinska, P. Kustrowski, R. Dronskowski and A. Slabon, *Langmuir*, 2018, **34**, 3845–3852.
14 R. G. Pearson, *J. Am. Chem. Soc.*, 1963, **85**, 3533–3539.
15 X. Meng, F. Liang, W. Yin, Z. Lin and M. Xia, *New J. Chem.*, 2019, **43**, 9766–9770.
16 R. Riedel, A. Greiner, G. Miehe, W. Dressler, H. Fuess, J. Bill and F. Aldinger, *Angew. Chem., Int. Ed. Engl.*, 1997, **36**, 603–606.
17 M. Kubus, J. Glaser, A. Kłonkowski and H.-J. Meyer, *Z. Anorg. Allg. Chem.*, 2010, **636**, 991–995.
18 M. Löber, M. Ströbele, C. P. Romao and H.-J. Meyer, *Eur. J. Inorg. Chem.*, 2021, **2021**, 4572–4578.
19 K. D. Röseler, K. Eichele, M. Ströbele and H.-J. Meyer, *Eur. J. Inorg. Chem.*, 2024, **27**, 1–6.
20 J. Glaser and H.-J. Meyer, *Angew. Chem.*, 2008, **120**, 7658–7661.
21 K. Dolabdjian, C. Schedel, D. Enseling, T. Jüstel and H.-J. Meyer, *Z. Anorg. Allg. Chem.*, 2017, **643**, 488–494.
22 D. Dutczak, M. Ströbele, D. Enseling, T. Jüstel and H.-J. Meyer, *Eur. J. Inorg. Chem.*, 2016, **2016**, 4011–4016.
23 J. Glaser, H. Bettentrup, T. Jüstel and H.-J. Meyer, *Inorg. Chem.*, 2010, **49**, 2954–2959.
24 Z. Chen, M. Löber, A. Rokicińska, Z. Ma, J. Chen, P. Kuśtrowski, H.-J. Meyer, R. Dronskowski and A. Slabon, *Dalton Trans.*, 2020, **49**, 3450–3456.
25 M. Löber, K. Dolabdjian, M. Ströbele, C. P. Romao and H.-J. Meyer, *Inorg. Chem.*, 2019, **58**, 7845–7851.
26 K. Dolabdjian, A. L. Görne, R. Dronskowski, M. Ströbele and H.-J. Meyer, *Dalton Trans.*, 2018, **47**, 13378–13383.
27 X. Liu, A. Decker, D. Schmitz and R. Dronskowski, *Z. Anorg. Allg. Chem.*, 2000, **626**, 103.
28 K. Dolabdjian and H.-J. Meyer, *Z. Anorg. Allg. Chem.*, 2017, **643**, 1898–1903.
29 H. Kageyama, H. Ogino, T. Zhu and T. Hasegawa, *Mixed-anion Compounds*, Royal Society of Chemistry, 2024.
30 T. Oldag and H.-L. Keller, *Z. Anorg. Allg. Chem.*, 2006, **632**, 1267–1272.
31 H.-J. Meyer, *Dalton Trans.*, 2010, **39**, 5973–5982.
32 C. N. R. Rao and K. Biswas, *Essentials of Inorganic Materials Synthesis*, Wiley, New Jersey, 2015, pp. 17–21.
33 M. Löber, C. S. Geißenhöner, M. Ströbele, C. P. Romao and H.-J. Meyer, *Eur. J. Inorg. Chem.*, 2021, **2021**, 283–288.
34 S. M. Grimes, S. R. Johnston and I. Abrahams, *J. Chem. Soc., Dalton Trans.*, 1995, 2081–2086.
35 P. Makuła, M. Pacia and W. Macyk, *J. Phys. Chem. Lett.*, 2018, **9**, 6814–6817.
36 W. W. Wesley and H. G. Hecht, *Reflectance Spectroscopy*, Wiley, New York, NY, USA, 1966, p. 298.
37 C. Lu, J. Chen, K. Piętak, A. Rokicińska, P. Kuśtrowski, R. Dronskowski, J. Yuan, S. Budnyk, S. Złotnik, R. H. Coridan and A. Slabon, *Chem. Mater.*, 2022, **34**, 6902–6911.
38 Z. Ma, T. Thersleff, A. L. Görne, N. Cordes, Y. Liu, S. Jakobi, A. Rokicinska, Z. G. Schichtl, R. H. Coridan, P. Kustrowski, W. Schnick, R. Dronskowski and A. Slabon, *ACS Appl. Mater. Interfaces*, 2019, **11**, 19077–19086.
39 T. R. Harris-Lee, F. Marken, C. L. Bentley, J. Zhang and A. L. Johnson, *EES Catal.*, 2023, **1**, 832–873.
40 H. Folkerts, M. Hamstra and G. Blasse, *Chem. Phys. Lett.*, 1995, **246**, 135–138.
41 H. F. Folkerts and G. Blasse, *J. Mater. Chem.*, 1995, **5**, 273–276.
42 H. Folkerts and G. Blasse, *Chem. Mater.*, 1994, **6**, 969–972.
43 M. Yılmaz and E. Erdoğmuş, *J. Lumin.*, 2020, **218**, 116868.
44 P. Yang, M. K. Lü, C. F. Song, S. W. Liu, F. Gu and S. F. Wang, *Inorg. Chem. Commun.*, 2004, **7**, 268–270.
45 X. Liu, A. Decker, D. Schmitz and R. Dronskowski, *Z. Anorg. Allg. Chem.*, 2000, **626**, 103–105.
46 *CrysAlisPro Software System*, Rigaku Oxford Diffraction, 2024.
47 G. M. Sheldrick, *Acta Crystallogr., Sect. A: Found. Crystallogr.*, 2008, **64**, 112–122.
48 G. M. Sheldrick, *Acta Crystallogr., Sect. C: Struct. Chem.*, 2015, **71**, 3–8.
49 O. V. Dolomanov, L. J. Bourhis, R. J. Gildea, J. A. K. Howard and H. Puschmann, *J. Appl. Crystallogr.*, 2009, **42**, 339–341.
50 A. T. Schwarz, N. Petersen, M. Ströbele, D. Enseling, T. Jüstel, A. Slabon and H.-J. Meyer, CCDC 2389167: Experimental Crystal Structure Determination, 2025, DOI: **10.5517/ccdc.csd.cc2l63xv**.

Supplementary Information (SI) for Dalton Transactions.
This journal is © The Royal Society of Chemistry 2025

A Mixed-Anion Compound based upon a $[Pb_4O_4]$ Heterocubane Unit: Synthesis, Structure and Electronic Properties of $Pb_8O_4I_6(CN_2)$

Albert T. Schwarz,[a] Nele Petersen,[c] Markus Ströbele,[a] David Enseling,[b] Thomas Jüstel,[b] Adam Slabon[c] and H.-J. Meyer [*a]

Corresponding Author

*Prof. Dr. H.-Jürgen Meyer
Section for Solid State and Theoretical Inorganic Chemistry
Institute of Inorganic Chemistry
University of Tübingen
Auf der Morgenstelle 18
72076 Tübingen

E-mail: juergen.meyer@uni-tuebingen.de

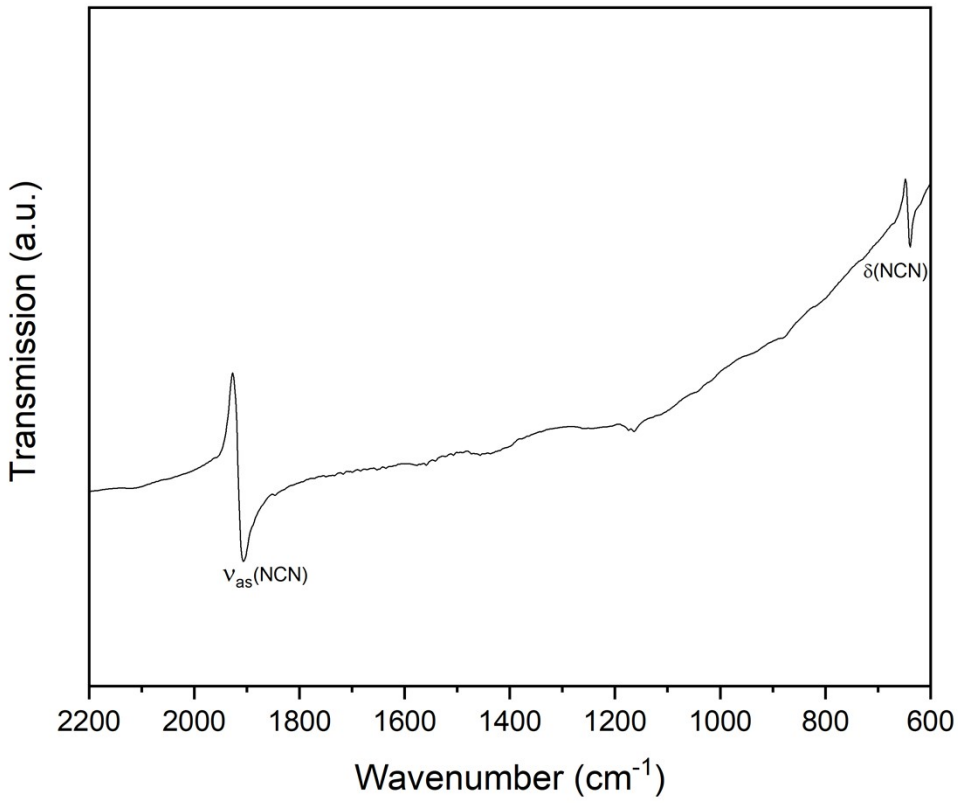

Figure S 1: Infrared measurement of $Pb_8O_4I_6(CN_2)$.

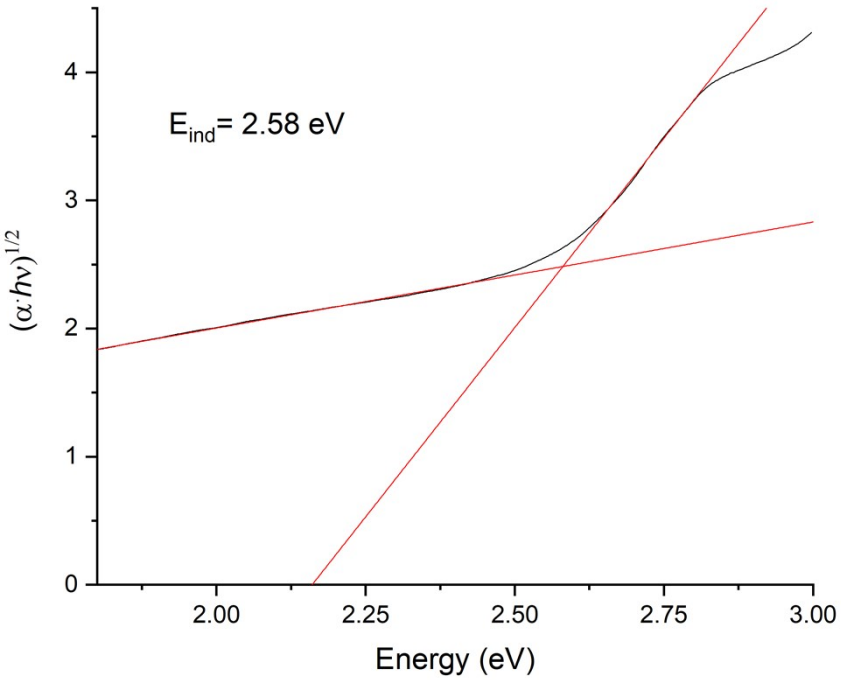

Figure S 2: Tauc plot for indirect allowed transition of the compound $Pb_8O_4I_6(CN_2)$.

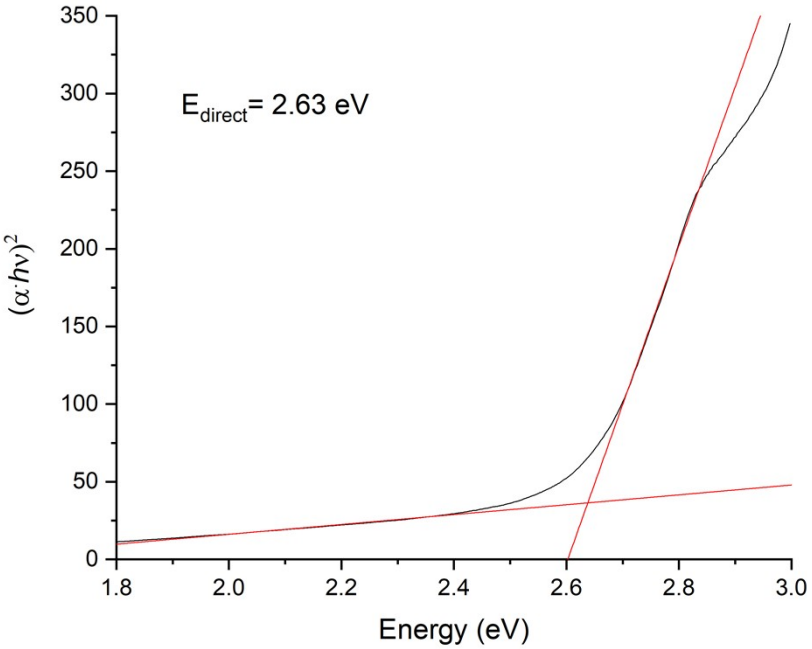

Figure S 3: Tauc plot for direct allowed transition of the compound $Pb_8O_4I_6(CN_2)$.

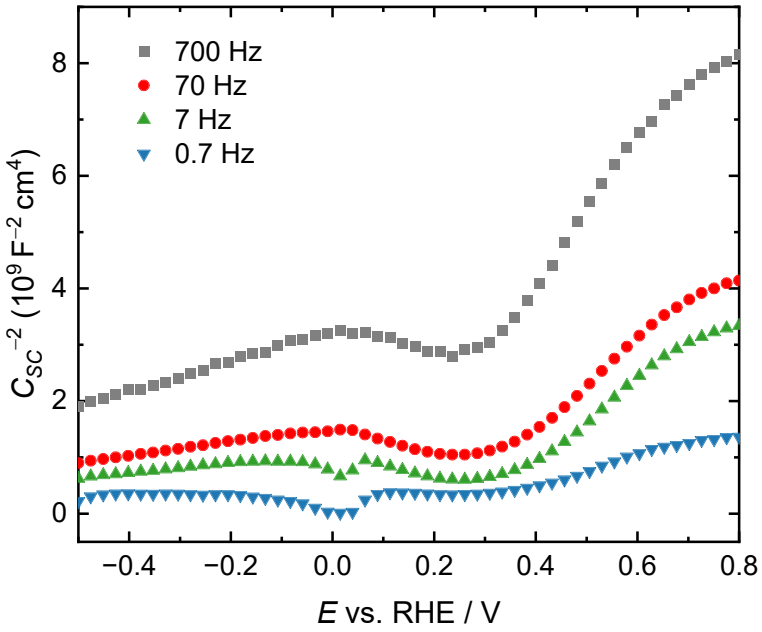

Figure S 4: Mott-Schottky plot of $Pb_8O_4I_6(CN_2)$ on FTO substrate in 0.1M KPi-electrolyte (Sørensen) with pH 7.0 at frequencies of 0.7 Hz (blue triangle), 7 Hz (green triangle), 70 Hz (red circle) and 700 Hz (grey square).

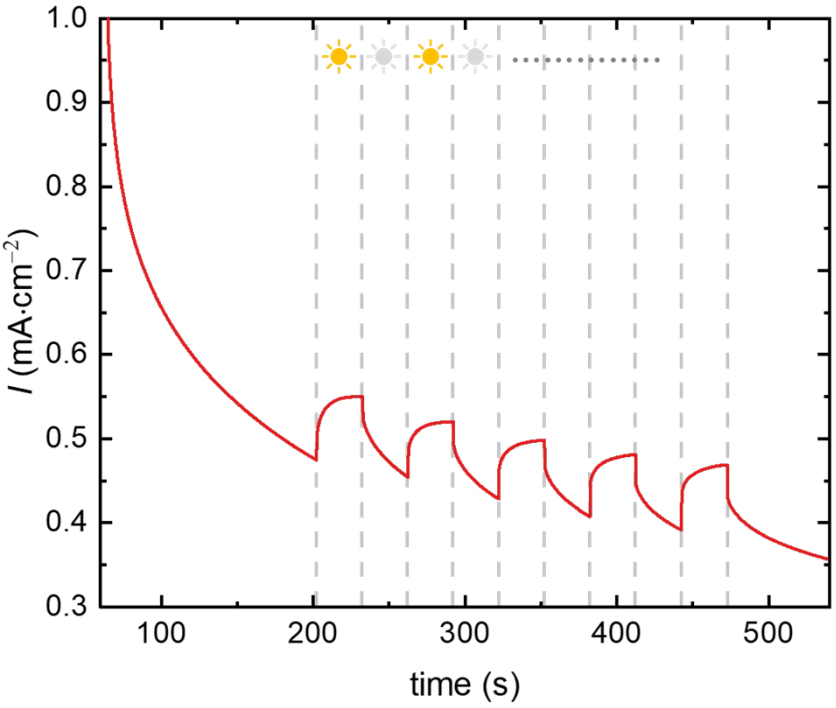

Figure S 5: CA curves recorded at 0 V vs. RHE of $Pb_8O_4I_6(CN_2)$ in 0.1 M KPi (pH 7.0) under interrupted AM 1.5G illumination. The light source is switched on in areas marked with a yellow sun and switched off in time intervals marked with a grey sun.

Publication 5

From Heterocubane Units to Extended Networks: Synthesis, Structure, and Optical Properties of $Pb_9O_2I_8(CN_2)_3$ and $Pb_{16}O_5I_{14}(CN_2)_4$

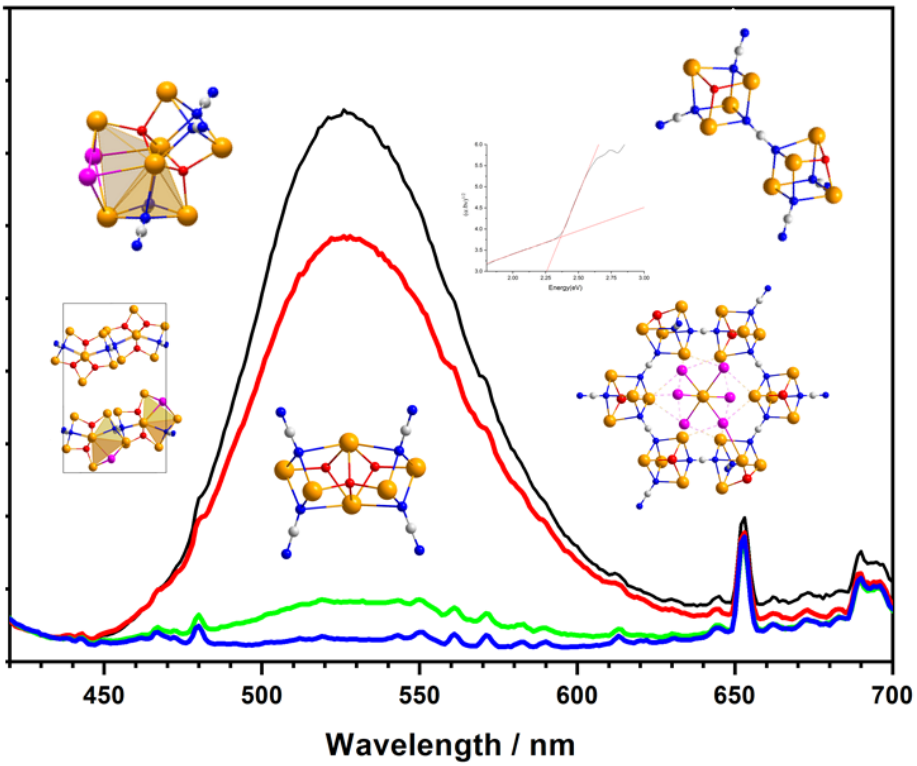

https://doi.org/10.1002/zaac.202500205

Reprinted from

Z. Anorg. Allg. Chem. **2025**, 0, e202500205

with permission from

Copyright © 2025 Wiley-VCH GmbH

Check for updates

Zeitschrift für anorganische und allgemeine Chemie

Journal of Inorganic and General Chemistry
ZAAC
Zeitschrift für anorganische und allgemeine Chemie

RESEARCH ARTICLE OPEN ACCESS

From Heterocubane Units to Extended Networks: Synthesis, Structure, and Optical Properties of $Pb_9O_2I_8(CN_2)_3$ and $Pb_{16}O_5I_{14}(CN_2)_4$

Albert T. Schwarz[1] | Markus Ströbele[1] | David Enseling[2] | Thomas Jüstel[2] | H.-Jürgen Meyer[1]

[1]Section for Solid State and Theoretical Inorganic Chemistry, Institute of Inorganic Chemistry, Eberhard Karls University, Tübingen, Germany | [2]Department of Chemical Engineering, FH Münster University of Applied Science, Steinfurt, Germany

Correspondence: H.-Jürgen Meyer (juergen.meyer@uni-tuebingen.de)

Received: 15 September 2025 | **Revised:** 11 December 2025 | **Accepted:** 16 December 2025

Keywords: carbodiimide | crystal structure | heterocubane | luminescence

ABSTRACT

The compounds $Pb_9O_2I_8(CN_2)_3$ and $Pb_{16}O_5I_{14}(CN_2)_4$ were synthesized via solid-state methods and structurally characterized by single-crystal X-ray diffraction. Both materials feature heterocubane units interconnected through iodide and carbodiimide ligands. Optical measurements reveal indirect bandgaps of 2.35 eV and 2.36 eV, respectively. Photoluminescence spectra at 80 K show a broad green emission centered at 520 nm. The results demonstrate the structural and optical potential of heteroanionic Pb-based carbodiimide frameworks.

1 | Introduction

The chemistry of lead and tin compounds incorporating oxide, halide, and carbodiimide ions has attracted considerable interest due to their structural diversity. Low-valent main group elements such as Pb^{2+} and Sn^{2+} are particularly notable in this context, as their stereochemical active lone pairs often give rise to anisotropic coordination environments and unusual bonding topologies. These effects can lead to either hemidirected or holodirected geometries, depending on the ligand environment and coordination number [1–3]. Dinitridocarbonates, appearing as carbodiimides and cyanamides, have emerged as highly versatile building blocks in solid-state and coordination chemistry. Due to their isolobal relationship with classical chalcogenide ions (O^{2-}, S^{2-}), they enable the construction of pseudo-oxide analogs with modified electronic and structural characteristics [4–10]. While early investigations focused primarily on alkali and alkaline earth metal carbodiimides, recent developments have increasingly explored the chemistry of heavier p-block elements, particularly tin and lead. For divalent group 14 metals, such as Sn^{2+} and Pb^{2+}, the bonding situation in carbodiimide-containing compounds is notably complex. The binary lead carbodiimide $Pb(CN_2)$ crystallizes in a layered structure in which Pb^{2+} is fivefold coordinated by nitrogen atoms in a distorted trigonal bipyramidal geometry. The layers are held together by weak van der Waals interactions, as there are no significant Pb–N contacts between adjacent layers [11]. Expanding on this foundation, Dolabdjian et al. have reported a family of lead carbodiimide halides of the general formula $APb_2X_3(CN_2)$ (A = Li, Na, Ag; X = Cl, Br) [12], synthesized via solid-state metathesis. These compounds crystallize in the cubic space group $Fd\,\bar{3}\,m$ and exhibit interpenetrating three-dimensional networks of $[Pb_4(NCN)_{4/2}]$ polyhedra and corner-linked $[AX_6]$ octahedra (A = Li, Na, Ag; X = Cl, Br), structurally related to the mineral bideauxite. Remarkably, the Pb^{2+} cations in these frameworks adopt high coordination numbers (up to nine) with holodirected geometries and the $(NCN)^{2-}$ ligands approach D_∞ symmetry, as confirmed by infrared spectroscopy (IR). These findings suggest that in extended, highly symmetric frameworks, the $6s^2$ lone pair of Pb^{2+} can become

In memoriam of Prof. Dr. Harald Hillebrecht.

This is an open access article under the terms of the Creative Commons Attribution License, which permits use, distribution and reproduction in any medium, provided the original work is properly cited.

© 2026 The Author(s). *Zeitschrift für anorganische und allgemeine Chemie* published by Wiley-VCH GmbH.

stereochemical inactive. Nevertheless, in less constrained environments or in the presence of lower coordination numbers, the lone pair remains stereochemical active and contributes significantly to the geometry and connectivity of Pb- or Sn-centered units. A particularly intriguing motif in this regard is the $[T_4O_4]$ (T = Pb, Sn) heterocubane cluster, composed of four cations bridged by four μ_3-oxygen atoms. This pseudo-cubic arrangement is well established in lead oxide halides, tin-oxide-halides, and organometallic compounds, where it often serves as a core structural building block [13–16]. However, its integration into mixed-anion carbodiimide networks is a more recent development. The tin-based $Sn_9O_5Cl_4(CN_2)_2$ [17] contains an $[Sn_4O_4]$ heterocubane core embedded in a mixed-anion framework of chlorides and carbodiimides. In recent work, the compound $Pb_8O_4I_6(CN_2)$ was reported, which features discrete $[Pb_4O_4]$ heterocubane units connected via iodide bridges and further linked into a three-dimensional network by bridging $(NCN)^{2-}$ ligands. It exhibits green photoluminescence at low temperatures and semiconducting behavior, underlining the structural and functional potential of such heteroanionic materials [18]. These findings highlight the versatility of $(NCN)^{2-}$ ligands in stabilizing cluster-based architectures in combination with oxide and halide anions. Motivated by this, we have continued to investigate the structural chemistry of lead-based oxide–halide–carbodiimide compounds. In the present study, we introduce two novel compounds, $Pb_9O_2I_8(CN_2)_3$ and $Pb_{16}O_5I_{14}(CN_2)_4$, both of which extend the structural chemistry of the heterocubane motif into the dinitridocarbonate-based materials.

2 | Results and Discussion

2.1 | Syntheses of $Pb_9O_2I_8(CN_2)_3$ and $Pb_{16}O_5I_{14}(CN_2)_4$

One of the most frequently employed preparative methods is the so-called ceramic method [19]. This method involves the grinding of powders comprising oxides, carbonates, and halides, along with the relevant metals. Subsequent to this, the reaction mixture is subjected to the desired temperature for conversion.

In this study, the compounds presented have been obtained from PbI_2, PbO, and $Pb(CN_2)$ in the stoichiometric ratio according to the following reaction equations.

$$4\,PbI_2 + 2\,PbO + 3\,Pb(CN_2) \rightarrow Pb_9O_2I_8(CN_2)_3$$

$$7\,PbI_2 + 5\,PbO + 4\,Pb(CN_2) \rightarrow Pb_{16}O_5I_{14}(CN_2)_4$$

The reactions were carried out at 420°C for 5 days, resulting in the formation of dark yellow powders. For $Pb_{16}O_5I_{14}(CN_2)_4$, elemental lead was observed as a minor secondary phase, which is attributed to the partial thermal reduction power of the $(NCN)^{2-}$ unit under the applied conditions (Figure S1 and S2). The powders obtained were then exposed to air for a period of 3 weeks. Subsequent measurements with X-ray powder diffractometry showed no change in the respective powders with the compounds to be analyzed. Consequently, it can be considered that the compounds behave stable under ambient conditions. In order to verify the composition of the compounds, energy-dispersive X-ray (EDX) spectroscopy was performed at nine points for $Pb_9O_2I_8(CN_2)_3$ and three points for $Pb_{16}O_5I_{14}(CN_2)_4$. The EDX measurements demonstrated a lead to iodine ratio of 9:7.99(8) for $Pb_9O_2I_8(CN_2)_3$ and 16:14.01(3) for $Pb_{16}O_5I_{14}(CN_2)_4$.

2.2 | Crystal Structure of $Pb_9O_2I_8(CN_2)_3$

The crystal structure of $Pb_9O_2I_8(CN_2)_3$ was solved and refined on a yellow plated-shaped single crystal by X-ray diffraction with the orthorhombic space group *Pbcn*. Some crystal structure and refinement data are given in Table 1.

Single-crystal X-ray diffraction analysis of $Pb_9O_2I_8(CN_2)_3$ revealed the presence of five crystallographically distinct lead sites (Pb1–Pb5), each embedded in a unique coordination environment formed by iodide, oxygen, and carbodiimide ligands (Figure 1). Pb1 is coordinated by six iodide ligands in a distorted octahedral geometry, representing the most symmetric coordination environment among the five sites. Pb2 is eightfold coordinated by five iodide anions and three $(NCN)^{2-}$ ligands, resulting in a bicapped trigonal prismatic environment. This coordination polyhedron is comparable in geometry to that of Pb4, which is also eight coordinate, but comprises four iodide ions, two $(NCN)^{2-}$ units, and two oxygen atoms. Pb3 adopts a monocapped trigonal prismatic geometry, with a coordination sphere comprising four iodide anions, two $(NCN)^{2-}$ units, and a single oxygen atom. Pb5 is surrounded by four iodines, two $(NCN)^{2-}$ units, and one oxygen. An overview of the coordination polyhedra around Pb1–Pb5 is depicted in Figure 1. The lead coordination polyhedra include Pb–I distances ranging from 3.0443(3) Å to 3.7614(4) Å and Pb–N separations ranging from 2.474(4) Å to

TABLE 1 | Selected crystal and structure refinement data for $Pb_9O_2I_8(CN_2)_3$ and $Pb_{16}O_5I_{14}(CN_2)_4$ at 150K.

Empirical formula	$Pb_9O_2I_8(CN_2)_3$	$Pb_{16}O_5I_{14}(CN_2)_4$
CCDC code	2385668	2415837
Formula weight ($g{\cdot}mol^{-1}$)	3032.00	5331.76
Wavelength (Mo-K_α)	0.71073	0.71073
Crystal system	Orthorhombic	Monoclinic
Space group	*Pbcn*	$P2_1/n$
Unit cell dimensions (Å)	a = 15.4421(2) b = 10.84480(1) c = 17.0827(3)	a = 20.5040(3) b = 12.0617(2) c = 21.3191(3) β = 104.436(2)
Volume (Å^3)	2860.78(7)	5106.02(14)
Z	4	4
Density (calculated) (g cm^{-3})	7.040	6.936
Absorption coefficient (mm^{-1})	61.404	61.025
Final R indices ($I>2\sigma(I)$)	R_1 = 0.0117, wR_2 = 0.0254	R_1 = 0.0108, wR_2 = 0.0214
R indices (all data)	R_1 = 0.0125, wR_2 = 0.0256	R_1 = 0.0113, wR_2 = 0.0215
GooF	1.181	1.092

15213749, 0, Downloaded from https://onlinelibrary.wiley.com/doi/10.1002/zaac.202500205 by Universitatsbibliothek, Wiley Online Library on [26/01/2026]. See the Terms and Conditions (https://onlinelibrary.wiley.com/terms-and-conditions) on Wiley Online Library for rules of use; OA articles are governed by the applicable Creative Commons License

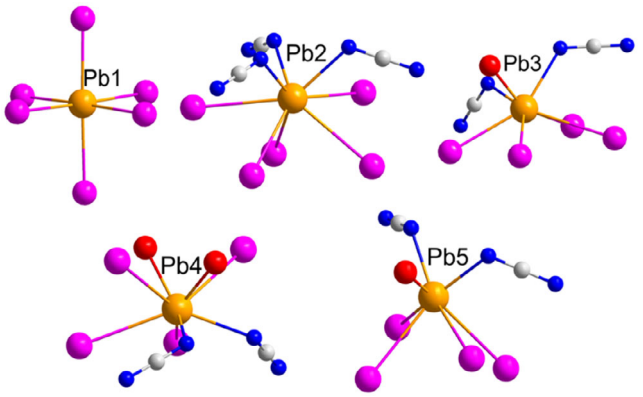

FIGURE 1 | The different lead atoms with their unique environment in the compound $Pb_9O_2I_8(CN_2)_3$. Iodine is shown in purple, oxygen in red, carbon in white and nitrogen in blue.

2.751(3) Å, which are similar to the distances in the related lead compounds $Pb_7I_6(CN_2)_4$ (2.48–2.60 Å) [20], $PbCN_2$ (2.31–2.62 Å) [21], $LiPb_2Cl_3(CN_2)$ (2.54 Å), $LiPbCl(CN_2)$ (2.39–2.70 Å) [12] and $Pb_8O_4I_6(CN_2)$ [18]. The Pb–O bond lengths within this arrangements range from 2.301(3) Å to 2.492(3) Å. The structural analysis revealed that the $(NCN)^{2-}$ units occupy two crystallographic distinct positions in the crystal lattice (Figure 2). In the $(NCN)^{2-}$ unit centered at C1, the presence of a crystallographic twofold rotational axis results in identical C–N lengths of 1.233(4) Å and a linear N–C–N angle of 179.8(6)°, confirming the formation of a carbodiimide-type geometry. In contrast, the $(NCN)^{2-}$ unit centered at C2 displays a slightly distorted linear arrangement with a N–C–N angle of 179.0(5)° and minor asymmetry in the C–N distance, suggesting a subtle deviation from perfect symmetry. Despite the minor asymmetry, this unit can be considered also as carbodiimide unit. These structural features are consistent with IR spectroscopic data, which confirm the presence of asymmetric stretching vibrations at 1881 cm^{-1} and deformation vibrations at 625 cm^{-1}, which are characteristic of carbodiimide ligands (Figure S3).

A particularly prominent structural motif in $Pb_9O_2I_8(CN_2)_3$ is the formation of discrete $[Pb_4O(CN_2)_{3/2}]$ units (Figure 3), which closely resemble the arrangement of atoms in a distorted heterocubane cluster. In this unit, a single oxygen atom adopts a μ_3-coordination mode, bridging three Pb^{2+} cations and forming an approximately trigonal $[Pb_3O]$ core. The Pb–Pb distances within this unit span from 3.7109(4) Å to 4.0301(4) Å. Notably, the coordination geometries around the Pb^{2+} centers are influenced by

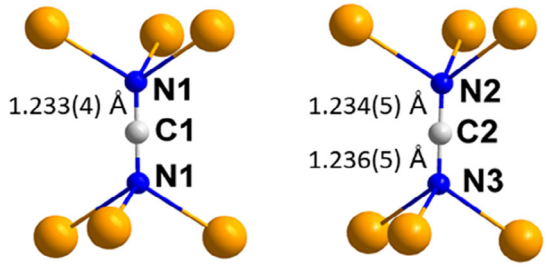

FIGURE 2 | Two crystallographic distinct $(NCN)^{2-}$ units in the compound $Pb_9O_2I_8(CN_2)_3$, which are coordinated nearly trigonal antiprismatically by lead (orange).

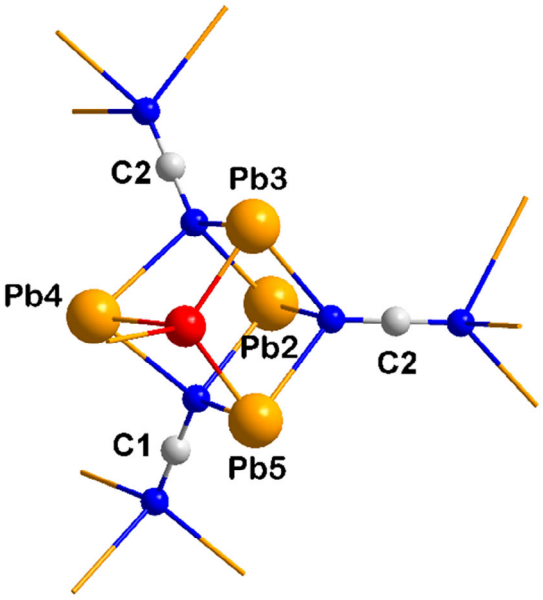

FIGURE 3 | The heterocubane $[Pb_4O(CN_2)_{3/2}]$ unit embedded into a tetrahedral environment. Oxygen is shown in red, carbon in white, and nitrogen in blue. Iodide atoms are omitted for clarity to highlight the unit.

the stereochemical active $6s^2$ lone pair, which contributes to the hemidirected character of the polyhedra. Additionally, heterocubane units connect via shared $(NCN)^{2-}$ unit into a tetrahedral arrangement with an additional linkage provided through a shared oxygen atom. This motif contributes significantly to the overall framework connectivity. Starting from the heterocubane building block, the framework forms an annular assembly of six heterocubane unit arranged into a ring, stabilized by a octahedral $[PbI_6]^{4-}$ unit in its center (Figure 4). The Pb–I bond length between the lead and the iodine of the octahedra (scattered bonds) ranges from 3.5053(3) Å to 3.7614(4) Å. Within the unit cell, the structure can be described as a layered arrangement

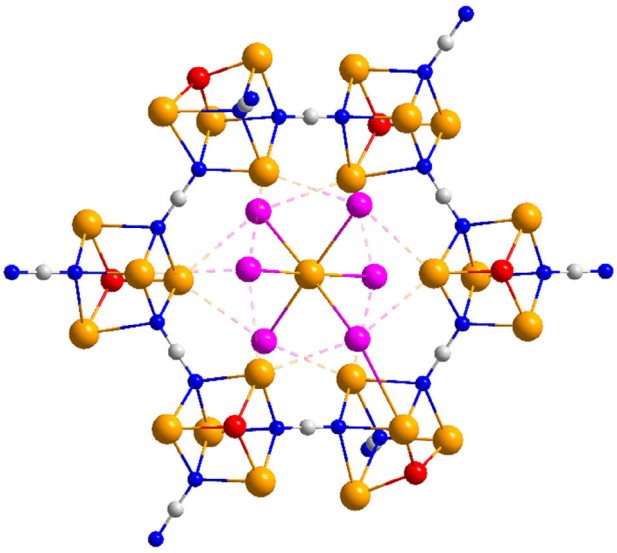

FIGURE 4 | The annular assembly of the heterocubane units (ring system) in $Pb_9O_2I_8(CN_2)_3$. The $[PbI_6]^{4-}$ octahedron serves as the cohesive agent, binding the constituent units together.

15213749, 0, Downloaded from https://onlinelibrary.wiley.com/doi/10.1002/zaac.202500205 by Universitatsbibliothek, Wiley Online Library on [26/01/2026]. See the Terms and Conditions (https://onlinelibrary.wiley.com/terms-and-conditions) on Wiley Online Library for rules of use; OA articles are governed by the applicable Creative Commons License

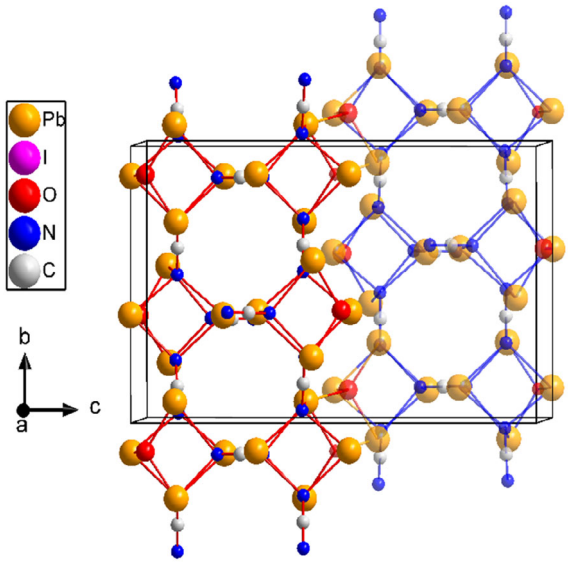

FIGURE 5 | Section of a heterocubane-based ring system in the unit cell of $Pb_9O_2I_8(CN_2)_3$. For clarity, the lead–iodide octahedron ($[PbI_6]^{4-}$) and iodide ions have been removed, and each ring is shown with different transparency levels and colors to enhance visual distinction.

composed of heterocubane-based ring systems (Figure 5), which propagate diagonally relative to the *ac* plane of the unit cell. These structural layers are interconnected through bridging $(NCN)^{2-}$ units, iodine atoms, and common oxygen atoms, which mediate the linkage between adjacent heterocubane units and define the directional extension of the framework (Figure 6). Accordingly, the sum formula $Pb_9O_2I_8(CN_2)_3$ results from the linkage of two $[Pb_4O(CN_2)_{3/2}]$ heterocubane units, complemented by one $[PbI_6]^{4-}$octahedron and two additional iodide bridges. In analogy to silicates and aluminosilicates, where corner-sharing $[SiO_4]$/$[AlO_4]$ tetrahedra form rings, layers, and

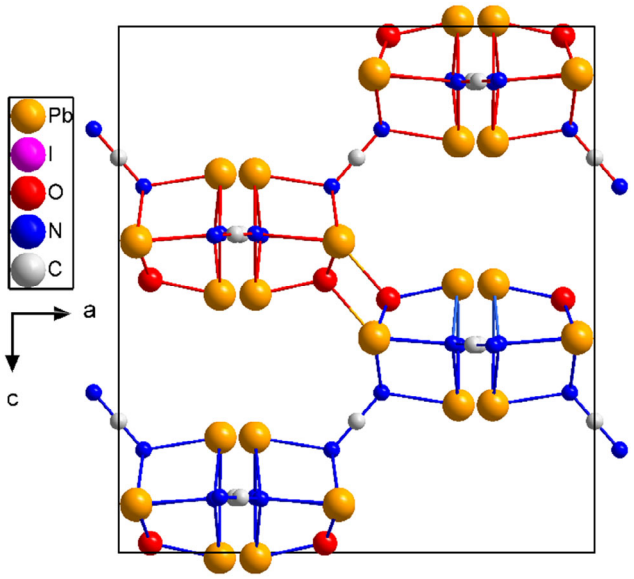

FIGURE 6 | Unit cell of $Pb_9O_2I_8(CN_2)_3$ viewed along the *b*-axis. The ring systems are interconnected via shared oxygen atoms. For clarity, the $[PbI_6]^{4-}$ octahedra and iodine atoms have been omitted, and the bonds of each ring-system are color-coded to enhance visual distinction.

other frameworks, the heterocubane-based rings here behave as a cationic counterpart to those tetrahedral building units (Figure 4).

2.3 | Crystal Structure of $Pb_{16}O_5I_{14}(CN_2)_4$

The compound $Pb_{16}O_5I_{14}(CN_2)_4$ crystalizes in the monoclinic space group $P2_1/n$ as block-shaped yellow air-stabile crystals. Some crystallographic data are presented in Table 1. The crystal structure refinement revealed sixteen crystallographic distinct lead sites, each embedded in a unique coordination environment. The coordination numbers of these lead centers range from five to nine, reflecting the structural complexity and the variability of local bonding motifs within the framework. A detailed overview of the individual Pb coordination environments is provided in the SI (Figure S4). The structure contains four distinct $(NCN)^{2-}$ units (Figure 7), each nitrogen atom is bound to three lead atoms, forming a trigonal antiprismatic coordination polyhedron, as in the previously described compound $Pb_9O_2I_8(CN_2)_3$. The $(NCN)^{2-}$ unit centered at C1 exhibits typical carbodiimide character, with symmetrical C–N bond lengths of 1.229(6) Å. In contrast, the other $(NCN)^{2-}$ units (centered at C2, C3, and C4) display slight differences in its C–N distances, ranging from 1.220(6) Å to 1.240(6) Å. However, since the difference between the two distances remains small, the IR spectrum (Figure S5) predominantly reflects carbodiimide features, as evidenced by the asymmetric stretching vibrations at 1924 cm^{-1} and the deformation modes at 656 cm^{-1}.

Two distinct structural motifs are observed in the compound. In both arrangements, heterocubane-type units serve as the central building blocks, as already seen in the crystal structure of $Pb_9O_2I_8(CN_2)_3$. However, the connectivity between these units differs significantly. In the motif presented in Figure 8, two heterocubane units are corner-linked via shared lead (Pb3 and Pb4) and oxygen atoms, resulting in the formation of a $[Pb_7O_3(CN_2)_{4/2}]$-cluster. Within this arrangement, each oxygen atom adopts a tetrahedral coordination by four Pb atoms,

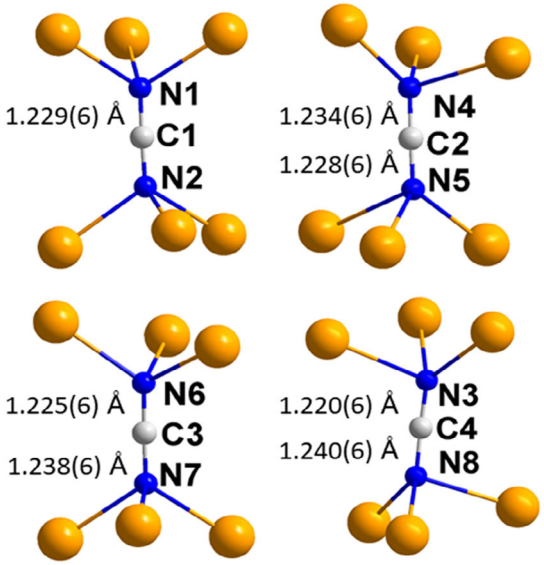

FIGURE 7 | Four crystallographic distinct $(NCN)^{2-}$ units with their surrounding lead atoms (orange).

15213749, 0, Downloaded from https://onlinelibrary.wiley.com/doi/10.1002/zaac.202500205 by Universitatsbibliothek, Wiley Online Library on [26/01/2026]. See the Terms and Conditions (https://onlinelibrary.wiley.com/terms-and-conditions) on Wiley Online Library for rules of use; OA articles are governed by the applicable Creative Commons License

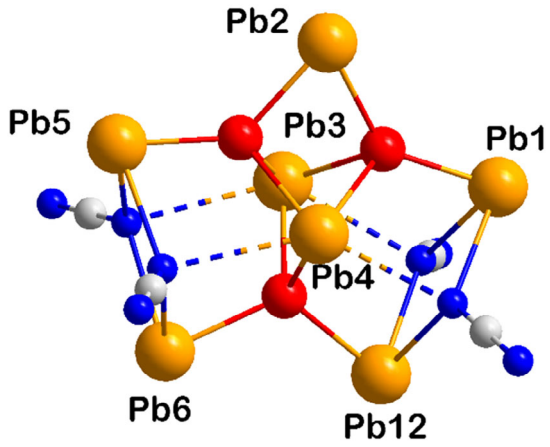

FIGURE 8 | Section of the $[Pb_7O_3(CN_2)_{4/2}]$ cluster-like arrangement in the compound $Pb_{16}O_5I_{14}(CN_2)_4$. Oxygen atoms are shown in red, carbon in white, and nitrogen in blue. Additional iodine atoms are omitted to highlight the arrangement of lead atoms.

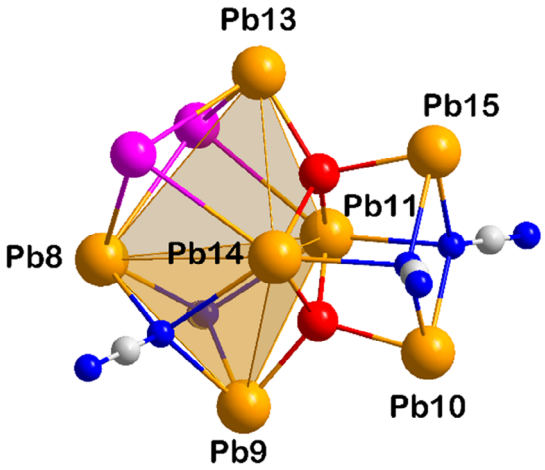

FIGURE 9 | Section of the $[Pb_7O_2I_2(CN_2)_{4/2}]$ unit in the compound $Pb_{16}O_5I_{14}(CN_2)_4$. For clarity, the trigonal bipyramidal Pb_5-polyhedra is highlighted. Iodine is shown in purple, oxygen in red, carbon in white, and nitrogen in blue. Additional iodine atoms are omitted to highlight the arrangement of lead atoms.

forming $[Pb_4O]$ subunits with Pb–O distance ranging from 2.181(3) to 2.500(3) Å. These distances are largely consistent with values reported for comparable lead–oxygen distances in the literature [22]. Notably, the shortest Pb–O distances, namely Pb1–O at 2.181(3) Å and Pb5-O at 2.188(3) Å, are slightly contracted, likely due to spatial constraints imposed by the central Pb2 atom within the cluster core. The peripheral lead atoms located at the corners of the fused heterocubane (Pb1, Pb5, Pb6, and Pb12) each coordinate two $(NCN)^{2-}$ units and one oxygen atom. In contrast, the central lead atom Pb2 is coordinated by two oxygen atoms and the lead atoms Pb3, and Pb4 are each coordinated by three oxygen atoms, reflecting their central role in the $[Pb_7O_3(CN_2)_{4/2}]$ cluster unit. Within this arrangement Pb–Pb distances ranges from 3.388(1) Å to 4.163(1) Å. The cluster exhibits Pb–N distances ranging from 2.458(4) Å to 2.855(5) Å. The longer Pb–N distances, particularly those between Pb3 and Pb4 and the $(NCN)^{2-}$ units (scattered bond), result from distortions within the heterocubane framework and are best described as weakly coordinating contacts.

The second cluster in the structure consists of a heterocubane unit fused with a face capped distorted trigonal bipyramid of lead atoms to yield a $[Pb_7O_2I_2(CN_2)_{4/2}]$ unit, linked together by shared lead and oxygen atoms (Figure 9). The trigonal bipyramidal arrangement observed in the structure can alternatively be described as two face-sharing Pb_4 tetrahedra. One tetrahedron is capped by two iodide and an oxygen atom, while the other is capped by two $(NCN)^{2-}$ units and an oxygen atom. The trigonal Pb_3 plane formed by of Pb8, Pb11, and Pb14 within the $[Pb_7O_2I_2(CN_2)_{4/2}]$ unit features Pb–Pb distances ranging from 3.6449(2) Å to 4.4204(1) Å, which are significantly longer than typical distances within Pb clusters [23] and are thus best interpreted as nonbonding interactions. This heterocubane motif present comprises central oxygen atoms in a tetrahedral coordination by four Pb atoms to a $[Pb_4O]$ unit. The peripheral lead atoms forming the corners of the heterocubane are further coordinated by oxygen and $(NCN)^{2-}$ ligands. Within this $[Pb_7O_2I_2(CN_2)_{4/2}]$ unit, Pb–N distances range from 2.409(4) to 2.619(4) Å, Pb–O distances span from 2.266(3) to 2.364(3) Å, and Pb–I distances span 3.1671(4)–3.5000(1) Å; the longer values reflect distortion of the coordination environment. Within the overall structure, Pb–I distances, including the previously mentioned distances range between 3.1671(4) and 3.8366(1) Å. The longer separations arise from distortions of the coordination environments within the structure. As in other metal carbodiimide compounds, the overall structure can be interpreted as a layered arrangement (Figure 10 bottom), in which the individual layers are separated by iodide ions and $[PbI_6]^{4-}$ octahedral units. Each layer is composed of the two heterocubane-based motifs described above, which are interconnected in a zigzag chain-like pattern through bridging $(NCN)^{2-}$ ligands and iodide atoms (Figure 10 top). Thus, the overall composition $Pb_{16}O_5I_{14}(CN_2)_4$ arises from the assembly of the two characteristic cluster motifs $[Pb_7O_3(CN_2)_{4/2}]$ and $[Pb_7O_2I_2(CN_2)_{4/2}]$, complemented by two PbI_6 octahedra (Pb7 and Pb16).

2.4 | Bandgap Determination of $Pb_9O_2I_8(CN_2)_3$ and $Pb_{16}O_5I_{14}(CN_2)_4$

The optical bandgaps of $Pb_9O_2I_8(CN_2)_3$ and $Pb_{16}O_5I_{14}(CN_2)_4$ were investigated upon using UV–vis diffuse reflectance spectroscopy. The reflectance spectrum was converted to a pseudo-absorbance spectrum via the Kubelka–Munk function,

$$F(R_\infty) = \frac{\alpha}{S} = \frac{(1-R_\infty)^2}{2R_\infty}$$

where R_∞ symbolizes the reflectance of a semi-infinitely thick sample, while α defines the absorption coefficient and S is the scattering coefficient. For samples consisting of particles larger than the wavelength of the incident light, the scattering coefficient can be assumed to be approximately constant over the measured spectral range. In this condition, the Kubelka–Munk function becomes directly proportional to the absorption coefficient α, and thus serves as a suitable approximation for evaluating the optical absorption behavior of the material [24]. The absorption edge was analyzed using the Tauc formalism, which relates the absorption coefficient α to the photon energy $h\nu$ according to the equation:

15213749, 0, Downloaded from https://onlinelibrary.wiley.com/doi/10.1002/zaac.202500205 by Universitatsbibliothek, Wiley Online Library on [26/01/2026]. See the Terms and Conditions (https://onlinelibrary.wiley.com/terms-and-conditions) on Wiley Online Library for rules of use; OA articles are governed by the applicable Creative Commons License

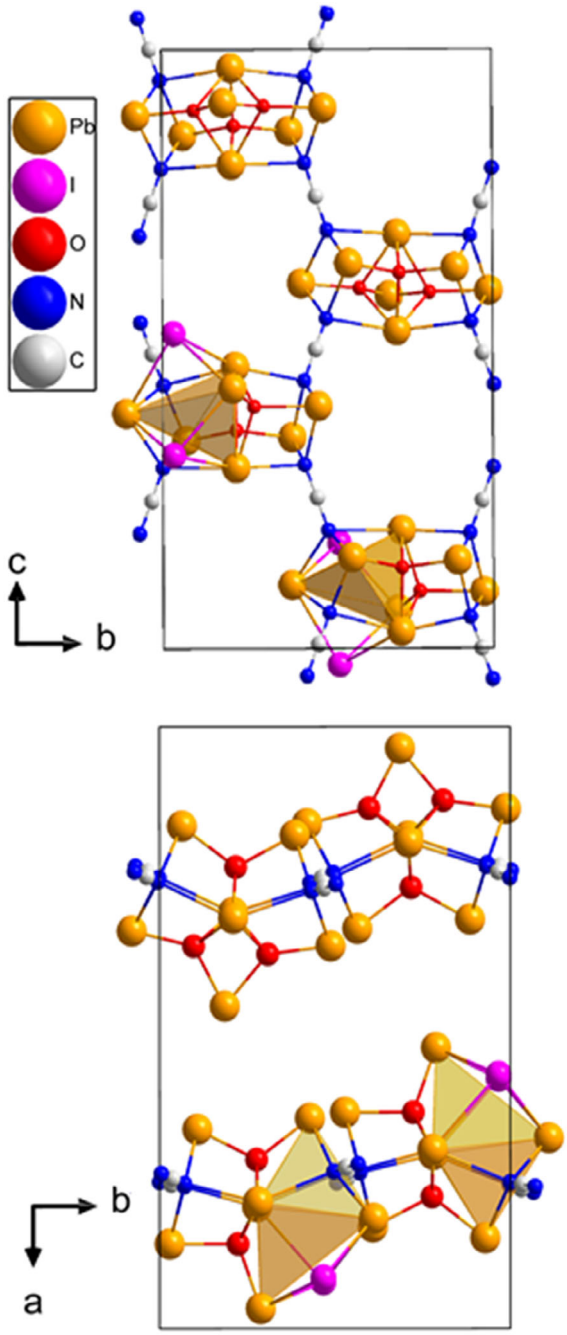

FIGURE 10 | Section of a single layer within $Pb_{16}O_5I_{14}(CN_2)_4$ (top) along *a*-axis and the layered arrangement in the unit cell (bottom) along *c*-axis. For better visualization, the iodine sublattice including the $[PbI_6]^{4-}$ units has been removed to emphasize the layered structure.

$$(\alpha \cdot h\nu)^{1/\beta} = A(h\nu - E_g)$$

where α is the absorption coefficient, h is the Planck's constant, ν is the frequency of the incident light, A is a material-dependent constant, and E_g is the optical bandgap. The exponent β defines the nature of the electronic transition: $\beta = 1/2$ for direct allowed transitions and $\beta = 2$ for indirect allowed transitions [25].

By substituting the Kubelka–Munk function $F(R_\infty)$ for α the equation becomes:

$$(F(R_\infty) \cdot h\nu)^{1/\beta} = A(h\nu - E_g)$$

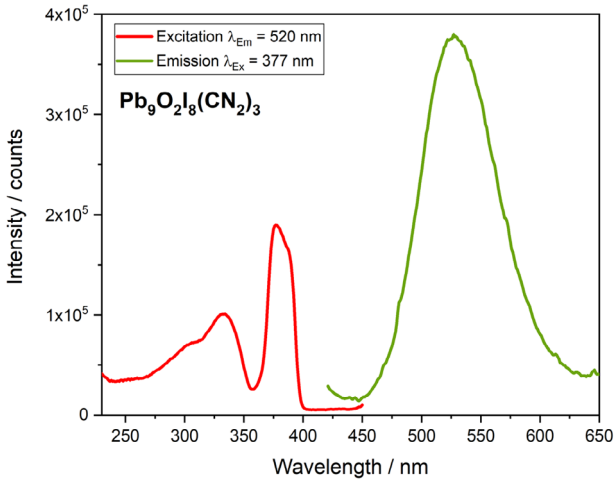

FIGURE 11 | Excitation and emission spectra of $Pb_9O_2I_8(CN_2)_3$ at 80 K.

The bandgap energy E_g was determined by extrapolating the linear region of the Tauc plot, corresponding to the onset of optical absorption. The optical analysis of $Pb_9O_2I_8(CN_2)_3$ yielded an indirect bandgap of 2.35 eV and a direct allowed transition energy of 2.36 eV, as determined from Tauc plot analysis (Figure S6 and S7). For $Pb_{16}O_5I_{14}(CN_2)_4$, the corresponding values were 2.36 eV for the indirect bandgap and 2.39 eV for the direct transition (Figure S8 and S9).

2.5 | Photoluminescence Studies of $Pb_9O_2I_8(CN_2)_3$ and $Pb_{16}O_5I_{14}(CN_2)_4$

Improvements in lighting and display systems have been achieved through the development of new solid inorganic luminescent materials. Since the 1930s, a significant number of investigators have focused their research on the optical properties of so-called s^2 ions, including Tl^+, Pb^{2+}, and Bi^{3+} [26–31]. Consequently, the focus of research in material containing $(NCN)^{2-}$ units has therefore recently been directed toward materials that include Pb^{2+}, functioning as an activator, thereby facilitating the enhancement of desired properties or phenomena within the materials under consideration. It is widely agreed that the luminescence properties of the Pb^{2+} ion in the $6s^2$ configuration are due to the ground state $^1S_0$ and two excited states, the singlet $^1P_1$ and the triplet $^3P_{0,1,2}$ [20, 32–34]. Figures 11 and 12 show the luminescence spectra of the compound $Pb_9O_2I_8(CN_2)_3$ and $Pb_{16}O_5I_{14}(CN_2)_4$. The excitation spectra were observed for monitoring the 520 nm (19200 cm^{-1}) emission and result from the superposition of several subbands peaking at around 301 nm (33200 cm^{-1}), 333 nm (30000 cm^{-1}), and 377 nm (26500 cm^{-1}) for $Pb_9O_2I_8(CN_2)_3$ and 304 nm (32900 cm^{-1}), 336 nm (29800 cm^{-1}), and 377 nm (26500 cm^{-1}) for the compound $Pb_{16}O_5I_{14}(CN_2)_4$.

Comparison with the literature suggests [35, 36] that the excitation bands correspond to the transition from the ground state $^1S_0$ to the excited states of the singlet $^1P_1$ and of the triplet, which splits into $^3P_2$ and $^3P_1$ states. The emission spectrum of $Pb_9O_2I_8(CN_2)_3$ at 80 K shows a single broad band peaking at 520 nm as well as the emission band of $Pb_{16}O_5I_{14}(CN_2)_4$, which can be assigned to the transition of the triplet state $^3P_1$ to the

15213749, 0, Downloaded from https://onlinelibrary.wiley.com/doi/10.1002/zaac.202500205 by Universitatsbibliothek, Wiley Online Library on [26/01/2026]. See the Terms and Conditions (https://onlinelibrary.wiley.com/terms-and-conditions) on Wiley Online Library for rules of use; OA articles are governed by the applicable Creative Commons License

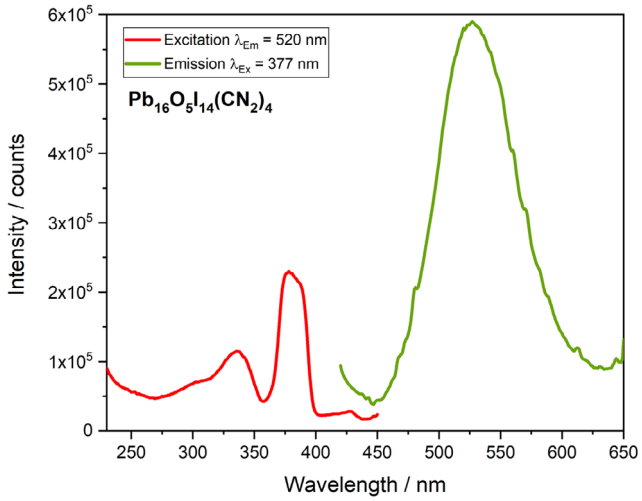

FIGURE 12 | Excitation and emission spectra of $Pb_{16}O_5I_{14}(CN_2)_4$ at 80 K.

TABLE 2 | PL data of $Pb_9O_2I_8(CN_2)_3$ and $Pb_{16}O_5I_{14}(CN_2)_4$ in comparison with selected compounds.

Composition	Exc., nm	Emis., nm	Stokes shift, cm^{-1}	Ref.
$Pb_9O_2I_8(CN_2)_3$	377	520	7400	This work
$Pb_{16}O_5I_{14}(CN_2)_4$	377	520	7400	This work
$Pb_7I_6(CN_2)_4$	378	525	7500	[20]
$Pb_8O_4I_6(CN_2)$	377	520	7400	[18]

ground state $^1S_0$, although at low temperatures the strongly forbidden $^3P_0$–$^1S_0$ transition is also observed [37]. However, at 150 K, the luminescence of both compounds is found to be nearly completely quenched, as shown in the supporting information (Figure S10 and S11). In both cases, the photoluminescence emission at 520 nm exhibits a mono-exponential decay behavior, with decay times of approximately $\tau_1/_e = 361$ ns and $\tau_1/_e = 265$ ns, respectively (Figure S12 and S13). These values are consistent with the $^3P_1$–$^1S_0$ transition of Pb^{2+}. In contrast, the $^3P_0$–$^1S_0$ transition typically shows significantly longer decay times and is thus unlikely to be responsible for the observed emission [33, 34, 38, 39]. The following Table 2 shows an overview of the received data from the measurements made in comparison with selected compounds from the literature.

3 | Conclusions

The two new compounds $Pb_9O_2I_8(CN_2)_3$ and $Pb_{16}O_5I_{14}(CN_2)_4$ extend the family of heteroanionic lead carbodiimide materials through the presence of heterocubane-type clusters in combination with iodide and carbodiimide ligands. Their crystal structures reveal complex three-dimensional networks built from discrete and fused heterocubane units, with diverse coordination environments around Pb. Optical measurements confirm semiconducting behavior with indirect bandgaps around 2.35 eV (19000 cm^{-1}) suitable for photocatalytic studies. Both compounds show strong temperature-dependent photoluminescence with characteristic green emission. These results underline the structural versatility of carbodiimide-based lead compounds and provide further insight into the role of mixed-anion chemistry.

4 | Experimental Section and Calculation Details

4.1 | Preparation of $Pb_9O_2I_8(CN_2)_3$

The powders of $Pb(CN_2)$ (synthesized as described in the literature [21]), PbI_2 (purchased from Sigma–Aldrich, 99.999% purity), and PbO (purchased from Sigma–Aldrich, 99.999% purity) were mixed in a glove box under dry argon atmosphere in a 3:4:2 molar ratio (total amount of 250 mg). The reaction powder was then transferred into a silica ampoule and sealed under vacuum. The ampoule was heated in a crucible furnace to 420°C at a rate of 2 K min^{-1}, held at this temperature for 5 days, and then cooled at the same rate. The compound was obtained as a dark yellowish powder, with an estimated yield of 90% with a minor side phase.

4.2 | Preparation of $Pb_{16}O_5I_{14}(CN_2)_4$

The powders of $Pb(CN_2)$ (synthesized as described in the literature [21]), PbI_2 (purchased from Sigma–Aldrich, 99.999% purity) and PbO (purchased from Sigma–Aldrich, 99.999% purity) were mixed in a glove box under dry argon atmosphere in a 4:7:5 molar ratio (total amount of 250 mg). The reaction powder was then transferred into a silica ampoule and sealed under vacuum. The ampoule was then heated in a crucible furnace at 420°C at a heating and cooling rate of 2 K min^{-1} and a holding time of 5 days. The compound was obtained as a dark yellowish powder, with an estimated yield of 85%, and elemental lead as a side phase.

4.3 | Single-Crystal XRD

Single-crystal XRD studies were performed using a Rigaku XtaLab Synergy-S diffractometer with monochromatic Mo-K_α ($\lambda = 0.71073$ Å) radiation and a mirror monochromator. Measurements were conducted under N_2 cooling at 150 K. Corrections for absorption effects of the X-ray intensities were applied with a numerical method using CrysAlisPro 1.171.43.121 (Rigaku Oxford Diffraction, 2024) [40]. The structure was solved by ShelXT (Sheldrick, 2008) [41]. The model was refined with ShelXL 2019/3 (Sheldrick, 2015) [42]. using full-matrix least-squares implemented in Olex2 1.5-ac5–024 (Dolomanov et al., 2009 [43]).

4.4 | Powder XRD

The powder samples were analyzed using an X-ray powder diffractometer (STOE Darmstadt, STADI-P, Ge-monochromator) with Cu-$K_{\alpha 1}$ radiation ($\lambda = 154.0598$ pm) in the 2θ range of 5° to 70° for $Pb_9O_2I_8(CN_2)_3$ and in the 2θ range of 5° to 45° for $Pb_{16}O_5I_{14}(CN_2)_4$.

15213749, 0, Downloaded from https://onlinelibrary.wiley.com/doi/10.1002/zaac.202500205 by Universitatsbibliothek, Wiley Online Library on [26/01/2026]. See the Terms and Conditions (https://onlinelibrary.wiley.com/terms-and-conditions) on Wiley Online Library for rules of use; OA articles are governed by the applicable Creative Commons License

4.5 | IR-Spectroscopy

Infrared spectra were recorded using a VERTEX 70 FT-IR Spectrometer in the range of 400 cm^{-1} to 4000 cm^{-1} using KBr pellets. Samples were prepared in a glove-box under argon atmosphere.

4.6 | Photoluminescence Spectroscopy

Excitation and emission spectra of $Pb_9O_2I_8(CN_2)_3$ and $Pb_{16}O_5I_{14}(CN_2)_4$ samples were recorded using a fluorescence spectrometer FLS920 (Edinburgh Instruments) equipped with a 450 W xenon discharge lamp (OSRAM) as the radiation source. For powder samples, a mirror optic was mounted inside the sample chamber. For the collection of data, an R2658P single-photon-counting photomultiplier tube from Hamamatsu was used. For temperature adjustment, a cryostat 'MicrostatN' from the company Oxford Instruments had been applied to the present spectrometer. Liquid nitrogen was used as a cooling agent. The photoluminescence decay curve was also measured on the FLS920 spectrometer, while a 375 nm ps laser diode from Edinburgh Instruments was used as an excitation source.

4.7 | Diffuse Reflectance Spectroscopy

The reflectance spectra were recorded on an OceanOptics Maya 2000 Pro spectrometer equipped with a Harrick Praying Mantis sample chamber. A deuterium tungsten lamp (DH 200 BAL) from OceanOptics was used as the light source. The measurement was performed with the following settings: scans to average = 100, boxcar width = 10, and integration time = 300 ms using OceanView 1.6.7 (lite) software from OceanOptics. To determine the optical bandgap E_g, the Tauc equation was used: $(\alpha \cdot h\nu)^{1/r} = A\,(h\nu\text{-}E_g)$, where α is the absorption coefficient, h is the Planck constant, A is a material related constant, and $h\nu$ is the photon energy. For a direct allowed bandgap transition, $r = 1/2$, and for an indirect allowed bandgap transition, $r = 2$.

4.8 | EDX Spectroscopy

The EDX spectroscopy was performed with a Hitachi SU8030 scanning electron microscope equipped with a Bruker QUANTAX 6G EDX detector.

Acknowledgments

We gratefully acknowledge the support provided by the Deutsche Forschungsgemeinschaft (DFG-Bonn) for this research project (ME 914/34–1).

Open Access funding enabled and organized by Projekt DEAL.

Conflicts of Interest

The authors declare no conflicts of interest.

Data Availability Statement

The data that support the findings of this study are available in the Supporting Information of this article. Crystallographic data have been deposited at the Cambridge Crystallographic Data Centre (CCDC) under the following deposition numbers: 2385668 ($Pb_9O_2I_8(CN_2)_3$), and 2415837 ($Pb_{16}O_5I_{14}(CN_2)_4$).

References

1. C. Harriswangler, A. Freire-García, S. Argibay-Otero, et al., "Structural Effects of the Pb^{2+} $6s^2$ Lone Aair Activity: Eccentricity," *Coordination Chemistry Reviews* 529 (2025): 216434.

2. A. Cicirello, A. Swindle, and J. Wang, "Visualizing the Alignment of Lone Pair Electrons in $La_3AsS_5Br_2$ and $La_5As_2S_9Cl_3$ to form an Acentric or Centrosymmetric Structure," *Crystal Engineering Communications* 25 (2023): 6354–6360.

3. O. C. Gagne, and F. C. Hawthorne, "Bond-Length Distributions for Ions Bonded to Oxygen: Results for the Non-Metals and Discussion of Lone-Pair Stereoactivity and the Polymerization of PO_4," *Acta Crystallographica Section B: Structural Science, Crystal Engineering and Materials* 74 (2018): 79–96.

4. X. Tang, H. Xiang, X. Liu, M. Speldrich, and R. Dronskowski, "A Ferromagnetic Carbodiimide: $Cr_2(NCN)_3$," *Angewandte Chemie International Edition* 49 (2010): 4738–4742.

5. P. Kallenbach, M. Ströbele, and H.-J. Meyer, "Missing Carbodiimide and Oxide Carbodiimide of Scandium: $Sc_2(CN_2)_3$ and $Sc_2O_2(CN_2)$," *Zeitschrift für anorganische und allgemeine Chemie* 646 (2020): 1281–1284.

6. A. T. Schwarz, M. Ströbele, and H.-J. Meyer, "The Mixed-Anion Compound $La_2S_2(CN_2)$," *Zeitschrift für anorganische und allgemeine Chemie* 650, no. 15 (2024): 1–4.

7. H. Yasuhiro, T. Masao, K. Shinichi, and K. Fumikazu, "Syntheses of Rare Earth Dioxymonocyanamides ($Ln_2O_2CN_2$, Ln = La, Ce, Pr, Nd, Sm, Eu, Gd)," *Chemistry Letters* 23 (1994): 1963–1966.

8. U. Berger, and W. Schnick, "Syntheses, Crystal Structures, and Vibrational Spectroscopic Properties of $MgCN_2$, $SrCN_2$, and $BaCN_2$," *Journal of Alloys and Compounds* 206 (1994): 179–184.

9. Y. Hashimoto, M. Takahashi, S. Kikkawa, and F. Kanamaru, "Synthesis and Crystal Structure of a New Compound, Lanthanum Dioxymonocyanamide ($La_2O_2CN_2$)," *Journal of Solid State Chemistry* 114 (1995): 592–594.

10. K. Dolabdjian, A. L. Görne, R. Dronskowski, M. Ströbele, and H.-J. Meyer, "Tin(II) Oxide Carbodiimide and its Relationship to SnO," *Dalton Transactions* 47 (2018): 13378.

11. X. Liu, A. Decker, D. Schmitz, and R. Dronskowski, "Crystal Structure Refinement of Lead Cyanamide and the Stiffness of the Cyanamide Anion," *Zeitschrift für anorganische und allgemeine Chemie* 626 (2000): 103.

12. K. Dolabdjian, and H.-J. Meyer, "Lead Carbodiimides Related to the Mineral Bideauxite," *Zeitschrift für anorganische und allgemeine Chemie* 643 (2017): 1898–1903.

13. M. Westerhausen, M. Krofta, S. Schneiderbauer, and H. Piotrowski, "Transmetallierung von Zinn(II) in $[Sn(\mu_3\text{-}PSitBu_3)]_4$ durch Barium – von Sn_4P_4-Heterocuban-Strukturen zu heterobinuklearen Käfigverbindungen mit einem zentralen $BanSn_4-nP_4$-Heterocuban-Polyeder (n = 1, 2 und 3)," *Zeitschrift für anorganische und allgemeine Chemie* 631 (2005): 1391–1396.

14. S. Traut, and C. von Hänisch, "Würfelspiele im Bereich der Heterokubane: Synthese und Charakterisierung von Molekülverbindungen der Systeme Sn/E und Pb/E (E = P/As)," *Zeitschrift für anorganische und allgemeine Chemie* 637 (2011): 1777–1783.

15. M. Scheikowski, and H. Müller-Buschbaum, "Zur Kristallchemie der Blei-Lanthanoid-Oxoaluminate. Zur Kenntnis von $Pb_2HoAl_3O_8$ und $Pb_2LuAl_3O_8$," *Zeitschrift für anorganische und allgemeine Chemie* 619 (1993): 1755–1758.

16. M. Löber, C. S. Geißenhöner, M. Ströbele, C. P. Romao, and H.-J. Meyer, "Synthesis, Structure and Electronic Properties of Three

15213749, 0, Downloaded from https://onlinelibrary.wiley.com/doi/10.1002/zaac.202500205 by Universitatsbibliothek, Wiley Online Library on [26/01/2026]. See the Terms and Conditions (https://onlinelibrary.wiley.com/terms-and-conditions) on Wiley Online Library for rules of use; OA articles are governed by the applicable Creative Commons License

Tin Oxide Halides," *European Journal of Inorganic Chemistry* 2021 (2021): 283–288.

17. M. Löber, C. S. Geißenhöner, M. Ströbele, S. Indris, C. P. Romao, and H.-J. Meyer, "Synthesis, Structure, and Electronic Properties of $Sn_9O_5Cl_4(CN_2)_2$," *Inorganic Chemistry* 58 (2019): 14560–14567.

18. A. T. Schwarz, N. Petersen, M. Ströbele, et al., "A Mixed-Anion Compound based Upon a $[Pb_4O_4]$ Heterocubane Unit: Synthesis, Structure and Electronic Properties of $Pb_8O_4I_6(CN_2)$," *Dalton Transactions* 54 (2025): 15169–15175.

19. C. N. R. Rao, and K. Biswas, *Essentials of Inorganic Materials Synthesis*, Wiley, (2015): 17–21.

20. A. T. Schwarz, M. Ströbele, C. P. Romao, D. Enseling, T. Jüstel, and H.-J. Meyer, "The Luminescent Semiconductor $Pb_7I_6(CN_2)_4$," *Dalton Transactions* 53 (2024): 6416–6422.

21. X. Liu, A. Decker, D. Schmitz, and R. Dronskowski, "Crystal Structure Refinement of Lead Cyanamide and the Stiffness of the Cyanamide Anion," *Zeitschrift für anorganische und allgemeine Chemie* 626 (2000): 103–105.

22. T. Oldag, and H.-L. Keller, "Synthese und Kristallstruktur von Blei(II)-oxidhalogenid-Alkoholaten mit unterschiedlichen Verknüpfungsvarianten von Pb_4O_4-Heterokubaneinheiten," *Zeitschrift für anorganische und allgemeine Chemie* 632 (2006): 1267–1272.

23. K. W. Klinkhammer, Y. Xiong, and S. Yao, "Molecular Lead Clusters —From Unexpected Discovery to Rational Synthesis," *Angewandte Chemie International Edition* 43 (2004): 6202–6204.

24. W. W. Wendlandt, and H. G. Hecht, *Reflectance Spectroscopy*, Wiley, (1966): 298.

25. P. Makuła, M. Pacia, and W. Macyk, "How To Correctly Determine the Band Gap Energy of Modified Semiconductor Photocatalysts Based on UV–Vis Spectra," *The Journal of Physical Chemistry Letters* 9 (2018): 6814–6817.

26. X. Wang, F. Jahanbazi, J. Wei, C. U. Segre, W. Chen, and Y. Mao, "Charge Transfer-Triggered Bi^{3+} Near-Infrared Emission in $Y_2Ti_2O_7$ for Dual-Mode Temperature Sensing," *ACS Applied Materials & Interfaces* 14 (2022): 36834–36844.

27. R. Alexey, R. Mariana, and G. Veronika, "Optical Properties of Pb_2MoO_5 and Pb_2WO_5 Single Crystals as Materials for Practical Applications," *Optik: International Journal for Light and Electron Optics* 226 (2021): 165912.

28. A. B. Gawande, J. T. Ingle, R. P. Sonekar, and S. K. Omanwar, "Photoluminescence in Pb^{2+} Activated SrB_4O_7 and SrB_2O_4 Phosphors," *Journal of Luminescence* 149 (2014): 236–239.

29. P. Yang, M. K. Lü, C. F. Song, S. W. Liu, F. Gu, and S. F. Wang, "Photoluminescence of Pb^{2+} Ions in Sol–Gel Derived Zn_2SiO_4," *Inorganic Chemistry Communications* 7 (2004): 268–270.

30. W. C. Collins, and J. H. Crawford, "Polarized Luminescence of Pb^{2+} in NaCl," *Solid State Communications* 9 (1971): 853–856.

31. J. A. Groenink, and G. Blasse, "Some New Observations on the Luminescence of $PbMoO_4$ and $PbWO_4$," *Journal of Solid State Chemistry* 32 (1980): 9–20.

32. H. Folkerts, M. Hamstra, and G. Blasse, "The Luminescence of Pb^{2+} in Alkaline Earth Sulfates," *Chemical Physics Letters* 246 (1995): 135–138.

33. H. F. Folkerts, and G. Blasse, "Luminescence of Pb^{2+} in Several Calcium Borates," *Journal of Materials Chemistry* 5 (1995): 273–276.

34. C. P. Joshi, and S. V. Moharil, "Luminescence of Pb^{2+} in Some Aluminates Prepared by Combustion Synthesis," *Physica Status Solidi (B)* 220 (2000): 985–989.

35. J. Chen, S. Wang, Y. Du, and L. Chen, "Study on the Spectroscopic Properties of Pb^{2+} Doped SrI_2 Single Crystals," *Journal of Alloys and Compounds* 597 (2014): 249–257.

36. N. Yamashita, T. Ohira, H. Mizuochi, and S. Asano, "Luminescence of Pb^{2+} Centers in SrS and SrSe Phosphors," *Journal of the Physical Society of Japan* 53 (1984): 419–426.

37. Y. Liang, F. Liu, Y. Chen, K. Sun, and Z. Pan, "Long Persistent Luminescence in the Ultraviolet in Pb^{2+}-doped $Sr_2MgGe_2O_7$ Persistent Phosphor," *Dalton Transactions* 45 (2016): 1322–1326.

38. J. Chen, S. Wang, Y. Du, and L. Chen, "Temperature-Dependent Photoluminescence Study of Pb^{2+} Doped Strontium Iodide," *2013 IEEE Nuclear Science Symposium and Medical Imaging Conference (NSS/MIC)*, (2013): 1–6.

39. G. Blasse, and B. C. Grabmaier, *A General Introduction to Luminescent Materials*, in *Luminescent Materials*, Springer, (1994): 1–9.

40. CrysAlisPro Software System, Rigaku Oxford Diffraction, (2024).

41. G. M. Sheldrick, "A Short History of SHELX," *Acta Crystallographica. Section A, Foundations of Crystallography* 64 (2008): 112–122.

42. G. M. Sheldrick, "Crystal Structure Refinement with SHELXL," *Acta Crystallographica Section C: Structural Chemistry* 71 (2015): 3–8.

43. O. V. Dolomanov, L. J. Bourhis, R. J. Gildea, J. A. K. Howard, and H. Puschmann, "OLEX2: A Complete Structure Solution, Refinement and Analysis Program," *Journal of Applied Crystallography* 42 (2009): 339–341.

Supporting Information

Additional supporting information can be found online in the Supporting Information section. **Supporting Fig. S1:** Powder XRD of compound $Pb_9O_2I_8(CN_2)_3$. **Supporting Fig. S2:** Powder XRD of compound $Pb_{16}O5I_{14}(CN_2)_4$. **Supporting Fig. S3:** Infrared spectrum of $Pb_9O_2I_8(CN_2)_3$. **Supporting Fig. S4:** Crystallographic distinct lead position and surrounding in the compound $Pb_{16}O_5I_{14}(CN_2)_4$. **Supporting Fig. S5:** Infrared spectrum of $Pb_{16}O_5I_{14}(CN_2)_4$. **Supporting Fig. S6:** Tauc plot for indirect allowed transition of the compound $Pb_9O_2I_8(CN_2)_3$. **Supporting Fig. S7:** Tauc plot for direct allowed transition of the compound $Pb_9O_2I_8(CN_2)_3$. **Supporting Fig. S8:** Tauc plot for indirect allowed transition of the compound $Pb_{16}O_5I_{14}(CN_2)_4$. **Supporting Fig. S9:** Tauc plot for direct allowed transition of the compound $Pb_{16}O_5I_{14}(CN_2)_4$. **Supporting Fig. S10:** Temperature dependent emission spectra of $Pb_9O_2I_8(CN_2)_3$ upon 377 nm excitation between 80 and 200 K. **Supporting Fig. S11:** Temperature dependent emission spectra of $Pb_{16}O_5I_{14}(CN_2)_4$ upon 377 nm excitation between 80 and 200 K. **Supporting Fig. S12:** Decay measurement of the 520 nm emission of $Pb_9O_2I_8(CN_2)_3$ at 80 K after excitation at 377 nm. **Supporting Fig. S13:** Decay measurement of the 520 nm emission of $Pb_{16}O5I_{14}(CN_2)_4$ at 80 K after excitation at 377 nm. **Supporting Table S1:** Selected interatomic distances for $Pb_9O_2I_8(CN_2)_3$ in [Å]. **Supporting Table S2:** Selected interatomic distances for $Pb_{16}O_5I_{14}(CN_2)_4$ in [Å].

15213749, 0, Downloaded from https://onlinelibrary.wiley.com/doi/10.1002/zaac.202500205 by Universitatsbibliothek, Wiley Online Library on [26/01/2026]. See the Terms and Conditions (https://onlinelibrary.wiley.com/terms-and-conditions) on Wiley Online Library for rules of use; OA articles are governed by the applicable Creative Commons License

From Heterocubane Units to Extended Networks: Synthesis, Structure, and Optical Properties of $Pb_9O_2I_8(CN_2)_3$ and $Pb_{16}O_5I_{14}(CN_2)_4$

Albert T. Schwarz,[a] Markus Ströbele,[a] David Enseling,[b] Thomas Jüstel,[b] and H.-Jürgen Meyer *[a]

Corresponding Author

*Prof. Dr. H.-Jürgen Meyer
Section for Solid State and Theoretical Inorganic Chemistry
Institute of Inorganic Chemistry
University of Tübingen
Auf der Morgenstelle 18
72076 Tübingen

E-mail: juergen.meyer@uni-tuebingen.de

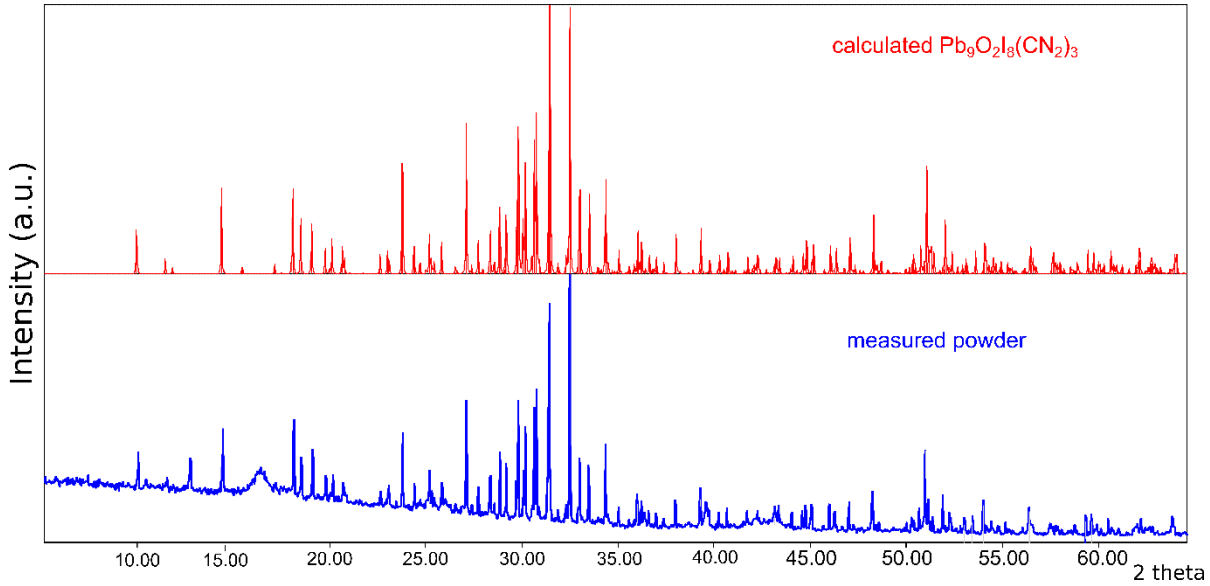

Figure S 1: Powder XRD of compound $Pb_9O_2I_8(CN_2)_3$.

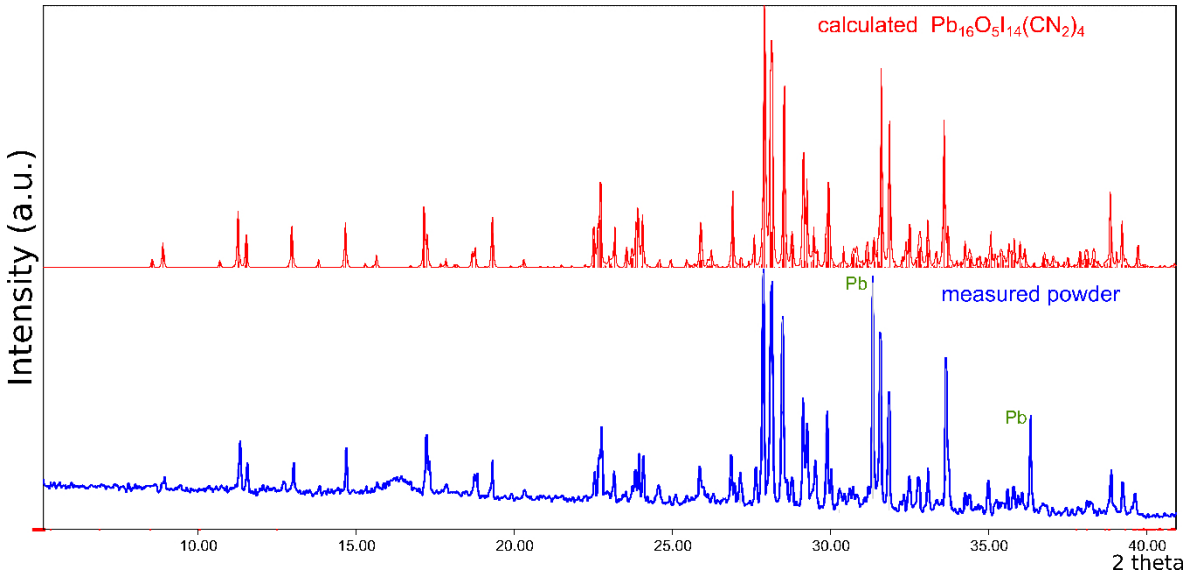

Figure S 2: Powder XRD of compound $Pb_{16}O_5I_{14}(CN_2)_4$.

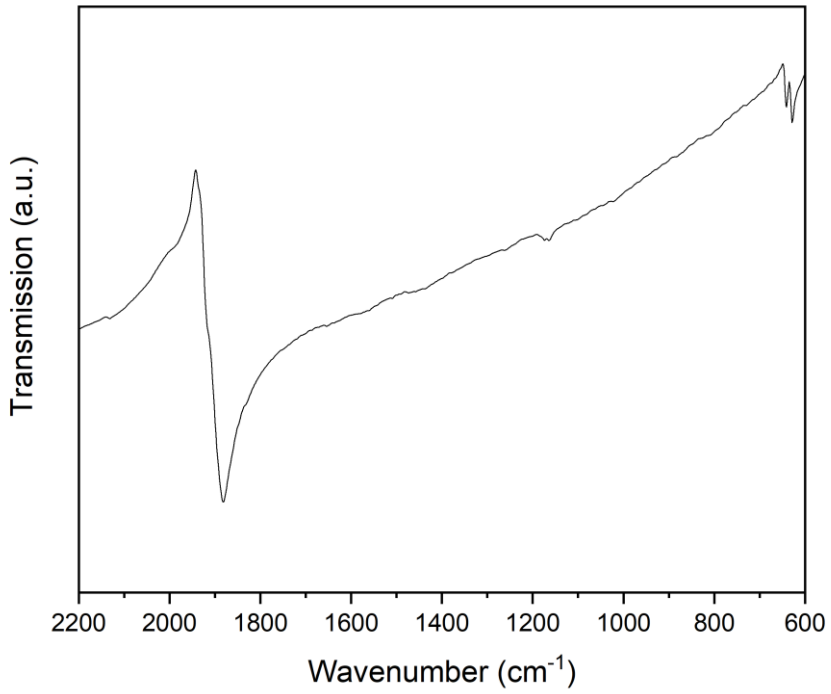

Figure S 3: Infrared spectrum of $Pb_9O_2I_8(CN_2)_3$.

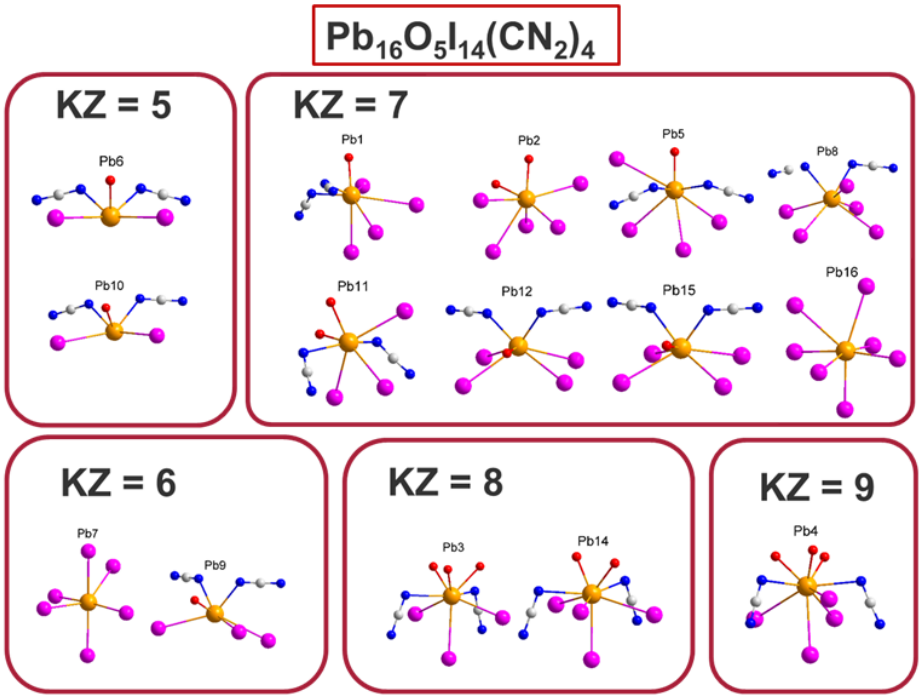

Figure S 4: Crystallographic distinct lead position and surrounding in the compound $Pb_{16}O_5I_{14}(CN_2)_4$.

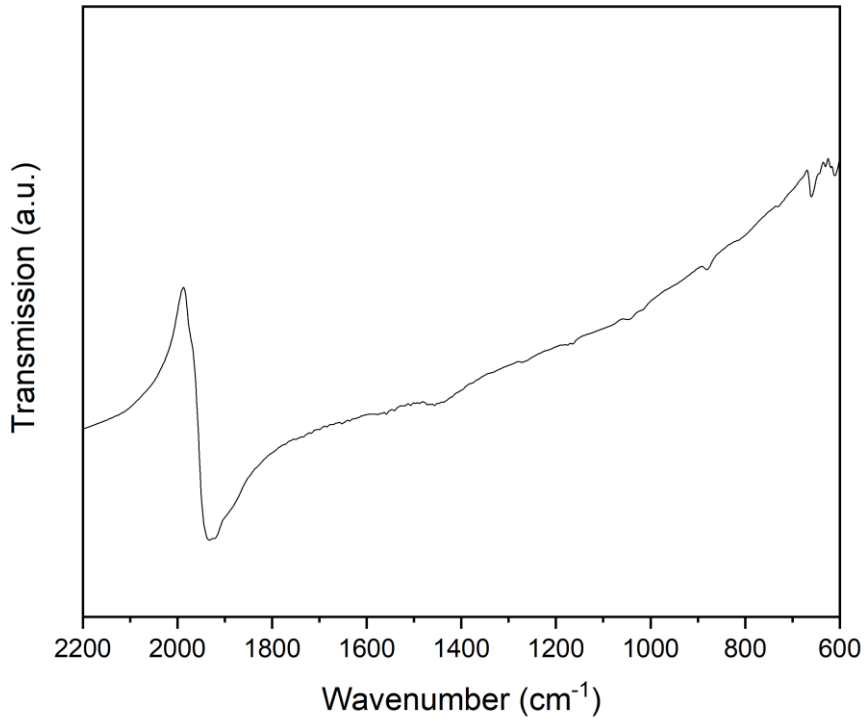

Figure S 5: Infrared spectrum of $Pb_{16}O_5I_{14}(CN_2)_4$.

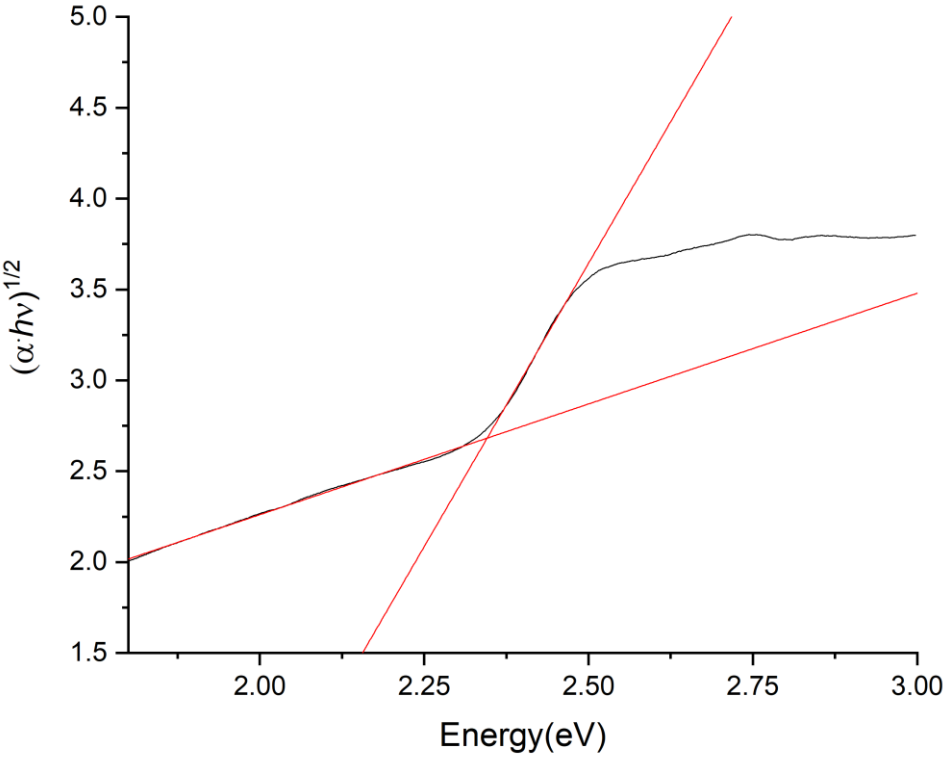

Figure S 6: Tauc plot for indirect allowed transition of the compound $Pb_9O_2I_8(CN_2)_3$.

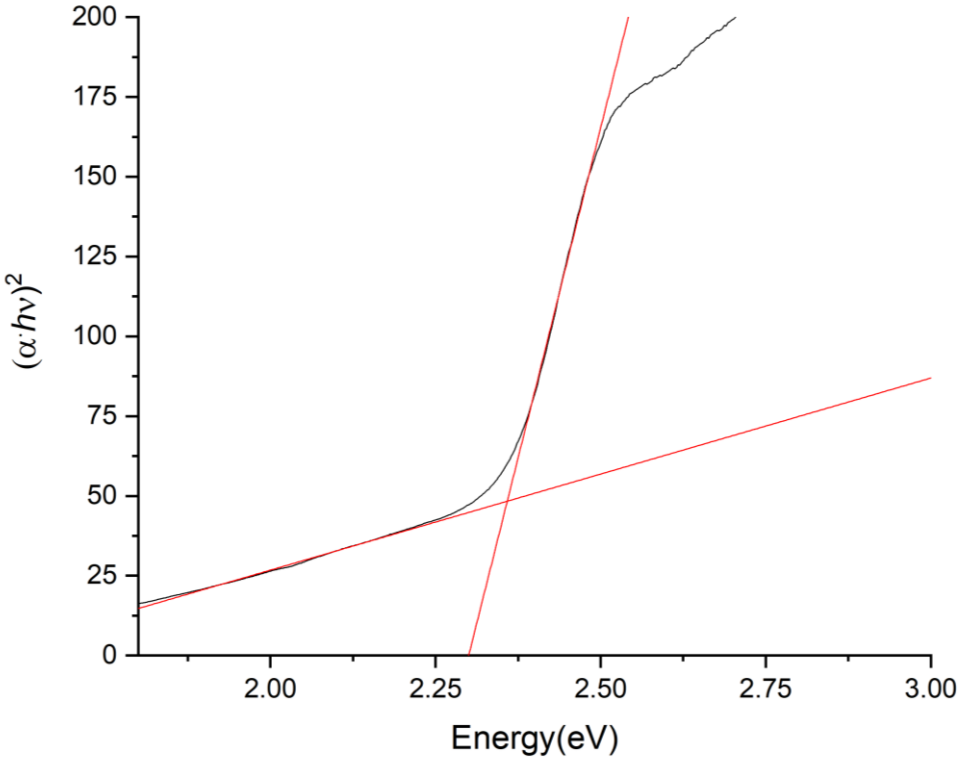

Figure S 7: Tauc plot for direct allowed transition of the compound $Pb_9O_2I_8(CN_2)_3$.

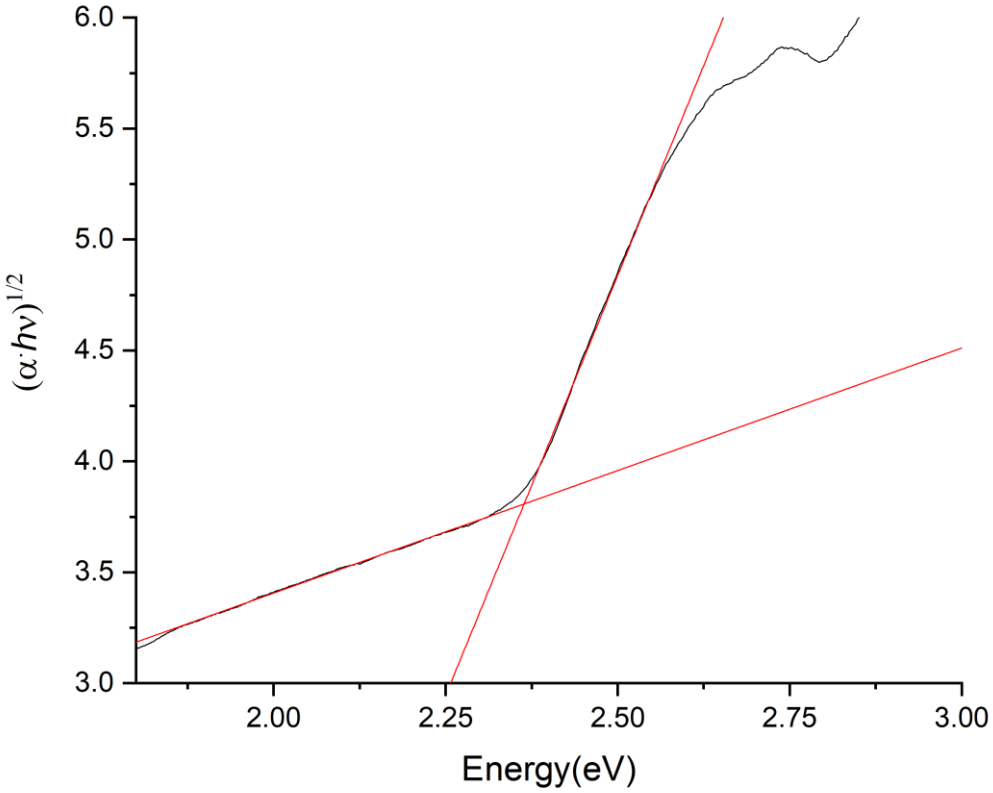

Figure S 8: Tauc plot for indirect allowed transition of the compound $Pb_{16}O_5I_{14}(CN_2)_4$.

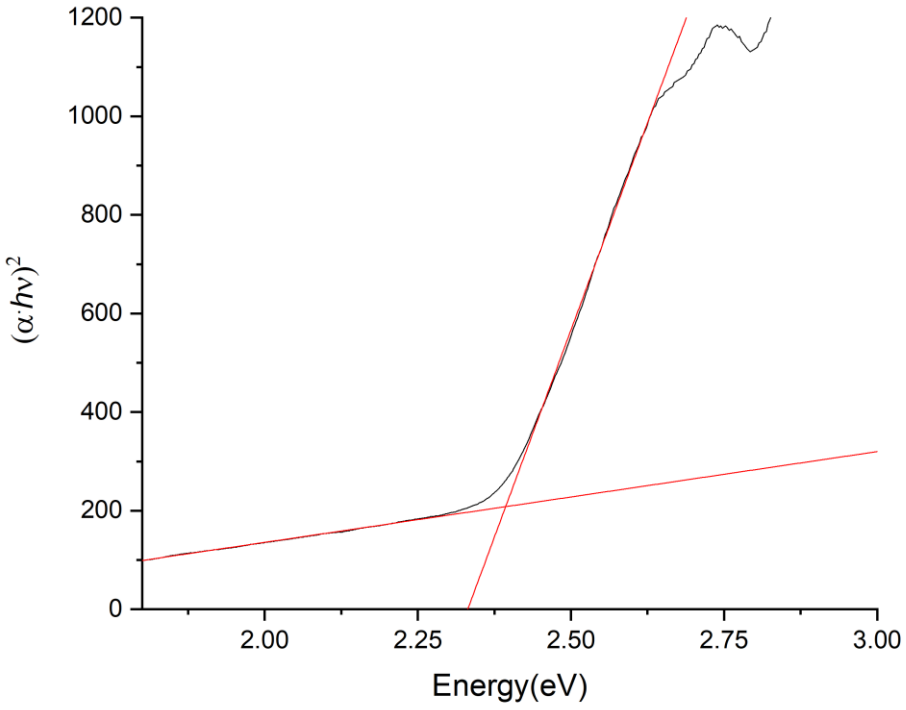

Figure S 9: Tauc plot for direct allowed transition of the compound $Pb_{16}O_5I_{14}(CN_2)_4$

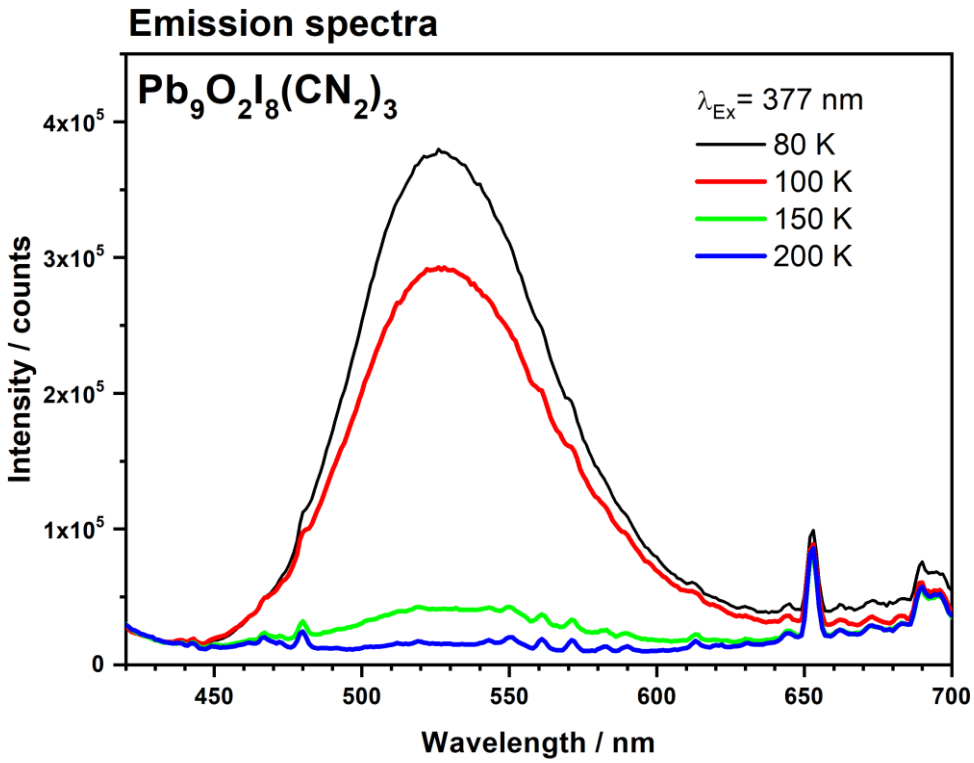

Figure S 10: Temperature dependent emission spectra of $Pb_9O_2I_8(CN_2)_3$ upon 377 nm excitation between 80 and 200 K.

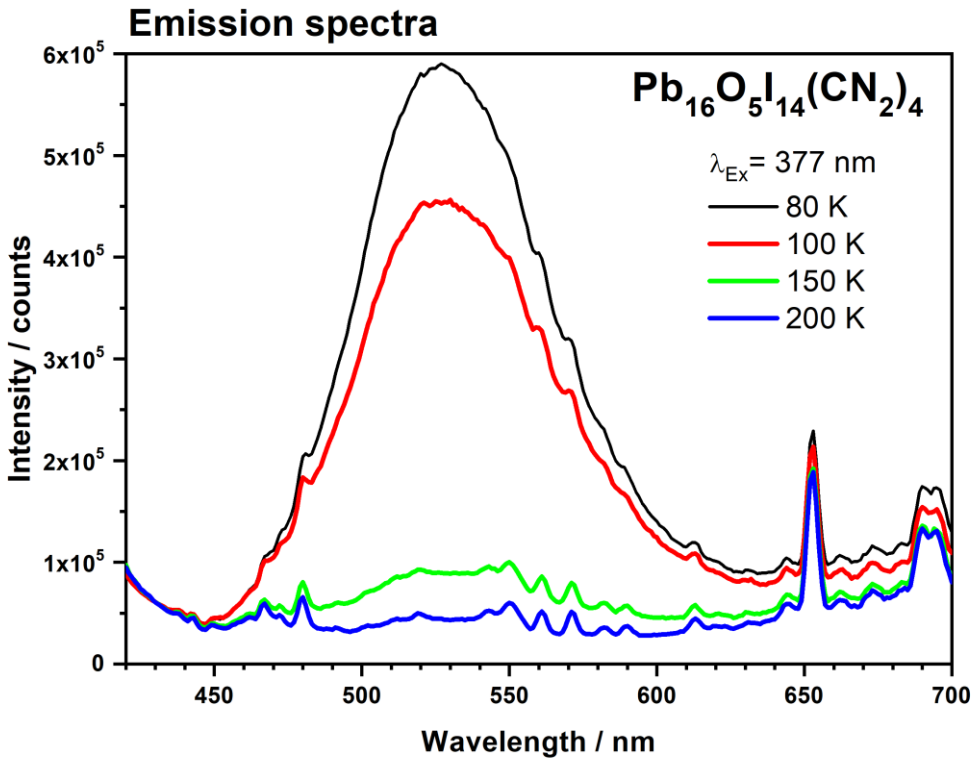

Figure S 11: Temperature dependent emission spectra of $Pb_{16}O_5I_{14}(CN_2)_4$ upon 377 nm excitation between 80 and 200 K.

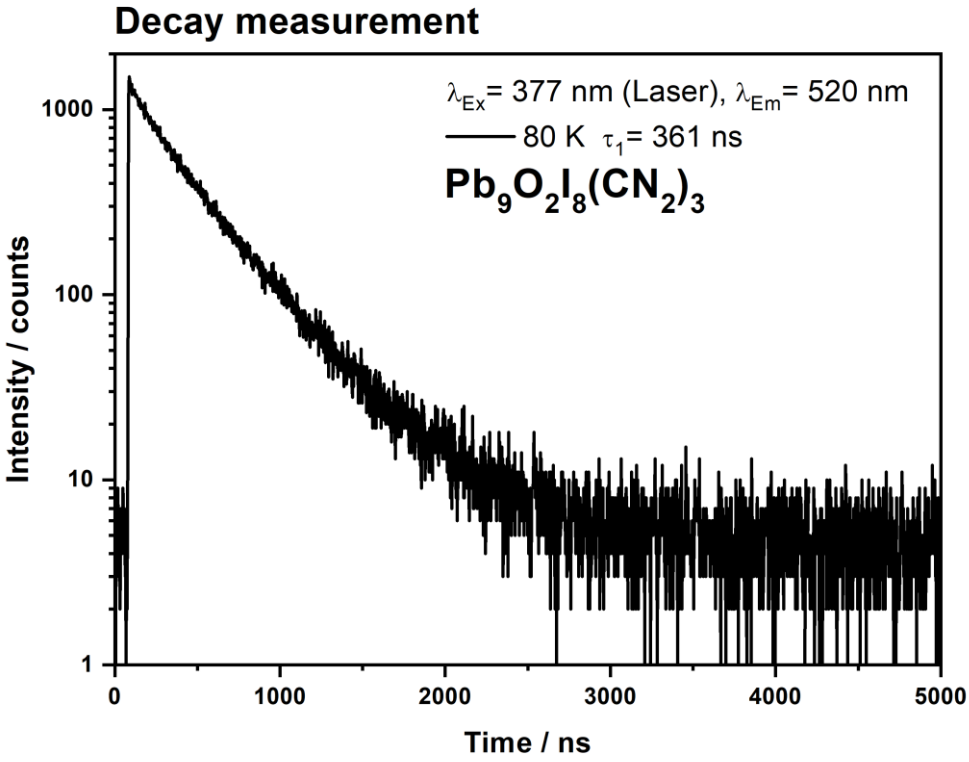

Figure S 12: Decay measurement of the 520 nm emission of $Pb_9O_2I_8(CN_2)_3$ at 80 K after excitation at 377 nm.

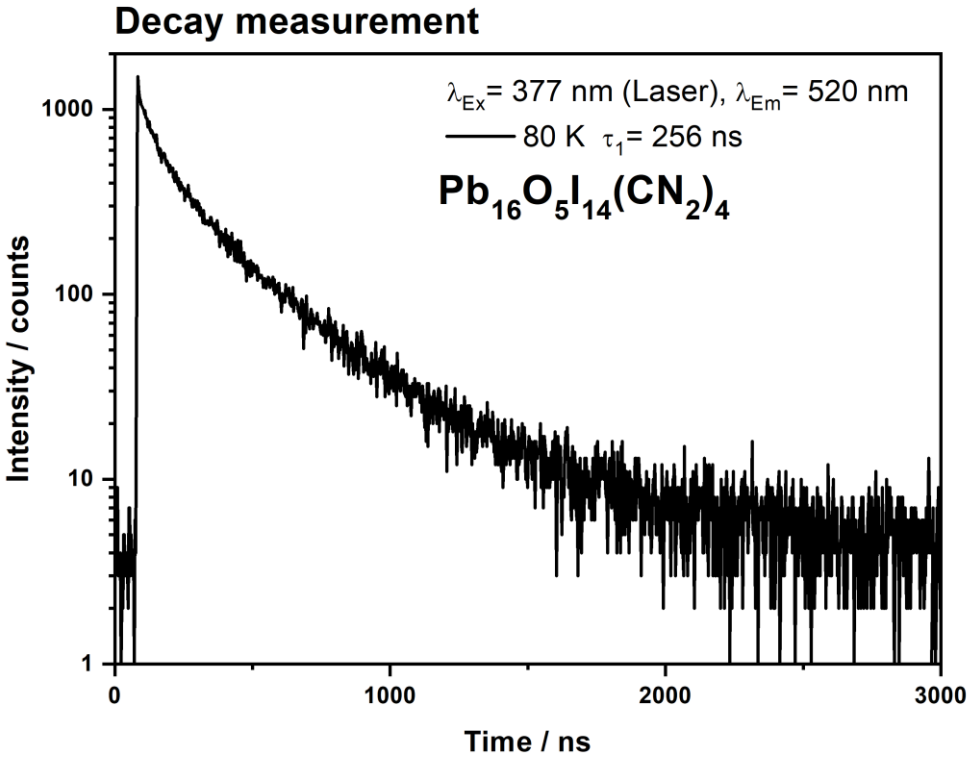

Figure S 13: Decay measurement of the 520 nm emission of $Pb_{16}O_5I_{14}(CN_2)_4$ at 80 K after excitation at 377 nm.

Table S1: Selected interatomic distances for $Pb_9O_2I_8(CN_2)_3$ in [Å]

Pb(1)-I(1) **#1**	3.1975(3)
Pb(1)-I(1)	3.1976(3)
Pb(1)-I(2)	3.1835(3)
Pb(1)-I(2) **#1**	3.1835(3)
Pb(1)-I(3)	3.0443(3)
Pb(1)-I(3) **#1**	3.0443(3)
Pb(2)-I(3)	3.3944(3)
Pb(2)-N(1)	2.528(4)
Pb(2)-N(2)	2.658(4)
Pb(2)-N(3)	2.504(4)
Pb(3)-I(4)	3.1665(3)
Pb(3)-O(1)	2.301(3)
Pb(3)-N(2)	2.607(4)
Pb(3)-N(3)	2.526(4)
Pb(4)-Pb(4) **#2**	3.5814(3)
Pb(4)-O(1) **#2**	2.492(3)
Pb(4)-O(1)	2.335(3)
Pb(4)-N(1)	2.750(4)
Pb(4)-N(3)	2.751(3)
Pb(5)-I(4) **#2**	3.3833(3)
Pb(5)-O(1)	2.295(3)
Pb(5)-N(1)	2.474(4)
Pb(5)-N(2)	2.543(3)
N(1)-C(1)	1.233(4)
N(2)-C(2)	1.234(5)
N(3)-C(2) **#3**	1.236(5)

Symmetry transformations used to generate equivalent atoms:
#1 -x+1,y,-z+1/2, **#2** -x,-y+1,-z+1, **#3** -x+1/2,y+1/2,z

Table S2: Selected interatomic distances for $Pb_{16}O_5I_{14}(CN_2)_4$ in [Å].

Pb(1)-O(1)	2.181(3)
Pb(1)-N(2) **#1**	2.501(4)
Pb(1)-N(5) **#2**	2.475(4)
Pb(2)-Pb(3)	3.5260(3)
Pb(2)-Pb(4)	3.4068(3)
Pb(2)-I(2) **#2**	3.3640(4)
Pb(2)-O(1)	2.287(4)
Pb(2)-O(2)	2.262(3)
Pb(3)-Pb(4)	3.3892(2)
Pb(3)-O(1)	2.369(3)
Pb(3)-O(2)	2.394(3)
Pb(3)-O(4) **#2**	2.345(3)
Pb(4)-O(1)	2.500(3)
Pb(4)-O(2)	2.406(3)
Pb(4)-O(4) **#2**	2.308(3)
Pb(4)-N(1)	2.798(4)
Pb(5)-O(2)	2.188(3)
Pb(5)-N(1)	2.458(4)
Pb(5)-N(3)	2.493(4)
Pb(6)-I(1)	3.3601(4)
Pb(6)-I(7) **#2**	3.4016(4)
Pb(6)-O(4) **#2**	2.292(3)
Pb(6)-N(1)	2.482(4)
Pb(6)-N(3)	2.506(4)
Pb(7)-I(1)	3.2077(4)
Pb(7)-I(2)	3.1229(4)
Pb(7)-I(3)	3.0522(4)
Pb(7)-I(4)	3.2454(4)
Pb(7)-I(5)	3.2946(4)
Pb(8)-I(4)	3.2885(4)
Pb(8)-I(6)	3.3683(4)
Pb(8)-I(7)	3.3539(4)
Pb(8)-I(9) **#3**	3.3991(4)
Pb(8)-N(4)	2.491(4)
Pb(8)-N(6)	2.514(4)
Pb(9)-O(3)	2.283(3)
Pb(9)-N(4)	2.460(4)

Pb(9)-N(6)	2.492(4)
Pb(10)-Pb(11)	3.6983(3)
Pb(10)-O(3)	2.266(3)
Pb(10)-N(7) **#3**	2.425(4)
Pb(10)-N(8)	2.409(4)
Pb(11)-Pb(14) **#3**	3.6449(2)
Pb(11)-I(8)	3.3671(4)
Pb(11)-I(10) **#3**	3.4073(4)
Pb(11)-O(3)	2.361(3)
Pb(11)-O(5) **#3**	2.364(3)
Pb(11)-N(8)	2.619(4)
Pb(12)-O(4)	2.287(3)
Pb(12)-N(2) **#4**	2.424(4)
Pb(12)-N(5)	2.423(4)
Pb(13)-I(5)	3.3565(4)
Pb(13)-I(9)	3.1671(4)
Pb(13)-I(10)	3.2610(4)
Pb(13)-I(11)	3.3837(4)
Pb(13)-O(5)	2.270(3)
Pb(14)-I(9)	3.3761(4)
Pb(14)-O(3) **#5**	2.328(3)
Pb(14)-O(5)	2.324(3)
Pb(14)-N(7)	2.603(4)
Pb(15)-I(11)	3.3784(4)
Pb(15)-O(5)	2.351(3)
Pb(15)-N(7)	2.528(4)
Pb(15)-N(8) **#5**	2.494(4)
Pb(16)-I(11)	3.2845(4)
Pb(16)-I(12)	3.1814(4)
Pb(16)-I(13)	3.0521(4)
Pb(16)-I(14)	3.0833(4)
N(1)-C(1)	1.229(6)
N(2)-C(1)	1.229(6)
N(3)-C(4) **#6**	1.220(6)
N(4)-C(2)	1.234(6)
N(5)-C(2)	1.228(6)
N(6)-C(3)	1.225(6)
N(7)-C(3)	1.238(6)
N(8)-C(4)	1.240(6)

Symmetry transformations used to generate equivalent atoms:

#1 -x+1/2,-y+1/2,z+3/2, **#2** x-1/2,-y+3/2,-z-1

#3 -x+3/2,-y-1/2,z+3/2, **#4** -x+1,y+1,-z+5/2, **#5** -x+3/2,-y+1/2,z+3/2

#6 x-1/2,-y+1/2,-z-1,

Publication 6

Synthesis, Structure, and Eu^{3+}-Activated Photoluminescence of the Mixed-Anion Carbodiimide $NaLa_2F_3(CN_2)_2$

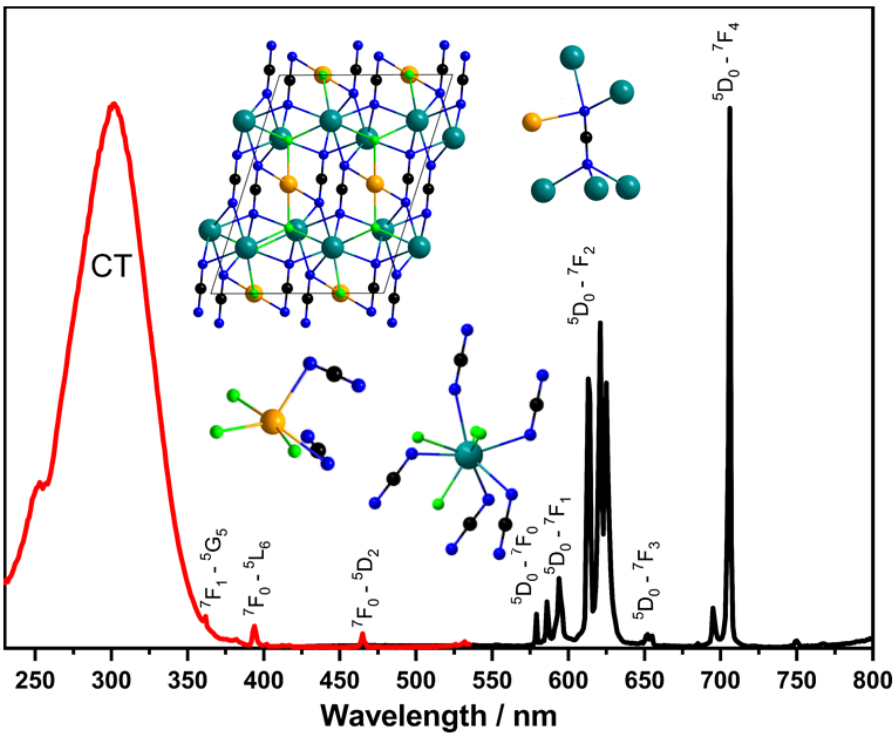

https://doi.org/10.1002/zaac.202500221

Reprinted from

Z. Anorg. Allg. Chem. ***2025****, 0, e202500221*

with permission from

Copyright © 2025 Wiley-VCH GmbH

Check for updates

Zeitschrift für anorganische und allgemeine Chemie

Journal of Inorganic and General Chemistry
ZAAC
Zeitschrift für anorganische und allgemeine Chemie

RESEARCH ARTICLE OPEN ACCESS

Synthesis, Structure, and Eu^{3+}-Activated Photoluminescence of the Mixed-Anion Carbodiimide $NaLa_2F_3(CN_2)_2$

Albert T. Schwarz[1] | Markus Ströbele[1] | David Enseling[2] | Thomas Jüstel[2] | H.-Jürgen Meyer[1]

[1]Section for Solid State and Theoretical Inorganic Chemistry, Institute of Inorganic Chemistry, Eberhard Karls University, Tübingen, Germany | [2]Department of Chemical Engineering, FH Münster University of Applied Science, Steinfurt, Germany

Correspondence: Thomas Jüstel (tj@fh-muenster.de) | H.-Jürgen Meyer (juergen.meyer@uni-tuebingen.de)

Received: 7 October 2025 | **Revised:** 16 November 2025 | **Accepted:** 19 November 2025

Keywords: carbodiimide | crystal structure | lanthanum | luminescence

ABSTRACT

The mixed-anion compound $NaLa_2F_3(CN_2)_2$ was synthesized by solid-state metathesis from LaF_3 and $Na_2(CN_2)$, and structurally characterized by single-crystal X-ray diffraction. Its framework structure consists of distorted La polyhedra linked by $[NCN]^{2-}$ ligands and fluorine atoms, with Na cations in interstitial sites. Eu^{3+}-doped $NaLa_2F_3(CN_2)_2$ shows a broad charge-transfer excitation band and the characteristic $^5D_0-^7F_J$ emissions, dominated by a $^5D_0-^7F_4$ transition.

1 | Introduction

The exploration of rare-earth (*RE*) carbodiimide compounds has advanced significantly in recent years, largely driven by the development of solid-state metathesis (SSM) reactions. These enable efficient access to *RE*-carbodiimides under moderate thermal conditions, avoiding high-pressure or solution-based routes [1]. The central anionic motif in this chemistry is the linear and highly polarizable carbodiimide $(N{=}C{=}N)^{2-}$ ion, which offers capabilities for connecting metal centers and forming extended frameworks or clusters. Binary *RE* carbodiimides with the formula $RE_2(CN_2)_3$ have been synthesized for nearly the entire *RE* series [2–4]. The recent successful synthesis of $La_2(CN_2)_3$, previously a missing member of the series, has helped clarify the structural trends within this family. $La_2(CN_2)_3$ displays a layered arrangement of La^{3+} ions and carbodiimide ligands with a notably expanded coordination sphere, reflecting the relatively large ionic radius of La^{3+} [5]. Structural diversification through mixed-anion chemistry has led to novel *RE* carbodiimide compounds such as $La_2S_2(CN_2)$, the first *RE* sulfide-carbodiimide [6]. This compound exhibits a layered structure analogous to that of $La_2O_2(CN_2)$ [7], in which $(NCN)^{2-}$ and S^{2-} or O^{2-} occupy alternating layers. These materials illustrate how the combination of anionic building blocks modulates both local coordination and extended structure, and how even subtle anion substitutions (O^{2-} vs. S^{2-}) impact the resulting topology and properties. Parallel to these developments, *RE* carbodiimide halides have attracted growing attention, especially for their structural richness and the possibility of hosting mixed-valent cations [8–12]. A key example is $Eu_4F_5(CN_2)_2$, a compound containing three Eu^{2+} and one Eu^{3+} per formula unit, as confirmed by Mössbauer spectroscopy [13]. Its crystal structure features four crystallographically distinct europium sites and shows evidence of charge ordering. Interestingly, its tetragonal structure (space group $p\bar{4}2_1c$) can be rationalized as a distortion of a higher-symmetry arrangement, as demonstrated by the compound $LaSr_3F_5(CN_2)_2$, which crystallizes in the space group $I\bar{4}2m$ [14]. This connection provides a rare example of structural control over electronic configuration in *RE* carbodiimide architectures. Carbodiimides of the general composition $ARE[Si(CN_2)_4]$ and $ARE[Ge(CN_2)_4]$ (A = alkali metal, RE = La–Gd) complement this chemistry by introducing rigid, tetrahedrally coordinated anionic building blocks. These materials display photoluminescent behavior, particularly when doped with Eu^{3+} or Tb^{3+}, and have been investigated for their nonlinear optical and luminescence properties [15–18]. Within this broader framework of *RE* carbodiimide

This is an open access article under the terms of the Creative Commons Attribution License, which permits use, distribution and reproduction in any medium, provided the original work is properly cited.

© 2025 The Author(s). *Zeitschrift für anorganische und allgemeine Chemie* published by Wiley-VCH GmbH.

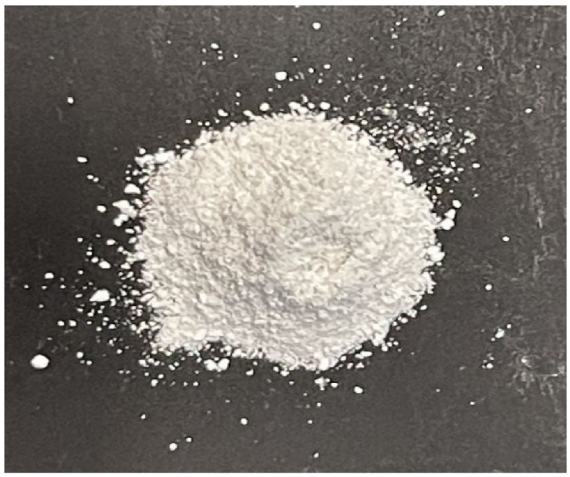

FIGURE 1 | White crystal powder of $NaLa_2F_3(CN_2)_2$.

chemistry, the $RE_8O(CN_2)_{10}Br_2$ compounds (RE = La, Ce, Pr, Nd) [19] represent a class of cluster-based mixed-anion materials. Their structures are composed of oxygen-centered octahedral *RE* clusters of the type $[RE_6O(NCN)_8]$, that are interconnected by bridging carbodiimide units into a three-dimensional network. This topology deviates markedly from the common layered or chain-like motifs and demonstrates how the interplay of oxide, halide, and carbodiimide anions can stabilize unique structural motifs. Notably, the cerium-containing variant, $Ce_8O(CN_2)_{10}Br_2$, exhibits broad yellow photoluminescence under UV excitation, underscoring the potential of such cluster-based systems for optical applications. This result highlights how compositional and structural design in *RE* carbodiimide frameworks can be used to systematically tune functional properties. Because of the stability and the structural as well as functional diversity of *RE* carbodiimides, the present work focuses on the synthesis and characterization of a new mixed-anion carbodiimide.

2 | Results and Discussion

2.1 | Synthesis of $NaLa_2F_3(CN_2)_2$

The preparation of carbodiimide-based solids has frequently been achieved by SSM reactions, a concept well established in synthetic solid-state chemistry. The method exploits the formation of thermodynamically stable alkali-metal halides (LiCl, LiF, NaCl, etc.) as a driving force, enabling the synthesis of crystalline carbodiimide phases at relatively moderate temperatures [1]. A classical example includes the straightforward reaction of a *RE* halide with $Li_2(CN_2)$ or $Na_2(CN_2)$ to yield binary $RE_2(CN_2)_3$ compounds

$$2RECl_3 + 3Li_2(CN_2) \rightarrow RE_2(CN_2)_3 + 6LiCl \quad (1)$$

Such reactions are typically carried out in sealed silica or copper ampoules to avoid (oxide) contamination, and the coproduced alkali halide, that appears as metathesis salt, can be removed by simple washing procedures. The versatility of this method has enabled the expansion of carbodiimide chemistry from binary phases to more complex systems including $Li_2SrGd_2(CN_2)_5$ [20].

In this context, the SSM pathway was employed for the synthesis of the air- and moisture-stable compound $NaLa_2F_3(CN_2)_2$. It was obtained from appropriate amounts of LaF_3 and $Na_2(CN_2)$ following the metathesis reaction (2) as a white powder (Figure 1) in high yield and sufficient purity (Figure 2).

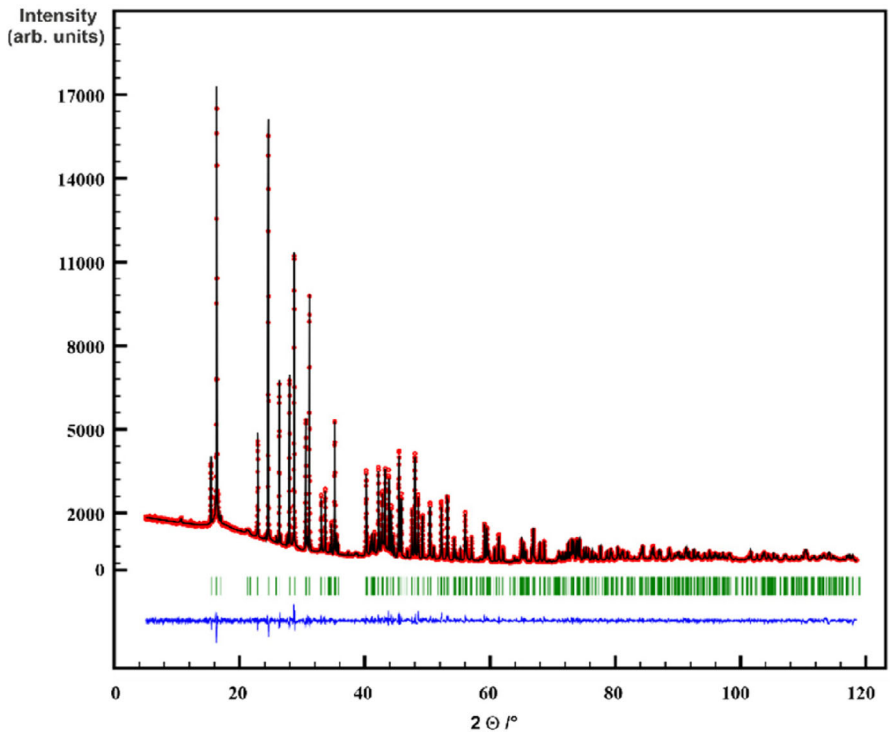

FIGURE 2 | Rietveld refinement of the XRD powder pattern of $NaLa_2F_3(CN_2)_2$. Observed intensities are marked as red circles, and calculated intensities as black lines. Bragg positions are marked as green lines, the difference curve $I_{observed} - I_{calculated}$ as blue line.

15213749, 0, Downloaded from https://onlinelibrary.wiley.com/doi/10.1002/zaac.202500221 by Universitatsbibliothek, Wiley Online Library on [29/12/2025]. See the Terms and Conditions (https://onlinelibrary.wiley.com/terms-and-conditions) on Wiley Online Library for rules of use; OA articles are governed by the applicable Creative Commons License

$$2LaF_3 + 2Na_2(CN_2) \rightarrow NaLa_2F_3(CN_2)_2 + 3NaF \quad (2)$$

This reaction demonstrates once again that *RE* fluorides are also suitable starting materials in SSM reactions leading to carbodiimide-based mixed-anion compounds.

2.2 | Crystal Structure of $NaLa_2F_3(CN_2)_2$

The crystal structure of $NaLa_2F_3(CN_2)_2$ was solved and refined by single-crystal X-ray diffraction (XRD) based on recorded single-crystal data. The refinement led to the monoclinic space group *I*2/*a*. Additional crystal structure and refinement data are summarized in Table 1.

We note that the structure of $NaLa_2F_3(CN_2)_2$ is isotypic to that of a series of compounds having the composition $LiRE_2F_3(CN_2)_2$, which were reported in the symmetry-equivalent space group *C*2/*c* [21]. Motivated by the white appearance and air stability of $NaLa_2F_3(CN_2)_2$, prompted an investigation of its luminescence properties upon Eu^{3+} doping, described in a following section.

The structure of $NaLa_2F_3(CN_2)_2$ contains one La^{3+} site, one Na^+ site, two crystallographically distinct fluorine sites, and a nearly linear carbodiimide anion $[NCN]^{2-}$. The La^{3+} cation is surrounded by five nitrogen atoms from $[NCN]^{2-}$ ligands and by four fluorine atoms, forming a $[La(NCN)_5F_4]$ polyhedron (Figure 3) that can be described as distorted tricapped trigonal prism. The La—N distances range from 2.632(1) to 2.699(2) Å, while the La—F distances are shorter, between 2.201(1) and 2.546(1) Å. These polyhedra are connected through shared fluorine atoms and bridging carbodiimide ligands, giving rise to a three-dimensional framework. The Na^+ ion occupies interstitial positions in this network and are surrounded by three fluorine atoms and two nitrogen atoms from $[NCN]^{2-}$ ligands, resulting in a distorted tetragonal-pyramidal environment (Figure 3).

TABLE 1 | Selected crystal and structure refinement data for $NaLa_2F_3(CN_2)_2$ measured at 250 K.

Empirical formula	**$NaLa_2F_3(CN_2)_2$**
CCDC code	2 326 720
Formula weight (g mol^{-1})	437.85
Wavelength (Mo-K$_\alpha$)	0.71073
Crystal system	monoclinic
Space group	*I*2/*a*
Unit cell dimensions (Å)	a = 8.5848(7) b = 6.7559(4) c = 11.3786(8) β = 107.621(8)°
Volume (Å^3)	628.97(8)
Z	4
Calculated density (g cm^{-3})	4.624
Absorption coefficient (mm^{-1})	13.464
Final R indices ($I > 2\sigma$(I))	R_1 = 0.0104 wR_2 = 0.0209
R indices (all data)	R_1 = 0.0112 wR_2 = 0.0212
GooF	1.139

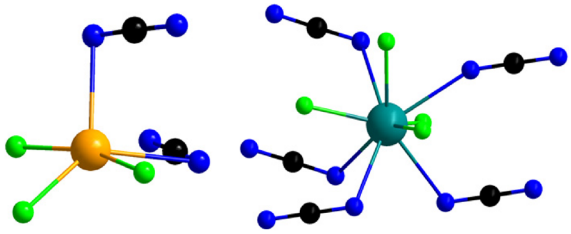

FIGURE 3 | Coordination environment of the sodium atoms (left) and of the lanthanum atoms (right). Fluorine atoms are shown in green, lanthanum in turquoise, sodium in orange, carbon in black, and nitrogen in blue.

The Na—F distances range between 2.201(1) and 2.271(2) Å, and the Na—N bond length of 2.571(2) Å falls within the range reported for sodium carbodiimide analogs [22–24]. The $[NCN]^{2-}$ ion includes an N—C—N angle of 178.5(2)° and C—N bond lengths of $d_{C1\text{-}N1}$ = 1.246(2) Å and $d_{C1\text{-}N2}$ = 1.220(4) Å, shown in Figure 4. The terminal nitrogen atoms exhibit different coordination modes: N2 binds to two La^{3+} and one Na^+, while N1 is coordinated exclusively with La^{3+}. Thus, the $[NCN]^{2-}$ group acts as a bridging ligand, linking La-centered polyhedra and simultaneously connecting to the Na sublattice. Infrared (IR) spectroscopy supports this assignment (Figure 5), showing the

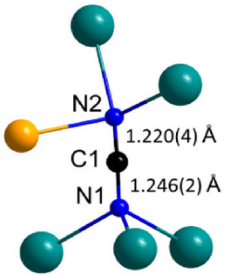

FIGURE 4 | Representation of the $[NCN]^{2-}$ anion with its surrounding in the structure of $NaLa_2F_3(CN_2)_2$. Lanthanum atoms are shown in turquoise and the sodium atom is displayed in orange.

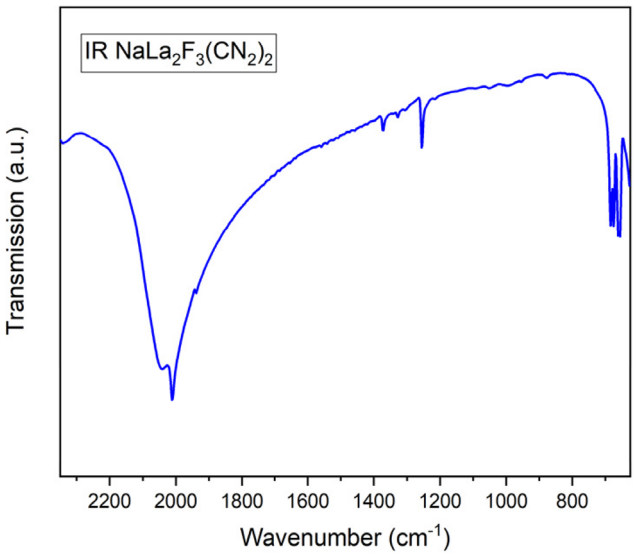

FIGURE 5 | Infrared spectrum of $NaLa_2F_3(CN_2)_2$.

15213749, 0, Downloaded from https://onlinelibrary.wiley.com/doi/10.1002/zaac.202500221 by Universitatsbibliothek, Wiley Online Library on [29/12/2025]. See the Terms and Conditions (https://onlinelibrary.wiley.com/terms-and-conditions) on Wiley Online Library for rules of use; OA articles are governed by the applicable Creative Commons License

characteristic asymmetric stretching vibration of $[NCN]^{2-}$ in the region of 2011 cm^{-1} and bending modes at 682, 673, and 656 cm^{-1}, and the appearance of a *pseudo* symmetrical vibration at 1255 cm^{-1} in agreement with other *RE* carbodiimides (Table 2) especially with the isotypic compound $LiPr_2F_3(CN_2)_2$ [21, 25]. The presence of minor fractions of an X-ray–amorphous phase cannot be excluded.

A comparison of $La_2(CN_2)_3$ and $NaLa_2F_3(CN_2)_2$ is particularly meaningful, as both crystallize in the monoclinic space group *I*2/*a* and share La^{3+} cations coordinated by $[NCN]^{2-}$ units. The unit cells of $NaLa_2F_3(CN_2)_2$ and $La_2(CN_2)_3$ both reveal a layered arrangement (Figure 6). In $La_2(CN_2)_3$, La^{3+} is coordinated exclusively by carbodiimide ligands, forming nearly regular $[La(NCN)_8]$ dodecahedra (Figure 6, right). The absence of additional ions leads to a more compact layering. In $NaLa_2F_3(CN_2)_2$, by contrast, fluorine competes with carbodiimide nitrogen atoms for coordination, giving rise to distorted La-centered polyhedra. Unlike $La_2(CN_2)_3$ or other *RE* carbodiimides, the layers in $NaLa_2F_3(CN_2)_2$ consist of alternating La—F and carbodiimide-fluorine arrangements. Within the carbodiimide layers, sodium cations are incorporated into the $[NCN]^{2-}$ sublattice (Figure 6 left), producing a more open and less compact stacking motif than in $La_2(CN_2)_3$.

This reduced compactness can be rationalized by the fact that one $[NCN]^{2-}$ unit of the binary structure ($La_2(CN_2)_3$) is replaced by a Na^+ ion. This replacement formally leaves a negative charge imbalance, which is compensated by the incorporation of three additional fluoride anions, thereby preserving overall charge neutrality. Thus, the altered stoichiometry does not simply reflect a loss of carbodiimide units, but rather a redistribution of anions between $[NCN]^{2-}$ and F^-, stabilized by the mixed-cation environment. From a formal perspective, the structure of $NaLa_2F_3(CN_2)_2$ can therefore be regarded as an alkali-salt derivative of $La_2(CN_2)_3$, corresponding to an idealized ionic partitioning into $[NaF_3][La_2(CN_2)_2]$. Alternatively it may be interpreted as an sodium fluoride adduct to the previously reported compound $LaF(CN_2)$ [21], corresponding to the formula $NaF{\cdot}2LaF(CN_2)$.

TABLE 2 | Selected vibrational frequencies from rare-earth carbodiimides [5, 21, 25, 26].

Compound	$\upsilon_{as}[NCN]^{2-}$ (cm^{-1})	$\upsilon_{s}[NCN]^{2-}$ (cm^{-1})	$\delta[NCN]^{2-}$ (cm^{-1})
$La_2(CN_2)_3$	2029, 1929	—	685, 660, 621
$Lu_2(CN_2)_3$	2080, 2009	—	680, 640
$NaLa_2F_3(CN_2)_2$	2011	1255	683, 675, 656
$LiPr_2F_3(CN_2)_2$	2024	1260	682,673,646
$BaZn(CN_2)_2$	2038, 1975	1249	678, 663, 641

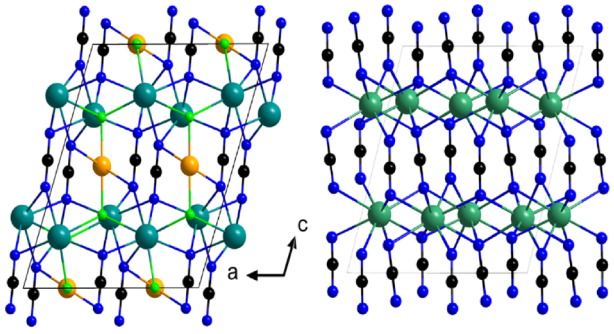

FIGURE 6 | Comparison of the unit cell of $NaLa_2F_3(CN_2)_2$ (left) and $La_2(CN_2)_3$ (right). Fluorine atoms are shown in green, lanthanum in turquoise, sodium in orange, carbon in black, and nitrogen in blue.

2.3 | Photoluminescence Properties of $NaLa_2F_3(CN_2)_2$: Eu^{3+}

Lanthanide-doped carbodiimides and related mixed-anion compounds have recently attracted considerable attention as promising luminescent materials due to their structural diversity and the possibility to fine-tune their optical properties by variation of the host lattice anions [18, 27, 28]. In particular, Eu^{3+} ion is well-established activator, providing sharp 4f–4f emission lines in the red and near-infrared (NIR) spectral regions, respectively, which are of high relevance for applications in phosphors, displays, and optoelectronic devices. The incorporation of these activators into oxide carbodiimide and cyanamide-based hosts such as $La_2O_2(CN_2)$ [29], $La_3Cl(CN_2)O_3$ [9], or related mixed-anion systems has demonstrated that the local coordination environment and symmetry of the *RE* sites strongly influence excitation pathways and emission intensities. With this background, the luminescence properties of europium-doped $NaLa_2F_3(CN_2)_2$ were investigated. The excitation spectrum of $NaLa_2F_3(CN_2)_2$:Eu (Figure 7), monitored for the intraconfigurational $^5D_0$–$^7F_2$ transition at 613 nm, displays a broad and intense band centered at 302 nm. This feature is attributed to a ligand-to-metal charge transfer from the $[NCN]^{2-}$ groups to Eu^{3+}, with the relatively low energy of the transition reflecting the high polarizability of the carbodiimide anions.

Additional weak excitation bands in the near UV and visible range correspond to characteristic 4f–4f transitions of the [Xe] $4f^6$ configuration, observed at 361 nm ($^7F_1$–$^5G_5$), 394 nm ($^7F_0$–$^5L_6$), and 465 nm ($^7F_0$–$^5D_2$). The emission spectrum recorded under excitation at 302 nm consists of five bands located at 578, 593, 613, 653, and 706 nm, which are assigned to the $^5D_0$–^7F_J transitions with $J = 0$–4. Notably, the Eu^{3+} emission is dominated by the $^5D_0$–$^7F_4$ transition. The unusually strong intensity of the $^5D_0$–$^7F_4$ emission of Eu^{3+} can be attributed to the local geometry of the activator site. A low site symmetry combined with the high polarizability of the surrounding anion ($[NCN]^{2-}$) enhances the Judd–Ofelt parameter Ω_4, thereby increasing the transition probability according to the Judd–Ofelt formalism [30, 31]. As a result, the $^5D_0$–$^7F_4$ band, which is typically weak in many host matrices, becomes particularly intense in the present compound [32–34]. This observation contrasts with the more common case where the $^5D_0$–$^7F_2$ hypersensitive transition dominates the Eu^{3+} emission, reflecting its stronger dependence on asymmetry in the local environment. This unusual dominance of the $^5D_0$–$^7F_4$ emission highlights the strong impact of the host lattice geometry and ligand polarizability on the Eu^{3+} emission profile and underlines the

15213749, 0, Downloaded from https://onlinelibrary.wiley.com/doi/10.1002/zaac.202500221 by Universitatsbibliothek, Wiley Online Library on [29/12/2025]. See the Terms and Conditions (https://onlinelibrary.wiley.com/terms-and-conditions) on Wiley Online Library for rules of use; OA articles are governed by the applicable Creative Commons License

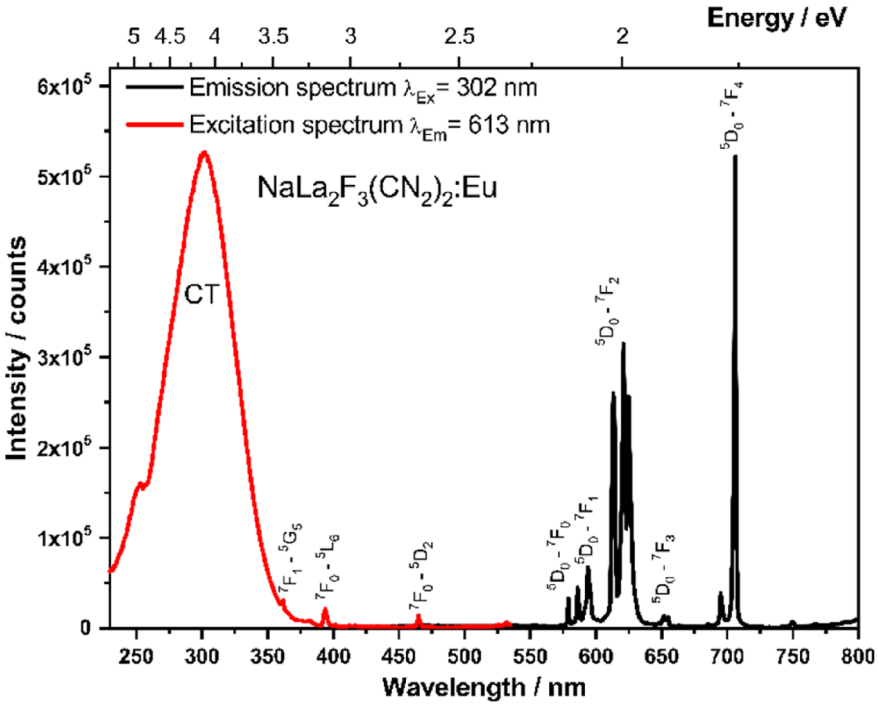

FIGURE 7 | Excitation and emission spectra of $NaLa_2F_3(CN_2)_2:Eu^{3+}$.

potential of carbodiimide-based mixed-anion compounds as versatile platforms for tuning lanthanide luminescence.

3 | Conclusions

The mixed-anion compound $NaLa_2F_3(CN_2)_2$ was synthesized and structurally characterized. Its framework is built from distorted La polyhedra, in which fluorine and carbodiimide ligands create an asymmetric coordination environment. These distortions, together with the polarizability of the $[NCN]^{2-}$ groups, strongly affect the local electronic structure. Eu^{3+}-doped $NaLa_2F_3(CN_2)_2$ shows the expected $^5D_0-^7F_J$ ($J = 0–4$) emissions, but with an intense $^5D_0-^7F_4$ band. This enhancement is linked to the low-symmetry La sites and can be explained by an increased Ω_4 parameter in Judd–Ofelt theory. Overall, the results highlight the structural flexibility of carbodiimide-based mixed-anion hosts and their potential for tailoring lanthanide luminescence.

4 | Experimental Section and Calculation Details

4.1 | Synthesis of $NaLa_2F_3(CN_2)_2$

Stoichiometric (1:1) amounts of LaF_3 (anhydrous, ≥99.99%) and $Na_2(CN_2)$ were weighed in an argon-filled glovebox and thoroughly homogenized in an agate mortar. For luminescence studies, EuF_3 (2 mol-%, corresponding to $NaLa_{2.96}Eu_{0.04}F_3(CN_2)_2$) was added to the mixture, as a substitute for some LaF_3. The resulting reaction mixtures were transferred into a niobium or alternatively a copper ampoule, which was sealed under argon in a quartz container [35]. The reaction was carried out in a muffle furnace at 550°C for 12 h with heating and cooling rates of 2 K min^{-1}. After cooling to room temperature, the metathesis salt (NaF) and minor impurities were washed several times with deionized water, followed by drying in an oven (110°C). The final products were obtained in high purity as air-and moisture-stable white crystalline powders with an estimated yield of 95%.

4.2 | Synthesis of $Na_2(CN_2)$

The syntheses od $Na_2(CN_2)$ was carried out in Schlenk tubes with a length of 40 cm and an inner diameter of 35 mm, closed with a GL45 cap equipped with a silicon seal (Schott AG, Mainz, Germany). The starting materials NaH and $Na(HCN_2)$ were mixed in a 1:1 molar ratio and homogenized in an agate mortar, inside a glove box under argon atmosphere. The mixture was transferred into an open vial (Chroma Globe, Kreuzau, Germany) and subsequently placed into the Schlenk tube. The synthesis was carried out analogous to a previously reported procedure [35]. The tube was heated in a Simon–Müller furnace at 450°C with heating and cooling rates of 2 K min^{-1} and a holding time of 30 min. The reaction yielded $Na_2(CN_2)$ together with $Na_5(CN)(CN_2)_2$ [36] as a side phase (estimated < 15%).

4.3 | Single-Crystal XRD

Single-crystal XRD studies were performed using a Rigaku XtaLab Synergy-S diffractometer with monochromatic Mo-K_α (λ = 0.71073 Å) radiation and a mirror monochromator. Measurements were conducted under N_2 cooling at 250 K. Corrections for absorption effects of the X-ray intensities were applied with a numerical method using CrysAlisPro 1.171.43.121 (Rigaku Oxford Diffraction, 2024) [37]. The structure was solved by ShelXT (Sheldrick, 2008) [38] and refined against F^2 by full-matrix least squares with ShelXL 2019/3 (Sheldrick, 2015) [39] as implemented in Olex2 1.5-ac5–024

15213749, 0, Downloaded from https://onlinelibrary.wiley.com/doi/10.1002/zaac.202500221 by Universitatsbibliothek, Wiley Online Library on [29/12/2025]. See the Terms and Conditions (https://onlinelibrary.wiley.com/terms-and-conditions) on Wiley Online Library for rules of use; OA articles are governed by the applicable Creative Commons License

(Dolomanov et al., 2009) [40]. A Rietveld fit of the recorded powder pattern was performed with Winplotr (Fullprof).

4.4 | Powder XRD

The powder samples were analyzed using an X-ray powder diffractometer (STOE Darmstadt, STADI-P, Ge-monochromator) with Cu-Kα_1 radiation ($\lambda = 154.0598$ pm) in the 2θ range between 5° and 120°.

4.5 | IR Spectroscopy

IR spectra were recorded using a VERTEX 70 FT-IR Spectrometer in the range of 400–4000 cm^{-1} using KBr pellets of $NaLa_2F_3(CN_2)_2$. Samples were prepared in a glove-box under argon atmosphere.

4.6 | Photoluminescence Spectroscopy

Excitation and emission spectra of $NaLa_2F_3(CN_2)_2$:Eu were obtained on an Edinburgh Instruments FLS920 fluorescence spectrometer equipped with a 450 W xenon discharge lamp (OSRAM) as the excitation source. For powder measurements, a mirror optic was installed inside the sample chamber. Detection was carried out using a Hamamatsu R2658P single-photon-counting photomultiplier tube. Temperature-dependent measurements were performed with an Oxford Instruments 'MicrostatN' cryostat attached to the spectrometer, using liquid nitrogen as the cooling medium. Photoluminescence decay curves were also recorded with the FLS920 system, employing a 375 nm picosecond laser diode (Edinburgh Instruments) for the excitation pulses.

Acknowledgments

The authors gratefully acknowledge the support provided by the Deutsche Forschungsgemeinschaft (DFG-Bonn) for this research project (ME 914/34–1).

Open Access funding enabled and organized by Projekt DEAL.

Conflicts of Interest

The authors declare no conflicts of interest.

Data Availability Statement

Crystallographic data have been deposited at the Cambridge Crystallographic Data Centre (CCDC) under the following deposition number: 2326720.

References

1. H.-J. Meyer, "Solid State Metathesis Reactions as a Conceptual Tool in the Synthesis of New Materials," *Dalton Transactions* 39 (2010): 5973–5982.

2. M. Neukirch, S. Tragl, and H.-J. Meyer, "Syntheses and Structural Properties of Rare Earth Carbodiimides," *Inorganic Chemistry* 45 (2006): 8188–8193.

3. J. Glaser, L. Unverfehrt, H. Bettentrup, G. Heymann, H. Huppertz, T. Jüstel, H. -J. Meyer, "Crystal Structures, Phase-Transition, and Photoluminescence of Rare Earth Carbodiimides," *Inorganic Chemistry* 47 (2008): 10455–10460.

4. O. Reckeweg and F. J. DiSalvo, "$EuCN_2$ —The First, but Not Quite Unexpected Ternary Rare Earth Metal Cyanamide," *Zeitschrift für Anorganische und Allgemeine Chemie* 629 (2003): 177–179.

5. P. Schneiderhan, E. Bayat, M. Ströbele, D. Enseling, T. Jüstel, and H.-J. Meyer, "$La_2(CN_2)_3$ –The Missing Link of Rare-Earth Carbodiimides, Prepared Through an Efficient Synthetic Route and its Ce^{3+} Activated Photoluminescence," *Dalton Transactions* 54 (2025): 4909–4917.

6. A. T. Schwarz, M. Ströbele, and H.-J. Meyer, "The Mixed-Anion Compound $La_2S_2(CN_2)$," *Zeitschrift für Anorganische und Allgemeine Chemie* 650 (2024): e202400038.

7. Y. Hashimoto, M. Takahashi, S. Kikkawa, and F. Kanamaru, "Syntheses of Rare Earth Dioxymonocyanamides ($Ln_2O_2CN_2$, Ln = La, Ce, Pr, Nd, Sm, Eu, Gd)," *Journal of Solid State Chemistry* 114 (1995): 592–594.

8. R. Srinivasan, M. Ströbele, and H.-J. Meyer, "Chains of [RE_6] Octahedra Coupled by (NCN) Links in the Network Structure of $RE_2Cl(CN_2)N$. Synthesis and Structure of Two Novel Rare Earth Chloride Carbodiimide Nitrides with Structures Related to the RE_2Cl_3 Type," *Inorganic Chemistry* 42 (2003): 3406–3411.

9. M. Kubus, D. Enseling, T. Jüstel, and H.-J. Meyer, "A Luminescent Material: $La_3Cl(CN_2)O_3$ Doped with Eu^{3+} or Tb^{3+} Ions," *European Journal of Inorganic Chemistry* 2013 (2013): 3195–3199.

10. D. Dutczak, A. Siai, M. Ströbele, D. Enseling, T. Jüstel, and H.-J. Meyer, "Solid-State Preparation and Luminescence Investigation of Rare Earth Iodide Carbodiimide Nitrides $RE_2I(CN_2)N$ (RE = La, Gd) and $LaI(CN_2)$," *European Journal of Inorganic Chemistry* 2020 (2020): 3954–3958.

11. W. Liao and R. Dronskowski, "Crystal Structures of Extended Europium Cyanamide–Carbodiimide Compounds Derived from Different Reaction Conditions: Temperature-Controlled Syntheses of $In_{0.08}Eu_4(NCN)_3I_3$, $Eu_8I_9(CN)(NCN)_3$, and $In_{0.28}Eu_{12}(NCN)_5I_{14.91}$," *Inorganic Chemistry* 45 (2006): 3828–3830.

12. W. Liao and R. Dronskowski, "Carbodiimides with Extended Structures by an Azide-Cyanide Route: Synthesis and Crystal Structure of M_2Cl_2NCN (M = Eu and Sr)," *Zeitschrift für Anorganische und Allgemeine Chemie* 631 (2005): 496–498.

13. L. Unverfehrt, M. Ströbele, J. Glaser, T. Langer, R. Hoffmann, R. Pöttgen, H. -J. Meyer, "Refined Crystal Structure and Idealized Structure of Mixed-Valent $Eu_4F_5(CN_2)_2$: Transition Possible," *Inorganic Chemistry* 50 (2011): 6010–6018.

14. L. Unverfehrt, M. Ströbele, and H.-J. Meyer, "$LaSr_3F_5(CN_2)_2$: A Prototype Structure for Mixed-Valent $Eu_4F_5(CN_2)_2$," *Inorganic Chemistry* 51 (2012): 12925–12928.

15. J. Glaser and H. J. Meyer, "Multilateral Solid-State Metathesis Reactions for the Preparation of Materials with Heteroanions: The $[Si(CN_2)_4]^{4-}$ Ion," *Angewandte Chemie International Edition* 47 (2008): 7547.

16. M. Kalmutzki, D. Enseling, J. E. Wren, S. Kroeker, V. V. Terskikh, T. Jüstel, H. -J. Meyer, "Solid State Complex Chemistry: Formation, Structure, and Properties of Homoleptic Tetracyanamidogermanates $RbRE[Ge(CN_2)_4]$ (RE= La, Pr, Nd, Gd)," *Inorganic Chemistry* 52 (2013): 12372.

17. J. Glaser, H. Bettentrup, T. Jüstel, and H.-J. Meyer, "Synthesis and properties of tetracyanamidosilicates $ARE[Si(CN_2)_4]$," *Inorganic Chemistry* 49 (2010): 2954–2959.

18. D. Dutczak, M. Ströbele, D. Enseling, T. Jüstel, and H.-J. Meyer, "$Eu_2(CN_2)_3$ and $KEu[Si(CN_2)_4]$: Missing Members of the Rare Earth Metal Carbodiimide and Tetracyanamidosilicate Series," *European Journal of Inorganic Chemistry* 25 (2016): 4011–4016.

15213749, 0, Downloaded from https://onlinelibrary.wiley.com/doi/10.1002/zaac.202500221 by Universitatsbibliothek, Wiley Online Library on [29/12/2025]. See the Terms and Conditions (https://onlinelibrary.wiley.com/terms-and-conditions) on Wiley Online Library for rules of use; OA articles are governed by the applicable Creative Commons License

19. A. Siai, C.-D. Brand, M. Ströbele, D. Enseling, T. Jüstel, and H.-J. Meyer, "Carbodiimide Bridged Network Structure of $[RE_6O(NCN)_6]$ Clusters in the Structure of $RE_8O(CN_2)_{10}Br_2$, RE = La, Ce, Pr, Nd," *Journal of Cluster Science* 34 (2023): 1001–1008.

20. L. Unverfehrt, M. Ströbele, and H.-J. Meyer, "The New Carbodiimide $Li_2Gd_2Sr(CN_2)_5$ Having a Crystal Structure Related to That of $Gd_2(CN_2)_3$," *Zeitschrift für Anorganische und Allgemeine Chemie* 639 (2013): 84–88.

21. L. Unverfehrt, J. Glaser, M. Ströbele, S. Tragl, K. Gibson, and H.-J. Meyer, "The Versatility of Solid-State Metathesis Reactions: From Rare Earth Fluorides to Carbodiimides," *Zeitschrift fur Anorganische und Allgemeine Chemie* 635 (2009): 479–483.

22. M. Becker, J. Nuss, M. Jansen, "Synthese und Charakterisierung von Natriumcyanamid," *Zeitschrift für Anorganische und Allgemeine Chemie* 626 (2000) 2505–2508.

23. A. J. Corkett, K. Chen, and R. Dronskowski, "It's All in the (Cyanamide) Tilt: Synthesis and Structure of $NaSc(NCN)_2$," *European Journal of Inorganic Chemistry* (2020): 2596–2602.

24. K. Dolabdjian, C. Castro, and H.-J. Meyer, "Layered Carbodiimides $A_2M(CN_2)_3$ with Tetravalent Cations M = Sn, Zr, and Hf," *European Journal of Inorganic Chemistry* 14 (2018): 1624–1630.

25. A. J. Corkett, P. M. Konze, and R. Dronskowski, "Synthesis, Crystal Structure, and Chemical-Bonding Analysis of $BaZn(NCN)_2$," *Inorganics* 6 (2018): 1.

26. M. Neukirch, Dissertation, Eberhard Karls Universität Tübingen, (2007).

27. K. Dolabdjian, C. Schedel, D. Enseling, T. Jüstel, and H.-J. Meyer, "Synthesis, Luminescence and Nonlinear Optical Properties of Homoleptic Tetracyanamidogermanates $ARE[Ge(CN_2)_4]$ (A = K, Cs, and RE = La, Ce, Pr, Nd, Sm, Eu, Gd)," *Zeitschrift für Anorganische und Allgemeine Chemie* 643 (2017): 488–494.

28. J. Goldmann, T. Pier, and T. Jüstel, "On the luminescent properties of Eu^{3+} doped $La_2Hf_3(WO_4)_9$," *Journal of Luminescence* 280 (2025): 121091.

29. X. Guo, J. Wang, X. Dong, W. Yu, and G. Liu, "New strategy to Achieve $La_2O_2CN_2$:Eu^{3+} Novel Luminescent One-Dimensional Nanostructures," *CrystEngComm* 16 (2014): 5409–5417.

30. B. R. Judd, "Optical Absorption Intensities of Rare-Earth Ions," *The Physical Review* 127 (1962): 750–761.

31. G. S. Ofelt, "Intensities of Crystal Spectra of Rare-Earth Ions," *The Journal of Chemical Physics* 37 (1962): 511–520.

32. R. A. Sá Ferreira, S. S. Nobre, C. M. Granadeiro, H. I. S. Nogueira, L. D. Carlos, and O. L. Malta, "A Theoretical Interpretation of the Abnormal $^5D_0 \rightarrow {}^7F_4$ Intensity based on the Eu^{3+} Local Coordination in the $Na_9[EuW_{10}O_{36}]\cdot 14H_2O$ Polyoxometalate," *Journal of Luminescence* 121 (2006): 561–567.

33. W.-L. Chan, Z. Liu, S. Lu, P. A. Tanner, and K.-L. Wong, "The Reported Anomalous Emission Intensity of the $^5D_0 \rightarrow {}^7F_4$ transition of Eu^{3+} in a Molybdate Double Perovskite," *Journal of Materials Chemistry C* 3 (2015): 960–963.

34. L. Xiang, X. Zhou, L. Li, F. Ling, Y. Li, J. Li, H. Yang , "Comparative Study on the Anomalous Intense $^5D_0 \rightarrow {}^7F_4$ emission in Eu^{3+} doped Sr_2MNbO_6 (M=Ga, In, Gd) phosphors," *Journal of Luminescence* 267 (2024): 120370.

35. M. Ströbele, E. Bayat, and H.-J. Meyer, "A Systematic Study of the Solid-State Pathway from Melamine via Melaminate to Carbodiimide under Evolution of Hydrogen," *Inorganic Chemistry* 63 (2024): 16565–16572.

36. S. Zhang, D. A. Zherebtsov, F. J. DiSalvo, and R. Niewa, "$Na_5[CN_2]_2[CN]$, $(Li, Na)_5[CN_2]_2[CN]$, and $K_2[CN_2]$: Carbodiimides from High-Pressure Synthesis," *Zeitschrift fur Anorganische und Allgemeine Chemie* 638 (2012): 2111–2116.

37. CrysAlisPro Software System Rigaku Oxford Diffraction (2024).

38. G. M. Sheldrick, "A Short History of SHELX," *Acta Crystallographica. Section A* 64 (2008): 112–122.

39. G. M. Sheldrick, "Crystal structure refinement with SHELXL," *Acta Crystallographica. Section C* 71 (2015): 3–8.

40. O. V. Dolomanov, L. J. Bourhis, R. J. Gildea, J. A. K. Howard, and H. Puschmann, "OLEX2: a Complete Structure Solution, Refinement and Analysis Program," *Journal of Applied Crystallography* 42 (2009): 339–341.

15213749, 0, Downloaded from https://onlinelibrary.wiley.com/doi/10.1002/zaac.202500221 by Universitatsbibliothek, Wiley Online Library on [29/12/2025]. See the Terms and Conditions (https://onlinelibrary.wiley.com/terms-and-conditions) on Wiley Online Library for rules of use; OA articles are governed by the applicable Creative Commons License